TECHNISCHE UNIVERSITÄT WIEN

DISSERTATION

Monolithic integration of mid-infrared photonics

ausgeführt zum Zwecke der Erlangung des akademischen Grades eines Doktors der technischen Wissenschaften

unter der Leitung von

Univ.-Prof. Dr. Gottfried Strasser
Institut für Festkörperelektronik

eingereicht an der

Technischen Universität Wien
Fakultät für Elektrotechnik und Informationstechnik

von

Dipl.-Ing. Benedikt Schwarz, B.Sc.

Mat.Nr. 0725036
Kölblgasse 22/29
A-1030 Wien

Wien, November 2015

1. Gutachter: Prof. Gottfried Strasser
2. Gutachter: Prof. Boris Mizaikoff

Tag der mündlichen Prüfung: 27.11.2015

"The importance of QCDs certainly goes beyond the introduction of a novel MIR detection scheme; as these devices share the material system with QCLs, an important step toward future monolithic on-chip integration of light source, waveguide, and detector is expected to be achieved in the near future.", S. Kim, C. Young and B. Mizaikoff on "Miniaturized Mid-Infrared Sensor Technologies" (2007) [1].

Abstract

Mid-infrared spectroscopy is an extremely useful and versatile technique to identify the chemical composition of gases, liquids, and solids via their unique absorption lines. The miniaturization of sensing systems is an important research topic, gaining momentum during the last couple of years. So far, all miniaturized concepts have been demonstrated with external optics, lasers or detectors. This thesis reports the realization of a monolithic approach, combining the source, the interaction region and the detector on a single chip. This work involved the full range and variety from the initial idea and concept development over the design and modelling to the device fabrication and experimental demonstration. Moving from the state-of-the-art to a single-chip solution required several important steps.

In a first step, a new class of intersubband devices was developed combining emission and detection capabilities with the very same semiconductor heterostructure. Simply by changing the applied bias, the quantum cascade device can be switched between laser and detector operation. Once the layer structure has been grown on a substrate, different parts of the chip can be used for lasers and others for detectors. With the introduction of a refined design approach, the horizontal-vertical extraction scheme led to high performance bi-functional quantum cascade laser and detectors with output power levels and efficiencies comparable to conventional lasers. Owing to direct coupling and the optimized quantum design, their photodetection capability provides a better performance than available discrete detectors operated at the same temperature.

In a second step, the lasers and detectors were connected with a surface plasmon polariton (SPP) waveguide. SPPs are optical surface waves that propagate along a metal/dielectric interface and are perfectly suited for on-chip sensing applications. Owning to their evanescent nature, 96% of the mode stays outside and interacts with substances, which are present on the waveguide surface. The introduction of the dielectric loading concept for mid-infrared plasmonics enabled to solve several fundamental problems that previously prohibited the exploitation of their full potential. The commonly weakly confined SPPs are squeezed, such that they are stronger bound to the interface and enable the direct coupling to and from the active devices. Furthermore, the elimination of the metal edges in narrow, laterally single mode waveguides leads to a reduction of the attenuation by one order of magnitude.

In a first prototype experiment, the entire device was submerged into a mixture of ethanol and water. A limit of detection of 0.06% over a wide range of concentrations from

0 to 60% clearly demonstrated the huge potential of the presented integration concept. In a second experiment, the device was extended to a multi-wavelength sensor combining multiple laser/waveguide/detector elements, each sensitive to another wavelength. Narrow mode laser emission at defined wavelengths was achieved by incorporating distributed feedback gratings on the laser waveguides. The additional spectral information, as well as the reduction of pulse-to-pulse and temperature induced noise provides the capability to detect single or multiple chemicals in a complex mixture of chemicals with ppm resolution.

The presented on-chip concept is now at a stage, where it can be adapted to particular applications. This thesis provides the required information and background of all electrical and optical parts and initializes a new class of miniaturized sensing devices.

Kurzfassung

Wie viel Glucose ist im Blut, wie sauber ist das Wasser oder wie rein ist der Treibstoff? Um diese Fragen zu beantworten benötigt man kompakte Sensorsysteme, die vor Ort eine schnelle Antwort liefern. Diese Arbeit beschreibt einen neuartigen Sensor-Chip mit dem genau das erreicht werden kann – ausgehend von der Idee und der Konzeptentwicklung über elektrisches und optisches Design bis hin zur Fertigung und experimentellen Realisierung. Laserstrahlen im Infrarotbereich werden von unterschiedlichen Molekülen unterschiedlich stark absorbiert. Basierend auf diesem einfachen Prinzip wurde eine neue Sensortechnologie realisiert, die alle notwendigen Komponenten, wie Laser, Interaktionszonen für chemische Stoffe und Detektoren durch die Kombination von Quantenkaskaden Strukturen und Oberflächenplasmonen auf einem einzigen Chip integriert.

Ein ganz spezielles Quantendesign ermöglicht es, einen Laser und einen Detektor aus ein und der selben Schichtfolge gleichzeitig auf einem Chip herzustellen – und zwar so, dass die Wellenlänge des Laserlichtes auch genau der Wellenlänge entspricht, welche vom Detektor gemessen werden kann. Mit einem verbessertem Design, dem Horizonal-Vertikal-Extraktionskonzept, konnte die optische Leistung im Laserbetrieb von der bi-funktionalen Quanten Kaskaden Laser/Detektor Strukturen um eine Größenordnung verbessert werden. Damit erreicht die zweite Generation vergleichbare optische Leistungen wie reine Laserdesigns. Zusätzlich erlaubt das vorgestellte Integrationskonzept die Verwendung von direkt gekoppelten Wellenleiter-Detektoren. Die Wellenleiterstruktur und die optimierten Quantenstrukturen erlauben integrierte Detektoren mit höherer Leistungsfähigkeit im Vergleich zu ungekühlten externen Detektoren.

Verbunden werden Laser und Detektoren mit einem speziellen Oberflächenplasmonen-Wellenleiter. Oberflächenplasmonen sind elektromagnetische Wellen, die sich an einer Grenzschicht zwischen einem Metall und einem Dielektrikum ausbreiten. Das Licht wird an dessen Außenseite geführt und kann dort mit den Molekülen wechselwirken und abhängig von ihrer Art unterschiedlich stark absorbiert werden. Ein zusätzlicher Trick erlaubt es, gleich mehrere Probleme zu lösen, die die Anwendbarkeit von Oberflächenplasmonen im mittleren Infrarotbereich bisher stark limitiert haben. Eine nur 200 nm dünne dielektrische Schicht aus Siliziumnitrit führt zu stärker gebundenen Moden und ermöglicht die gezielte Optimierung der Kopplung zu den Lasern und Detektoren. Weiters kann die dünne dielektrische Schicht zur lateralen Wellenführung verwendet werden und verhindert damit optische Verluste durch Streuung an Metallkanten.

Getestet wurden die Sensoren mit einer Lösung aus Wasser und Ethanol. In einem ersten Experiment konnte die Zusammensetzung über einen weiten Konzentrationsbereich auf 0.06% genau bestimmt werden. Um eine Auflösung im ppm-Bereich zu ermöglichen, wurde der Sensor-Chip mit schmalbandig Lasern und integrierter Temperaturüberwachung erweitert. Mehrere solcher Laser/Wellenleiter/Detektor-Elemente auf dem selben Chip können verwendet werden, um mehrere chemische Substanzen gleichzeitig zu identifizieren.

Das präsentierte Integrationskonzept ist der Startpunkt für eine neue Generation von miniaturisierten Sensoren für chemische und biologische Analysen. Mit der Wahl der Wellenlänge kann der Sensor-Chip auf eine Vielzahl verschiedener Stoffe angepasst werden und durch die Integration aller Komponenten ist er klein und kostengünstig. Diese Arbeit beinhaltet alle notwendigen Schritte und Informationen, um den Sensor-Prototypen auf spezifische Anwendungen anzupassen.

Acknowledgement

The time as a PhD student was a great experience, which I would never want to miss. The great people that contributed to this work were a main reason for the pleasure and the scientific outcome. I am very grateful to all group members for their collaboration and contributions to the scientific work, but also for the nice work environment, the discussions during the coffee breaks and the many after work events. The cheese, wine and whiskey tastings and the joint activities at conferences: the Mauterndorf ski race, the midnight bath in the Mediterranean see were important parts beside the many hours in the lab and the nervous minutes before the talks.

Special thanks go to my advisor, Prof. Gottfried Strasser for giving me the opportunity to work in his group, his great support and guidance. I am very thankful for his initial idea that triggered this work and the support for curiosity driven research that allowed me to follow my own ideas. In this thesis, you will find the ones that led to major results. I would like to thank Peter Reininger with whom I shared and discussed nearly every result during the whole time working on this thesis regardless if it was relevant or not. Many thanks go to Daniela Ristanic for the close collaboration during the last two years, which was a great enrichment for both, the scientific output and the work atmosphere. I am thankful to Werner Schrenk for his great support and the many fruitful and sometimes demanding discussions that led to important ideas and improvements. His advise often saved me a lot of time. The work on detectors was greatly supported by Stefan Kalchmair and Andreas Harrer, thank you for the collaboration. A special credit goes to our MBE team, Donald McFarland, Tobias Zederbauer, Hermann Detz and Aaron Maxwell Andrews, for providing me in average one grown wafer every seven weeks, enabling many more projects than covered by the 150 pages of this thesis. Further thanks go to Aaron Maxwell Andrews for his valuable comments on the papers, which significantly improved my English scientific writing. A particular acknowledgment goes to Prof. Hans Kosina and Oskar Baumgartner for the collaboration on the device simulator.

I especially would like to thank Prof. Federico Capasso for opportunity to visit his group at Harvard University. It was a great pleasure and benefit for my professional and also personal experience. I am grateful to Tobias Mansuripur for the close collaboration during my research visit and to Antonio Ambrosio for his assistance on the near-field measurements. I am much obliged for Prof. Boris Mizaikoff for the reviewing and co-examination of this PhD thesis. I also thank all other persons that contributed to this

work: the reviewers of the papers, members of the doctoral school Solids4Fun and members of collaborating groups.

Finally many thanks go to my family and my friends. Especially, I thank my girlfriend Simone Schuler for the great support during the entire time of my PhD and for bringing me back to real life the many times I was flying away, lost in my thoughts.

Contents

Chapter 1

Introduction

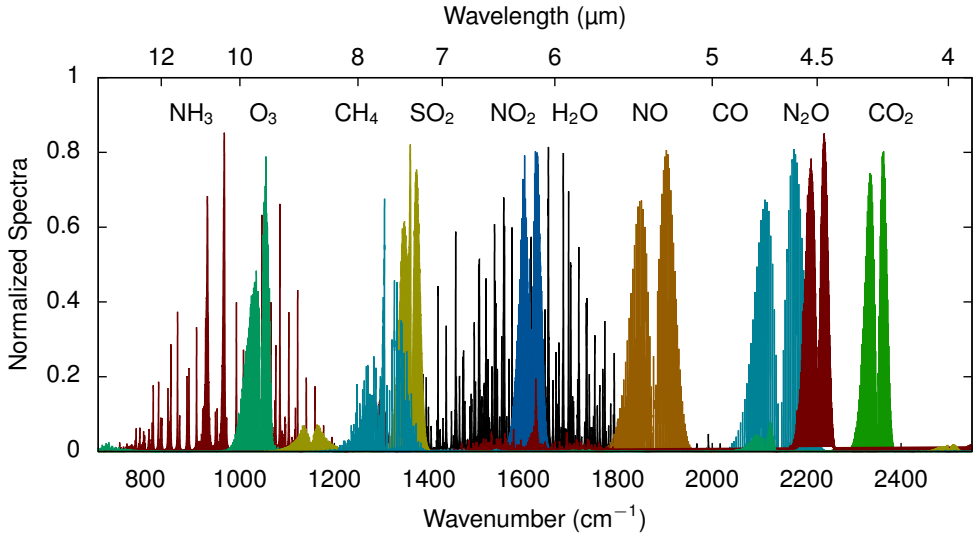

Figure 1.1: "Fingerprint" of several trace gases. The individual absorption features can be identified by measuring the mid-infrared transmission. The data is taken from the Hitran database [2]

The mid-infrared is particularly interesting for chemical spectroscopy, as the fundamental absorption lines of molecules lie exactly in this spectral region, giving rise to the name "Fingerprint" region. The interaction between mid-infrared radiation and the vibration of atoms or atomic groups in molecules allows identification of the chemical composition of gases, liquids, and solids. No other spectral range enables the same sensitivity and selectivity [3]. Mid-infrared spectroscopy is used in a number of applications including chemical sensing, environmental monitoring, as well as label-free medical and microbiological diagnosis. As an example, figure 1.1 shows the mid-infrared aborption spectra of several important trace gases.

Conventional mid-infrared spectroscopic setups typically consist of a broadband SiC thermal source, external optics, such as lenses and mirrors, a broadband detector and a Fourier-transform infrared spectrometer (FTIR). Depending on the application, the beam

may have to be aligned to an additional optical component holding the analyte. For gas sensing this can be a multipass cell, for fluid sensing a fluidic cell, or an attenuated total reflection geometry setup can be used to probe the analyte in the evanescent field. However, these spectroscopic setups are mostly limited to laboratories due to their large footprint.

1.1 QCL based spectroscopy

QCLs are excellent compact and bright sources for spectroscopic applications such as biological and chemical sensing in gas- and liquid-phase [4]. Due to their high optical output power levels, they do not require liquid nitrogen cooled detectors. Their small size enables compact and battery power systems. Fabricated as single mode lasers, they can achieve narrow linewidth as low as 1–3 MHz, which makes them very attractive to identify the sharp absorption lines of gases. In order to identify multiple species, external cavity QCLs have been developed, which are tunable over a wide spectral range of up to $432\,\mathrm{cm}^{-1}$ [5]. QCLs have been fabricated as arrays of DFB lasers to cover a similar broad spectral range [6]. However, their practical used requires beam-combining, which is usually done with diffractive optics [7]. On-chip beam combining has been demonstrated using hybrid integration of InP based QCLs with SiGe waveguides [8]. Particularly interesting are single device approaches that inherently provide single facet emission, such as using sampled grating reflectors [9].

More recently, broadband frequency comb emission from QCLs has been demonstrated [10]. This enabled the realization of a QCL based dual-comb spectroscopy setup which can acquire a high-resolution spectrum in a single shot [11]. Thereby, two combs with slightly different spacing are used and the individual lines are detected via the down-converted RF detector signal. A major goal in the field of QCL frequency combs is to increase the spectral width to cover one octave. This has a significant advantage, as octave spanning combs are inherently stabilized via self-referencing [12].

Tremendous progress in QCL-based sensing systems has been achieved during the last fifteen years. Trace gas detection down to ppb and ppt levels, human breath analysis, remote detection of explosives, and blood serum analysis are just some of their many different applications. The most impressive results for gas sensing have been achieved using multi-pass cells, as well as cavity ring down and photo-acoustic spectroscopy. A sketch of the various techniques is shown in figure 1.2. Multipass cells allow very long interaction paths of several meters in a very small footprint and enable highly sensitive and compact gas sensing systems. They are commonly operated at a reduced pressure to narrow the gas absorption lines and increase the spectral resolution [16, 17]. Cavity ring down spectroscopy utilizes the temporal intensity decay due to induced loss within a high quality factor cavity and is a sensitive and very fast method [18]. Very compact

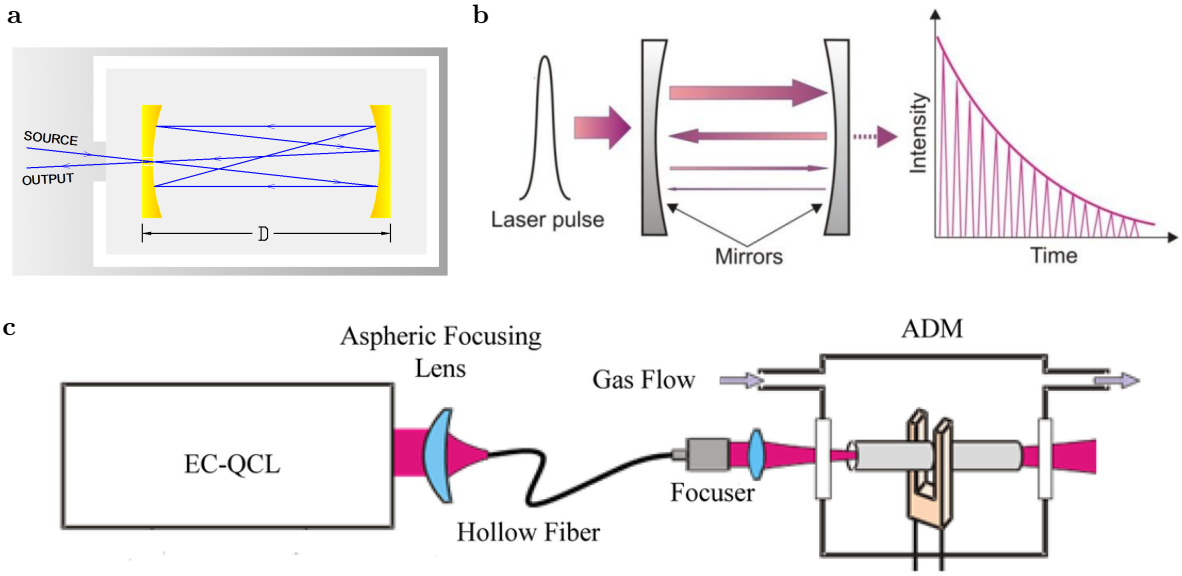

Figure 1.2: Sketch of a multipass cell (a), the cavity ring-down technique (b) and a quartz enhanced photo-acoustic setup (c). Taken from [13–15].

systems can be built using photo-acoustic techniques, in which an acoustic mode is excited by thermally induced expansion of a gas via a modulated high power laser beam at the gas absorption resonance [19]. Impressive results have been achieved using quartz tuning forks or cantilevers with piezoelectric or interferometric detection [15, 20].

Another class of sensing devices is based on waveguide-enhanced techniques, such as hollow fiber for gas detection. As an alternative to flow cells, waveguide-enhanced sensors are very attractive to identify chemical species in liquid phase and have a huge potential for on-chip integration [1, 3]. Integrated chalcogenide waveguides combined with micro-fluidics have been demonstrated in the near-infrared [21], but can also be used in the mid-infrared [22]. A germanium ridge waveguide on silicon, embedded in a micro-fluidic chamber was used to detect cocaine in a liquid solution [23]. Another example is a Mach-Zehnder interferometer built from GaAs/AlGaAs waveguides to measure the refractive index change due to a surrounding liquid. One arm serves as interaction region and the other as a reference [24].

1.2 Motivation and outlook - A single-chip solution

In the last years, technological advances in optics and engineering have enabled the miniaturization of individual optical components such as sources, detectors and waveguides, down to chip scale dimensions. A single chip solution, however, requires the integration of all of these components on the same substrate.

In this thesis, a novel concept for monolithic integration is presented and the first single-chip sensor solution based on mid-infrared spectroscopy is demonstrated. In order

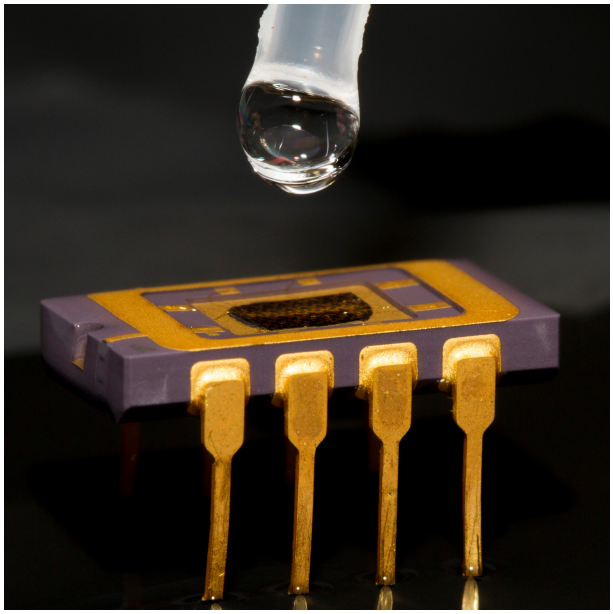

Figure 1.3: Featured image of the publication "Monolithically integrated mid-infrared lab-on-a-chip utilizing plasmonics and quantum cascade structures" published in Nature Communications [25].

to realize this, two major technologies were combined: intersubband devices and plasmonics. In the first step, a new quantum cascade active region was developed, which can be used both as a laser and as a detector. Depending on the applied bias, the heterostructure can generate or detect mid-infrared radiation in the same spectral range. Following an overview on mid-infrared technology in chapter 2 and theoretical discussion of intersubband transitions in chapter 3, the bi-functional quantum cascade laser and detector is introduced in chapter 4. The second step involves the integration of surface plasmon polariton (SPP) waveguides to efficiently guide the light from the laser to the detector. In particular, the concept of dielectric loading has been applied, solving multiple issues that previously prohibited the straightforward use of SPPs at mid-infrared frequencies. The theoretical background and results of dielectric loaded SPPs are presented in chapter 5. Coming to the final result, the first experimental realization of a monolithically integrated mid-infrared lab-on-a-chip is presented in chapter 6.

Chapter 2

Mid-infrared technology - A historic overview

Infrared radiation was discovered around 1800 by W. Herschel [26]. In an experiment, he measured the temperature of the different colors of sunlight using a prism. He discovered that the highest temperature occurs beyond the red end of the spectrum through radiation invisible to the human eye.

The development of the first electronic infrared detectors in the early 19^{th} century was a major breakthrough in the research of infrared radiation [27, 28]. This enabled M. Melloni to prove that infrared radiation follows the rules of reflection, refraction and polarization similar to visible light. In 1866, Maxwell's electromagnetic theory indicated that infrared radiation can be viewed as electromagnetic waves and leads to thermal effects when absorbed by matter [29]. In 1847, H. Fizeau and L. Focault discovered the presence of atmospheric absorption lines in the infrared spectrum.

In 1900, M. Planck explained the radiation spectrum of sunlight, based on modern physics and quantum theory [31]. Planck's law describes the electromagnetic radiation emitted by a black body in thermal equilibrium at a specific temperature, shown in figure 2.1. The power emitted per unit area of the body, per unit solid angle, and per unit wavelength is given by

$$B(\lambda, T) = \frac{2\mathrm{h}c^2}{\lambda^5} \frac{1}{\exp\left(\frac{\mathrm{h}c}{\lambda \mathrm{k_B} T}\right) - 1}, \tag{2.1}$$

where h is the so called Planck constant, c_0 the light in vacuum, λ the optical wavelength, T the temperature of the black body and $\mathrm{k_B}$ the Boltzmann constant.

Today, the infrared region is important for many scientific and industrial applications ranging from telecommunication and imaging to chemical sensing and medical diagnosis. The infrared is commonly split into three regions: the near-infrared (700 nm–3 µm), the mid-infrared (3 µm–50 µm) and the far-infrared, nowadays referred to as THz (50 µm–300 µm).

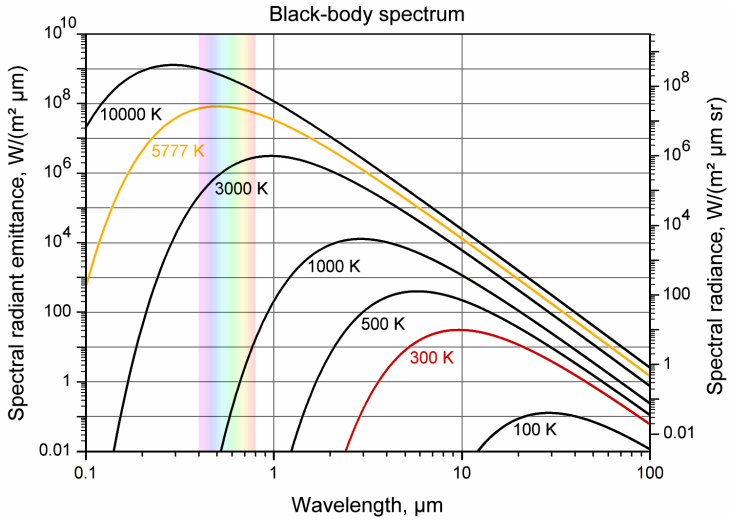

Figure 2.1: Planck's law describing black body radiation spectra for different temperatures [30]. The visible part of the spectrum is highlighted with the particular colors.

2.1 Mid-infrared sources

Sources based on blackbody radiation are still some of the most important sources in the infrared. The so called Globar, a silicon carbide rod heated to $1000 - 1600°C$, is a broadband source commonly used in Fourier transform infrared spectrometers (FTIR). This section gives an overview of available mid-infrared sources, focusing on semiconductor sources. A more detailed description can be found in the books [32, 33].

Early semiconductor sources

Mid-infrared emission with semiconductors was demonstrated in 1963 using InAs and InSb p-n junctions at 3.1 µm and 5.3 µm, respectively [34, 35]. It turned out that IV-VI semiconductors, such as PbTe, PbSn, PbS, PBSe (lead salts) and their compounds were much more promising for mid-infrared lasers [36]. The invention of the double heterostructure laser by Zh.I. Alferov and R.F. Kazarinov, as well as H. Krömer in 1963 [37, 38] and its realization in 1970, as well as the advances in epitaxial growth have led to a significant improvement of mid-infrared lasers. Double heterostructure lasers based on lead salt compounds remained as a standard until 1990. Nowadays, three major technologies for semiconductor mid-infrared lasers are used: antimonide type-II quantum well diode lasers, quantum cascade lasers (QCLs) and interband cascade lasers (ICLs).

Type-II semiconductor diode lasers

The emission wavelength of interband semiconductor lasers is basically limited by the bandgap of the materials used. Several III-V materials with narrow bandgaps are available and can be further tuned using strain engineering, but are limited to wavelength below

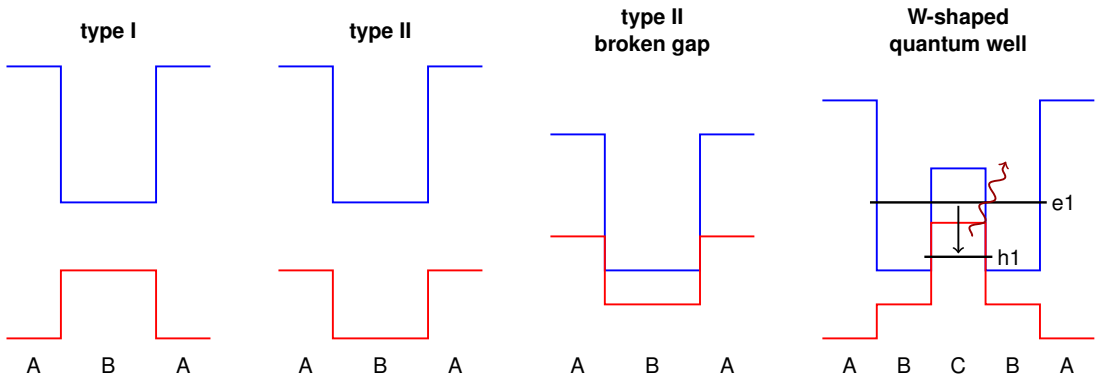

Figure 2.2: Band alignment of type-I, type-II and type-II broken gap semiconductor heterostructures, as well as a type-II "W"-shaped quantum well structure. The broken gap alignment allows smaller emission wavelength and reduced Auger recombination rates.

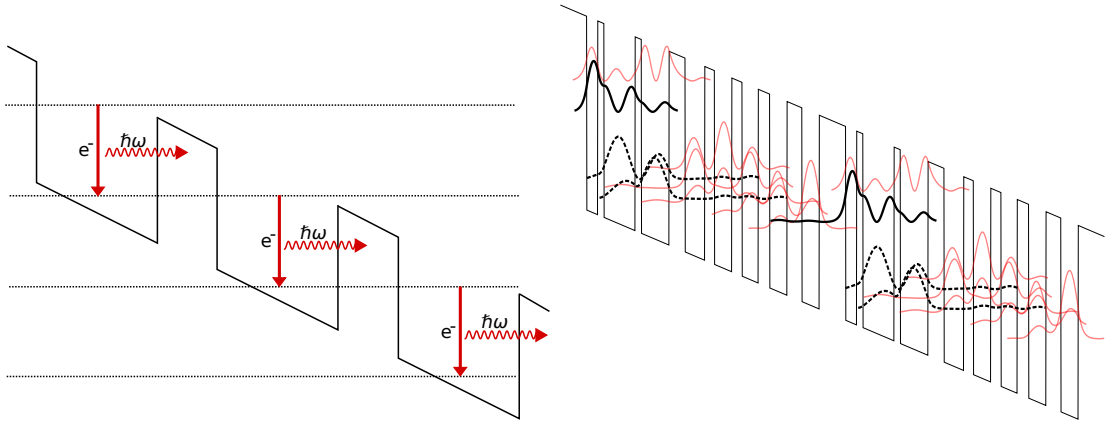

Figure 2.3: Sketch of the cascade concept to recycle electrons (left). Band diagram of a 3-well active region QCL (right). Taken from [41, 42].

3 µm. The extension of the wavelength range is challenging because of the difficultly of epitaxial high quality growth and increasing Auger recombination rates. Using type-II semiconductor heterostructures, such as GaInSb/InAs, it was possible to circumvent this issue. Type II semiconductor quantum wells show a reduced Auger recombination [39] and, using broken gap band alignment, the wavelength limit can be further increased up to approximately 5 µm [40]. Figure 2.2 shows the different heterostructure alignments and a "W"-shaped quantum well structure using a broken gap type-II alignment.

Quantum cascade lasers

QCLs are unipolar devices based on intersubband transitions in a heterostructure of coupled quantum wells. As indicated by the name, the active region is cascaded such that a single electron can lead to multiple stimulated emission processes (see figure 2.3). Following the idea of stimulated emission in superlattices by Kazarinov and Suris [43] in 1971 the QCL was experimentally demonstrated about two decades later by Faist et al. [44].

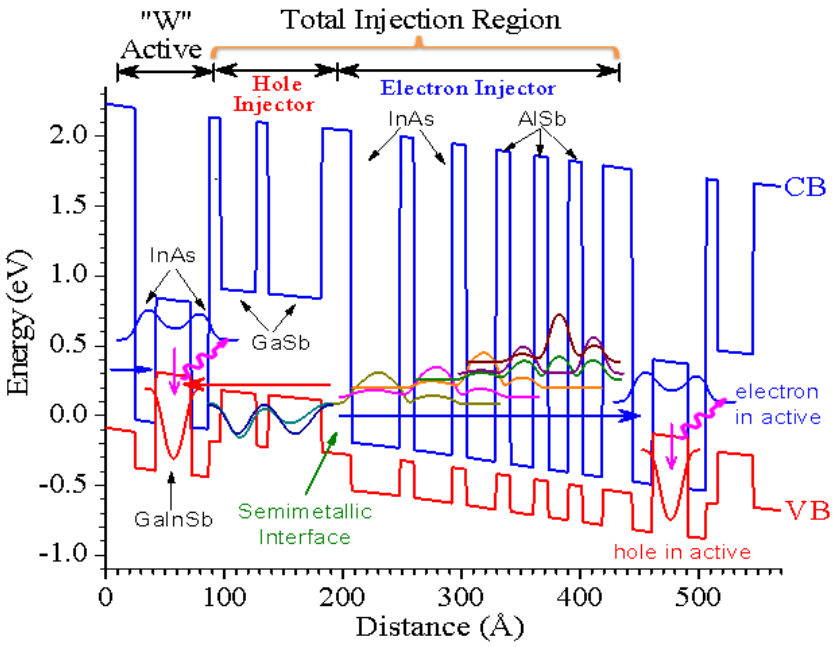

Figure 2.4: Band diagram of an interband cascade laser using a "W"-shaped quantum well gain section. Taken from [51].

Today, their demonstrated narrow spectral linewidth and their flexibility in designing the emission wavelength in a broad range of 2.5–300 µm are key properties [45, 46]. Mid-infrared QCLs are compact devices, that can emit at room temperature with high output power levels [47]. QCLs can achieve a wall-plug efficiency exceeding 50 % [48, 49] and can be designed for broadband emission [50]. The operation principle of QCLs is described in more detail in section 4.1.

Interband cascade lasers

ICLs were first proposed in 1994 by Yang et al. [52]. They combine type-II interband transitions and the cascade concept of the QCLs to recycle the electron for multiple optical transitions. The first ICL was experimentally realized 3 years later [53], but was limited to cryogenic temperatures. Since then, the device design improved significantly, e.g. shorter injectors, "W"-shaped quantum well gain region, carrier rebalancing, etc. The band diagram of a modern ICL is shown in figure 2.4. Todays ICLs can operate continuous wave at room temperature with several hundred milliwatt of optical output power [54]. A review on ICLs can be found in Ref. [55].

Other sources

Other mid-infrared sources are non-linear sources, gas lasers, solid-state (crystal) lasers, fiber laser and the free electron laser [32, 56]. Non-linear sources are based on difference

frequency generation or parametric amplification. Difference frequency generation is also used for THz source using two high power mid-infrared beams. Two widely used examples for gas lasers are the He-Ne laser (3.391 µm) and the CO_2 laser (10,6µm). Solid-state lasers can be build with doped insulators, e.g. Cr doped ZnSe (3.5 µm) or Fe dopend ZnSe (3.1–5.1 µm). In a free electron laser, high velocity electons are traveling through a periodically modulated magnetic field, inducing the electromagnetic radiation [57]. Free electron lasers cover an extremely wide wavelength range from the THz to the near-infrared, but with the drawback that they are extremely big. Worldwide only a few free electron laser have been built.

2.2 Mid-infrared detectors

Mid-infrared detectors can be categorized by the underlying physical mechanism. Thermal detectors measure the heat generated by the absorbed infrared radiation, while photonic detectors rely on the photoelectric effect. Photonic detectors can be subdivided into photoemissive detectors, interband and intersubband detectors. Thermal detectors are generally broadband detectors with a spectral range determined by the absorption layer. Interband detectors are sensitive to photons with energies larger than the bandgap and intersubband detectors are typically narrowband, matching the transition energy between the involved subbands.

Thermal detectors

Thermal detectors are indirect detectors that sense infrared radiation through a temperature increase or gradient. Based on the underlying physical phenomena, they are subdivided into thermopiles, bolometers and pyroelectric detectors.

The first electronic infrared detector, the thermopile, was developed around 1829 by L. Nobili and M. Melloni based on the thermoelectric effect discovered by T.J. Seebeck in 1821 [58]. There, an output voltage is generated by a temperature gradient over a series of stacked thermocouples.

The bolometer was invented in 1878 by S.P. Langley [59]. In a bolometer, the temperature of an absorber is measured with thermal conductors that vary in resistance as a function of the temperature. Due to the large heat capacity of the absorber, these are generally very slow detectors. Cooled superconducting bolometers provide outstanding sensitivity and are often used in astronomy [60]. The miniaturized version, the microbolometer, allows room temperature operation and increased response times due to the smaller heat capacity [61]. Long wavelength infrared camera systems are commonly based on microbolometer focal plane arrays. Cooled bolometers are also used for THz detection.

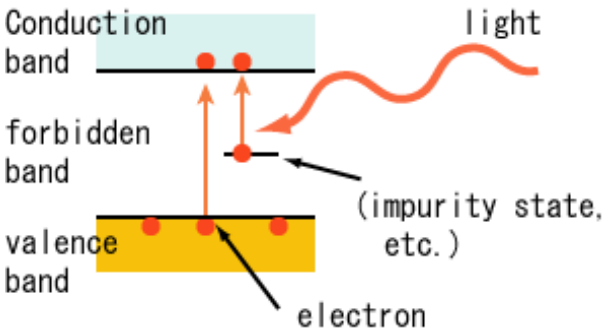

Figure 2.5: Sketch of the internal photoelectric effect. An electron hole pair is generated by the excitation of an electron from the valence band to the conduction band. Transitions are also possible to and from impurity levels. Taken from [63]

Pyroelectric detectors utilize the ability of certain materials to change their polarization with temperature [62]. A change in temperature results in a change of the polarization and consequently causes a temporary voltage across the crystal. Thus, they are only sensitive to temporary changing light fields and show a strong frequency dependent responsivity. Pyroelectric detectors based on deuterated Triglycine sulfate (DTGS) are commonly used in Fourier transform infrared spectrometers.

Interband detectors

Interband detectors are based on the internal photoelectric effect [64]. Thereby, electrons are excited from the valence band to the conduction band. Alternatively, transitions can also occur between bound states or impurity levels. They can be subdivided according to the physical effect into photoconductive and photovoltaic detectors.

In photoconductive detectors, the electrical conductivity of the material is changed as a function of the incident light intensity. A further subdivision can be made, depending on the particular transition. If the transition takes place between the valence band and conduction band, generating electron-hole pairs, it is referred to as intrinsic photoconductivity. In extrinsic photoconductors, the optical transition occurs between impurity states and either the valence band or conduction band. Their operational principle can lead to high photoconductive gain, which is given by the recombination or capture time (lifetime of minority carriers) divided by the transit time of the majority carriers. A high photoconductive gain can be achieved by trapping one carrier type, e.g. the holes, or with extrinsic photoconductors. The resulting charge imbalance leads to an increased injection of majorities carriers until one is captured and recombined with the trapped minority. This additional current is indistinguishable from the photo-generated current and leads to the gain mechanism.

A photovoltaic detector uses a built-in field, e.g. a p-n junction or Schottky contact, to separate the charged carriers and can be operated at zero bias. Photodiodes can be

operated in photovoltaic mode, but commonly a reverse bias is used to increases the width of the depletion junction. This results in a higher responsivity and lower capacitance (faster response), but leads to a small dark current that increases the noise. Furthermore, photodiodes are commonly p-i-n diodes, where the additional intrinsic region leads to a larger depletion region and thus to a larger absorption area and a lower capacitance.

The photoconductive effect was discovered in 1873 by Smith, during experiments with selenium as an insulator for submarine cables [65]. Several years later in 1917, T.W. Case developed photoconductive detectors with much higher responsivity thallium and sulfur [66]. It was mainly the advances in material engineering that have led to the rapid improvement of photoconductive detectors. The first practical detector was based on lead PbS, developed in 1933 by Kutzscher [67]. Today, the most widely used photonic mid-infrared detectors are based on InSb and HgCdTe.

Indium antimonide (InSb) is a direct semiconductor with a narrow bandgap of 0.17 eV at 300K and a high electron mobility [64]. InSb photodetectors are sensitive in the 1–5 µm wavelength range and provide excellent performance. InSb detectors have been fabricated since the late 1950s and are mainly used in a p-n junction or Schottky configuration similar to photovoltaic detectors.

Mercury cadmium telluride (MCT or HgCdTe) is a variable bandgap material (0–1.5 eV), which allows a large degree of freedom [64, 68]. Where narrower bandgaps lead to a higher cut-off wavelength, larger bandgaps are beneficial in terms of noise performance, e.g. dark current and device resistance. MCT detectors can cover the entire mid-infrared spectra. The first MCT detector was demonstrated in 1962 and is now one of the most important infrared photodetectors, available in both photoconductive and photovoltaic configurations. Photoconductive detectors show higher responsivity and are beneficial for detecting small signals. Photovoltaic detectors show a lower noise, faster response, and higher saturation threshold. They are better suited for high optical input powers or higher operational temperatures, but require more advanced amplifiers with a better noise figure. MCT detectors have excellent performance but still show large device to device variations due to the difficulty of high quality epitaxial growth. Especially for focal plane arrays with a large number of pixels, growth stability is a serious issue.

A relative new kind of mid-infrared detectors are interband cascade detectors (ICDs) [69]. Similar to ICLs, they are based on interband transitions in type-II broken gap heterostructures. ICDs already show very good performances especially in the short wavelength region of the mid-infrared and their absorption efficiency can be increased using superlattice absorber [70]. With their relative high detectivity at room-temperature [71] and the potentially stable and reliable growth, ICDs are a very promising technology.

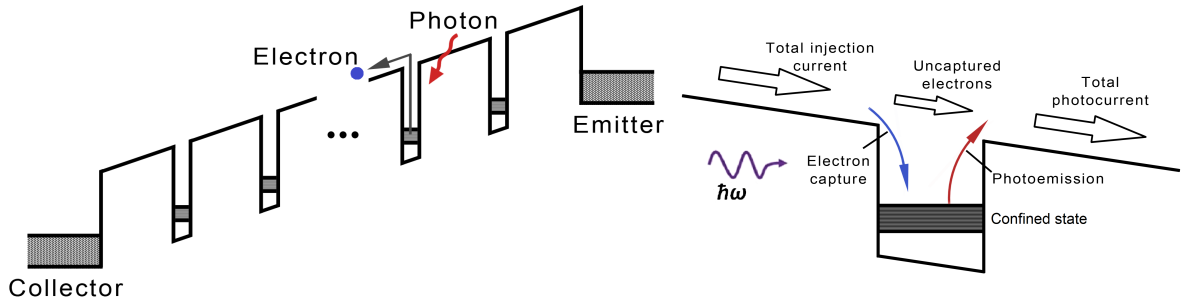

Figure 2.6: Band diagram of a quantum well infrared photodetector and illustration of the gain mechanism. Taken from [72, 73].

Intersubband detectors

Intersubband (ISB) detectors are unipolar devices based on optically induced transitions of electrons between confined states in the same band, typically the conduction band, of a semiconductor. The confined electron states arise from the electronic confinement of lower dimensional systems, e.g. quantum wells, nanowires and quantum dots. The idea of using confined states for photodetection was proposed by Chang et al. [74] and first realized by Levine et al. [75]. The most widely used intersubband detectors are photoconductive quantum well photodetectors (QWIPs) [76]. As illustrated in figure 2.6, they consist of multiple periods of quantum wells, formed by alternating layers of two semiconductor materials with similar lattice structure and period, typically GaAs and AlGaAs. The optical transition typically occurs between a confined and a quasi-bound state within the quantum wells. The detection wavelength can be engineered by designing the layer structure, which form the quantum wells. When a bias is applied, the excited electrons can escape into the continuum where they contribute to the photocurrent. Due to the high purity of epitaxially grown GaAs/AlGaAs heterostructures, QWIPs fabricated from this material system are very attractive for focal plane arrays. As a main drawback, intersubband detectors are only sensitive to light polarized into growth direction due to the intersubband selection rule, described in more detail in section 3.3.1. This requires special coupling schemes for surface incident light. Photovoltaic QWIPs utilize resonant tunneling and a built-in field to extract the electrons from the excited state and thus can operate at zero bias. As is typical for photovoltaic detectors, they have a smaller responsivity due to the lack of photoconductive gain, but show lower noise and high frequency response [77]. Photovoltaic QWIPs are often used in scientific experiments where fast response is required, e.g. laser beat note experiments. Quantum cascade detectors (QCDs) are a special type of photovoltaic QWIPs utilizing resonant tunneling and scattering between states of coupled quantum wells for electron extraction [78–80]. QCDs are described in more detail in the corresponding section, 4.2.

Intersubband transitions have also been studied in 0D structures, i.e. quantum dots.

Initially proposed for lasers [81], they have also been successfully used for infrared detectors [82]. Their advantages over quantum wells for ISB detectors is the independence of the light polarization (allowing normal incidence operation) and the higher confinement, which potentially reduces the dark current. However, the growth of homogeneously distributed dots with controlled size is difficult, which currently prevents them form mainstream use. Dot-in-a-well (DWELL) detectors combine both technologies in order to merge the advantages of both approaches [83]. There, the optical transition occurs between the ground state of the dot and the excited states defined by the quantum well. This reduces the influence of the size of the quantum dots on the detection wavelength, making growth easier.

2.2.1 Fourier transform infrared spectrometer

Fourier transform infrared spectrometers are an extremely versatile tool for chemical spectroscopy as well as device characterization [84]. Commonly built with reflective optics, they can cover a spectral range from near- to far-infrared by only changing the beamsplitter. The FTIR is based on a Michelson interferometer, which was invented in 1880 by A.A. Michelson and E. Morley [85], who were awarded with the Nobel Prize in Physics in 1907. The initial aim of the Michelson interferometer was to test the existence of "the relative motion of the earth and the luminiferous ether", which most physicists at that time believed was the medium through which light propagates. The negative result of the experiment questioned the entire foundation of physics at that point and led to the special theory of relativity, proposed by Einstein.

Michelson knew the possibility to use his interferometer to measure the spectra, but the manual measurement it involved was very time consuming. The development of computers and the invention of fast Fourier transform (FFT) by J.W. Cooley and J.W. Tukey made the technique practical in the 1960s. The first commercial FTIR already included many features of todays FTIRs, e.g. He-Ne reference laser to precisely measure the mirror displacement.

Figure 2.7 sketches the functional principle of an FTIR with a Michelson interferometer consisting of four arms. The light passes a beamsplitter which splits the intensity equally. Each beam is reflected back from a mirror, where one mirror is fixed and the other can be moved. The reflected light again passes the beamsplitter, where the beams interfere. The difference δ in the path length of the two beams leads to a phase difference of $\Delta\phi = 2\pi\tilde{\nu}\delta$. $\tilde{\nu}$ denotes the spectral wavenumber $\tilde{\nu} = 1/\lambda$, where λ is the wavelength. The intensity of the beam towards the detector can be expressed as

$$I_{\text{out}}(\delta, \tilde{\nu}) = I_1 + I_2 + 2\sqrt{I_1 I_2}\cos(\Delta\phi) \tag{2.2}$$

$$= I_{\text{in}}(\tilde{\nu})\left(1 + \cos(2\pi\tilde{\nu}\delta)\right), \tag{2.3}$$

where $I_i n$,I_1, and I_2 are the intensities of the incoming and the two interfering beams,

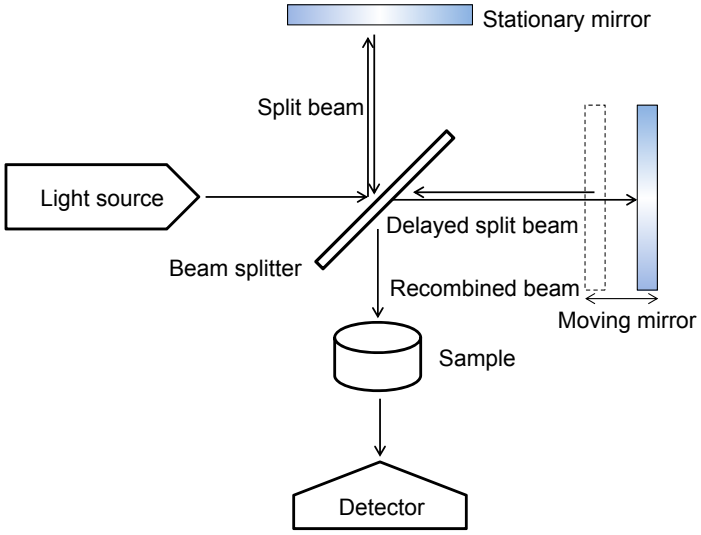

Figure 2.7: Sketch of a Fourier transform infrared spectrometer. Taken from [86].

Constructive interference occurs at every mirror displacement where the phase of both beams is equal, $\delta = n\lambda$ with an integer number n. Destructive interference occurs at $\delta = (n + 1/2)\lambda$. By continuous or stepwise movement, an interferogram can be recorded. To determine the achievable resolution, one can assume an incoming beam composed of two wavelength described by the wavenumbers $\tilde{\nu}_1$ and $\tilde{\nu}_2$. Both beams are in phase at $\delta = 0$ and at $\delta = 1/\Delta\tilde{\nu}$. To resolve the spectrum, it is required to record one period of the interference pattern. The resolution of an FTIR is thus given by the inverse of the path difference

$$\Delta\tilde{\nu} = \frac{1}{\delta} \tag{2.4}$$

As a drawback of high-resolution spectra, the signal-to-noise ratio is proportional to the resolution, because longer interferograms measure more noise, but can be increased by averaging. The initial spectral components can be recovered because the cosine functions span an orthogonal space. The detector measures the total impinging intensity, which results in

$$I_{\text{out}}(\delta) = \int I_{\text{in}}(\tilde{\nu})\,(1 + \cos(2\pi\tilde{\nu}\delta))\,d\tilde{\nu} \tag{2.5}$$

This equals to the Fourier cosine transform and an offset. Thus the spectrum can be calculated using its inverse (projection on the cosine basis states) [84]

$$I_{\text{in}}(\tilde{\nu}) = \int (4I_{\text{out}}(\delta) - 2I_{\text{out}}(\delta = 0))\cos(2\pi\tilde{\nu}\delta)\,d\delta. \tag{2.6}$$

Chapter 3

Intersubband transitions in III-V heterostructures

In 1963, Zh.I. Alferov and R.F. Kazarinov, as well as H. Krömer invented the heterostructure laser [37, 38]. There, the benefit of using semiconductor heterostructures was described as providing a blocking barrier for electron diffusion. Later, researchers in this field were wondering, what would happen, if these heterostructure layers become extremely thin. In 1970, L. Esaki and R. Tsu considered a one-dimensional periodic potential in a monocrystaline semiconductor by changing the alloy composition during epitaxial growth [87]. With a periodic modulation smaller than the electron mean free path, allowed and forbidden bands will be formed, further enabling the design of an artificial bandstructure. R.F. Kazarinov and R.A. Suris proposed in 1971 the amplification of light using discrete subband states, considering quantum wells separated by barriers at high electric fields [43].

C.H. Henry, who was working on integration and waveguides, saw an analogy between the confinement of light in a slab waveguide and the confinement of electrons in a potential well formed by semiconductor heterostructures [88]. He calculated how the resulting electron quantization will alter the optical absorption and concluded, that it will show a series of steps instead of the square root behavior of bulk semiconductors, as shown in figure 3.1. However, low pressure epitaxy was not sufficient to grow such thin layers as required to see electronic confinement. It was the practical realization of the molecular beam epitaxy (MBE) by A.Y. Cho in 1971 at Bell Laboratories, proposed by J.R. Arthur in 1968 [88, 89], which enabled the growth of atomically sharp interfaces. Figure 3.2 shows TEM images of quantum wells grown by MBE. Finally in 1974, R. Dingle, W. Wiegmann and C.H. Henry experimentally observed the optical absorption in III-V GaAs/AlGaAs quantum wells, showing that confined states in quantum wells lead to a higher density of states and thus should lead to a lower threshold compared to standard heterostructure lasers [90]. First experimentally realized by J.P. van der Ziel et al. [91], the quantum well laser is still the leading technology in the visible an near infrared spectral range.

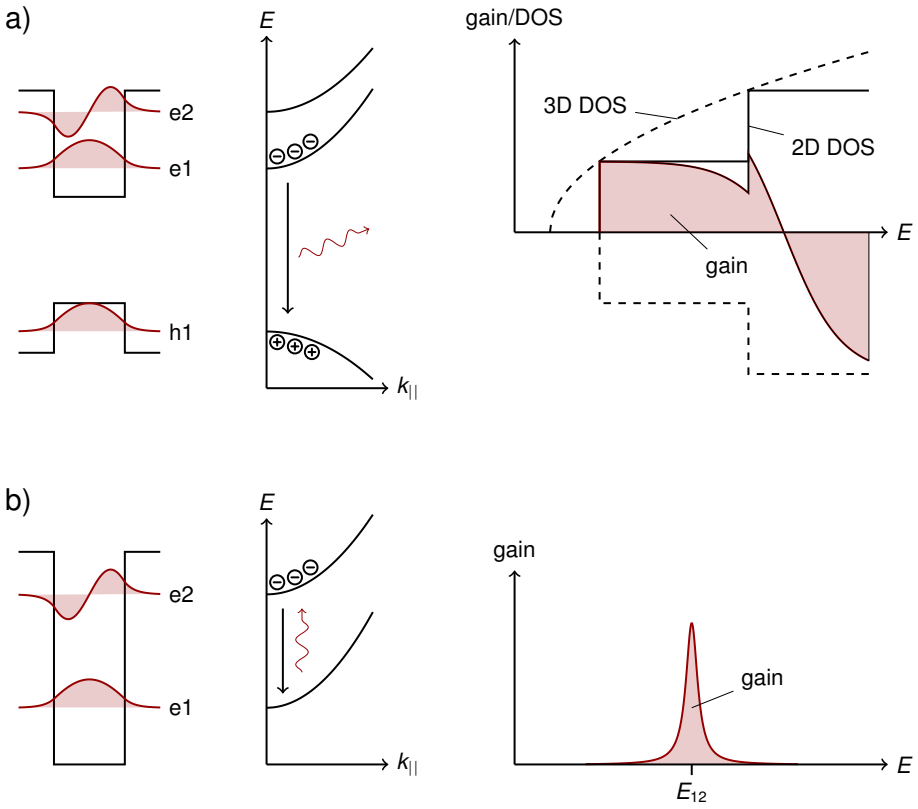

Figure 3.1: Interband transitions (a) vs. intersubband transitions (b) in a quantum well. Interband transition occur between confined states of the valence and the conduction band. The step shaped 2D density of states (DOS) leads to a lower threshold current for quantum well lasers compared to normal heterostructure lasers with a 3D DOS. Intersubband transition occur between confined states within the same band, e.g. the conduction band. The similar in-plane dispersion leads to a narrow gain or absorption peak.

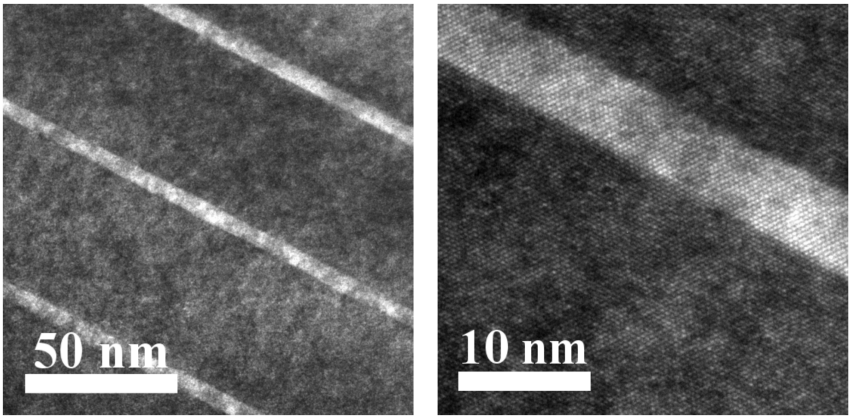

Figure 3.2: TEM images of 4.5 nm wide $In_{0.53}Ga_{0.47}As$ quantum wells sandwiched between 50 nm $Ga_{0.51}As_{0.49}Sb$ barriers, grown by molecular beam epitaxy. Taken from [92].

In parallel, researchers started to investigate optical transitions between confined states within the same band. Figure 3.1 sketches the difference of interband and intersubband transitions. Interband transitions occur between electronic states in different bands. The different sign and value of the in-plane mass describing negatively charged electrons and the positively charged quasi-particles, the electron holes, lead to broad emission and absorption spectra. The width of these spectra increase with higher temperature due to the broader in-plane momentum (k-space) distribution of the carriers. Intersubband (ISB) transitions occur between the electronic states in a single or in coupled quantum wells within the same band. There, the effective mass of the electrons describing the in-plane motion of electrons have the same sign and roughly the same value in both subbands, leading to narrow optical emission and absorption spectra.

First experimental observations of these so called intersubband transitions have been done in Si/SiO_2 inversion layers, summarized in [93]. The first emission from ISB transitions has been reported by E. Gornik and D.C. Tsu in 1976 using a heated electron gas in an Si/SiO_2 inversion layer [94]. Later, in 1985, L.C. West and S.J. Eglash observed ISB transitions with much stronger dipole strength using the GaAs/AlGaAs material system [95]. In 1987, B.F. Levine et al. pioneered the quantum well infrared detector [75], which later has been intensively studied and summarized by H. Schneider and H.C. Liu in their book [76]. The experimental investigation of resonant tunneling through a double barrier by F. Capasso et al. [96] and the first observation of light emission from a superlattice by M. Helm et al. [97] were important steps toward the realization of the first ISB based laser in 1994 by J. Faist and co-workers [44] at AT&T Bell Laboratories.

A more detailed historic overview on the research on heterostructure laser, to quantum wells over intersubband transitions to quantum cascade lasers can be found in the two books: Foreword by C.H. Henry in book "Quantum well lasers" by P.S. Zory [88], as well as "Quantum cascade lasers" by J. Faist [98].

This chapter gives an introduction to the electronic and optoelectronic properties of III-V semiconductor heterostructures, but can be extended to II-VI heterostructures. It will provide the necessary physical background on semiconductor bandstructure calculations, scattering processes and transport models for quantum cascade lasers. A more detailed description can be found in [98–101].

3.1 III-V semiconductors

Most semiconductor heterostructures for mid-infrared optoelectronic devices are made from III-V materials, such as GaAs, AlAs, InAs, GaSb, AlSb, GaP, InP, as well as their ternary compounds AlGaAs, InAlAs, InGaAs, GaAsSb, AlAsSb, etc. Most III-V semiconductors have a zinc-blende crystal structure, as shown in figure 3.3. It consists of two face-centred cubic lattices, where one is displaced by one fourth of its main diagonal [100].

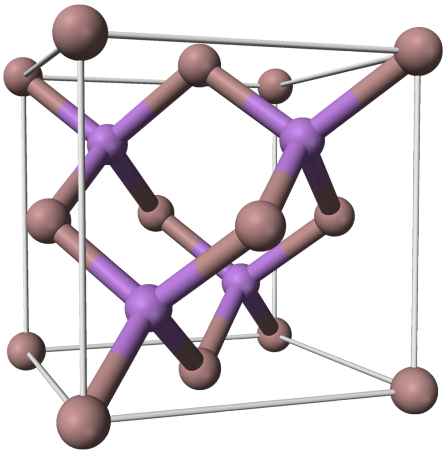

Figure 3.3: Arrangement of the atoms in a zinc-blende crystal structure. Taken from [102].

Another possible crystal structure is the wurzite structure, e.g. of GaN, AlN, etc.. The zinc-blende crystal structure itself cannot be classified as a Bravais lattice, but can be described by a Bravais lattice using a two atom basis. Its reciprocal lattice is a body centered cubic lattice and its first Brillouin zone a truncated octahedron.

III-V semiconductors have 8 electrons per unit cell, that contribute to the chemical bond [100]. All other electrons are highly bound to the nuclei and do not contribute to the electronic properties near the bandgap. The 8 covalent electrons (3+5 for the III-V semiconductors) hybridize to tetrahedral bonds. The bonding s levels are deeply bound and occupied by two electrons. The other six electrons fill the three bonding p-type orbitals, that form the valence band. The anti-bonding orbitals are empty and form the conduction band. In III-V semiconductors the band edge of the valence band is at the Γ point (centre of the Brillouin zone). The conduction band edge is either at the Γ or near the L or X point. The heavier the cations the more likely it is that the conduction band edge can be found at the Γ point. As an example, the conduction band edge of InSb is at the Γ point, where for AlSb it is at the X point. Furthermore, there is a general trend, that the bandgap increases as the cations become lighter. The increased ionicity leads to a higher splitting between the bonding and anti-bonding p-orbitals, which are responsible for the highest valence and lowest conduction band.

It is possible to mix III-V compounds to ternary or quaternary compounds. Strictly speaking, these alloys are not crystalline due to the random distribution of the atoms, e.g. Ga and Al for $Ga_xAl_{1-x}As$. In approximation, one can use an averaged potential using the weighted average $\langle V \rangle = xV_{\mathrm{Ga}} + (1-x)V_{\mathrm{Al}} + V_{\mathrm{As}}$, described in more detail in section 3.2.1. This restores the translational invariance required for Bloch's theorem and allows the definition of the commonly used description of semiconductors in terms of bandgaps, effective masses, etc.. For binaries with very similar bandstructures, the band parameters of their alloys depend nearly linear on their composition, e.g. $Hg_xCd_{1-x}Te$.

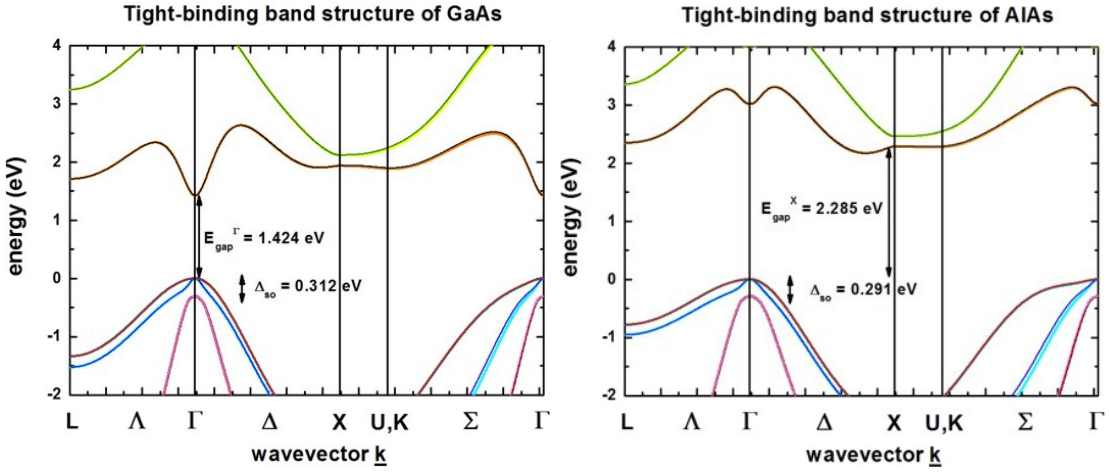

Figure 3.4: Bandstructure of GaAs and AlAs calculated with Nextnano using the tight-binding method including spin-orbit coupling using the sp3s parameters from Klimeck et al. [103]. Reprinted with permission from [104].

However, if their lattice period differs significantly, their bandgap varies strongly nonlinear with their composition, e.g. $In_xAs_{1-x}Sb$. Also for materials, where the lattice period is similar but the band structure differs, the behavior is strongly nonlinear, e.g. $Ga_xAl_{1-x}As$. Figure 3.4 shows the bandstructure of GaAs and AlAs calculated with the tight-binding method. It is an atomistic method, which considers a limited number of neighboring atoms in a single electron picture. In GaAs the conduction band edge is at the Γ point forming an direct semiconductor. In AlAs the conduction band edge is near the X point. The bandstructure of their alloy varies strongly nonlinear with the ratio.

The epitaxial growth of such semiconductor alloys requires either lattice matching or sufficient strain compensation in order not to reach the critical thickness, where the grown layer would start to relax. The growth of locally highly strained layers below their critical thickness, with overall compensation is an additional knob to alter the bandstructure for particular purposes, e.g. higher conduction band offset for short wavelength QCLs. The particular effects of strain on the electronic properties is discussed in section 3.5.5.

3.1.1 Bloch's theorem

The bandstructure of semiconductors is based on quantum mechanical wavefunctions for electrons in a periodic lattice. The Bloch's theorem is the basis for this concept [100]. The zinc-blende lattice can be described using a Bravais lattice, where each lattice point or cell contains two different atoms.

A Bravais lattice can be described by three so called primitive translation vectors a_1, a_2 and a_3. As a fundamental property of a crystal, the background potential $V(\vec{r}) = V(\vec{r}+\vec{R})$ is invariant to translation with any vector $\vec{R}$ of the form

$$\vec{R} = b_1\vec{a}_1 + b_2\vec{a}_2 + b_3\vec{a}_3, \tag{3.1}$$

with any combination of integer numbers b_1, b_2 and b_3. The same is true for the Hamiltonian of the electrons

$$\hat{H}(\vec{r}) = \frac{p^2}{2m_0} + V(\vec{r}) = \frac{p^2}{2m_0} + V(\vec{r}+\vec{R}) = \hat{H}(\vec{r}+\vec{R}), \tag{3.2}$$

where m_0 is the electron mass and p the momentum operator, is

As each cell of the crystal is identical, the electron probability $|\psi(\vec{k},\vec{r})|^2$, but not the wavefunction $\psi(\vec{k},\vec{r})$ itself, has to be translation invariant with $\vec{R}$.

$$|\psi(\vec{k},\vec{r})|^2 = |\psi(\vec{k},\vec{r}+\vec{R})|^2 \tag{3.3}$$

The key essence is to define a translation operator

$$\hat{T}\psi(\vec{k},\vec{r}) = \psi(\vec{k},\vec{r}+\vec{R}), \tag{3.4}$$

which according to Bloch's theorem has the from

$$\hat{T} = \mathrm{e}^{i\vec{k}\cdot\vec{R}}, \tag{3.5}$$

leading to

$$\psi(\vec{k},\vec{r}+\vec{R}) = \mathrm{e}^{i\vec{k}\cdot\vec{R}}\,\psi(\vec{k},\vec{r}). \tag{3.6}$$

This leads to the well known translation relation for the wavefunctions in a periodic lattice

$$\psi(\vec{k},\vec{r}) = \mathrm{e}^{i\vec{k}\cdot\vec{R}}\,u(\vec{k},\vec{r}), \tag{3.7}$$

with the so called Bloch function $u(\vec{k},\vec{r})$, which is translation invariant to $\vec{R}$.

$$u(\vec{k},\vec{r}) = u(\vec{k},\vec{r}+\vec{R}) \tag{3.8}$$

3.1.2 k · p theory

The k · p theory is a widely used and accurate method to describe the bandstructure of bulk semiconductors, as well as heterostructure quantum wells, wires and dots near the band edges [100]. It relies on the knowledge of the bandstructure at the high-symmetry points and expands its k-space using perturbation theory. It has to be noted, that the k · p - theory is not limited to the conduction band edge and is commonly also applied for the other high-symmetry points L and X, resulting in different values for the effective mass, etc..

For simplicity, the spin-orbit coupling is neglected in this introduction to the k · p - theory, although it has to be considered for III-V materials. A more detailed description including spin-orbit coupling can be found in [100]. The Schrödinger equation for static or harmonic potentials at the high symmetry point $\vec{k} = \vec{k}_0$ neglecting spin-orbit coupling is

$$\hat{H}_0\,\psi_n(\vec{k}_0,\vec{r}) = E_n(\vec{k}_0)\,\psi_n(\vec{k}_0,\vec{r}), \tag{3.9}$$

with the Hamiltonian

$$\hat{H}_0 = \frac{p^2}{2m_0} + V(\vec{r}). \tag{3.10}$$

Inserting the wavefunctions in Bloch form (eq. 3.7), multiplying by $\mathrm{e}^{-i\vec{k}\cdot\vec{r}}$ on both sides, and considering the relation $\vec{p} = -i\hbar\vec{\nabla}$, where $\hbar$ is the Planck constant, we can obtain the Schrödinger equation for the Bloch functions $u(\vec{k},\vec{r})$

$$\hat{H}\, u(\vec{k},\vec{r}) = E_n(\vec{k})\, u(\vec{k},\vec{r}), \tag{3.11}$$

with the Hamiltonian

$$\hat{H} = \frac{p^2}{2m_0} + \frac{\hbar}{2m_0}\vec{k}\cdot\vec{p} + \frac{\hbar^2 k^2}{2m_0} + V(\vec{r}) \tag{3.12}$$

The Hamiltonian $\hat{H}$ has the from of an unperturbed, k-independent $\hat{H}_0$ plus a k-dependent perturbation

$$\hat{W}(\vec{k}) = \frac{\hbar}{2m_0}\vec{k}\cdot\vec{p} + \frac{\hbar^2 k^2}{2m_0}. \tag{3.13}$$

The idea of the $k\cdot p$ approximation is to obtain the Bloch functions and eigen energies at the high symmetry points using the equation

$$\hat{H}_0\, u(k_0,\vec{r}) = E_n(k_0)\, u(k_0,\vec{r}) \tag{3.14}$$

and expand the solution to the vicinity of the band edge by perturbation theory using the Bloch functions $u(k_0,\vec{r})$ as a basis

$$u(\vec{k},\vec{r}) = \sum_n b_n(\vec{k})\, u_n(\vec{k}_0,\vec{r})\, \mathrm{e}^{i(\vec{k}-\vec{k}_0)\cdot\vec{r}}, \tag{3.15}$$

with the coefficients b_n.

From perturbation theory one can obtain the second order energy correction for the conduction band

$$E_c(k) = E_c(0) + \frac{\hbar^2 k^2}{2m_0} + \frac{\hbar}{m_0}\sum_{m\neq c}\frac{|p_{cm}|^2}{E_c - E_{m,0}}, \tag{3.16}$$

where the matrix elements $p_{cm} = \langle u_c(0,\vec{r})|\vec{p}|u_m(\vec{k},\vec{r})\rangle$ describe the coupling strength between the conduction band c and all other energy bands m that are considered.

From a second order Taylor expansion, the effective electron mass at the conduction band edge m_c^* can be expressed as

$$\frac{m_0}{m_c^*} = 1 + \frac{2}{m_0}\sum_{m\neq c}\frac{|p_{cm}|^2}{E_c(0) - E_m(0)}. \tag{3.17}$$

3.1.3 The Kane model: Beyond a quadratic approximation

For the same momentum $\vec{k}$, a lighter effective mass leads to a larger kinetic energy $E_c(\vec{k}) - E_c(0)$. Especially for narrow bandgap materials this term is not negligible. In this case, a perturbation beyond second order is required, but would yield an enormous increase of the calculation effort.

E. Kane proposed a different approach to go beyond the quadratic approximation [105]. As an example, in InSb the light hole band and the conduction band are energetically close, but all other bands are well separated. The small bandgap results in a high non-parabolicity, which requires an accurate treatment of the conduction and valence band interaction, while the other bands can be treated by second-order perturbation theory.

He extended the basis formally to

$$u(\vec{k}, \vec{r}) = \sum_m c_m(\vec{k}) u_m(k_0, \vec{r}) \tag{3.18}$$

and restricted the sum to a limited number of relevant bands m. The accuracy improves, when considering more bands. The Hamiltonian can be expressed in this basis using the projection onto the state $u_M(0, \vec{r})$ as

$$\left(E_M(0) + \frac{\hbar k^2}{2m_0} - E_n(\vec{k}) \right) c_M(\vec{k}) + \sum_{m \neq M} \frac{\hbar}{m_0} \vec{k} \cdot \langle u_M(0, \vec{r}) | \vec{p} | u_m(0, \vec{r}) \rangle = 0. \tag{3.19}$$

Two-band Kane model

In the two-band model, the impact of the three degenerated valence bands on the conduction band c is described via one effective valence band v. Thereby, the Bloch wavefunction are extended by a part describing the valence band

$$u(\vec{k}, \vec{r}) = a_c(\vec{k}) u_c(0, \vec{r}) + a_v(\vec{k}) u_v(0, \vec{r}) \tag{3.20}$$

Commonly, the matrix element between the conduction band and the effective valence band is expressed using the so called Kane energy $E_\mathrm{P} = \frac{2}{m_0} p_{cv}$, where $p_{cv} = \langle u_c(0, \vec{r}) | \vec{p} | u_v(\vec{0}, \vec{r}) \rangle$. The two-band Kane model leads to the following expressions for the conduction band energy

$$E_c(k) = E_c(0) + \frac{\hbar^2 k^2}{2m_0} \left(1 + \frac{E_\mathrm{P}}{E_\mathrm{g}} \right) \tag{3.21}$$

where E_g is the band gap.

Three-band Kane model

The three-band model considers the impact of the light hole band and the spin-off band on the conduction band, but neglects the heavy hole valence band. It has to be pointed out, that the parameters for a two-, three-, or four-band model are not directly interchangeable.

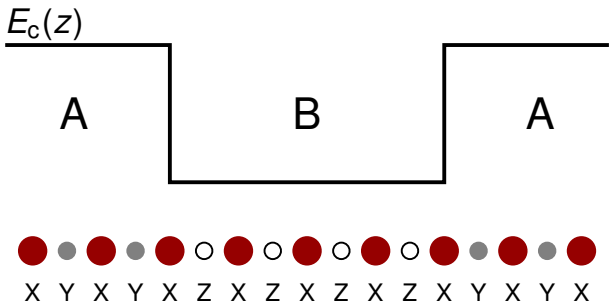

Figure 3.5: Sketch of a semiconductor heterostructure of materials A and B. Material A consist of atoms X and Y, while material B consists of atoms X and Z. The different conduction band edge energies introduce an additional potential.

The band parameters are commonly obtained empirically to fit the experimental data. The three band model is a good compromise for most III-V based intersubband devices and has been used for this work. A main reason is further its comparability to literature data as it is widely used [98, 106].

The corresponding matrix elements between the conduction band and the light hole valence band, as well as, the conduction band and the split-off band are assumed to be $\frac{2}{3}\frac{m_0}{2}E_\mathrm{P}$ and $\frac{1}{3}\frac{m_0}{2}E_\mathrm{P}$, respectively. With the additional Kane parameter F

$$F = \frac{1}{m_e}\sum_{m\neq c}\frac{|p_{cm}|^2}{E_c(0) - E_m(0)}, \tag{3.22}$$

which parametrizes higher-band contributions. The effective mass of the conduction band can be expressed as

$$\frac{m_0}{m_c^*} = 1 + 2F + \frac{2}{3}\frac{E_\mathrm{P}}{E_\mathrm{g}} + \frac{1}{3}\frac{E_\mathrm{P}}{E_\mathrm{g} + \Delta_\mathrm{so}}, \tag{3.23}$$

where $E_\mathrm{g} = E_C(0) - E_{LH}(0)$ is the band gap energy between the conduction and the light hole valence band and Δ_so is the separation between the light hole and the split-off valence band. The non-parabolic mass is often expressed with the non-parabolicity coefficient γ as

$$m_c^*(E) = m_c^*(0)(1 + \gamma E). \tag{3.24}$$

3.2 Electronic states

3.2.1 Envelope Function Approximation

Quantum cascade structures are established from a crystalline layer structure of different semiconductor materials with similar lattice parameters. Duch a heterostructure is a combination of at least two different materials A and B, as illustrated in figure 3.5. Due to their different conduction band edge quantum wells are formed, resulting in confined electron wavefunctions and the possibility to create artificial bandstructures. For

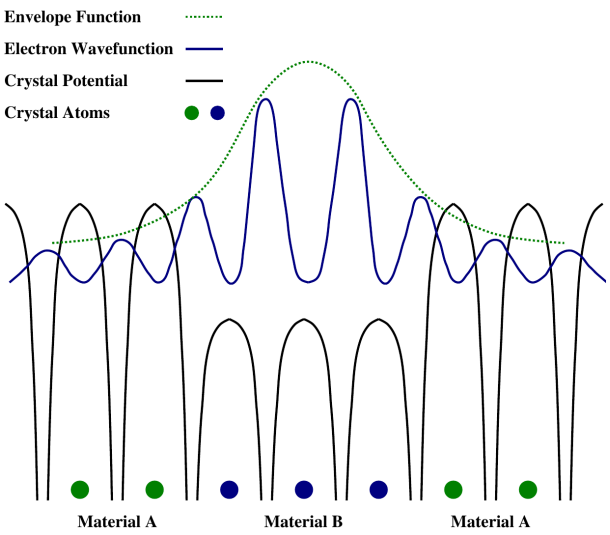

Figure 3.6: Only the envelope of the electron wavefunctions is considered in the calculation for the quantum well. The atomic potential only survives in the effective parameters, e.g. effective electron mass tensor, band offsets, interband matrix elements. Taken from [92].

such complicated layer structures, it is too calculation intensive to resolve the electron wavefunctions to the atomic level. Thus, the wavefunctions are commonly split into a Bloch part and a slowly varying envelope function [100], as shown in figure 3.6. The Bloch part describes the crystal lattice and the slowly varying envelope the impact of the heterostructure. For simplicity the interfaces between two semiconductor materials are assumed to be sharp and translational invariant with the in-plane coordinates. The roughness and finite thickness of the interfaces is treated only as additional scattering effect and linewidth broadening. The sum of slowly varying envelope functions $f_l^{A,B}(\vec{r})$ that modulate the Bloch functions of the material can be written as

$$\psi(\vec{r}) = \sum_l f_m^{A,B}(\vec{r})\, u_{m,\vec{k}_0}(\vec{r}), \tag{3.25}$$

with identical Bloch function $u_{m,\vec{k}_0}(\vec{r})$ in all layers of the heterostructure and summing over the contributions of all considered bands m.

The envelope function approximation is a very efficient and widely used way to calculate the energy levels in a heterostructure. However, one has to keep in mind that this method is restricted to the vicinity of high-symmetry points in the host's Brillouin zone (Γ,X,L) [100]. For actual devices this is is mostly the case.

With this approach the microscopic details of the heterostructure disappear and the different material properties only survive through effective parameters: the interband matrix elements, the effective mass tensor and the band offsets. If these parameters are known, the energy levels for a particular heterostructure can be calculated. The Hamiltonian for this calculation only contains the potential due to the heterostructure and not the microscopic details of the atom potentials. Semiconductor alloys are treated

using an average material potential and the random distribution of the atoms is only considered as additional scattering, the so called alloy scattering (see section 3.3.3).

3.2.2 Hartree potential

The versatile functionality of semiconductor materials is grounded on the ability to change the carrier densities in a wide range by doping, e.g. to form semi-insulating p- or n-type conductors with low or high resistivity. For quantum cascade laser active regions the doping densities are generally relatively low and the location of the carriers has a minor effect on the bandstructure. However, the impact can be enormous, if the doping densities are higher and the carriers are spatially separated from the remaining ionized doping atoms. For example, this is the case for quantum cascade detector active regions, which are doped in the extractor part instead of the active well.

The potential due to charged carriers and ionized dopants can be treated by adding the so called Hartree potential $V_{\mathrm{H}}(\vec{r})$ to the Hamitolian [98]

$$H_0 = \frac{p^2}{2m_0} + V(\vec{r}) + V_{\mathrm{H}}(\vec{r}). \tag{3.26}$$

The Hartree potential is calculated from the charge density $\varrho(z)$ using Poisson's equation

$$\frac{\partial^2 V_{\mathrm{H}}(z)}{\partial z^2} = \frac{\varrho(z)}{\epsilon(z)}, \tag{3.27}$$

where ϵ is local static dielectric constant.

For n-type doping as it is usually the case in unipolar quantum cascade structures, the charge density consists of the electrons and the remaining ionized donors

$$\varrho(z) = \mathrm{e}N_{\mathrm{D}}(z) - \mathrm{e}\sum_i n_i |\psi_i(z)|^2, \tag{3.28}$$

where $N_{\mathrm{D}}(z)$ is the donor density, as well as n_i the population and $|\psi_i(z)|^2$ the probability density of the ith subband. The populations n_i are initially not known and have to be calculated using the solution of Schrödinger's equation. Furthermore, the energy states also depend on the population through the Hartree potential. Thus, the Schrödinger equation, the populations n_i and the Poisson equation have to be calculated in an iterative loop until convergence is achieved.

In thermal equilibrium the populations n_i can be calculated using Fermi's distribution with a common chemical potential and assuming charge neutrality for each cascade. This is a very good approximation for quantum cascade detectors, as they commonly operate near zero bias in thermal equilibrium. Quantum cascade lasers operate at high bias voltages far from equilibrium. Thus, assuming a thermal population is rather inaccurate. The accurate way is to calculate the subband population via suitable transport models. However, the computational effort can be very high, often too high for a self-consistent

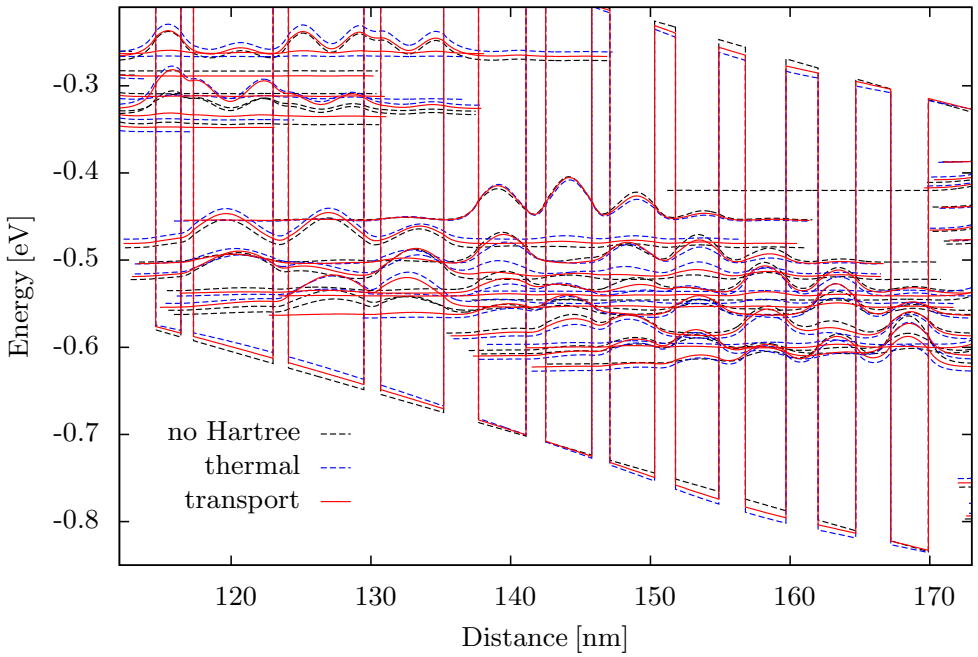

Figure 3.7: Influence of the Hartree potential on the banddiagram of a QCL. With thermal population the Hartree potential is overestimated and gives a similar error compared to the simulation without Hartree potential.

loop. Figure 3.7 shows a the banddiagram of a QCL calculated with VSP2 [106] for three cases: neglecting the Hartree potential, assuming thermal equilibrium and using populations obtained by the Monte-Carlo transport model. For the QCL, the thermal population model overestimates the Hartee potential and gives a similar error compared to neglecting it. Therefore, its additional value is questionable, but it might give an idea about the strength of the effect and if it has to be considered in the design.

3.3 Scattering mechanisms

In the weak coupling regime, the time dependence is treated as scattering between unperturbed basis states of the time independent Schrödinger's equation. Any interaction is treated as perturbation

$$\hat{H} = \hat{H}_0 + \hat{H}_{\text{int}}(t), \tag{3.29}$$

which modifies the electron populations but not the electronic structure itself. The term scattering refers to the transition of carriers from one to another basis state. The scattering rate from the static basis state i to f is generally evaluated using Fermi's golden rule

$$W_{\text{if}} = \frac{2\pi}{\hbar}|\langle\psi_{\text{i}}|H_{\text{int}}|\psi_{\text{f}}\rangle|^2\delta(E_{\text{f}} - E_{\text{i}} - \delta E), \tag{3.30}$$

where H_{int} is the perturbation Hamiltonian, $\psi_{\text{i}}, \psi_{\text{f}}$ the wavefunctions, E_i, E_j the energy of the initial and final state, δE the energy of the scattering process and δ the Dirac

function. The potential describing the particular scattering process can be static or time dependent, leading to two different classes: elastic and inelastic scattering. For elastic scattering the Hamiltonian is static and the energy of the carrier is conserved ($\delta E = 0$), leading to horizontal transition in the E(k) diagram. Perturbation Hamiltonians with harmonic time dependence are referred to as inelastic scattering and lead to a change of the carrier energy corresponding to the frequency of the perturbation, $\delta E = \hbar\omega_0$ for emission and $\delta E = -\hbar\omega_0$ for absorption.

A special case are multi-particle processes, where more than one carrier is involved. Especially for THz QCLs, electron-electron scattering is believed to be an important scattering process, but is commonly neglected in mid-infrared QCLs. The following is a brief summary of the relevant scattering mechanisms in QCLs. The scattering mechanisms considered in this work are: ionized impurities, interface roughness, alloy disorder, acoustic and optical phonons, as well as photon interaction. A more detailed description of the individual scattering processes and their implementation in a transport model is given in Ref [107].

3.3.1 Optical transitions

Photon scattering belongs to the group of inelastic processes. The interaction of electrons with a light field is commonly described in the dipole approximation.

The light field is described by a plane wave

$$\vec{E}(\vec{r},t) = \vec{E}_0 cos(\vec{q}\cdot\vec{r}-\omega t) = \frac{\vec{E}_0}{2}\left(\mathrm{e}^{j(\vec{q}\cdot\vec{r}-\omega t)} + \mathrm{e}^{-j(\vec{q}\cdot\vec{r}-\omega t)}\right), \tag{3.31}$$

where $\vec{E}(\vec{r},t)$ is the electric field, $\vec{q}$ the propagation vector, $\vec{E}_0$ the amplitude of the electric field polarised perpendicular to $\vec{q}$. With $\vec{E} = \frac{d\vec{A}}{dt}$, we obtain the vector potential $\vec{A}$

$$\vec{A}(\vec{r},t) = \frac{j\vec{E}_0}{2\omega}\left(\mathrm{e}^{j(\vec{q}\cdot\vec{r}-\omega t)} + \mathrm{e}^{-j(\vec{q}\cdot\vec{r}-\omega t)}\right). \tag{3.32}$$

Following [98, 100, 108], the electron momentum p in the presence of an optical field should be replaced by $\vec{p} + \mathrm{e}\vec{A}$ and the one-electron Hamiltonian changes to

$$\hat{H} = \frac{(\vec{p}+\mathrm{e}\vec{A})^2}{2m_\mathrm{c}^*} = \frac{\vec{p}^2 + \mathrm{e}\vec{A}\cdot\vec{p} + \mathrm{e}\vec{p}\cdot\vec{A}}{2m_\mathrm{c}^*}, \tag{3.33}$$

using the Coulomb gauge $\nabla\vec{A} = \vec{0}$. In the so called dipole approximation, we assume that the characteristic length of the electronic system, e.g. the quantum well, is much smaller than the optical wavelength. In this case $\vec{A}$ and $\vec{p}$ commute and equation 3.33 simplifies to

$$\hat{H} = \frac{\vec{p}^2 + 2\mathrm{e}\vec{A}\cdot\vec{p}}{2m_\mathrm{c}^*} = \hat{H}_0 + \hat{H}_\mathrm{int} \text{ with } \hat{H}_\mathrm{int} = \frac{\mathrm{e}\vec{A}\cdot\vec{p}}{m_\mathrm{c}^*}. \tag{3.34}$$

Using Fermi's golden rule (Eq. 3.30), the scattering rate for stimulated emission and absorption can be written as

$$W_{\mathrm{if}} = \frac{2\pi}{\hbar}\frac{\mathrm{e}^2 E_0^2}{4m_{\mathrm{c}}^{*2}\omega^2}|\langle\psi_{\mathrm{i}}|\vec{e}\cdot\vec{p}|\psi_{\mathrm{f}}\rangle|^2\delta(E_{\mathrm{f}} - E_{\mathrm{i}} \mp \hbar\omega), \tag{3.35}$$

where $\vec{e}$ is the polarization vector of the light field.

Let us recall the envelope function approximation (equation 3.25) considering only the conduction band

$$\psi_{(i,f)} = f_{(i,f)}u_{(\nu,\nu')}, \tag{3.36}$$

where $f_{(i,f)}$ is the slowly varying envelope and $u_{(\nu,\nu')}$ the Bloch part of the wavefunctions $\psi_{(i,f)}$.

Then the matrix element can be expressed as

$$\begin{aligned}\langle\psi_{\mathrm{i}}|\vec{e}\cdot\vec{p}|\psi_{\mathrm{f}}\rangle &= \langle f_i u_\nu|\vec{e}\cdot\vec{p}|f_f u_{\nu'}\rangle \\ &= \langle f_i|\vec{e}\cdot\vec{p}|f_f\rangle\langle u_\nu|u_{\nu'}\rangle + \langle f_i|f_f\rangle\langle u_\nu|\vec{e}\cdot\vec{p}|u_{\nu'}\rangle.\end{aligned} \tag{3.37}$$

The first term of Eq. 3.37, where the Bloch part is equal ($\nu = \nu'$), describes transitions between states within the same band (intersubband transitions). The latter describes transitions between states of different bands (interband transitions), where the Bloch parts of the wavefunctions are different ($\nu \neq \nu'$).

Following Bastard [100] we express the wavefunction due to spatial in-plane invariance as

$$f_i(\vec{r}_{||}, z) = \frac{1}{\sqrt{A}}\mathrm{e}^{j\vec{k}_{||}\cdot\vec{r}_{||}}\chi_i(z), \tag{3.38}$$

where $\vec{k}_{||}$ and $\vec{r}_{||}$ are the in-plane momentum and spatial coordinate and $\chi_i(z)$ the part into growth direction of the envelope wavefunction. and can write the so called dipole matrix element for intersubband transitions as

$$\begin{aligned}\langle f_i|\vec{e}\cdot\vec{p}|f_f\rangle\rangle\langle u_\nu|u_{\nu'}\rangle &= \frac{1}{A}\int \chi_i^*(z)\mathrm{e}^{-j\vec{k}_{||}\cdot\vec{r}_{||}}\left[\vec{e}\cdot\vec{p}\right]\chi_f(z)\mathrm{e}^{-j\vec{k}'_{||}\cdot\vec{r}_{||}}d^3r \\ &= \left[e_x p_x + e_y p_y\right]\delta_{i,f}\delta_{k_{||},k'_{||}} + e_z\delta_{k_{||},k'_{||}}\int \chi_i^*(z)p_z\chi_f(z)dz,\end{aligned} \tag{3.39}$$

where $\chi_i^*(z)$ is the complex conjugate of the envelope wavefunction $\chi_i^*(z)$ and $\delta_{i,j}$ the Kronecker delta function, which is one for $i = f$ and zero otherwise. The polarizations e_x and e_y only allow transitions within the same subband and can be seen as the two-dimensional analogue of the free-carrier absorption. However, due to the impossibility of energy and momentum conservation at the same time, free carrier absorption is forbidden in perfect heterostructures but can be induced by defects. Only the polarization e_z (electric field component in growth direction) can induce transitions between different subbands and the parity of the wavefunctions must have opposite sign. This is commonly referred to as intersubband selection rule and often requires special geometries in order to observe absorption due to intersubband transitions, described in more detail in section 4.2.2.

Homogeneous linewidth broadening due to the finite lifetimes is considered by replacing the delta function in Eq. 3.35 by a Lorentzian line shape of half width γ

$$\delta(E_f - E_i - \hbar\omega) \longrightarrow \Gamma(E_f - E_i - \hbar\omega) = \frac{\gamma/\pi}{(E_f - E_i - \hbar\omega)^2 + \gamma^2}. \tag{3.40}$$

Combining everything together, the rate for intersubband transition induced by an optical field can be written as

$$W_{\mathrm{if}} = \frac{\pi \mathrm{e}^2 E_{0,z}^2 z_{if}^2}{4\hbar} \Gamma(E_{\mathrm{f}} - E_{\mathrm{i}} \mp \hbar\omega), \tag{3.41}$$

with the so called dipole matrix element

$$z_{if} = \int \chi_i^*(z) z \chi_f(z) dz = \frac{1}{j m_{\mathrm{c}}^{*2} \omega} \int \chi_i^*(z) p_z \chi_f(z) dz, \tag{3.42}$$

It terms of intensity $I = \epsilon_0 n_r c \frac{E_0^2}{2}$ and gain cross section σ_{g} it can be expressed as

$$W_{\mathrm{if}} = \sigma_{\mathrm{g}} \frac{I_z}{\hbar\omega} \text{ with } \sigma_{\mathrm{g}} = \frac{\pi \mathrm{e}^2 \omega z_{if}^2}{\epsilon_0 n_r c} \Gamma(E_{\mathrm{f}} - E_{\mathrm{i}} \mp \hbar\omega), \tag{3.43}$$

where n_{r} is the optical refractive index. The absorption coefficient α is defined as absorbed energy per volume V, time and incident light intensity I. Considering all possible initial and final states the absorption coefficient can be expressed as

$$\alpha(\omega) = \frac{\hbar\omega \sum_{i,f} W_{\mathrm{if}}(N_i - N_f)}{I\ V} \tag{3.44}$$

here N_i and N_f are the total number of carriers in the subands i and f, respectively. If both subbands have the same in-plane mass and using Fermi-Dirac distribution, the absorption coefficient for z polarized light can be written as [98]

$$\alpha(\omega) = \frac{\pi \mathrm{e}^2 \omega z_{if}^2 (n_i - n_f)}{\epsilon_0 n_{\mathrm{r}} c} \Gamma(E_{\mathrm{f}} - E_{\mathrm{i}} \mp \hbar\omega) = \sigma_{\mathrm{g}}(n_i - n_f), \tag{3.45}$$

where $n_{i,f}$ are the three dimensional population densities of the initial and final state.

In-plane dispersion

In reality, the individual subbands have different in-plane masses and non-parabolic dispersion. Figure 3.8 shows the comparison of the calculated parabolic and non-parabolic in-plane dispersion of two subbands. The non-parabolicity leads to a lowering of the absorption energy for higher in-plane momentum $k_{||}$. At higher temperatures, due to the occupation of states with higher $k_{||}$, the intersubband absorption broadens and the peak position shifts towards longer wavelength. Figure 3.9 shows the simulated spectral absorption of a quantum well with parabolic and non-parabolic in-plane dispersion at 80 K and 300 K. It has to be noted, that for the spectral gain of QCLs the wavelength shift is not that pronounced, because the distributions within the subbands are not thermal. This shift is relevant for the optimization of the spectral overlap at room-temperature between the laser and detector functionality of the QCLD.

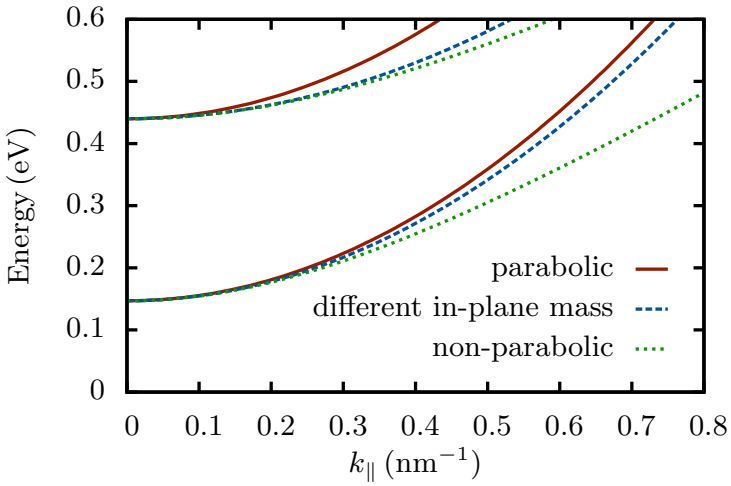

Figure 3.8: In-plane-dispersion of two subbands. The parabolic model uses the bulk conduction band edge mass as in-plane mass for all subbands. A better description uses different masses for the different subbands. The non-parabolic model also includes the non-parabolic in-plane dispersion.

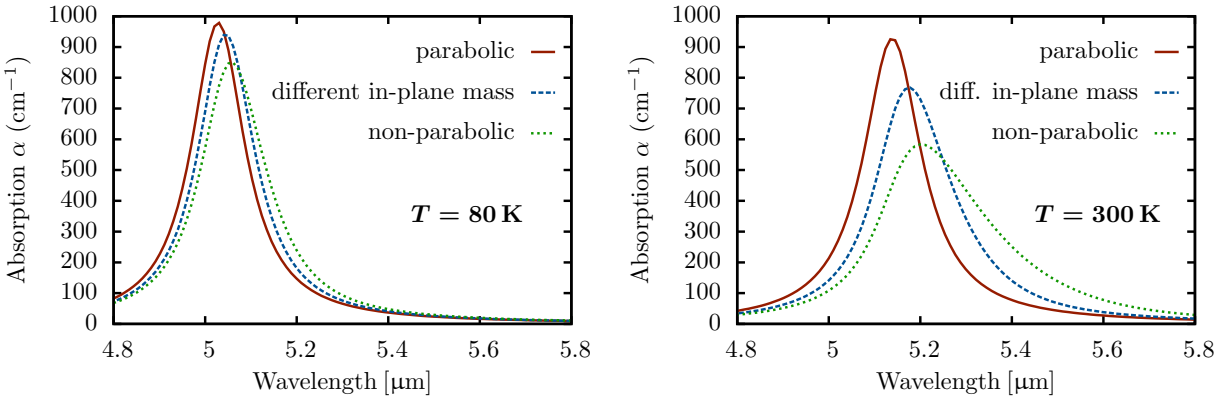

Figure 3.9: Calculated absorption of a 5.6 nm wide InGaAs/InAlAs quantum well at 80 K and 300 K with VSP2, described in more detail in section 4.9.1. In the parabolic model both subband have the same in-plane mass. Non-parabolicity of the in-plane mass introduces an additional wavelength shift, which is more pronounced at higher temperatures. As an approximation, one can use the weighted average of the barrier and well mass for each subband. In this case both subbands have a different but constant in-plane mass. The non-parabolic model also considers in-plane non-parabolicity.

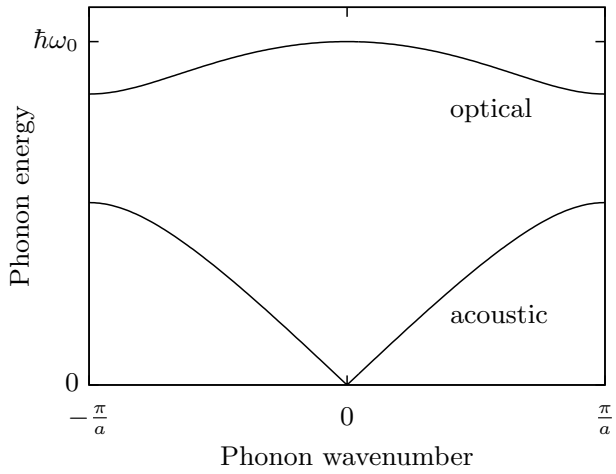

Figure 3.10: Dispersion relation of acoustic and optical phonons. A bi-atomic chain with atoms of different mass leads to two branches of vibrational modes. At small wavevectors, the particularly interesting region, the acoustic phonons have approximately a linear dispersion similar to sound waves and the optical phonons a constant energy similar to optical waves.

3.3.2 Phonon scattering

Phonon scattering is a non-radiative inelastic scattering process. A phonon is a quasi-particle describing the vibration of the crystal lattice. It represents an excited state of the quantized vibrational modes. These phonons perturb the strict periodicity and thus the stationary eigenstates. Phonons are divided into two branches, the acoustic and optical phonons. Figure 3.10 shows a typical dispersion relation of both branches.

Acoustic phonons

Acoustic phonons are sound waves, where two adjacent atoms move in the same direction. They follow a linear relation between the frequency and wavevector for small wavevectors, which is commonly approximated by a single sound wave velocity. Acoustic phonon scattering is more dominant at higer temperatures and a low number of impurities. However, in polar semiconductors it remains less important than optical phonons, due to the weaker interaction strength.

Optical phonons

Optical phonon scattering is the most important scattering process in III-V intersubband devices [109]. For optical phonon modes, two adjacent atoms move in opposite direction resulting in a much stronger local dipole momentum compared to acoustic phonons. As shown in Figure 3.10 they have a non-zero frequency for zero wavevectors. The interaction of electrons and phonons can be described by the Fröhlich hamiltonian [110]. Polar optical scattering is commonly approximated with a mono-energetic frequency of the bulk

material. However, the variation of the dielectric constant can result in confined phonon modes that significantly alter the local phonon populations [111]. However, confined phonons have not been considered in this work.

Assuming a constant energy and using the Fröhlich hamiltonian [98, 109] as well as Fermi's golden rule (Eq. 3.30), the LO-phonon scattering rate from subband i to f can be calculated by

$$W_{if} = \frac{m_c^* e^2 \omega_{\mathrm{LO}}}{2\hbar^2 \epsilon_{\mathrm{P}}} \int_0^{2\pi} \int\int \frac{\chi_i(z)\chi_f(z)\mathrm{e}^{-Q|z-z'|}\chi_i(z')\chi_f(z')}{Q} dz\, dz'\, d\theta \tag{3.46}$$

where $\chi(z)$ are the z-dependent parts of the envolope wavefunctions of the subbands (defined in equation 3.38), ω_{LO} the phonon frequency, $\epsilon_{\mathrm{P}}^{-1} = \epsilon_{\infty}^{-1} - \epsilon_{\mathrm{s}}^{-1}$ the effective dielectric constant in the Fröhlich Hamiltonian using the mid-infrared and static dielectric constants, and Q the momentum exchange, given by

$$Q = \sqrt{k_i^2 + k_f^2 - 2k_i k_f cos(\theta)}, \tag{3.47}$$

where $k_{i,f}$ are the momentum of the initial and final states.

The Q^{-2} dependence of the scattering rate implies, that optical phonon scattering is more efficient for small angle scattering. Thus, the extraction levels below the lower laser level are commonly separated to match the LO phonon energy, e.g. $\hbar\omega_{LO} \approx 33.5\,\mathrm{meV}$ for InGaAs [112]. A larger energy separation of the subbands leads to a reduced scattering time and further to a higher in-plane momentum of the scattered electrons. The extracted electrons from the lower laser levels will exhibit a large kinetic energy which leads to a strong non-thermal population of the injector. This should be considered in the injector design of QCLs and can be modeled with k-space resolved transport models.

3.3.3 Elastic scattering processes

The relevant elastic scattering processes in intersubband devices include impurity, interface roughness and alloy scattering.

Ionized impurities

Impurity scattering is a dominant elastic scattering process in QCLs. It describes the scattering of electrons at charged impurities such as ionized donors. The mean field of the charged impurities is already included in the Hartree potential through Poisson's equation, described in more detailed in section 3.2.2. The perturbation potential is given by the Coulomb potential.

Interface roughness

Interface roughness scattering is due to the imperfection of the interfaces between barriers and wells in a heterostructure. The layer by layer growth causes fluctuations of the

compositions at the interface in the order of at least one monolayer. The roughness is commonly described by a Gaussian auto-correlation function with the mean hight and in-plane correlation length. Also interface roughness is considered to have a significant impact on the device performance [113], but also has been utilized to increase the device performance of QCLs using additional scattering barriers [114]. Interface roughness is also considered as a source of inhomogeneous linewidth broadening. It has to be noted, that the two interfaces in a heterostructure can show a significant different roughness due to the growth direction. Beside doping migration, this is believed to be one reason, why symmetrically designed QCLs show significantly different performance figures, when operated in both directions [115].

Alloy disorder

In the envelope function approximation, the electron wavefunctions are described as Bloch functions modulated by a slowly varying envelope. With this approach the microscopic details of the heterostructure disappear and the different material properties only survive through effective parameters. In ternary semiconductor alloys, e.g. AlGaAs, the gallium and aluminum atoms are randomly distributed. Such alloys are treated using an average potential and an additional scattering mechanism to account for the random distribution, referred to as alloy scattering. Alloy scattering can be a dominant scattering mechanism that limits the mobility of high purity samples at low temperatures and becomes more relevant at short wavelength QCLs [98].

3.4 Carrier transport models

The ongoing development of QCLs and QCDs is accomplished by optimizing their electronic and optical properties. The development of reliable and accurate but also fast simulation methods and tools is an important and challenging task. Optoelectronic devices based on quantum cascade structures are complex devices which in principle would require a full quantum mechanical treatment including in-coherent scattering as well as the interaction with the light field in a self-consistent way. As this can be hardly achieved within a decent amount of time, researchers working in this field have developed a number of different models with reduced complexity using carefully considered or sometimes just necessary assumptions and simplifications.

The aim of the transport model is to calculate the microscopic as well as macroscopic quantities, such as electron distribution, current, gain and absorption, device resistance, photo response, etc.. Coupling the transport model to an optical cavity model one can then obtain parameters, such as output power, wall-plug efficiency, or even the optical spectra through Maxwell-Bloch's equations. The modelling of the spectral behaviour of QCL including mode competition, non-linear effects, e.g. four-wave mixing, is currently

gaining interest due to the emerging QCL based frequency comb technology [10, 116, 117].

This section provides an overview of some widely used methods for quantum cascade structures. A more detailed description of the models can be found in [98, 107].

3.4.1 Rate equation method

The rate equation model has the lowest complexity. It considers a fixed set of subbands to describe the quantum cascade heterostructure. Transport is modelled through transition rates that arise from in-coherent scattering between these subbands. The transition rates are calculated using the perturbation Hamiltonian, the material parameters, as well as the eigen-energies and envelope wavefunctions of the subbands. The rate equation of a subband can be expressed as

$$\frac{dn_i}{dt} = \sum_s \sum_{j \neq i} W^s_{ji} n_j - W^s_{ij} n_i, \tag{3.48}$$

where n_i is the population of the subband i and W^s_{ij} is the scattering rate from subband i to j corresponding to the scattering process s. The subband populations are found by solving the rate equations of all subbands for steady state $dn_i/dt = 0$. In periodic structures, such as QCLs and QCDs, the rate equations are commonly restricted to one period. Transitions to adjacent periods can be modelled by replacing W^s_{ij} by $\hat{W}^s_{ij} = W^s_{i,j-N} + W^s_{ij} + W^s_{i,j+N}$, where $j - N$ and $j + N$ correspond to the same subbands in the left and right adjacent periods, respectively. This additional rates can then be used to calculate the electric current through the structure.

The high numeric efficiency make the rate equation model attractive for the device design, where frequent iterations over the layer structure are required. However, the reduced complexity goes with several limitations.

The calculation of the scattering rates between two subband requires the knowledge of the electron distribution within the individual subbands. It requires the assumption of an electron distribution, usually thermal distribution within each subband using the lattice temperature. However, at typical QCL operation bias far from equilibrium (subband inversion) the electron temperature is typically much higher. This higher electron temperature can be approximated using the kinetic energy balance method [118]. It considers the electron energy generation rate per period and k-space segment resulting from intersubband scattering to calculate a common electron temperature.

3.4.2 Monte-Carlo approach

The Monte-Carlo approach particularly is not a transport model by itself, it is an advanced method to solve the rate equations based on statistical sampling of the scattering rates. It allows much higher complexity and number of dimensions and is thus often connected

to k-space resolved rate-equations. Instead of one rate equation for each subband, it considers segments resolving the k-space of each subband with its corresponding rate equation

$$\frac{df_{i,k}}{dt} = \sum_{s} \sum_{j \neq i} \sum_{k'} W^{s}_{jk',ik} f_{j,k'} - W^{s}_{ik,jk'} f_{i,k}, \tag{3.49}$$

known as Boltzmann transport equation. The semi-classical approach, referred to as single particle Monte-Carlo method describes the hopping of electrons between segments of the k-space. This work is based on the efficient single particle Monte-Carlo QCL simulation tool within the VSP2 simulation framework, described in more detail in [106, 119]. A further increase of accuracy can be achieved using the so called ensemble Monte-Carlo method. By sampling the scattering with a large number of carriers, it can also consider multi particle scattering processes, such as electron-electron scattering [120]. It further allows a time-dependent simulation, but is significantly slower compared to the single particle method.

3.4.3 Beyond semi-classical models

The lack of an appropriate description of coherent tunneling is the main drawback of semi-classical models [98]. Rate equation models rely on the fixed set of basis states obtained from Schrödinger's equation and cannot model their coherent superposition. To give a simple example, one can consider two coupled quantum wells with the same width separated by a relatively thick barrier, as shown in figure 3.11. The Schrödinger's equation is solved in a particular basis, commonly using Wannier-Stark states. The states in the two quantum wells will split to a bound and an anti-bound state. An electron occupying one of these states, is evenly distributed over both wells. The barrier height and width only modifies the splitting, but not the fact, that the electron is in both wells at any time. If we now consider a scattering event into one of the states on the left side of the barrier, the electron will instantaneously tunnel through the barrier and can immediately be scattered to another state on the right side of the barrier. This can be seen as a good approximation for relatively thin barriers, where the tunneling times are much shorter than the in-coherent scattering times of the involved states. However, the situation becomes unphysical for thicker barriers, leading to an overestimation of the current through the barrier. For thicker barriers (small coupling), one would expect an exponential decrease of the current with increasing barrier width.

In a coherent picture, the wavepacket describing the electron is not static. The states have a coherent evolution and the wavepacket oscillates between the two wells, with the Rabi frequency $\Omega = \Delta E/\hbar$. ΔE is the broadening of the states, which corresponds to the anti-crossing energy between the bonding and anti-bonding states. The tunneling time is half of one oscillation cycle, $\tau_{tun} = \pi/\Omega$. If this oscillation is fast, the semi-classical picture remains valid in terms of current, but still predicts two distinct energy states

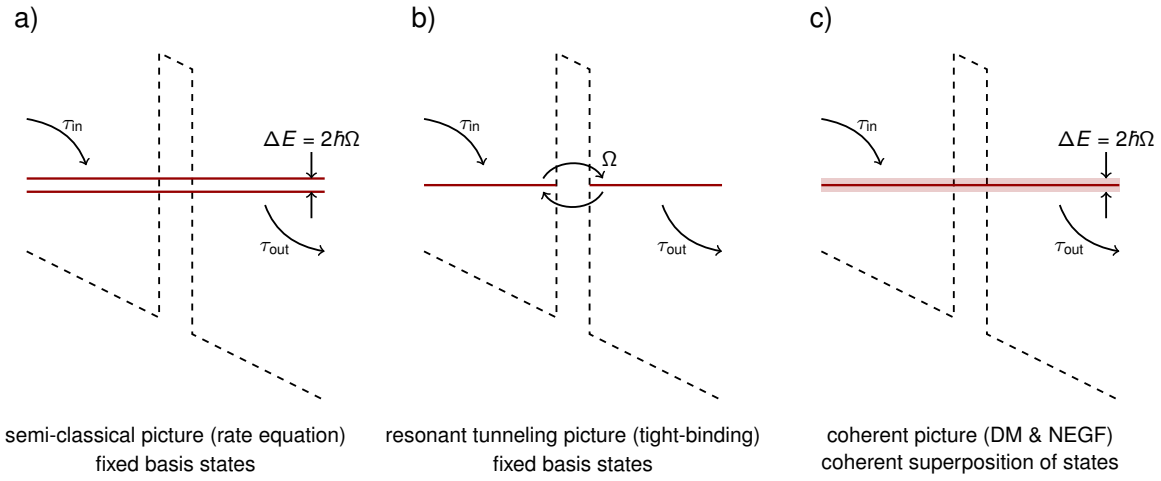

Figure 3.11: Illustration of the transport through a barrier in a semi-classical (a), tight-binding (b) and coherent (c) picture.

instead of one broadened. This results in a double peak gain spectra for QCLs at the anti-crossing point of the upper laser level and an injector level. If the lifetime due to in-coherent scattering is significantly shorter, also the prediction of the current fails and the wavepacket describing the electron is not uniformly distributed over both wells.

Coherent tunneling is sometimes approximated by treating the transport through specified barriers, e.g. the injection barrier, via a tight-binding approach [121]. However, this relies on the right choice of the relevant barriers and transport is modeled either by tunneling or in-coherent scattering.

A better approach is the density matrix formalism. In 1D, it can be seen as the generalization of the rate equation to include coherent effects, such as resonant tunneling and dephasing [107, 122, 123]. The density matrix formalism is not limited to a fixed set of states and can also represent mixed states. The diagonal elements of the density matrix describe the population of the states, where the off-diagonal elements describe the coherence. Similar to the simple rate equations, the 1D density matrix formalism does not resolve the k-space, requiring the assumption of a distribution function. Alternatively, it can also be extended to resolve the k-space, but the computational costs increase significantly.

The non-equilibrium Green's functions (NEGF) theory is seen as the most general scheme [124] and has been successfully applied to quantum cascade structures [125]. However, NEGF algorithms that also include in-coherent scattering through the self-consistent Born approximation are numerically extremely expensive. Thus, this method is commonly not used during the design of QCLs or QCDs, but is very useful for the verification of designs, to gain internal information, or even for the verification of other simulation tools, e.g. the 1D density matrix approach [126].

3.5 Materials

The additional potential induced by the heterostructure is determined by the width of the individual layers as well as the band offsets of the used materials. Most intersubband devices use confined electron states in the conduction band, which makes the conduction band offset one of the main material parameters for material selection. A large conduction band offset gives more flexibility for high subband separations (e.g. for short wavelength QCLs) but requires extremely thin layers for small transition energies (e.g. for THz lasers). It should be noted, that high conduction band offset material systems are often limited by the conduction band edge of the other valleys at the X and L high symmetry points. Confined states of the Γ valley above this energy have a significant coupling to the other valleys through intervalley scattering. The second main parameter for the selection of the material system is the effective electron mass. A smaller effective mass of the well material significantly increases the optical transition strength, which is important for optoelectronic devices. This section gives an overview of the most important III-V material systems used for optoelectronic intersubband devices. The material parameters for the bandstructure calculations are given in appendix D

3.5.1 GaAs/AlGaAs on GaAs

The GaAs/AlGaAs material system is very robust, because AlAs and GaAs have a very similar lattice constant. This also allows the growth of variable Al concentrations and thus a continuous adjustment of the conduction band offset. It is usually grown on GaAs wafers and was the first III-V material system, where intersubband absorption has been observed [95]. Due to the relatively small conduction band offset it is widely used for THz lasers. Depending on the ratio of aluminium and gallium in the barriers the conduction band offset can be adjusted from $\Delta E_\mathrm{c} = 0\,\mathrm{meV}$ to a practical limit of approximately $\Delta E_\mathrm{c} = 390\,\mathrm{meV}$ for $Al_{0.45}Ga_{0.55}As$. Above, the barrier hight starts to be limited by the X valley [127]. The effective electron mass at the conduction band edge is $m_c^* \approx 0.067 m_0$ [128].

3.5.2 InGaAs/InAlAs on InP

The first QCL has been realized in the InGaAs/InAlAs material system [44] and it became the working horse for mid-infrared intersubband devices. Lattice matched to InP, it has a conduction band offset of $\Delta E_\mathrm{c} = 520\,\mathrm{meV}$, which is sufficient for mid-infrared QCLs emitting above $\lambda = 6\,\mu\mathrm{m}$ and the effective mass of InGaAs at the band edge, $m_c^* \approx 0.044 m_0$, is smaller than in GaAs/AlGaAs. This material has several advantages over other material systems [98]:

1. A higher conduction band offset, which is important for short wavelength QCLs

2. A reduced effective mass of the well material, which leads to a higher gain

3. InP based waveguides can be used, which have low optical loss and a high thermal conductivity

The band offset can be further increased using strain engineering with higher indium content in the wells (InGaAs) and a lower indium content in the barriers (InAlAs) from $\Delta E_c = 520\,\text{meV}$ to $\Delta E_c \approx 900\,\text{meV}$ [98]. As an example, $In_{0.7}Ga_{0.3}As/In_{0.4}Al_{0.6}As$ has a conduction band offset of $\Delta E_c = 800\,\text{meV}$. However, each layer has to be below its critical thickness and the accumulated strain in one material has to be compensated by the other, such that the total strain remains sufficiently small. This requires more sophisticated designs and much more effort in terms of calibration and epitaxial growth.

3.5.3 InGaAs/GaAsSb on InP

The GaAsSb is an alternative barrier material for InGaAs/InAlAs on InP with a conduction band offset of $\Delta E_c \approx 360\,\text{meV}$ and is thus more suitable for long-wavelength QCLs [129, 130]. Furthermore, it can be combined with the InGaAs/InAlAs on InP, such that GaAsSb barriers are used in the gain to maintain the LO-phonon separation of the extractor levels for longer wavelength designs and InAlAs in the injector to prevent electrons from escape to the continuum.

3.5.4 InAs/AlSb on InAs

The InAs/AlAs material system on InAs is potentially attractive for short wavelength applications due to the high conduction band offset of $\Delta E_c^\Gamma \approx 2.1\,\text{eV}$ [98], but is practically limited by the L vally in InAs, which is 0.73 eV higher than the Γ valley. However, the achievable wavelength is often limited by interband transitions in InAs (in the waveguide cladding), which has a small bandgap of $E_g = 0.354\,\text{eV}$. Superlattice cladding regions and plasmonic effects can be used to further push this boundary [131]. Another important advantage of the InAs well material is the very low effective electron mass of $m_c^* \approx 0.023 m_0$ [131].

3.5.5 Impact of strain on the band parameters

Following [132], we start with the lattice constants to calculate the impact of strain on the band parameters. First, the total layer structure has to be strain compensated, following the relation

$$a_{||} = \frac{a_w G_w h_w + a_b G_b h_b}{G_w h_w + G_b h_b} = a_0, \tag{3.50}$$

where $a_{w,b}$ and a_0 are the lattice constant of the well, barrier and substrate material e.g. 5.87 Å for InP, and $h_{w,b}$ is the total thickness of the wells and barriers. The shear modulus

is given by

$$G_{\mathrm{w,b}} = 2\left(c_{11}^{\mathrm{w,b}} + c_{12}^{\mathrm{w,b}}\right)\left(1 - \frac{c_{12}^{\mathrm{w,b}}}{c_{11}^{\mathrm{w,b}}}\right), \tag{3.51}$$

where $c_{1x}^{\mathrm{w,b}}$ are the elastic constants of the well and barrier materials.

The in- and out-of-plane strain $\epsilon_{i\perp}$ and $\epsilon_{i||}$ in the layers i can be calculated via the relations

$$\epsilon_{i||} = \frac{a_{||}}{a_i} - 1, \tag{3.52}$$

$$a_{i\perp} = a_i(1 - 2\frac{c_{12}}{c_{11}}\epsilon_{i||}), \text{ and} \tag{3.53}$$

$$\epsilon_{i\perp} = \frac{a_{i\perp}}{a_i} - 1. \tag{3.54}$$

From the strain-components $\epsilon_{i||}$ and $\epsilon_{i\perp}$, one can calculate the fractional volume change

$$\frac{\Delta\Omega}{\Omega} = \epsilon_{xx} + \epsilon_{yy} + \epsilon_{zz} = (2\,\epsilon_{i||} + \epsilon_{i\perp}). \tag{3.55}$$

The impact of the strain onto the conduction band edge energy can be calculated by

$$\delta E_{\mathrm{c}} = a_{\mathrm{c}}\,\frac{\Delta\Omega}{\Omega} = a_{\mathrm{c}}\,(2\,\epsilon_{i||} + \epsilon_{i\perp}) = 2\,a_{\mathrm{c}}\frac{c_{11} - c_{12}}{c_{11}}\epsilon_{i||}, \tag{3.56}$$

where a_{c} is the hydrostatic deformation potential for the conduction band.

In order to calculate the effect onto the light hole and split-off valence bands, we follow the work of Sugawara et al. [133]. Different to the work of Van de Walle [132], he also considers the split-off band. Using

$$P_{\mathrm{e}} = a_{\mathrm{v}}(2\,\epsilon_{i||} + \epsilon_{i\perp}) = 2\,a_{\mathrm{v}}\frac{c_{11} - c_{12}}{c_{11}}\epsilon_{i||} \tag{3.57}$$

and

$$Q_{\mathrm{e}} = b(\epsilon_{i\perp} - \epsilon_{i||}) = -b\frac{c_{11} + 2\,c_{12}}{c_{11}}\epsilon_{i||}, \tag{3.58}$$

where a_{v} and b are the hydrostatic deformation potential, one can calculate the strain effect onto the light hole valence band to be

$$\delta E_{\mathrm{v}} = -P_{\mathrm{e}} + 0.5\,(Q_{\mathrm{e}} - \Delta_{\mathrm{so,unstrained}} + \sqrt{9Q_{\mathrm{e}}^2 + 2Q_{\mathrm{e}}\Delta_{\mathrm{so,unstrained}} + \Delta_{\mathrm{so,unstrained}}^2}) \tag{3.59}$$

and similarly for the split-off band to be

$$\delta\Delta_{\mathrm{so}} = -P_{\mathrm{e}} + 0.5\,(Q_{\mathrm{e}} - \Delta_{\mathrm{so,unstrained}} - \sqrt{9Q_{\mathrm{e}}^2 + 2Q_{\mathrm{e}}\Delta_{\mathrm{so,unstrained}} + \Delta_{\mathrm{so,unstrained}}^2}). \tag{3.60}$$

The effect onto the band gap energy then results in

$$\delta E_{\mathrm{g}} = \delta E_{\mathrm{c}} - \delta E_{\mathrm{v}}. \tag{3.61}$$

All other parameters, such as the Kane energy E_{p}, and the effective masses are assumed to depend only on the composition and not on the local strain in the layer.

Chapter 4

Bi-functional quantum cascade laser and detectors

This chapter is based on the publications "A bi-functional quantum cascade device for same-frequency lasing and detection", Applied Physics Letters 101, 191109 (2012), "Monolithically Integrated Mid-Infrared Quantum Cascade Laser and Detector", Sensors 13, 2196 (2013) and "High performance bi-functional quantum cascade laser and detector", Applied Physics Letters 107, 071104 (2015) [134–136].

Quantum cascade lasers (QCLs) have proven to be an extremely useful and versatile source of mid-infrared and THz radiation. Following the idea of stimulated emission in superlattices by Kazarinov and Suris [43] from 1971 the quantum cascade laser (QCL) was experimentally demonstrated about two decades later by Faist and Capasso et al. [44]. Since then, mid-infrared QCLs have been shown to emit watt level continuous wave output power at room temperature [137], achieve wall-plug efficiencies of up to 50% [48, 49], emit single mode using distributed feedback gratings [138] or emit over a broadband spectral range using multiple stacks of different active regions [50, 139]. Nowadays, QCLs are used in many sensing and spectroscopic applications ranging from environmental monitoring, e.g. for trace gas monitoring [140], to life sciences, e.g. for blood serum analysis [141].

Quantum cascade detectors (QCDs)[79, 80] originate from photovoltaic quantum well photodetectors developed by H. Schneider et al. [142] and photocurrent measurements of QCLs by D. Hofstetter et al. [78]. Although this structure was not optimized for detection, the concept of the quantum cascade detector (QCD) was born. In QCDs, absorbed electrons are extracted through a ladder of subbands that provides a preferential direction for the carriers through an effective built-in field and allows zero bias operation. Due to the short carrier lifetimes, QCDs are fast, have high saturation intensities and thus, they are an ideal counterpart for QCLs with high peak power levels.

Moving one step further, the QCL and QCD functionality can be combined within the very same epilayer material [134, 136]. Such bi-functional quantum cascade laser and

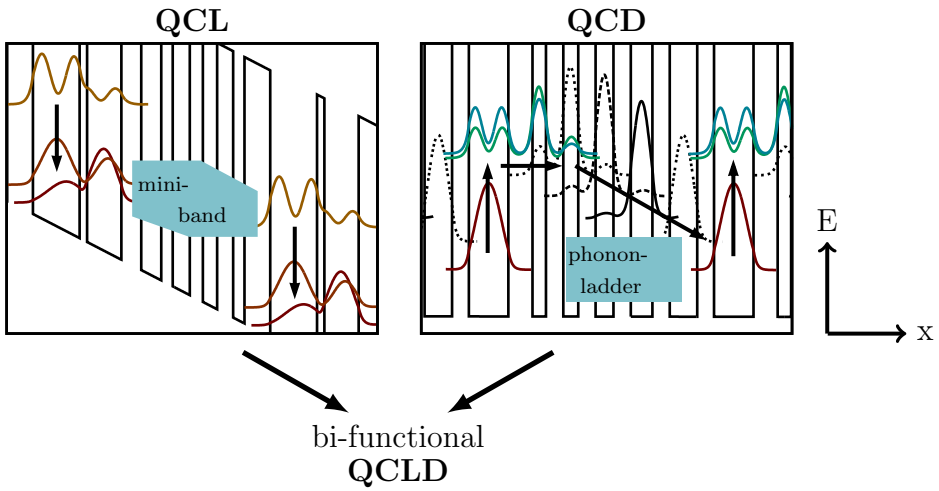

Figure 4.1: Schematic conduction band structure of a QCL and a QCD. The functionality of these devices is is combined into our QCLD, a bi-functional active region for same-frequency lasing and detecting. Published in [135].

detectors (QCLDs) enable the generation and detection of mid-infrared radiation of the same wavelength on the same chip and thus, provide an ideal platform for monolithic integration [25, 135]. Figure 4.1 illustrates the concept of bi-functional devices. At laser bias, the heterostructure provides optical amplification and can be operated similar to conventional QCLs. At zero bias, the very same layer structure can be used as a photodetector. The spectral overlap between both operation modes is thereby a crucial step in the device design and necessary requirement for monolithic integration.

This chapter introduces the bi-functional QCLD design concept developed in the course of this thesis and provides a profound background in electrical and optical design and modeling of the laser and the detector operation, as well as their fabrication and characterization.

4.1 Laser operation

The active region consists of a periodically repeated quantum cascade structure. Each period consists of two functional sections: the gain section and the injector section. In short, the gain section provides the optical gain through intersubband population inversion. Inversion is achieved through lifetime engineering, e.g. using efficient resonant LO-phonon scattering to reduce the lower laser lifetime. The injection region acts as an electron reservoir. These electrons are selectively injected to the upper laser level, while maintaining electric stability.

The following section gives an overview on the active region design for laser operation. Further information can be found in the review article [143] and the book [98].

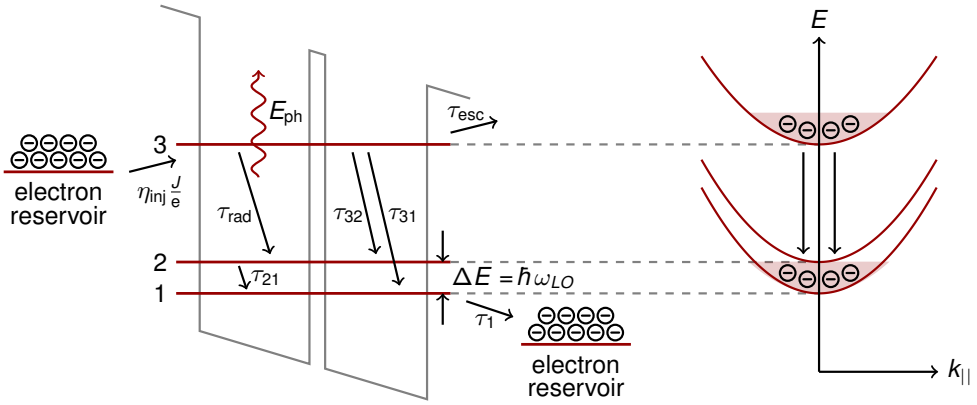

Figure 4.2: Illustration of the laser operation in a quantum cascade structure. Electrons from a reservoir are injected through resonant tunnelling into the upper laser state 3. Population inversion between the states 3 and 2 is achieved by lifetime engineering, e.g. using resonant LO-phonon scattering. The similar in-plane dispersion leads to the characteristic narrow gain bandwidth.

4.1.1 Gain section

As indicated by its name, the gain section is responsible to provide optical amplification through stimulated emission. This is achieved by providing population inversion and a high optical interaction strength (dipole matrix element). Population inversion is achieved through lifetime engineering using at least three subbands. Figure 4.2 shows the operation principle. In laser operation, the conduction band profile appears tilted due to the applied bias. Electrons are injected from a reservoir into subband 3 (upper laser level). Population inversion is achieved between subband 2 and 3, which requires the total out-scattering time from subband 2 to be smaller than the scattering time from subband 3 to 2.

$$\tau_2 < \tau_{32} \tag{4.1}$$

A low lifetime of the subband 2 is commonly realized using resonant LO-phonon scattering for electrons, which is known to be the fastest scattering process (see section 3.3.2). Thereof, the width of the wells and barrier are chosen such that subband 1 and 2 are separated to match the LO-phonon energy, e.g. $\Delta E = \hbar\omega_{\mathrm{LO}} \approx 33.5\,\mathrm{meV}$ in $In_{0.53}Ga_{0.47}As$ [112]. As will be discussed later, common mid-infrared QCL designs utilize two or more consecutive LO-phonon transitions to further reduce the lifetime. A high optical gain further requires a large dipole matrix element z_{32} between level 3 and 2, which describes the strength of the interaction between electrons and light polarized in growth direction (see section 3.3.1).

4.1.2 A simple rate equation model

The rate equation model based on this reduced 3 level representation gives an insight into the working principle and highlights the processes relevant for optimization. The rate equation for the upper and lower laser level corresponding to figure 4.2 reads

$$\frac{dn_3}{dt} = \eta_{\text{inj}}\frac{J}{\text{e}} - \frac{n_3}{\tau_{31}} - \frac{n_3}{\tau_{32}} - \frac{n_3}{\tau_{esc}} - \sigma\frac{I_z}{\hbar\omega}(n_3 - n_2) \tag{4.2}$$

$$\frac{dn_2}{dt} = \frac{n_3}{\tau_{32}} + \sigma\frac{I_z}{\hbar\omega}(n_3 - n_2) - \frac{n_2 - n_2^{\text{therm}}}{\tau_2}, \tag{4.3}$$

where n_i are the subband populations in terms of sheet density, η_{inj} is the injection efficiency, J the current density through the device, I_z the intensity of light polarized in growth direction. The scattering times are indicated in figure 4.2. τ_{31} and τ_{32} are the scattering times from state 3 to 1 and 3 to 2, respectively. τ_{esc} describes the escape into the continuum and τ_2 is the lifetime of state 2, which considers all outscattering processes.

Following [98], one can also include the parasitic scattering rate from the injector to the lower laser level by adding the term $\eta_{\text{inj},2}\frac{J}{\text{e}}$ into equation 4.3. Recalling its definition in section 3.3.1, the gain cross section is given by

$$\sigma_{\text{g}} = \frac{\pi \text{e}^2 \omega z_{if}^2}{\varepsilon_0 n_r c}\Gamma(E_{\text{f}} - E_{\text{i}} \mp \hbar\omega). \tag{4.4}$$

Following [98], thermal backfilling into the lower laser level can be approximately considered via $n_2^{\text{therm}} = n_g \exp(-\Delta/\text{k}_\text{B}T)$, where n_g is the sheet doping of the injector and Δ the energy separation between the lower laser level and the lowest level of the following injector. From this simple rate equation model one can obtain the gain to be

$$g = \frac{\sigma_{\text{g}}}{L_{\text{p}}}(n_3 - n_2) \tag{4.5}$$

$$= \frac{\hbar\omega\sigma_{\text{g}}}{\text{e}L_{\text{p}}}\frac{\eta_{\text{inj}}J\tau_3\tau_2 - J\eta_{\text{inj}}\tau_3\tau_{32} + \text{e}n_2^{\text{therm}}\tau_{32}}{I_z\sigma_{\text{g}}\tau_2\tau_3 - I_z\sigma_{\text{g}}\tau_2\tau_{32} - I_z\sigma_{\text{g}}t3\tau_{32} - \hbar\omega\tau_{32}}. \tag{4.6}$$

Different to the definition in equation 3.45, the carrier densities are expressed in terms of sheet doping, which requires the normalization on the length of one period L_{p}. A more useful way is to rewrite the gain in terms of unsaturated gain g_0 and gain saturation intensity I_{sat} as well as using the effective lifetime $\tau_{\text{eff}} = (\tau_{31}^{-1} + \tau_{32}^{-1} + \tau_{\text{esc}}^{-1})^{-1}(1 - \tau_2/\tau_{32})$

$$g = \frac{g_0}{1 + I_z/I_{\text{sat}}}, \text{ with} \tag{4.7}$$

$$g_0 = \frac{\sigma_{\text{g}}}{L_{\text{p}}}\left(\eta_{\text{inj}}\frac{J}{\text{e}}\tau_{\text{eff}} - n_2^{\text{therm}}\right), \text{ and} \tag{4.8}$$

$$I_{\text{sat}} = \frac{\hbar\omega}{\sigma_{\text{g}}(\tau_2 + \tau_{\text{eff}})}. \tag{4.9}$$

From this simple model, one expects a constant saturation intensity independent of the injection current. However, it will be slightly influenced via the bias voltage through the

changed electron states and lifetimes. For simplicity, we assume that the all lifetimes and dipole matrix elements of the gain section are constant. Furthermore, the depletion of the electron reservoir in the injector is neglected. A refined treatment can be done with advanced transport models considering the entire period including gain and injector section.

The unsaturated gain can also be parametrized with constant values using the so called gain coefficient g_c and transparency current density J_{tran}

$$g_0 = g_c(J - J_{\mathrm{tran}}), \text{ with} \tag{4.10}$$

$$g_c = \frac{\eta_{\mathrm{inj}}\sigma_{\mathrm{g}}\tau_{\mathrm{eff}}}{\mathrm{e}L_{\mathrm{p}}}, \text{ and} \tag{4.11}$$

$$J_{\mathrm{tran}} = \frac{\mathrm{e}n_2^{\mathrm{therm}}}{\eta_{\mathrm{inj}}\tau_{\mathrm{eff}}}. \tag{4.12}$$

At a certain current density, when the unsaturated gain overcomes the total loss of the laser cavity, the laser will start to lase. Above this so called threshold current density, the gain will be clamped to exactly compensate the total loss of the laser cavity. The increasing unsaturated gain with injection current leads to a higher intensity within the cavity, which is required to clamp the gain to the cavity loss. The additional scattering rate induced by the light field does not only lead to the gain saturation, but also to an increase of the current. In order to solve the rate equations including the light field, one has to consider the laser cavity. This commonly results in a rather complex non-linear problem with multiple spatial dependencies. To sketch the basic properties, the Fabry-Perót cavity can be treated assuming a constant intensity within the cavity, neglecting the increasing envelope of the light field, as well as spatial hole burning, mode competition, frequency mixing, etc. The constant intensity approximation leads to

$$\Gamma g = \alpha_{\mathrm{tot}} = \alpha_{\mathrm{w}} + \alpha_{\mathrm{m},1} + \alpha_{\mathrm{m},2}, \text{ with} \tag{4.13}$$

$$\alpha_{\mathrm{m},x} = \frac{1}{2L_{\mathrm{FP}}}\ln(R_x) \tag{4.14}$$

where Γ is the mode confinement factor of the active region in the waveguide (defined in equation 4.52), α_{w} the waveguide loss, $\alpha_{\mathrm{m},(1,2)}$ the mirror loss with the facet reflectivities $R_{1,2}$ and L_{FP} the length of the Fabry-Perót cavity. Models going beyond the constant saturation intensity approximation are described in section 4.8.2.

Combining both models, the current through the structure can be expressed by

$$J = \frac{\mathrm{e}\left[L_{\mathrm{p}}\alpha_{\mathrm{tot}}/\sigma_{\mathrm{g}} + \Gamma n_2^{\mathrm{therm}} + L_{\mathrm{p}}\alpha_{\mathrm{tot}}I_z/(\sigma_{\mathrm{g}}I_{\mathrm{sat}})\right]}{\Gamma\eta_{\mathrm{inj}}\tau_{\mathrm{eff}}} \tag{4.15}$$

or separating into the threshold current density J_{th} and the current density due to the

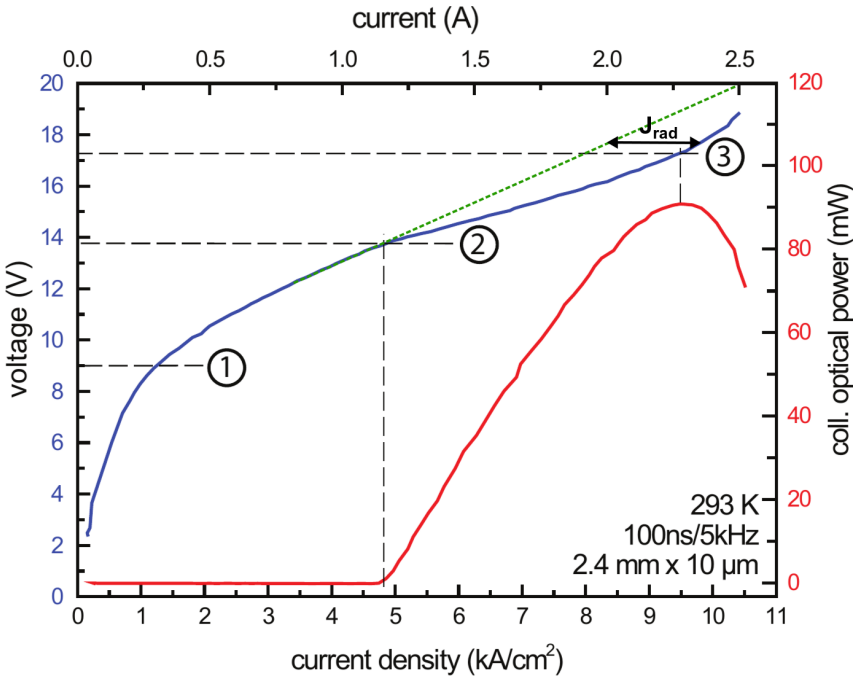

Figure 4.3: Light-current-voltage characteristic of a typical QCL. The characteristic points: band alignment, threshold and roll-over are indicated by the points 1–3. The dashed green line illustrates the current-voltage relation without light field. The difference between the two curves is due to the radiative current. Based on [144].

light field J_{rad}:

$$J = J_{\mathrm{th}} + J_{\mathrm{rad}}, \tag{4.16}$$

$$J_{\mathrm{th}} = \frac{\mathrm{e}L_{\mathrm{p}}\alpha_{\mathrm{tot}} + \mathrm{e}\Gamma\sigma_{\mathrm{g}}n_2^{\mathrm{therm}}}{\Gamma\eta_{\mathrm{inj}}\sigma_{\mathrm{g}}\tau_{\mathrm{eff}}}, \tag{4.17}$$

$$J_{\mathrm{rad}} = \frac{\mathrm{e}L_{\mathrm{p}}\alpha_{\mathrm{tot}}(\tau_2 + \tau_{\mathrm{eff}})}{\hbar\omega\Gamma\eta_{\mathrm{inj}}\tau_{\mathrm{eff}}}I_z. \tag{4.18}$$

In highly efficient QCLs, the radiative current can be very significant. Figure 4.3 shows a typical light-current-voltage characteristic of a QCL. The characteristic points in the curve are marked with the numbers 1 to 3. Point 1 indicates the voltage, where the band-structure aligns towards the operational point. There, the injector levels align with the upper laser level and population inversion starts to arise. At point 2, the threshold condition is fulfilled and the population inversion is sufficiently high, such that the provided optical gain can compensate the cavity loss. The light field increases approximately linear with the current till the maximal current density is achieved at the so called roll-over, indicated by point 3. The radiative current leads to a kink at the threshold condition and a flatter voltage-current characteristic between threshold and roll-over. The linear behavior of the light field over current above threshold is characterized by the so called

slope efficiency

$$\eta_{\text{slope}} = \frac{dP}{dI} = \alpha_{\text{m},1} N_{\text{p}} L_{\text{p}} \frac{dI_z}{dJ} = \frac{\alpha_{\text{m},1}}{\alpha_{\text{tot}}} \frac{N_{\text{p}} \hbar\omega}{\text{e}} \frac{\eta_{\text{inj}} \tau_{\text{eff}}}{(\tau_2 + \tau_{\text{eff}})}, \tag{4.19}$$

where N_{p} is the number of periods. The slope efficiency is a widely used parameter to experimentally characterize the performance of a laser. Together with the threshold current density one can calculate the so called wallplug efficiency, which gives the ratio of the optical output power over the electric input power

$$\eta_{\text{wp}} = \frac{J_{\max} - J_{\text{th}}}{J_{\max} U} \eta_{\text{slope}}, \tag{4.20}$$

where U is the bias voltage. From the threshold current density and the slope efficiency, one can easily identify the relevant parameters for the optimization of the laser operation. In order to achieve a low threshold current and a high slope efficiency, the active region should be optimized for

- high upper laser level lifetime τ_3 and τ_{32}
- low lower laser level lifetime τ_2
- a high gain cross section (high dipole matrix element z_{32} and small linewidth)
- a high injection efficiency η_{inj} (selective injection into upper laser level)
- minimize escape rate to the continuum (highly sensitive to temperature)
- minimize thermal backfilling into lower laser level n_2^{therm} (highly sensitive to temperature)

A trade-off has to be found between these requirements. To give an example, a higher dipole matrix element z_{32} goes with a higher overlap of the wavefunctions, which reduces the scattering time τ_{32}. One can also see, that the concept of cascading the active region is beneficial for the threshold current density and the slope efficiency, but there is an optimal value to achieve the maximal wall-plug efficiency as for larger number of periods, the confinement factor does not increase linearly with the number of periods.

A large portion of the optimization potential lies in the optimization of the laser cavity. The laser performance can be significantly increased with

- lower waveguide loss
- high-reflection coating on the back facet
- anti-reflection coating on the front facet
- lower thermal resistance (for high-duty cycle or continuous wave)

The cavity optimization using more sophisticated models is described in more detail in section 4.8.2.

4.1.3 Injector section

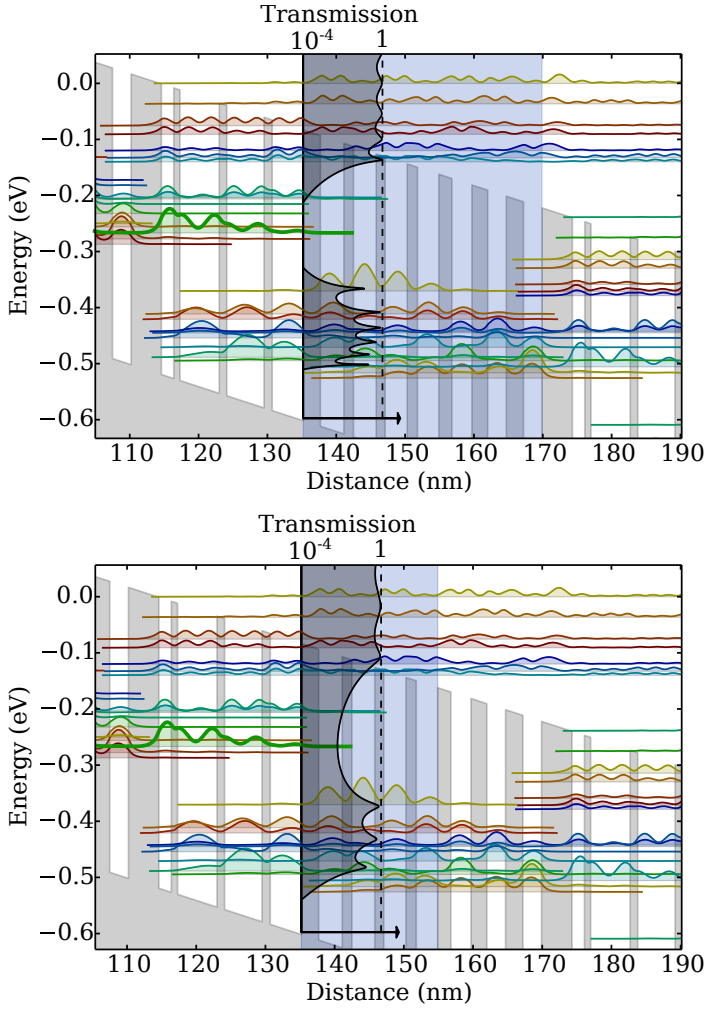

Figure 4.4: Band diagram of a 4-well active region design including the transmission probability into the injector section in logarithmic scale as an overlay. The injector is designed such that the transmission probability is high at the lower laser level and its extraction levels. A stop band is located around the upper laser level to prevent electrons to escape to the continuum. Due to the limited coherence length not all barriers will contribute, which results in a much weaker stop band. In the upper figure eight barriers are considered in the calculation, as highlighted in blue. In the lower figure only four barriers are considered, resulting in a much weaker stop band around the upper laser level.

Indicated by its name, the purpose of the injector section is the selective injection of electrons from a reservoir into the upper laser level. Crucial is to maintain electric stability through the entire bias region, where the laser should be operated. This commonly requires that the lowest injector level is energetically below the upper laser level, leading to a positive differential resistance. A negative differential resistance would result in domain formation and different bias fields in different periods. The injector provides an

effective applied field, which is lower than the external field. Electrons from the lower laser level of the previous gain section rise energy relative to the conduction band edge, such that they can be injected into the upper level of the following gain section. However, the effective field has to be large enough to prevent thermal backfilling into the lower laser level of the previous gain section. The region is doped to provide charged carriers. The doping position is chosen to prevent ionized impurity scattering in the active region.

Furthermore, the injector has to provide efficient electron depopulation from the lower laser level and its extraction levels of the gain section. A proper injector design also includes the prevention of tunnelling from the upper laser level to the continuum. This is commonly achieved by designing a graded stack of quantum wells with an allowed band at the lower laser level and its extraction levels and a stop band centred at the upper laser level of the previous gain section. Figure 4.4 shows a typical bandstructure of a QCL including the injector transmission probability as an overlay. The transmission T has been calculated with the transfer matrix method [145] on the highlighted layer structure: Thereby the potential is split into thin slices with constant potential. The transfer matrix of each slice i centred at x_i is

$$P_i = \frac{1}{2\sqrt{k(x_{i-1})k(x_i)}} \begin{bmatrix} k(x_{i-1}) + k(x_i) & k(x_{i-1}) - k(x_i) \\ k(x_{i-1}) - k(x_i) & k(x_{i-1}) + k(x_i) \end{bmatrix} \begin{bmatrix} \mathrm{e}^{-jk(x_i - x_{i-1})} & 0 \\ 0 & \mathrm{e}^{jk(x_i - x_{i-1})} \end{bmatrix}, \tag{4.21}$$

where the first matrix considered the interface condition between the slices $i-1$ and i and the second the propagation through slice i. The electron momentum $k(x)$ is obtained from the conduction band edge and the non-parabolic effective electron mass

$$k(x) = \frac{\sqrt{2m_e^*(E)(E - E_\mathrm{c} + eF_{bias}x)}}{\hbar}, \tag{4.22}$$

where E is the energy, E_c the conduction band edge and $eF_{bias}x$ the potential energy due to the external electric bias field F_{bias}. The transmission probability can be calculated using the product of all transfer matrices

$$T = \frac{1}{|\left(\prod_i P_i\right)_{(2,2)}|^2} \tag{4.23}$$

where the index $(2,2)$ denotes the element in the second row and column of the product series of the matrices P_i.

The design guideline for the injector can be concluded to

- preserve electrical stability (positive differential resistance at laser bias)
- reduce the applied field by lengthening the period

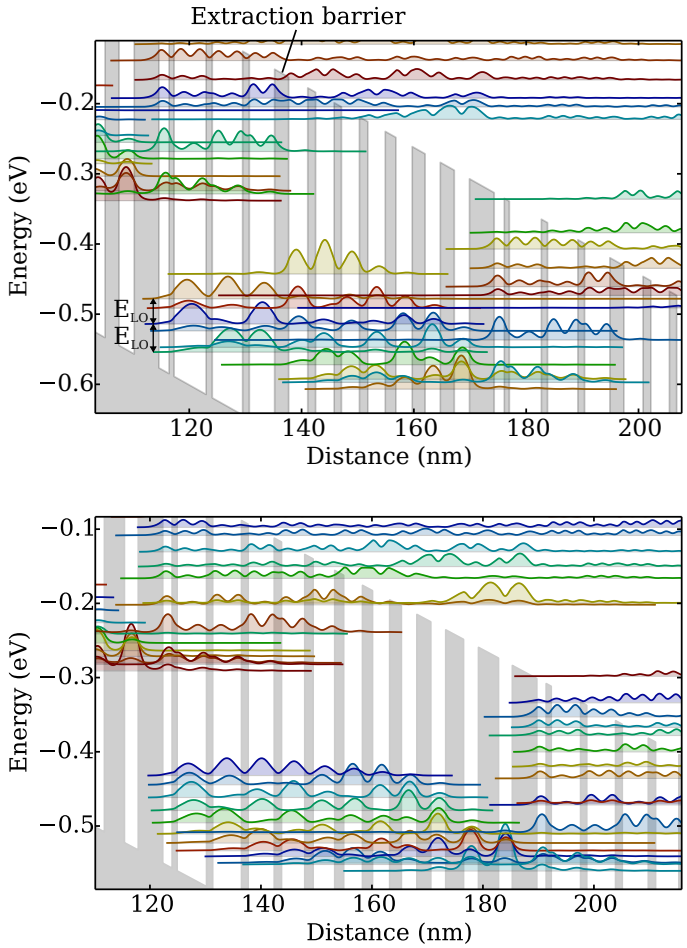

Figure 4.5: 4-well (upper) vs. bound-to-continuum (lower) active region design. The particular designs have been published in [146, 147].

- fast extraction from the lower level and its extraction levels of the previous gain section
- prevent electrons in the upper laser level from escaping to the continuum
- selective injection of electrons into the upper level of the following gain section

4.1.4 Common active region designs

The most widely used active region designs for mid-infrared QCLs are the 4-well design, also known as two-phonon design, as well as the bound-to-continuum design. Figure 4.5 shows two examples of these designs. The 4-well design originates from iterative improvement from the 2-well and 3-well designs. The initial idea in the 2-well design was to utilize resonant LO-phonon scattering to minimize the lifetime of the lower laser level. Later, an additional narrow well was introduced after the injection barrier, leading to the name 3-well design. The 3-well design has lead to the first high performance room temperature

QCL, presented in 1996 [148]. The idea of this well is to reduce the coupling of the injector levels to the lower laser level, but maintain the coupling to the upper laser level, resulting in a more selective injection. The 4-well design uses two resonant LO-phonon transitions to further reduce the lifetime of the lower laser level. The gain section is separated from the following injection section by a thicker extraction barrier, e.g. 2.5 nm for the shown design. The thin barriers in the gain section, which are required for the extraction level separation to match the LO-phonon energy, are also beneficial for a high dipole matrix element.

The bound-to-continuum design [149] originates from the so called superlattice [150] and chirped superlattice [151] active region designs. In the superlattice active region, first introduced in 1997, the active transition takes place between two mini-bands instead of discrete states. The bound-to-continuum design uses a chirped superlattice for the lower laser level and its extraction levels, but a discrete upper laser level. Instead of distinct extraction levels matched to LO-phonon transitions multiple extraction levels are coupled to the lower laser level. It does not have a defined separation barrier between the gain section and the following injector section. Also indicated by its name, the design allow optical transitions to several lower laser levels and thus shows a broader gain spectrum compared to the 4-well design. An electroluminescence spectrum as broad as $295\,\mathrm{cm}^{-1}$ has been demonstrated [147]. Several methods have been presented to further increase the spectral width of the gain medium. One approach is to use heterogeneous cascades with slightly different gain spectra [139]. With this approach a tunable single mode laser emission beyond $400\,\mathrm{cm}^{-1}$ was demonstrated using an external cavity [5]. Similar to the bound-to-continuum design, the active region can also be designed to show multiple upper laser levels, leading to designs referred to as continuum-to-continuum design [152].

4.1.5 Self heating and high duty cycle operation

Due to the relative high current densities and bias fields, the heat dissipation is a major issue for high performance QCLs. The large electric dissipation in QCLs leads to a fast increase of the active region temperature during a laser pulse. The increased temperature leads to an increase of the threshold current as well as a reduction of the gain coefficient and, thus, to a decreasing optical output power. High operation temperatures for the active region design and the thermal optimization of the laser cavity are important aspects, when aiming for high duty-cycle or continuous wave (cw) operation. The lateral overgrowth of a ridge laser with InP, as well as epi-up mounting on a AlO_2 substrate were important steps to reduce the thermal resistance and have led to continuous wave QCLs with watt level output powers [137]. Figure 4.6 shows the simulated pulse shape of the light emitted by a typical QCL. The active region is parametrized using the gain coefficient g_c and the transparency current J_{tran} as defined in eq.(4.12). The influence of the temperature is modeled through using temperature dependent parameters for the

active region. All parameters have been obtained by fitting to experimental data of a high power cw laser. The output power decreases very quickly during the first 500 ns due to the small heat capacitance and relatively large thermal resistance of the active region and waveguide. The slow decrease above 500 ns clearly indicates that this device works continuous wave.

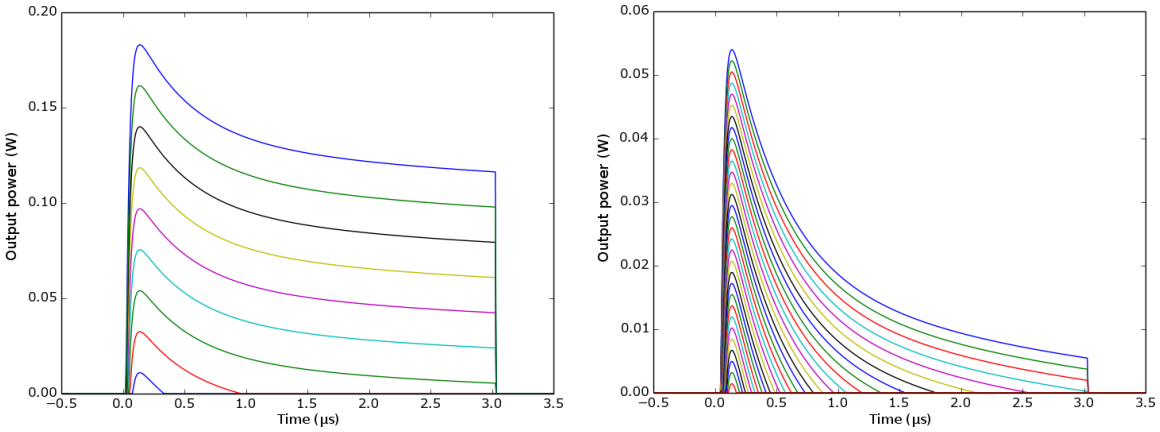

Figure 4.6: Simulated shape of an optical pulse of a QCL for increasing injection current or unsaturated gain (left) and increasing submount temperature from $T = 20°C$ in 1°C steps (right). Such measurements allow the extraction of the thermal properties, such as thermal resistances and capacitances of the ridge, substrate and submount.

4.2 Detector operation

Photocurrent measurements were widely used as a characterization method for QCLs. However, it was D. Hofstetter, who first called it photodetector and started to establish the so called quantum cascade detector [78]. As the structure was not optimized for detection, it showed a weak performance with a responsivity of 50 µA/W and 120 µA/W using a 9.3 µm bound-to-continuum and a 5.3 µm two-phonon resonance QCL structure, respectively. The operational principle is similar to the photovoltaic QWIP developed by H. Schneider [77]. The difference is the extraction method utilizing scattering between subbands similar to QCLs, which gives a larger design flexibility. The benefit over common photoconductive QWIPs lies not in the high responsivity, but in the superior noise behavior of the QCDs at higher temperatures as well as their fast response time.

In the following years, QCDs have been significantly improved and have been demonstrated for infrared and terahertz detection by Graf et al. [153] and by Gendron et al. [79]. QCDs have been fabricated from various material systems, e.g. GaAs/AlGaAs [79, 154], InGaAs/InAlAs [80, 155], InGaAs/AlAsSb [156] for MIR and THz, and GaN/AlGaN [157] for near infrared. Recently, the InAs/AlSb material has been applied, showing a large potential for short wavelength mid-infrared QCDs [158].

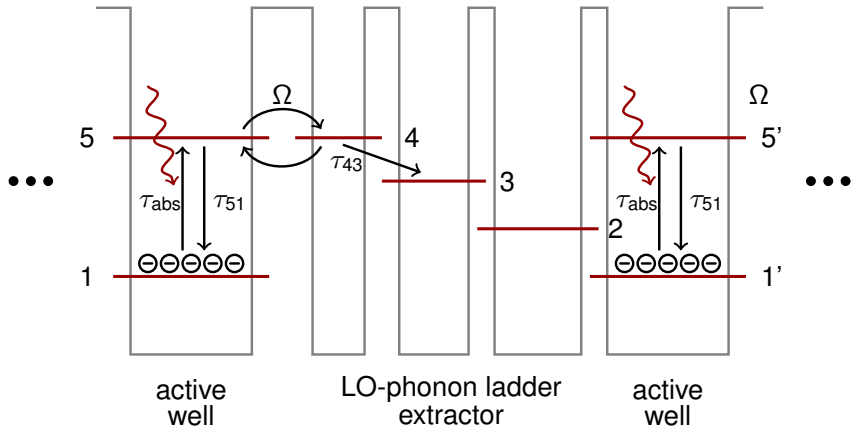

Figure 4.7: Illustration of the detector operation. Electrons are optically excited from level 1 to level 5, where they are extracted through resonant tunnelling and LO-phonon scattering to the ground level of the next period, level 1'. This process is repeated for all cascades.

Figure 4.7 sketches the working principle of a quantum cascade detector. QCDs commonly operate at zero bias or a small reverse bias [159]. Near thermal equilibrium most electrons are in the ground level (level 1), which is the lower detector state. When illuminating the device at the proper wavelength, electrons are excited to the upper detector level (level 5) by absorbing photons. With a finite probability these electrons are extracted via tunnelling to level 4 followed by LO-phonon scattering via the phonon-ladder down to the lower detector level of the next cascade (level 1'). This process is repeated for each cascade (typically 15-30 times).

The performance of photodetectors is commonly described in terms of spectral responsivity $\mathcal{R}$, noise equivalent power *NEP* and specific detectivity D^*. The so called noise equivalent temperature difference *NETD* is commonly used when aiming for thermal imaging. The responsivity is defined as the electric current due to the external light field (photocurrent) I_{ph} divided by the incident optical power P_{opt},

$$\mathcal{R} = \frac{I_{\mathrm{ph}}}{P_{\mathrm{opt}}}. \tag{4.24}$$

The responsivity is often written in terms of efficiencies, commonly using the external and internal quantum efficiencies. The external quantum efficiency η_{ext} describes the amount of generated electrons per incident photons. The internal quantum efficiency η_{int} describes the amount of generated electrons per absorption photons. However, for QCDs an other definition has been established, the absorption and extraction efficiency. The absorption efficiency η_{abs} describes the amount of light, which is absorbed by the desired optical transition divided by the incident power and is connected to the quantum efficiencies by

$$\eta_{\mathrm{ext}} = \eta_{\mathrm{abs}}\eta_{\mathrm{int}}. \tag{4.25}$$

However, it is sometimes unclear which parts of the system are considered to belong to the detector. As an example, the facet reflectivity is considered in this work, which is often neglected in the equation. The situation becomes even more complicated when considering ridge waveguide detectors. Significantly different values are obtained, if the coupling from free space propagation to the waveguide is considered or neglected. Both views have its eligibility, but care must be taken when comparing the performance of different detectors in literature. When aiming for discrete photodetectors, which detect light from free space propagation, the coupling region is an important part and should be considered. However, when aiming for on-chip detectors, one can neglect it, because the light is always guided in waveguides. There, the inclusion of the coupling efficiency of a waveguide coupler or direct end-fire coupling is more appropriate, which however, strongly depends on the particular application.

4.2.1 Extraction efficiency

The extraction efficiency p_e is the probability that an electron absorbed by the desired optical transition contributes to the photocurrent. The relation between the extraction efficiency and the internal quantum efficiency is

$$\eta_\mathrm{int} = \frac{p_\mathrm{e}}{N_\mathrm{p}}, \tag{4.26}$$

where N_p is the number of periods. In particular, electrons excited to the upper level (level 5 in figure 4.7) have a finite probability to relax to the ground level of the same well. In this case they do not contribute to the photocurrent. Assuming that the tunnelling is fast compared to the in-coherent scattering processes the extraction efficiency can be very roughly estimated by the ratio or the lifetimes

$$p_\mathrm{e} \approx \frac{\tau_{43}^{-1}}{\tau_{43}^{-1} + \tau_{51}^{-1}}. \tag{4.27}$$

However, at higher temperatures the back scattering from level 3 to 4 cannot be neglected, requiring a refined approach. Furthermore, an optimized detector has a reduced overlap of the following extractor levels to increase the differential device resistance making this approximation even worse.

A refined more precise model considers all possible scattering paths. The Monte-Carlo algorithm considers three periods, where the scattering times are only calculated for scattering from states of the middle period. If an electron is scattered from a state in the middle period to a state in the left or right period, it is accounted to contribute to the current (negative of positive) and reinjected to the same state in the middle period. The resulting scattering matrix consists of three $N_\mathrm{states} \times N_\mathrm{states}$ matrices which gives a $3N_\mathrm{states} \times N_\mathrm{states}$ matrix, where N_states is the number of states per period. The middle

matrix describes the scattering within the middle period, where the left and the right ones describe scattering to the adjacent periods

$$\left[\begin{array}{ccc}\mathbf{T}_{M,M-1} & \mathbf{T}_{M,M} & \mathbf{T}_{M,M+1}\end{array}\right] = \left[\left[\begin{array}{ccc}1/\tau_{11^*} & 1/\tau_{12^*} & \dots\\ 1/\tau_{21^*} & 1/\tau_{22^*} & \dots\\ \vdots & \vdots & \ddots\end{array}\right]\left[\begin{array}{ccc}0 & 1/\tau_{12} & \dots\\ 1/\tau_{21} & 0 & \dots\\ \vdots & \vdots & \ddots\end{array}\right]\left[\begin{array}{ccc}1/\tau_{11'} & 1/\tau_{12'} & \dots\\ 1/\tau_{21'} & 1/\tau_{22'} & \dots\\ \vdots & \vdots & \ddots\end{array}\right]\right], \quad (4.28)$$

with τ_{ij} the scattering time from states i to j within the middle period and j^* and j' denoting the target state to be in the left or right adjacent period, respectively.

To include all transitions, the scattering matrix is extended to also consider the adjacent periods

$$\mathbf{T} = \left[\begin{array}{ccc}\mathbf{T}_{M,M} & \mathbf{T}_{M,M+1} & 0\\ \mathbf{T}_{M,M-1} & \mathbf{T}_{M,M} & \mathbf{T}_{M,M+1}\\ 0 & \mathbf{T}_{M,M-1} & \mathbf{T}_{M,M}\end{array}\right]. \quad (4.29)$$

In the next step all out-scattering rates from the ground levels are deleted by setting the corresponding rows in matrix $\mathbf{T}$ to zero, obtaining the matrix $\mathbf{T}'$.

The initial situation assumes one electron to be in the upper level (level 5). This is described by a vector with the dimension $3N_{\text{states}}$, where only the corresponding entry is set to one. In case of the upper level (level 5), $\rho^{\text{init}}_{N_{\text{states}}+5}$ is set to 1 and all others are set to zero. By applying the scattering matrix to the initial population vector by multiplication, one gets the probabilities in which levels the electron has been scattered after one scattering event. After N_{e} scattering events and the deleted out-scattering from the ground levels, the population

$$\rho = {\mathbf{T}'}^{N_{\text{e}}}\rho^{\text{init}} \quad (4.30)$$

will converge to a situation, where only the ground levels are filled. The extraction efficiency can then be calculated by the difference between the electrons reaching the ground level of the right and left period. All electrons relaxing to the ground level of the middle period do not contribute to the photocurrent.

$$p_{\text{e}} = \rho_{0'} - \rho_{0^*} = \rho_{0+2N_{\text{states}}} - \rho_0 \quad (4.31)$$

This method considers all scattering rates within one period and to its adjacent periods. It can also be applied to calculate the extraction efficiency of the extractor levels, to identify bottlenecks in the extractor.

Figure 4.8 show the calculated extraction efficiencies of two 4.5 µm high performance QCDs for thermal imaging designed in the course of this thesis. The values correspond to the probability that an electron in the corresponding level reaches the ground level of the next cascade. The actual extraction efficiency of the effective upper level is the weighted average between the three upper detector levels. The weighing is based on their absorption strength, described by their dipole matrix element and broadening to the ground levels.

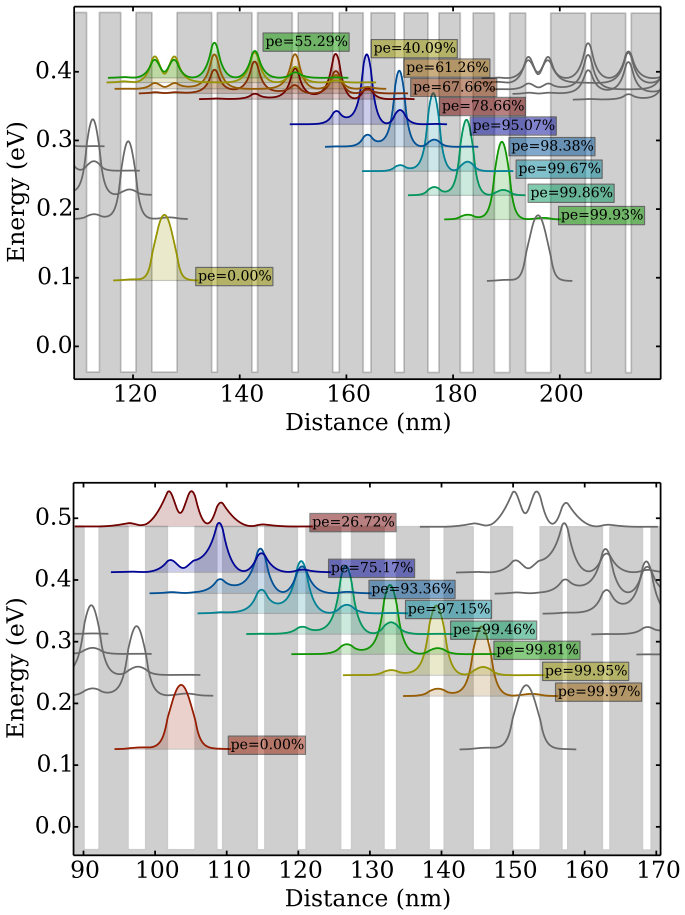

Figure 4.8: Band diagram of a vertical (upper) and diagonal transition (lower) 4.5 µm QCD designed for thermal imaging (operation temperature 240K) (samples C0115 & C0117). The growth sheets can be found in the appendix C. The extraction efficiency is plotted for all energy levels to identify bottlenecks. The vertical transition design shows a stronger dipole matrix element, but a lower extraction efficiency $p_e \approx 47\%$. The diagonal transition design has a smaller dipole matrix element, but a much higher extraction efficiency $p_e = 75\%$.

4.2.2 Absorption efficiency

The absorption efficiency can be calculated using the gain model for quantum cascade lasers. As described in more detail in section 3.3.1, the gain or absorption of intersubband transitions can be calculated using the dipole matrix element and the linewidth broadening. The absorption efficiency also considers the particular optical geometry. QCDs are typically characterized using the 45° polished facet double pass mesa geometry, illustrated in figure 4.9, to fulfill the polarization selection rule (see section 3.3.1). The absorption efficiency for a 45° mesa geometry, neglecting absorption due to the substrate

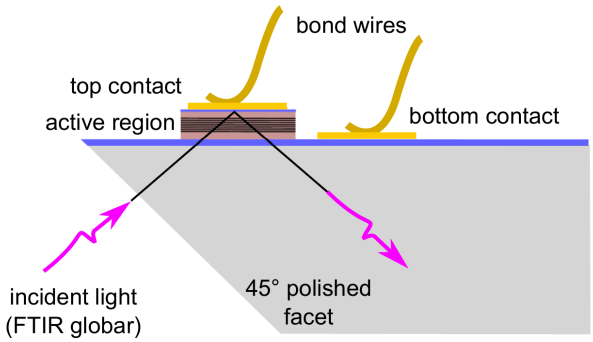

Figure 4.9: Sketch of the 45° polished facet double pass mesa geometry, which is commonly used to characterize intersubband detectors. The 45° incidence angle is required to fulfill the polarization selection rule. Take from [160].

and the contact layers, as well as interference effects, is

$$\eta_{\text{abs}} = T_{\text{facet}} \left(1 - \exp\left(-\frac{1}{\sqrt{2}}\alpha_{\text{isb}} N_{\text{p}} L_{\text{p}}\right)\right), \tag{4.32}$$

where T_{facet} is the facet transmission ($\approx$ 70% for the air/InP interface without anti-reflection coating), $N_{\text{p}}L_{\text{p}}$ the total thickness of the active region (typically 1–2 µm), and , $\alpha_{\text{isb}} = \sum_{i,f} \alpha_{if}$ the absorption coefficient due to intersubband transitions in the active region with all possible initial and final states i and f.

On-chip detectors can be fabricated as ridge waveguides, similar to QCLs. In this case, the absorption efficiency can be calculated by

$$\eta_{\text{abs}} = T_{\text{facet}} \left(1 - \exp(-(\Gamma\alpha_{\text{isb}} + \alpha_{\text{w}})L_{\text{w}})\right) \frac{\alpha_{\text{isb}}}{\alpha_{\text{isb}} + \alpha_{\text{w}}}, \tag{4.33}$$

where α_{w} is the waveguide loss due to free carrier absorption in the cladding and L_{w} the length of the ridge waveguide.

Typical 45° mesa QCDs show an absorption efficiency of 10–30% and require a relatively high doping due to the short absorption length. Ridge detectors do not show this limitation. Even at low doping densities and number of periods, the fraction due to intersubband absorption $\Gamma\alpha_{\text{isb}}$ is still larger compared to the absorption in the cladding α_{w}. The length is generally not a limitation. The waveguide coupled ridge detector geometry is a main benefit of the presented integration approach.

Due to the different effective absorption length, the absorption coefficient is more relevant in 45° mesa detectors compared to waveguide detectors. The absorption coefficient generally decreases with increasing temperature due to linewidth broadening and the increased occupation of higher energy levels. In order to decrease this effect, the next higher energy level above the ground level should be designed at higher energy. As shown in the band diagrams in figure 4.8, the last step of the LO-phonon ladder extraction region is

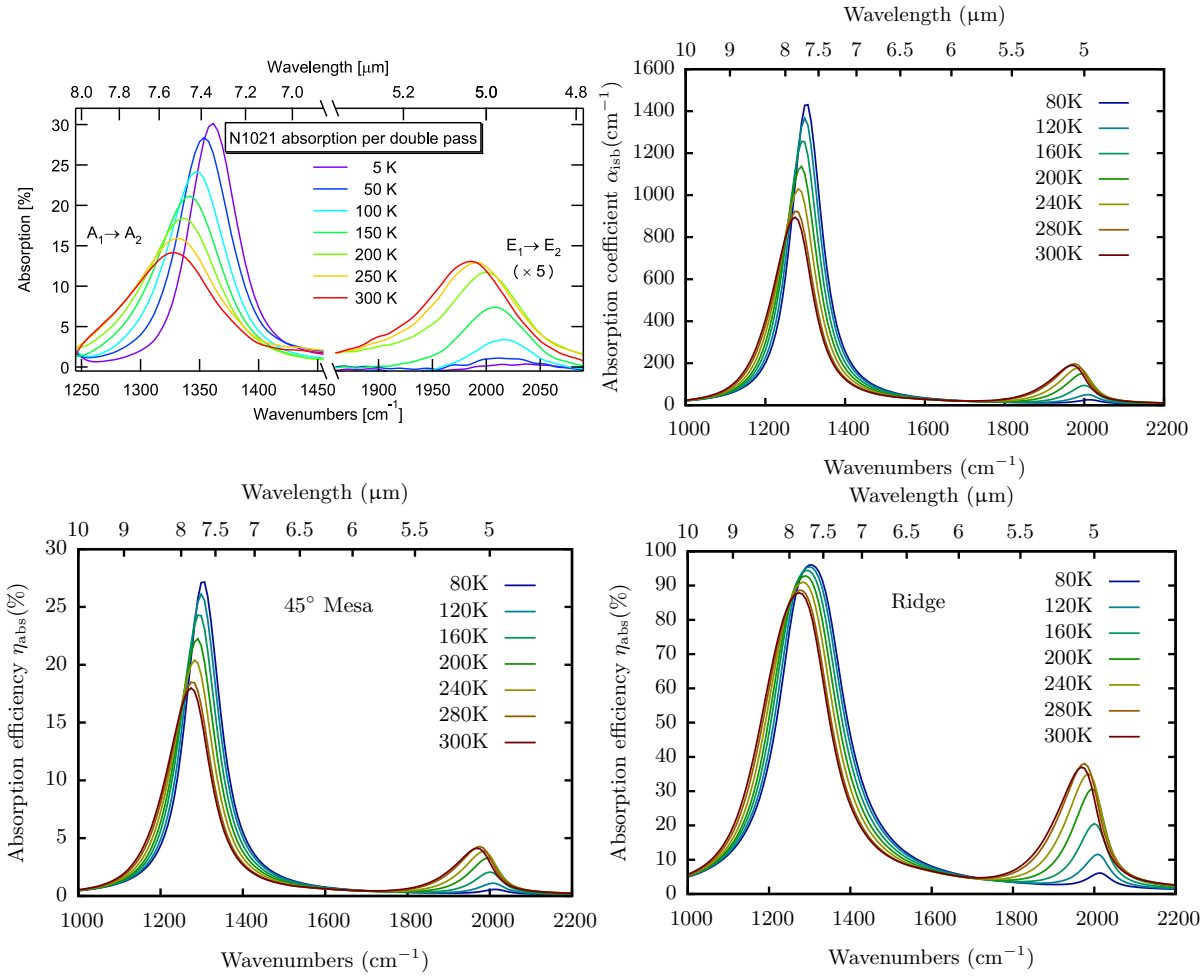

Figure 4.10: Absorption efficiency of a $\lambda = 7.5\,\mu\text{m}$ QCD. The plot for the measured data (left upper) is reprinted with permission from [161], note the different scale. The corresponding simulation is shown below. The decrease of the absorption efficiency is due to the decreased absorption coefficient (right upper). At short absorption length, as it is the case for the mesa geometry, the relation is approximately linear. A much higher absorption efficiency can be achieved using a ridge waveguide geometry (right lower). Due to much longer absorption length, the absorption efficiency is barely affected. The ridge length for the simulation was choosen to be 50 µm. The increased broadening with increased temperature is not correctly represented by the model.

larger compared to the others. In sufficient long waveguide detectors this effect is minor. Figure 4.10 shows a comparison of the model to the measured double pass absorption presented in [161]. A small wavelength shift is present and the increased broadening at higher temperatures is not correctly described by the model. The absorption efficiency of 90% for the ridge geometry is much higher compared to absorption efficiency of 15–30% for the double pass mesa. Thus, also the decrease of the responsivity with the temperature is much smaller. Figure 4.11 shows the measured responsivity for different temperatures

of a mesa and a ridge detector using the same active region.

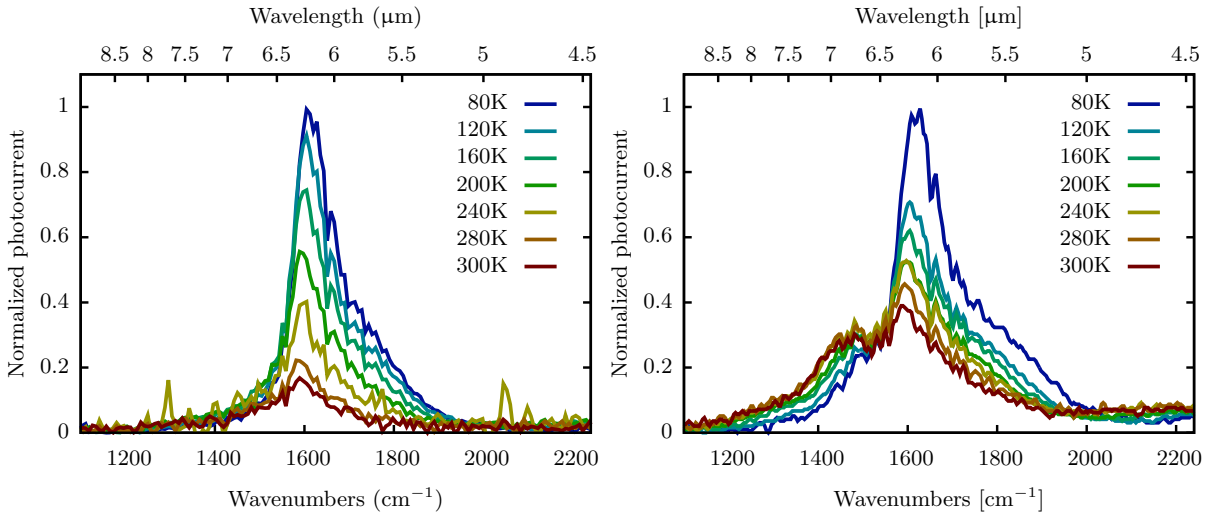

Figure 4.11: Temperature dependence of the responsivity depending on the detector geometry. The double pass mesa absorption geometry (left) leads to a much faster performance decrease with temperature compared to the ridge detector (right). Due to the much higher absorption efficiency of the ridge geometry, also other transitions are visible that lead to a more pronounced wavelength shift.

4.2.3 Responsivity

The responsivity is defined as the electric current due to the external light field (photocurrent) divided by the incident optical power. For QCDs, the responsivity can be expressed using the absorption efficiency η_{abs} and extraction efficiency p_{e} as

$$\mathcal{R} = \frac{I_{\mathrm{ph}}}{P_{\mathrm{opt}}} = \frac{\lambda \mathrm{e}}{hcN_{\mathrm{p}}} \eta_{\mathrm{abs}} p_{\mathrm{e}}. \tag{4.34}$$

If the contact resistance R_{cont} is not negligible compared to the resistance of the active region R_{AR}, the responsivity is

$$\mathcal{R} = \frac{R_{\mathrm{AR}}}{R_{\mathrm{AR}} + R_{\mathrm{cont}}} \frac{\lambda \mathrm{e}}{hcN_{\mathrm{p}}} \eta_{\mathrm{abs}} p_{\mathrm{e}}. \tag{4.35}$$

To consider the different extraction efficiencies for multiple upper detector levels, the responsivity of a particular structure is calculated considering all possible intersubband transitions individually. This is done by summing over all possible lower levels i and upper levels j with the corresponding intersubband absorption coefficient α_{ij} and extraction efficiency $p_{\mathrm{e},j}$. For the 45° facet double pass mesa geometry this leads to

$$\mathcal{R} = \frac{\lambda \mathrm{e}\, T_{\mathrm{facet}}}{hcN_{\mathrm{p}}} \frac{1 - \exp(\alpha_{\mathrm{isb}} N_{\mathrm{p}} L_{\mathrm{p}} / \sqrt{2})}{\alpha_{\mathrm{isb}}} \sum_{i,j} \alpha_{ij} p_{\mathrm{e},j} \tag{4.36}$$

and similarly for the ridge waveguide geometry to

$$\mathcal{R} = \frac{\lambda \mathrm{e}\, T_{\mathrm{facet}}}{hcN_{\mathrm{p}}} \frac{1 - \exp(-(\Gamma\alpha_{\mathrm{isb}} + \alpha_{\mathrm{wg}})L_{\mathrm{wg}})}{\Gamma\alpha_{\mathrm{isb}} + \alpha_{\mathrm{wg}}} \sum_{i,j} \Gamma\alpha_{ij} p_{\mathrm{e},j}. \tag{4.37}$$

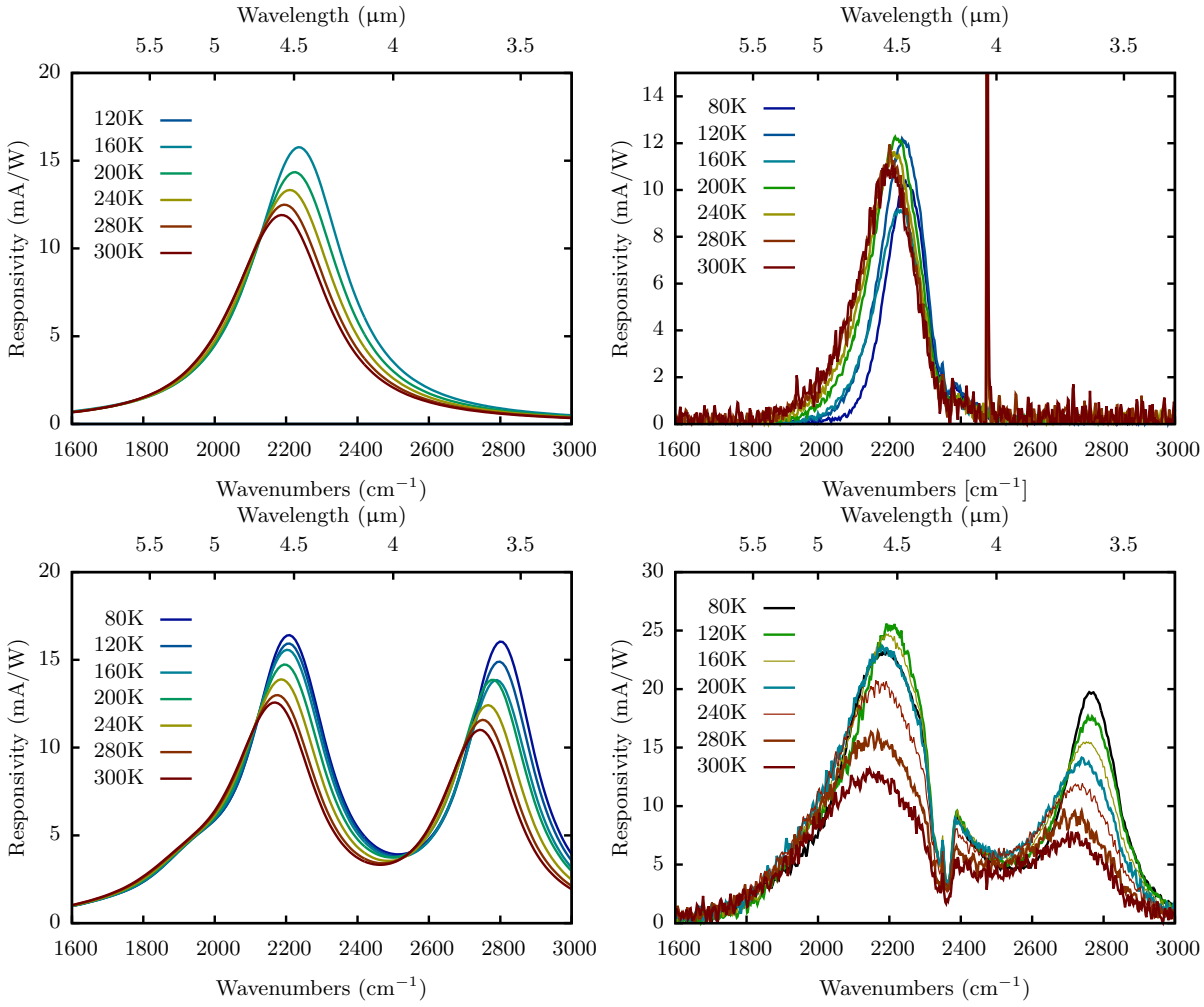

Figure 4.12: Simulated (left) and measured (right) spectral responsivity of the vertical (upper) and diagonal (lower) transition designs, corresponding to the band diagrams shown in figure 4.8. The dip in the spectra around 2350 cm^{-1} is due CO_2 absorption in the atmosphere.

Figure 4.12 shows the comparison of the measured and calculated responsivity of the 4.5 µm QCDs, samples C0115 & C0117 (see Appendix C). The bandstructure is shown in 4.8. The diagonal transition design has a better extraction efficiency ($p_{\mathrm{e}} = 75\%$ instead of 47%), but a smaller dipole matrix element. The benefit of a diagonal transition on the extraction efficiency is generally more pronounced at longer wavelength (smaller transition energies) [162, 163]. Going to smaller wavelength the extraction efficiency of both designs increases and the benefit becomes less significant. The transition energy of the diagonal design is mainly defined by the small well. Especially for short wavelength, this leads to

a much stronger linewidth broadening due to interface roughness and thickness gradients over the different cascades. The difference in broadening is not correctly predicted by the model. The doping of both designs has been adjusted to obtain the same peak responsivity in the calculation. The diagonal transition design has slightly more doping to compensate the reduced absorption strength. The experiment shows a slightly smaller peak responsivity for the vertical design. This might be due to inaccuracies in the doping. This difference is also present in the measured resistance compared to the model presented in the next section.

4.2.4 Johnson noise and differential resistance

QCDs are commonly operated near zero bias in thermal equilibrium. In this photovoltaic mode, the noise is dominated by thermal noise. It is the noise generated by the thermal agitation of charged carriers in an electric conductor. Thermal noise of a resistance was first measured by B. Johnson [164] and explained by H. Nyquist [165] at Bell Labs, thus it is often referred to as Johnson-Nyquist noise, Johnson noise or Nyquist noise. The Johnson noise of an unbiased resistor with resistance R_0 can be described by the root mean square of the current noise i_n as

$$i_\mathrm{n} = \sqrt{\frac{4\mathrm{k_B}\,T\Delta f}{R_0}}, \tag{4.38}$$

where Δf is the bandwidth over which the noise is measured.

The noise of a QCD can be calculated using the differential resistance at zero bias. Following the work of Delga et al. [166, 167], this can be done by replacing every scattering transition between two subbands i and j with a conductance

$$G_{ij} = \frac{|I_{if}| + |I_{fi}|}{4\mathrm{k_B}\,T} = \frac{2\mathrm{e}(\rho_i/\tau_{if} + \rho_f/\tau_{fi})}{4\mathrm{k_B}\,T}, \tag{4.39}$$

where I_{if} are the currents and τ_{if} the scattering times from subband i and ρ_i the population of subband i. This results in an equivalent circuit which can be solved with traditional network analysis methods.

Starting from the matrix (4.28), which contains the all scattering times between all subbands, one can calculate the scattering rate matrix by multiplying it with a diagonal matrix containing the populations of the subbands. This results in

$$\begin{bmatrix} \mathbf{S}_{M,M-1} & \mathbf{S}_{M,M} & \mathbf{S}_{M,M+1} \end{bmatrix} = \\ \left[\begin{bmatrix} \rho_1/\tau_{11^*} & \rho_1/\tau_{12^*} & \dots \\ \rho_2/\tau_{21^*} & \rho_2/\tau_{22^*} & \dots \\ \vdots & \vdots & \ddots \end{bmatrix} \begin{bmatrix} 0 & \rho_1/\tau_{12} & \dots \\ \rho_2/\tau_{21} & 0 & \dots \\ \vdots & \vdots & \ddots \end{bmatrix} \begin{bmatrix} \rho_1/\tau_{11'} & \rho_1/\tau_{12'} & \dots \\ \rho_2/\tau_{21'} & \rho_2/\tau_{22'} & \dots \\ \vdots & \vdots & \ddots \end{bmatrix} \right], \tag{4.40}$$

where ρ_i is the population of the subband i.

In a first rough approximation one can calculate the device resistance using the resistance of one period from the ground state of the active well to the ground state of the next periods active well multiplied by the number of periods. For this, we have to include the ground state of the next period in the scattering matrix. The modified matrix is

$$\mathbf{S} = \begin{bmatrix} \mathbf{S}_{M,M} & \mathbf{S}_{M,1'} \\ \mathbf{S}_{1',M} & 0 \end{bmatrix} = \begin{bmatrix} \begin{bmatrix} 0 & \rho_1/\tau_{12} & \dots \\ \rho_2/\tau_{21} & 0 & \dots \\ \vdots & \vdots & \ddots \end{bmatrix} \begin{bmatrix} \rho_1/\tau_{11'} \\ \rho_2/\tau_{21'} \\ \vdots \end{bmatrix} \\ \begin{bmatrix} \rho_1/\tau_{11^*} & \rho_1/\tau_{12^*} & \dots \end{bmatrix} \quad 0 \end{bmatrix}. \quad (4.41)$$

Note that due to periodicity $\rho_i = \rho_{i^*} = \rho_{i'}$, $\tau_{ii^*} = \tau_{i'i}$ and $\tau_{ii'} = \tau_{i^*i}$. However, this method does not properly account of scattering between two adjacent periods, as in this simple approach the ground state is the only state which connects two periods. All other inter-period scattering processes are neglected. A better approximation is to periodically repeat the scattering matrix corresponding to the number of periods and then again add an additional ground level.

$$\mathbf{S} = \begin{bmatrix} \mathbf{S}_{M,M} & \mathbf{S}_{M,M+1} & & & & & \\ \mathbf{S}_{M,M-1} & S_{M,M} & \mathbf{S}_{M,M+1} & & & & \\ & \ddots & \ddots & \ddots & & & \\ & & S_{M,M-1} & S_{M,M} & S_{M,M+1} & & \\ & & & \mathbf{S}_{M,M-1} & \mathbf{S}_{M,M} & \mathbf{S}_{M,1'} & \\ & & & & \mathbf{S}_{1',M} & 0 & \end{bmatrix} \quad (4.42)$$

In order to calculate the resistance of the device we express eq. 4.39 in matrix form

$$\mathbf{G} = \frac{2\mathrm{e}}{4\mathrm{k_B}\,T}(\mathbf{S} + \mathbf{S}^{\mathrm{T}}). \quad (4.43)$$

The conductivity matrix $\mathbf{G}$ represents a network of resistances representing all possible transitions between the subbands. This allows a straightforward calculation of the total device resistance using traditional network analysis methods, in particular the nodal analysis approach. In a first step, we construct the so called node matrix $\mathbf{A}$, which consists of the negative conductivity matrix from eq. (4.43) plus a diagonal matrix, where its elements are the line sum of matrix $\mathbf{G}$, which corresponds to the sum of the conductivities of all connected resistances to the node.

$$\mathbf{A} = -\mathbf{G} + \mathbf{G}\,[1\,1\,..\,1]^{\mathrm{T}}\,\mathbf{E}, \quad (4.44)$$

where $[1\,1\,..\,1]^{\mathrm{T}}$ is a unity vector and $\mathbf{E}$ the unity matrix with the same dimension as $\mathbf{G}$. In a next step we define node M (the added ground state) to be the ground reference for the node analysis by deleting the last column of the node matrix $\mathbf{A}$. Furthermore, we

can delete the last row of the node matrix **A**, as it equals the sum of the other rows and therefore contains no additional information. The resulting reduced node matrix **A**' is then again a square matrix. The node voltages relative to node M can be calculated by

$$\mathbf{U} = \mathbf{A'}^{-1}\,\mathbf{I}, \tag{4.45}$$

where **I** describes additional currents that flow towards the nodes. Using $\mathbf{I} = [1\,0\,..\,0]^{\mathrm{T}}$, the device resistance equals to the first element of **U** or just to the element (1,1) of the inverse of the reduced node matrix $\mathbf{A}'$.

$$R_{\mathrm{AR}} = [1\,0\,..\,0]\,\mathbf{A'}^{-1}\,[1\,0\,..\,0]^{\mathrm{T}} = (\mathbf{A'}^{-1})_{1,1} \tag{4.46}$$

The statistical approach of the Monte-Carlo approach leads to a significant error at low temperatures and high optical transition energies for a typically used number of events (10^7–10^9). This is due to the worse statistics for higher energy levels, as most scattering events occur in the lower energy levels. This issue is commonly not relevant for gain, absorption, etc., but has a significant impact on the device resistance. For low temperatures or high transition energies the subband population is thus calculated using Fermi-Dirac statistics, assuming thermal equilibrium.

Figure 4.13 show the comparison of this model to experiments. Four devices with two different active regions are compared., showing a very good agreement. At low temperatures one device shows a plateau, which is not present in the simulation nor the other devices. The plateau has also been observed in several other devices. It might be attributed to defects or surface currents resulting in a parasitic parallel resistance.

It has to be noted, that the device resistance is also crucial when aiming for heterogeneous cascade broadband designs. This approach has been followed in [168]. However, the measured spectral response was much weaker at longer wavelength compared to their simulation. This can be easily explained, considering the resistance of the different cascades. The resistance scales exponentially with the energy difference between the upper level E_2 and the Fermi level E_{F}, which is commonly expressed as activation energy $E_{\mathrm{act}} = E_2 - E_{\mathrm{F}}$ (this is also the reason, why the resistance in figure 4.13 follows a straight line). Thus, the cascades for longer wavelength have a significantly lower resistance. Recalling the responsivity including a series resistance eq. 4.35

$$\mathcal{R} = \frac{R_{\mathrm{AR}}}{R_{\mathrm{AR}} + R_{\mathrm{cont}}} \frac{\lambda \mathrm{e}}{hcN_{\mathrm{p}}} \eta_{\mathrm{abs}} p_{\mathrm{e}}, \tag{4.47}$$

one expects a lower efficiency for the long wavelength cascades due to the high series resistance induced by the short wavelength cascades. Thus, when aiming for broadband designs using heterogenous cascades, the difference in the resistance has to be corrected by doping and the number of cascades of each section. A better method to prevent this issue would be a two section device with separated contact layers. Obviously, this would require a more complicated fabrication.

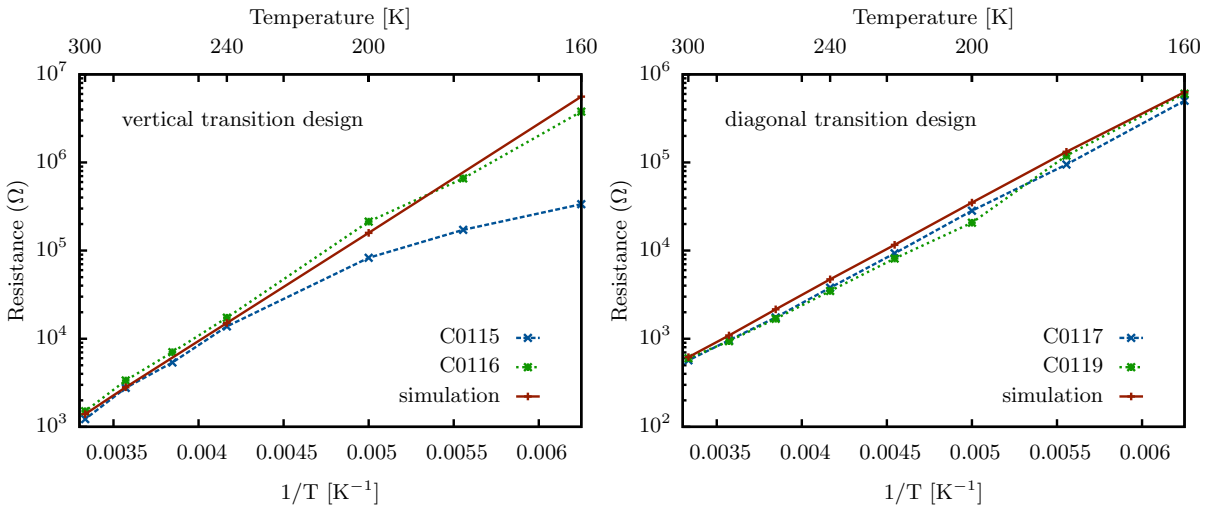

Figure 4.13: Comparison of the resistance model to experiments for a vertical transition QCD (left) and a diagonal transition QCD (right). For both designs two samples have been grown with nominally the same active region. Small derivations can be attributed to small inaccuracies in the doping density. Variations on the doping lead to a vertical shift as well as a slight change of the slope due to the changed Fermi level. Some devices show a plateau at low temperatures, which might be attributed to parasitic parallel channels.

4.2.5 Noise equivalent power and specific detectivity

The relevant performance parameter of a photodetector is the signal-to-noise ratio (SNR). In the context of photodetectors the SNR is commonly given in terms of noise equivalent power (NEP). It describes the optical input power, which leads to a signal with the same strength as the noise i_n

$$NEP = \frac{i_\mathrm{n}}{\mathcal{R}}. \tag{4.48}$$

For discrete detectors it is common to use the specific detectivity, which also includes the normalization on the optical area A_opt and the electric bandwidth Δf. This is useful, as the noise i_n and therefore also NEP scales with the square root of the electrical area $\sqrt{A_\mathrm{el}}$. The optical and electrical areas of the detector are often equivalent. The reduction of the electrical area is one method to increase the specific detectivity and was followed by designing an integrated plasmonic lens, which focuses normal incident light onto a small QCD section [169]. The Johnson-Nyquist noise limited specific detectivity is defined as

$$D^*_\mathrm{J} = \frac{\sqrt{A\Delta f}}{NEP}. \tag{4.49}$$

The maximal achievable value is given by the so called background limited specific detectivity. In this case, the noise due to the background radiation stronger exceeds the thermal noise. Following [76], the background limited specific detectivity of a photovoltaic

detector is

$$D^*_{\mathrm{BL}} = \sqrt{\frac{2\hbar\omega\Delta f P_{\mathrm{B}}}{\eta_{\mathrm{int}}}}, \tag{4.50}$$

where P_{B} is the optical power of the incident background radiation.

For thermal imaging applications it is common to use the noise equivalent temperature difference ($NETD$) as a benchmark. It is defined as the temperature difference ΔT at which the induced change of the background radiation power ΔP_{B} equals NEP

$$NETD = \frac{NEP}{dP_{\mathrm{B}}/dT}. \tag{4.51}$$

For waveguide coupled detectors, such as ridge detectors, the normalization onto the optical area is not meaningful. For these types of photodetectors the NEP or the detectivity D_{J} without normalization onto the optical area (not D^*_{J}) are more suitable.

4.2.6 Saturation

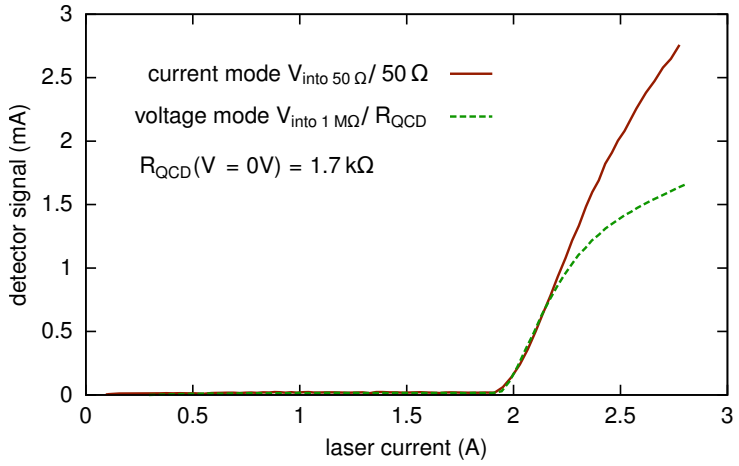

Figure 4.14: Light-current curve of the laser measured with the on-chip detector in voltage and current mode (see section 4.9). To compare the two operation modes, we divided both curves by the effective parallel resistance of the QCD to estimate the photocurrent. When the QCD is terminated by a high impedance (voltage amplifier), the QCD will be charged to a voltage corresponding to $V_{\mathrm{QCD}} \approx R_{\mathrm{QCD}} I_{\mathrm{ph}}$. As this is a relatively large reverse bias, it significantly alters the bandstructure and thus has an impact on the absorption and extraction efficiency, as well as the differential resistance of the device. This results in a saturation effect, which is only present, when the amplifier impedance is high. If the QCD is terminated by a small impedance, e.g. $50\,\Omega$ or a current amplifier, no such saturation effect could be observed. Published in supplemental material of Ref. [25]

A main advantage of QCDs is their high saturation threshold, due to the very short upper state lifetime. For ridge QCDs, the saturation effect is even smaller, as saturation

mainly effects the absorption coefficient. This means, that in case of very high optical signals, the absorption coefficient of the first few micrometers will saturate and the light will be absorbed in the following section. In our directly coupled on-chip detector, we measured a photocurrent, as high as 9 mA without observing any detector saturation. It has to be noted, that at such high optical power levels a low input impedance of the amplifier (transimpedance amplifier) or oscilloscope (50 Ω) is mandatory to maintain detector operation near zero bias. Figure 4.14 shows the detector signal of the on-chip detector versus the laser current. Terminated by a high impedance, the detector charges to a high reverse bias voltage (2-3 V), which significantly changes the alignment of the bandstructure, leading to a strong saturation effect. This saturation effect can be easily prevented using a low impedance amplifier, such as a transimpedance amplifier.

4.3 Wavelength matching

The following three sections (4.3, 4.4 and 4.5) are based on the publication "A bi-functional quantum cascade device for same-frequency lasing and detection", Applied Physics Letters 101, 191109 (2012) [134].

Same-frequency lasing and detection utilizing the identical device structure implies several difficulties. In principle, common QCLs can be also used as photodetectors. Hofstetter et al. [78] has reported a responsivity of 50 µA/W and 120 µA/W using a 9.3 µm bound-to-continuum and a 5.3 µm two-phonon resonance QCL structures as photodetectors. Figure 4.15 shows the band diagram as well as the gain in laser operation and the responsivity in detector operation for $T = 80$ K, calculated with the presented simulation models based on Monte-Carlo transport model within the VSP2 framework [106]. The device can, in principle, be used as photodetector. But first, it has a low efficiency and secondly and much more important, it detects at a different wavelength compared to the laser emission. As a laser, the device emits around 8.6–10.5 µm, while as a detector, it is sensitive to wavelength around 6.6–8 µm. The reason for this shift can be easily understood when considering a typical gain section. Figure 4.16 shows the gain section of a 4-well design. In laser operation, the optical transition occurs between the upper laser level and the lower laser level. But when using the same structure as a photodetector at zero bias, all electrons are in the ground state. The optical transition takes place between the ground state and the upper laser/detector level. This transition is much larger due to the extraction levels, which are separated to match the LO-phonon energy. As a result, the device is sensitive to much shorter wavelength compared to its emission at laser bias. When aiming for monolithic integration the inherent detection functionality of typical QCLs is not sufficient. Matching the emission and detection wavelength is the key point to design a bi-functional active region. The difficulty is to achieve wavelength

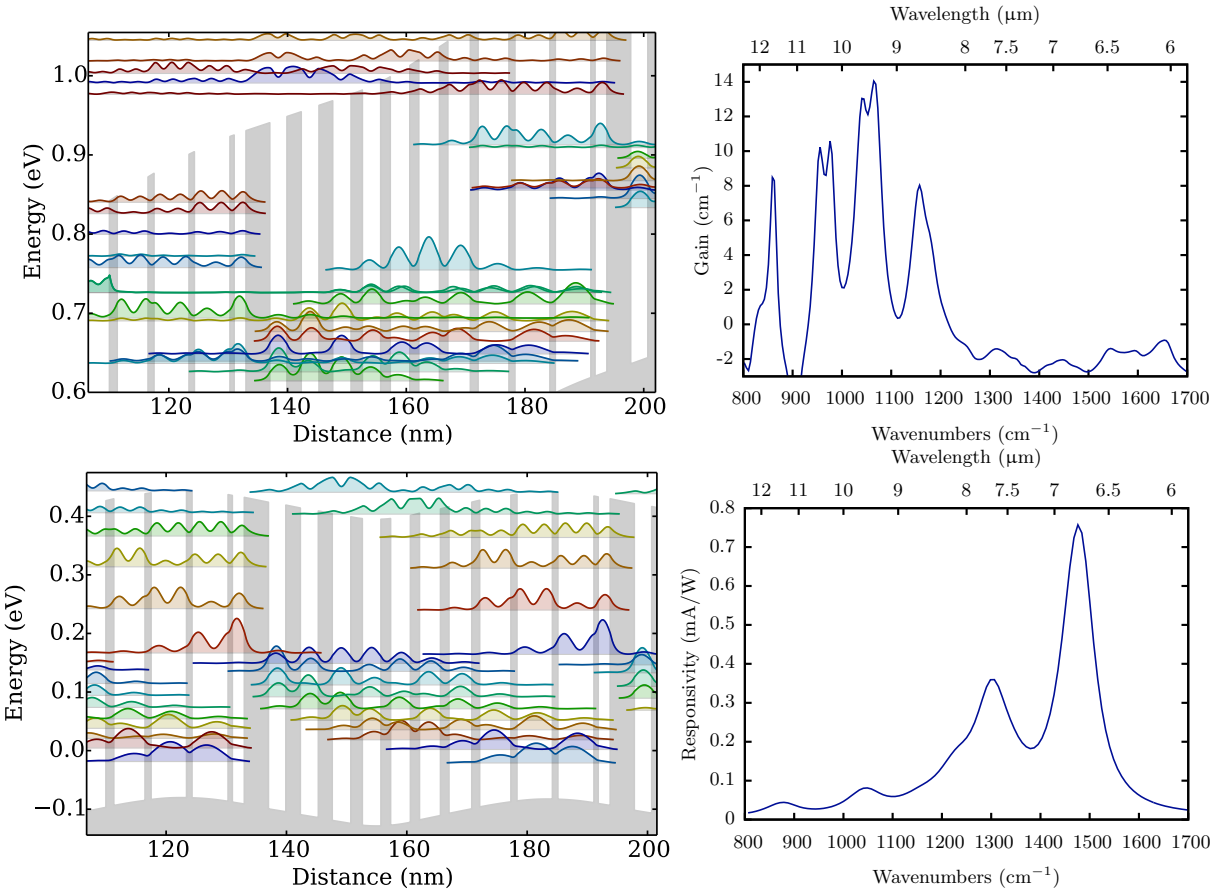

Figure 4.15: Band diagram of the 9.3 µm bound-to-continuum QCL for laser (upper) and detector (lower) operation. This device was used by Hofstetter et al. for the photocurrent measurments [78]. Details to the structure can be found in [149]. The calculated laser emission is located around 9.3 µm, while the photoresponse is at a much shorter wavelength around 7 µm. The band diagram, gain and responsivity where obtained with the presented models.

matching, while maintaining a similar lower laser level lifetime as can be achieved using typical 4-well or bound-to-continuum designs.

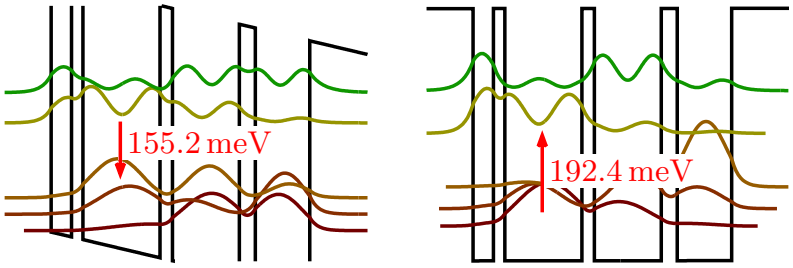

Figure 4.16: Using a 4-well active region as a detector leads to an intrinsic energy-shift between the laser and the detector. The detector is blue-shifted, because the optical transition occurs between the lowest extraction level and the upper laser level, not the lower laser level. Published in [136].

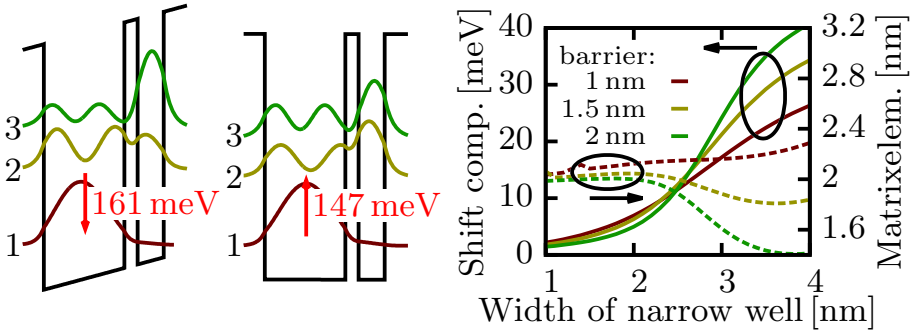

Figure 4.17: The intrinsic energy-shift between the laser's and the detector's optical transition is compensated by inserting a narrow well with its energy level strongly coupled to the upper level of the active well. The reduced coupling due to bias results in a red-shift of the detector transition compared to the laser transition. The plot on the right shows the compensation shift and the detectors dipole matrix element over the width of the narrow well for three different barrier width. Published in [136].

One approach is to introduce a Stark-shift to compensate for the inherent energy-shift. This can be achieved using the narrow well of the 4-well design, which is located between the injector barrier and the active wells. If strongly coupled to the active well, it produces a red-shift of the lasing transition compared to the detecting transition, as illustrated in Figure 4.17. The width of the narrow well is designed, such that its energy level matches the upper level of the active well, which causes the levels to degenerate (levels 2 and 3) at zero bias. The lower degenerated energy level (level 2) is used as the upper level for the laser and the detector. At laser bias the coupling is reduced, because the energy level of the narrow well is shifted towards higher energy. Thus, the detector transition (between levels 1 and 2) is red-shifted compared to the laser transition. However, in the case of a active region with a two-phonon extraction, this induced red-shift is still too small to fully compensate the blue-shift induced by the LO-phonon extraction concept. The compensating red-shift could be further increased by increasing the width of the narrow well, but the optical transition becomes more and more diagonal, which reduces the dipole matrix element and thus the device performance. One can overcome this issue by first reducing the coupling between the lower laser level and the laser extraction levels to minimize the intrinsic shift, before compensating it. This reduced coupling actually results in a structure similar to the well known bound-to-continuum design but with much smaller splitting between the individual levels. This design allows wavelength matching without a significant reduction of the dipole matrix element. However, the drawback is a higher lifetime of the lower laser level, which reduces the laser performance.

4.4 Extracting and injecting electrons

Apart from wavelength matching, such a device has to provide a good injection into the upper level if operated as a laser as well as a good extraction out of the upper level if operated as a detector. Considering the band diagram of the bound-to-continuum laser used for the first detector operation experiments (figure 4.15) one can easily identify the reason for the low photoresponse. The injection barrier separates the upper level from the following injector/extractor section. The limitation occurs in the tunnelling process due to the lack of resonantly coupled extractor states. Electrons excited to the upper level via optical absorption will more likely scatter back to the ground level rather than tunnel through the injection barrier to contribute to the photocurrent. The following part of a typical laser injector section provides a good extraction efficiency and thus, is mainly used for the laser performance optimization. Aiming for detector operation only, one would use a reduced coupling of the extractor levels to increase the device resistance. This approach, however, can not be followed, as it would prevent the laser operation completely. Furthermore, the device resistance can be significantly increased with the waveguide coupled ridge detector geometry, which overcompensates this drawback. To reduce thermal population, which in turn reduces the responsivity at higher temperatures, the seperation between the lower detector level and the lowest phonon ladder level was designed to be as large as possible to not reduce the laser performance. On the other hand, a small separation can be utilized to shift the detector spectrum at high operation temperatures towards longer wavelength.

In conclusion, the two or three highest extractor levels of the phonon ladder play a crucial role in the optimization of bi-functional devices. At zero bias these levels are designed to provide efficient extraction via resonant tunnelling and LO-phonon scattering. High scattering rates are provided by proper energy separation and optimized overlap integrals. At laser bias, these levels have to provide a selective electron injection to the upper laser level.

4.5 The first bi-functional active region

The band diagram of the first bi-functional active region is shown in figure 4.18. The sheet doping density has been chosen to be $2.1\times10^{11}\,\mathrm{cm}^{-2}$, which is a typical value for both QCLs and QCDs. Although, QCDs are commonly doped in the active well, we put the doping into the injector/extractor, as it is common for lasers. This requires the consideration of the Hartree potential through Poisson's equation self-consistently, described in more detail in section 3.2.2. The device was grown by molecular beam epitaxy (MBE) of sightly strain compensated InGaAs/InAlAs on an n-doped InP substrate (Si, $2\times10^{17}\,\mathrm{cm}^{-3}$), with a period mismatch $< 1\%$. The waveguide consists of 35 periods of the active region

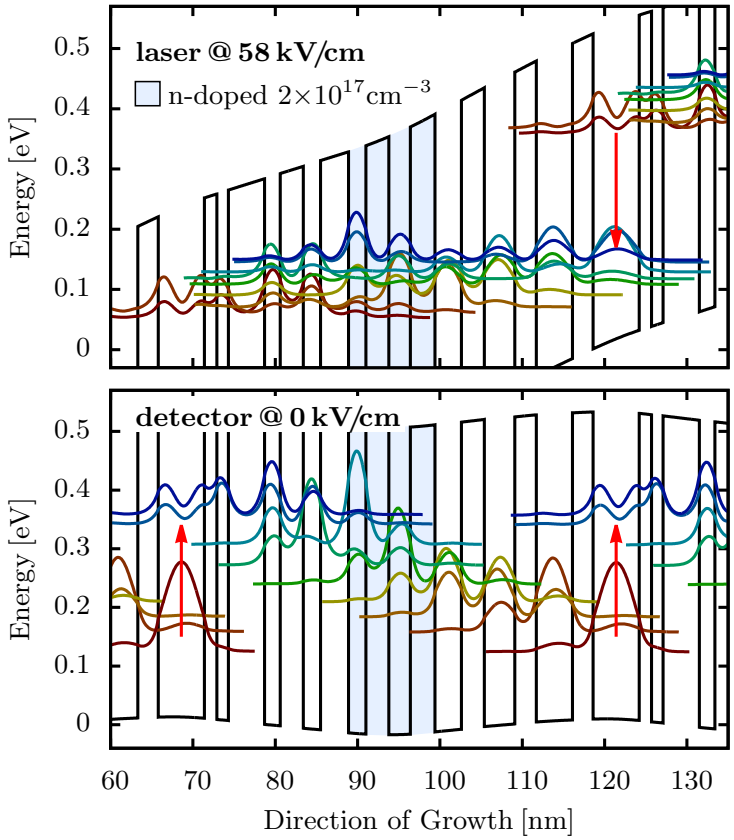

Figure 4.18: Bandstructure of the bi-functional active region at laser operation (a) and detector operation (b). The doped regions are highlighted in blue. Published in [136].

sandwiched between two InGaAs layers, an InAlAs top cladding layer, similar to the optimized waveguide design presented in [146]. More details on the waveguide design will be discussed in section 4.8. The confinement factor and waveguide losses were calculated as 0.64 and 5.54 cm^{-1}, however, from experiments we expect higher waveguide losses.

The laser and the detector characteristics were measured from a 10 µm × 2 mm and a 10 µm × 0.6 mm ridge. Figure 4.19 shows the emission spectrum of the laser, the photocurrent spectrum of the detector, as well as the electroluminescence spectrum measured slightly below laser threshold. The devices works at room temperature in both operation modes and and the detector response spectrum completely overlaps the laser emission spectrum. The electroluminescence spectrum perfectly matches the detector spectrum. This indicates that the device is capable to emit and detect in a broad spectral range from 6.2 µm to 7.1µm. This is important for chemical sensing applications to distinguish different chemicals with great selectivity and facilitated calibration [4], more detailed described in chapter 6.2.

The output power and current-voltage characteristic in laser operation are shown in Figure 4.20 for different temperatures. The first bi-functional device had a threshold current density of 8 $\mathrm{kA/cm}^2$ at room temperature. This can be mainly attributed to the

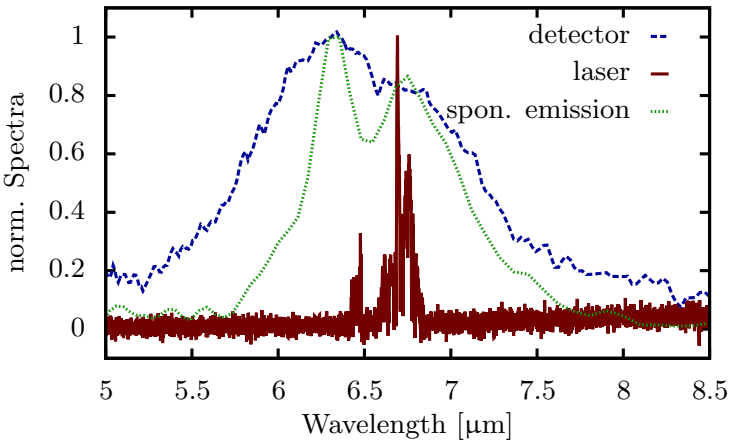

Figure 4.19: The measured spectrum of the first bi-functional active region design at room temperature. Both the laser and the electroluminescence spectrum were measured using a 10 µm × 2 mm ridge with 100 ns pulses at 5 kHz. The two peaks of the electroluminescence spectrum result from atmospheric absorption. The photocurrent spectrum of the detector was measured by focusing the light from a low intensity Globar source onto a 10 µm × 0.6 mm ridge facet and normalized by the atmospheric absorption spectrum. Published in [136].

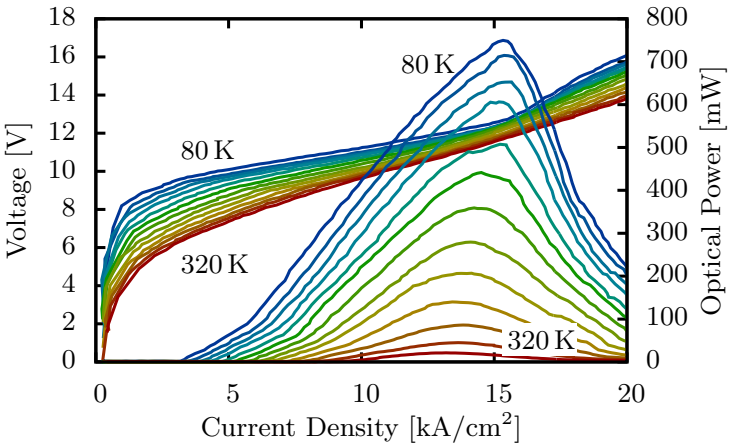

Figure 4.20: Optical output power and current-voltage characteristic of the bi-functional device. The curves are measured from a 10 µm×2 mm ridge laser with 100 ns pulses at 5 kHz. The absolute output power was measured with a calibrated DTGS pyroelectric detector. Published in [136].

increased lower laser level lifetime as well as thermal backfilling due to the increased barrier width resulting in a lower energy splitting of the extraction levels. The improvement of the electron extraction at laser bias was the main focus of following bi-functional designs.

Figure 4.21 shows the detector responsivity in 20 K steps from 80 K to 300 K. From the initial characterization presented in [134], the device has a peak responsivity of 10 mA/W at 80 K and 3.6 mA/W at 300 K, which already is a good value for QCD without bi-functional operation [155]. These values take the inefficient coupling from free space

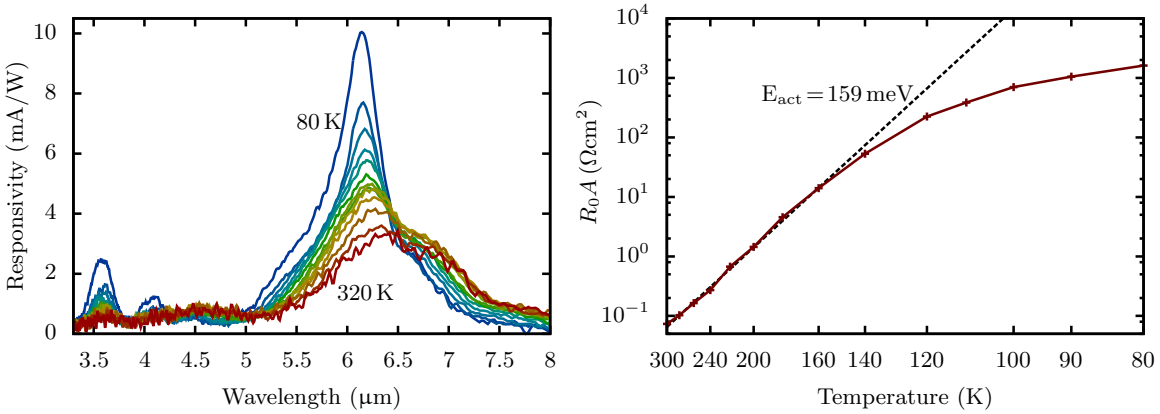

Figure 4.21: Spectral responsivity of the detector at different temperatures. The inset shows the resistance-area product R_0A as a function of inverse temperature. The spectra were measured from a 10 µm×0.6 mm ridge with a FTIR spectrometer and normalized by the atmospheric absorption spectrum. The absolute values were measured with a continuous wave laser adjusted to 10 mW. Considering the measured spot profile and the 5 µm×10 µm facet, as well as the transmission of the ZnSe cryo-window, the laser power was corrected for the responsivity calculation to 2.8 mW. Published in [136].

propagation into the ridge waveguide into account. Hence, for on-chip waveguide coupled detectors the coupling efficiency is much higher. The detector performance of all following bi-functional devices has been characterized for waveguide coupled operation showing responsivity values around 40 mA/W. This improvement is due to the refined measurement technique and not due the bandstructure design. The improvement of the bandstructure design has lead to a significant improvement of the laser performance but showed only a minor improvement of the detector performance. The first design was already well optimized for photodetection. The resistance-area R_0A product, shown in the inset, is essential for the characterization of the noise behavior for Johnson noise limited detectors, as it is the case for QCDs at zero bias and higher temperatures. The particular impact of the detector noise on the total noise of a monolithic sensor system is discussed in section 6.1.

4.6 Horizontal-vertical extraction scheme

This section is based on the publication "High performance bi-functional quantum cascade laser and detector", Applied Physics Letters 107, 071104 (2015) [136].

The main challenge in the design of QCLDs is the optimization of both operation modes, while maintaining the spectral overlap between the laser emission and the photoresponse. This requirement limits the achievable performance of QCLDs compared to conventional QCLs. The first designs [25, 134] showed room temperature operation for

both the laser and the detector, but were limited to low duty-cycle operation, due to the large threshold current densities and low wall-plug efficiencies. High performance QCL designs are commonly based on resonant optical phonon extraction, where thin barriers are used to maximize the overlap with the extractor subbands and to provide a large energy separation in order to prevent thermal back filling of electrons from the injector to the lower laser subband. For bi-functional QCLD designs, this optimization cannot be fully exploited as the strong coupling of the lower laser subband and the extractor subbands would lead to a large wavelength-shift between the laser and the detector operation mode. In previous QCLD designs, wavelength matching was achieved by using broader barriers, with the drawback of a significantly reduced laser performance in terms of threshold current, efficiency and output power.

The horizontal-vertical extraction scheme allows the design of bi-functional QCLDs with a similar laser performance as conventional QCLs. Also the detector can outperform available devices due to the benefit of using a waveguide coupled detector. The band diagram of the presented bi-functional active region for both operation modes is shown in Figure 4.22. Similar to the previous QCLDs (figure 4.18), thicker barriers are used to achieve wavelength matching between the laser and the detector. Additionally, a slightly more diagonal transition was used, giving another knob to compensate the stark-shift introduced by the extraction levels. The thicker barriers lead to a more horizontal electron extraction through scattering assisted tunnelling rather than the usually used vertical extraction via an LO-phonon ladder. For wavelength matching it is sufficient, that the first 2–3 barriers are thicker. The width of the following barriers does not influence the emission and detection wavelength. The second extractor part is designed with thin barriers to vertically extract electrons and to prevent thermal backfilling via several strongly coupled subbands with high energy separation. The concept of horizontal-vertical extraction gives a huge benefit for the laser operation. The energy separation of the lowest injector subband and the lower laser subband is 90 meV at threshold and 110 meV at the peak of the wallplug efficiency. This design approach also gives a higher separation of the upper laser subband and its next upper subband (60 meV at peak wallplug efficiency) as well as a minigap in the injector to reduce the electron escape probability to the continuum. As discussed in section 4.4, the third part (in figure 4.22 referred to as injector section) has to be designed to provide sufficient electron injection into the upper subband at the laser bias as well as to provide efficient extraction from the upper subband to the injector subbands at the detector bias (zero bias). The energetically highest subband in the injector section has no function at QCL bias, but acts as detector extraction level at zero bias. As a drawback, this subband may introduce a small additional electron escape probability through the subbands above the upper laser subbands to the continuum. The slightly diagonal transition is also beneficial to optimize the electron extraction efficiency from the upper subband in detector operation.

The structure was grown similar to the first structure by MBE and consists of lattice-

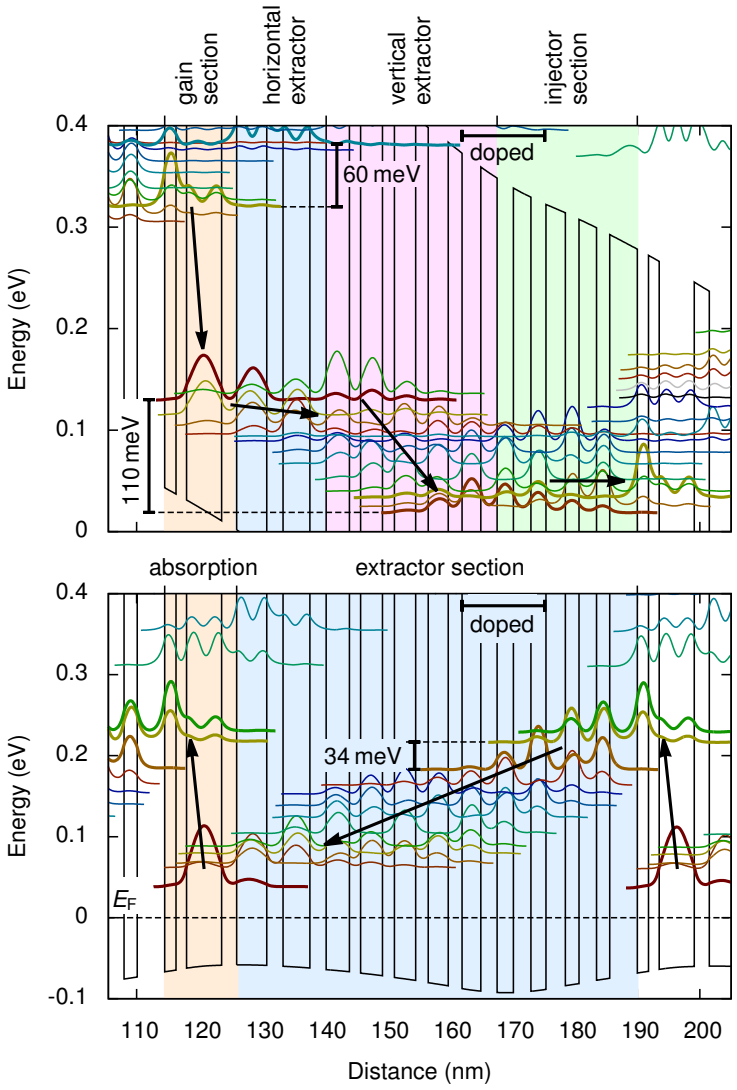

Figure 4.22: Band diagram of an improved bi-functional QCLD for laser bias at the maximal wallplug efficiency (upper) and zero bias (lower). The device is designed for a wavelength of $\lambda = 6.8\,\mu m$. The different logical sections are highlighted in color and the preferred electron transport direction is denoted with black arrows. The band diagrams are obtained solving Schrödinger's equation self-consistently with Poisson's equation using the subband populations calculated by single particle Monte-Carlo transport [106]. The detector is in thermal equilibrium with the Fermi level denoted by the dashed line. Published in [136].

matched InGaAs/InAlAs on InP. The 35 periods of the active region are embedded in two low-doped InGaAs layers to increase the confinement. Differently to before, specifically designed contact superlattice structures between the active region and the InGaAs layers have been included. These enable efficient filling of the first lower detector subband, as well as efficient charge transport at detector and laser biases to prevent charge accumulations and series resistances. Care must be taken to prevent the contact superlattices from introducing resonant absorption loss through intersubband transitions. The design of

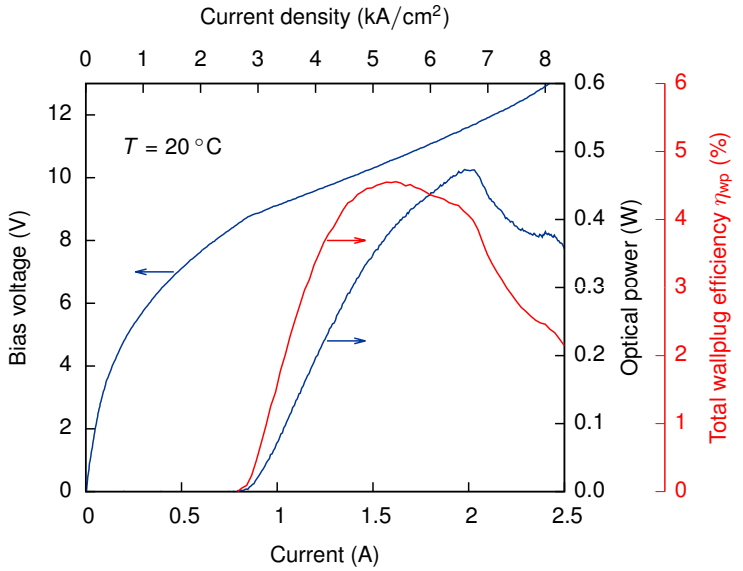

Figure 4.23: Bias voltage, optical output power and total wallplug efficiency in pulsed mode 100 ns @ 10 kHz of the uncoated 10 µm wide and 3 mm long ridge. The total wallplug efficiency includes the optical power emitted from both facets. Published in [136].

the contact regions is discussed in section 4.7. The layer structure, including the active region, the contact superlattices and the cladding can be found in the appendix C.2. The grown structure has been fabricated as epi-up mounted dry etched 10 µm wide laser and detector ridges, cleaved to 3 mm and 0.5 mm, respectively. More details on the fabrication and characterization can be found in appendixes A and B.

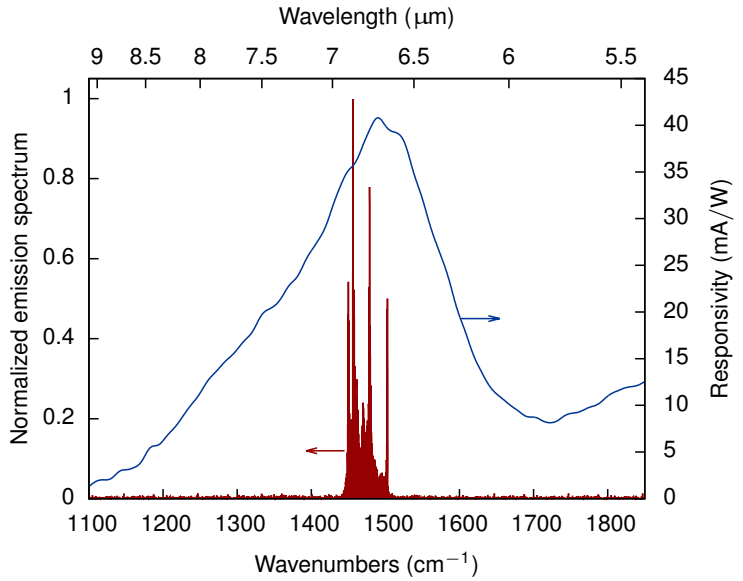

Figure 4.24: Overlap of the emission spectrum and the spectral responsivity of the presented QCLD structure. Published in [136].

The light, voltage and total wall-plug efficiency versus current characteristic of the

3 mm long Fabry-Perót ridge laser is shown in Figure 4.23. Compared to previous designs [25, 134] all characteristic parameters are improved by at least a factor of two. At room temperature, the threshold current is reduced from 8 kAcm^{-2} to 3 kAcm^{-2}. The optical output power is increased from 40 mW to 470 mW. The laser has a total wall-plug efficiency (considering both facets) of around 5%, which is a factor of two to three lower than for conventional high performance QCLs with comparable waveguide structures. Further improvements can be achieved by applying high- and anti-reflection coatings on the facets, as well as by using buried heterostructure waveguides with InP cladding to decrease the waveguide losses and increase the heat dissipation [170].

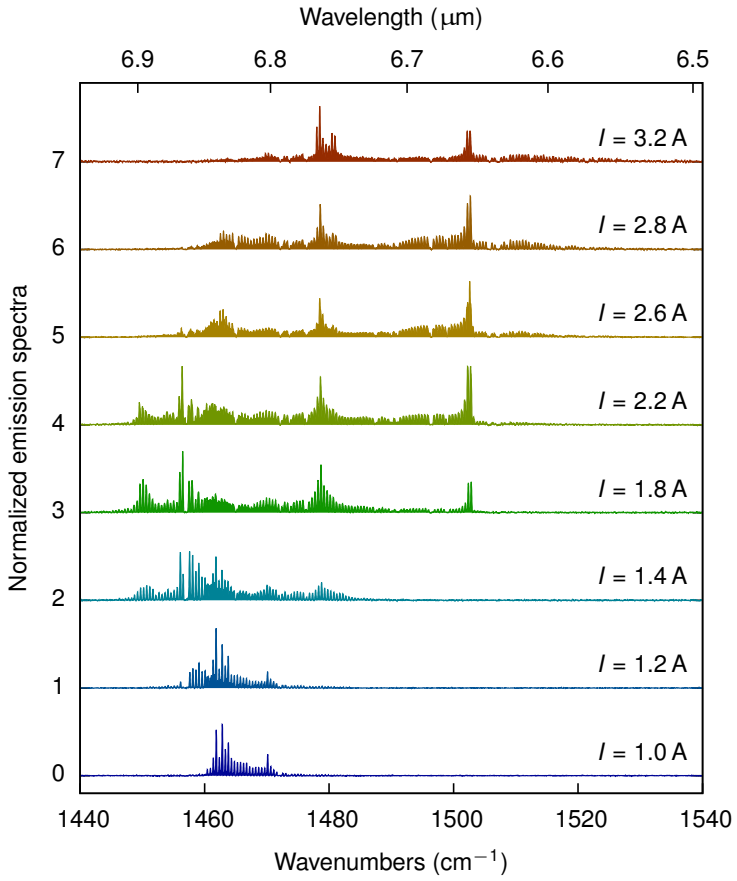

Figure 4.25: Pulsed laser emission spectra with increasing current. The laser spectrum shifts to shorter wavelength, which might be utilized for on-chip sensor to obtain spectral information of the absorption features. Published in [136].

Figure 4.24 shows the spectral overlap of the laser emission and the photoresponse. The presented detector has a peak responsivity of approximately 40 mA/W. The characterization was performed using an external source focused onto the detector ridge facet with a 10 cm focal length lens. The total power impinging on the detector was obtained by considering the beam-shape and the dimensions of the ridge facet, described in more detail in appendix B. The device has a differential resistance of 1.6 kΩ around zero bias, which

results in a Johnson/thermal noise limited noise equivalent power (NEP) of $80\,\mathrm{pW}/\sqrt{\mathrm{Hz}}$ at the peak wavelength at room temperature [167]. For practical reasons, the detector was cleaved to 0.5 mm length, although anything longer than 50 µm does not increase the absorption efficiency significantly, but reduces the device resistance. For the on-chip sensor configuration, where the detector length is defined by optical lithography and dry etching, much shorter devices in the order of tens of micrometers can be used. A length of 15 µm would give the optimal Johnson noise limited NEP, while slightly longer devices around 50 µm give a higher responsivity and are favorable if the noise is limited by other sources.

The emission spectra of the laser at different currents are shown in Figure 4.25. The slightly diagonal transition leads to laser an emission spectrum which tunes with increasing bias. This feature may be utilized to gain information about the typically broad spectral features of chemicals in liquid phase without the need of an array of single mode lasers.

4.7 Contact design

The design of the electric contact regions is a crucial step in the design of bi-functional devices. While the applied bias at laser operation allows a modification of the alignment of the contact regions to reduce the series resistance, this is not possible at detector operation. Thus, the design of the contact regions is much more important for the detector operation and becomes increasingly important when reducing the number of periods. At low intensities, bias arising from the charging due to the photocurrent is not sufficient to modify the alignment. Figure 4.26 shows the band diagram of five periods of the active region, which is sufficient to accurately simulate the contact regions. With an additional superlattice on both sides as well as doping engineering, the five active regions appear unbiased and their ground states are equally populated with electrons. Without such superlattice regions, the first and last period would feel a different effective field due to the band alignment and the first ground state would be depleted. This would result in a significant series resistance. The contact superlattice is not as crucial for the laser operation, as the different regions can align at different bias fields, but it leads to an additional voltage drop. Furthermore, the interface between the different materials e.g. InGaAs/InP or InGaAs/InAlAs introduce a large barrier. The effective barrier hight can be decreased by adding a superlattice between the layers as shown in figure 4.27. Very important is not to introduce additional optical loss due to intersubband transitions in the contact superlattices, which match the designed emission or detection wavelength of the active region.

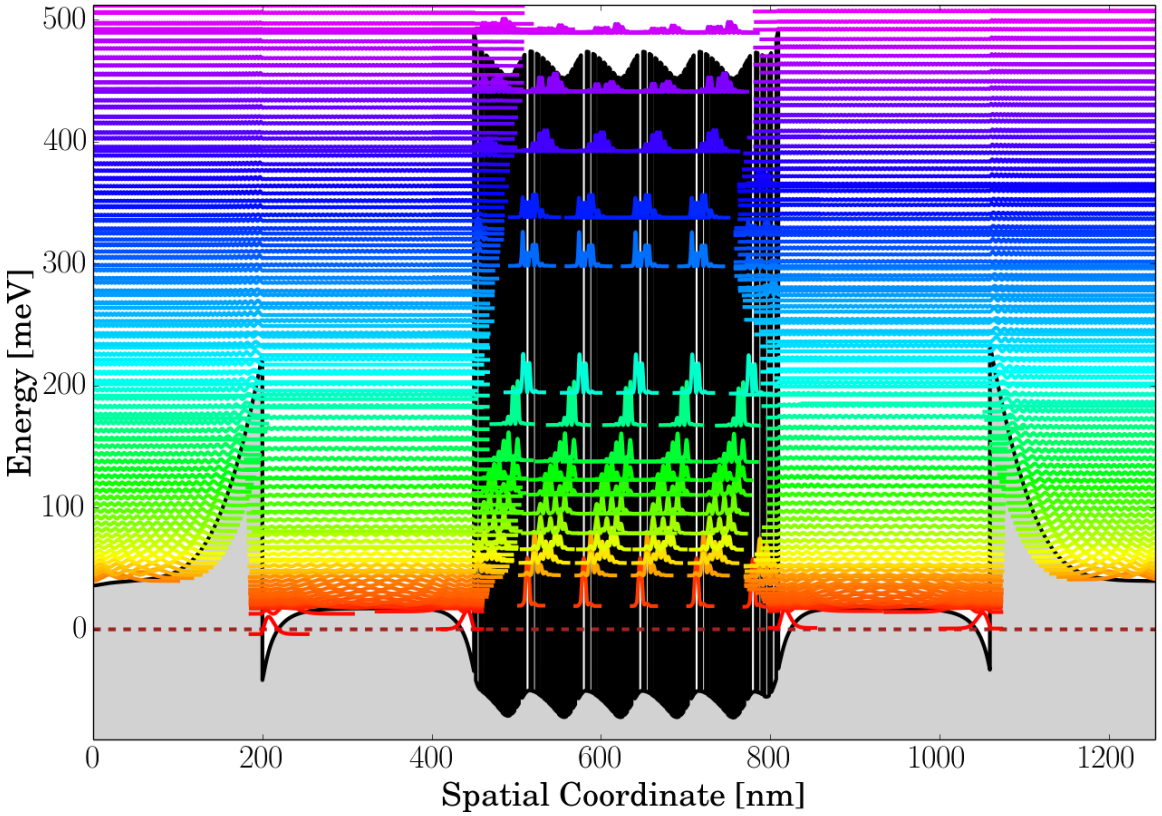

Figure 4.26: Band diagram and wavefunctions of a bi-funtional QCLD at zero bias including the contacts. To accurately simulate the contact regions it is sufficient to simulate a smaller number of active region periods. A flatband condition over all periods is maintained using particularly designed contact regions with engineered doping, such that ground levels of the active regions are at the same energy and equally filled with electrons. The remaining barriers due to the interface between InGaAs/InP can be effectively reduced adding additional superlattices (see figure 4.27).

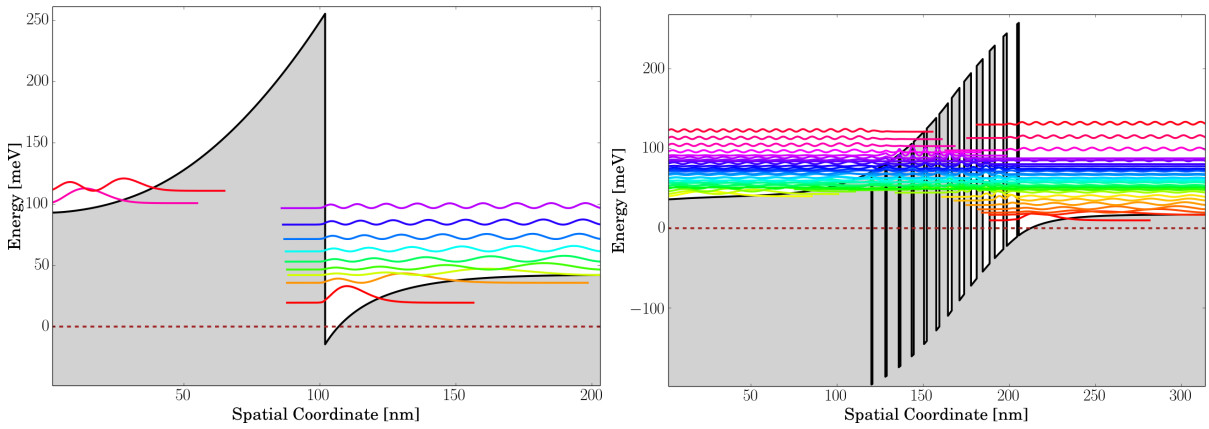

Figure 4.27: The interface between InGaAs/InP (or similarly for InGaAs/InAlAs) leads to a large barrier. This effective barrier height can be significantly reduced by adding a superlattice.

4.8 Optical design

4.8.1 Waveguide

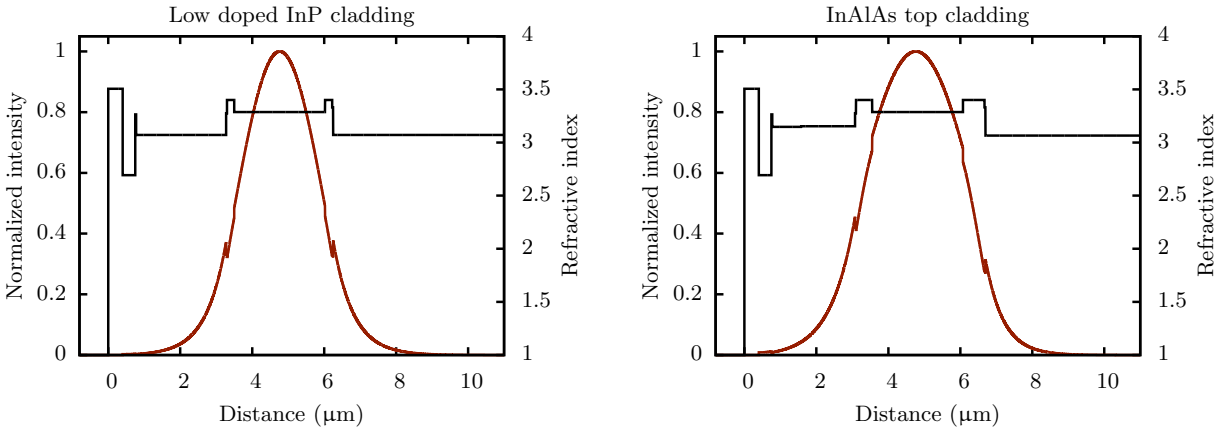

Figure 4.28: Low loss waveguide using low doped InP top and bottom cladding (left) and InAlAs top cladding and the InP substrate as bottom cladding (right). At $\lambda = 6.7\,\mu\text{m}$, the waveguide losses have been calculated to be $\alpha = 0.8\,\text{cm}^{-1}$ and $\alpha = 2.2\,\text{cm}^{-1}$, as well as the confinement factor to be $\Gamma = 80\%$ and $\Gamma = 70\%$, respectively. The InP cladding gives a benefit of more than a factor of three in addition to the higher thermal conductivity.

In order to obtain stimulated emission the active region is embedded into a waveguide which, together with optical feedback, forms the laser cavity. The key characteristics of the waveguide can be described by the confinement factor, which describes the part of the mode that overlaps with the active region, the waveguide loss and, if aimed for cw operation, the thermal resistance. The confinement factor is defined as

$$\Gamma = \frac{\int_{\text{AR}} |E(z)|^2 dz}{\int_{-\infty}^{\infty} |E(z)|^2 dz}, \tag{4.52}$$

where $\int_{\text{AR}}$ denotes the integral over the active region and $E(z)$ is the electric field of the optical mode.

Vertical confinement (in growth direction) can be achieved via dielectric, so called plasmonic enhanced or plasmon waveguides. Depending on the spectral range, e.g. mid-infrared or THz and the available materials each of these has its advantages. Mid-infrared QCLs are commonly built with dielectric waveguides. Low doped semiconductor materials are used as cladding materials for the vertical confinement, which further are used as electric contacts. A dielectric waveguide has low losses, but requires a compatible cladding layer material. In the case of the well established InGaAs/InAlAs material system InP is an ideal cladding layer material, apart from its problematic handling in MBE (phosphine is colorless, toxic and spontaneously flammable in air). As InP has not only a lower

refractive index than InGaAs and InAlAs, it has a high thermal conductivity, which makes it attractive for high duty-cycle or continuous wave operation.

The so called plasmonic enhanced waveguides are dielectric waveguides, where indicated by its name, the refractive index is reduced by the plasmon effect through high doping [171]. This approach can be applied, when either no appropriate cladding layer material is available (e.g. for GaAs/AlGaAs or InAs/AlAsSb based QCLs) or the index contrast is relatively low (e.g. for InGaAs/InAlAs based QCLs). In InGaAs/InAlAs based QCLs with an InAlAs top cladding layer, an additional highly doped InGaAs layer is used to screen the mode from the top metalization. This enables relatively low waveguide losses while keeping the cladding layer thickness in an appropriate range. Figure 4.28 shows the mode calculation of the vertical confinement in a mid-infrared QCL waveguide using a low doped InP cladding ($N_\mathrm{d} = 3\times10^{16}$) on both sides, as well as a InAlAs top cladding and the $N_\mathrm{d} = 3\times10^{17}\,\mathrm{cm}^{-3}$ doped substrate as bottom cladding. Both designs are plasmon enhanced to keep the top cladding thickness at a reasonable thickness. Due to the lower waveguide losses and increased confinement factor, as well as the increased thermal conductivity, a significantly higher laser performance can be expected using a low doped InP cladding on both sides.

The dimensions of a dielectric waveguide are in the order of the wavelength, which is an issue for longer wavelengths, especially in the THz. Plasmonic waveguides can be used to confine the mode far beyond the diffraction limit, which makes them especially interesting for THz QCLs. Large confinement factors can be achieved even in the THz with a total epi-layer thickness below $\approx 10\,\mu\mathrm{m}$, which is a reasonable upper limit for MBE growth. In plasmonic waveguides the losses are mainly dominated by ohmic losses in the metal, which are much lower at longer wavelengths. In the THz, QCLs are commonly embedded in a double metal plasmonic waveguide, which gives a confinement factor close to one and waveguide losses in the order of $16\,\mathrm{cm}^{-1}$. Plasmonic effects and passive waveguides are described more detailed in chapter 5.

The losses in dielectric waveguides are dominated by free carrier absorption due to doping required for electric conductivity. The refractive index of a semiconductor doped with the 3D density N_d is usually calculated using the Drude approximation

$$n(\omega, N_\mathrm{d}) = \sqrt{\varepsilon(\omega, N_\mathrm{d})} = \sqrt{\varepsilon_\infty \left(1 - \frac{\omega_\mathrm{p}^2}{\omega^2 \left(\frac{j}{\omega\tau}\right)}\right)}, \tag{4.53}$$

where ε_∞ is the high frequency dielectric constant. The so called plasma frequency ω_p is defined as

$$\omega_\mathrm{p} = \sqrt{\frac{N_\mathrm{d}}{\varepsilon_0 \varepsilon_\infty m^*}}, \tag{4.54}$$

and the relaxation time τ is defined as

$$\tau = \frac{\mu m^*}{\mathrm{e}}, \tag{4.55}$$

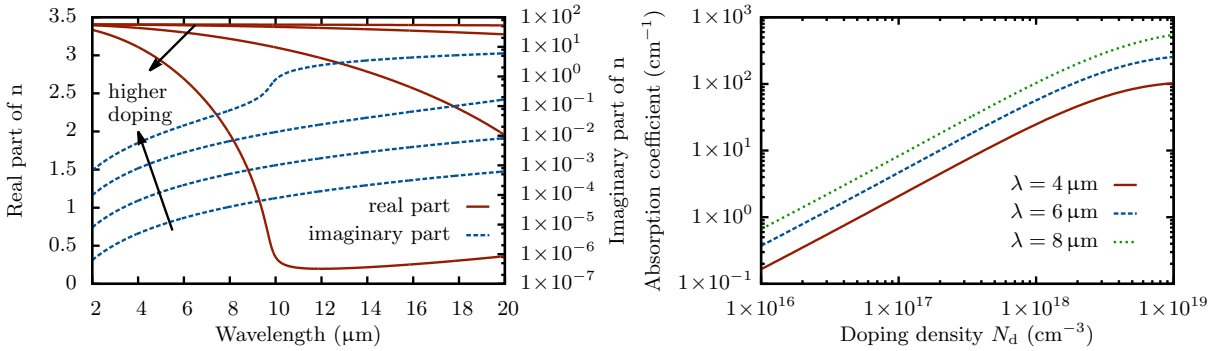

Figure 4.29: Calculated real and imaginary part of the refractive index of InGaAs for the doping densities 10^{16}, 10^{17}, 10^{18} and $10^{19}\,\mathrm{cm}^{-3}$ (left). Absorption coefficient of InGaAs depending on the doping density (right). The imaginary part of the refractive index and thus the absorption coefficient is stronger at longer wavelengths and higher doping densities. Very high doping densities of $N_\mathrm{d} > 3\times10^{18}\,\mathrm{cm}^{-3}$ lead to a plasmon effect at mid-infrared frequencies, which can be utilized in the waveguide design.

where μ is the mobility and m^* the effective mass, which also depend on the doping. The electron mobility is commonly obtained from Hall measurements. The induced absorption loss of a layer in the waveguide depends on the imaginary part of its refractive index and its overlap with the optical mode. The relation between the absorption coefficient and the refractive index is $\alpha = \frac{4\pi\,\mathrm{Im}(n)}{\lambda}$. Figure 4.29 shows the calculated real and imaginary part of the refractive index of InGaAs over the wavelength for different doping densities, as well as its absorption coefficient depending on the doping for selected wavelength.

Confinement in the lateral direction is achieved by fabricating a ridge waveguide. This can be done by dry or wet chemical etching. The narrow dimensions of a laterally single mode laser ($\sim 10\,\mu\mathrm{m}$ wide) requires extended contact pads. Figure 4.30 shows the 2D Comsol mode simulation of the ridge geometry used in this work [172]. The dry etched ridge is passivated with SiN and covered with gold for electric contacts. Alternatively, when aiming for continuous wave operation, the dry etched ridge can be laterally overgrown with InP, commonly referred to as buried-heterostructure [170]. A significant performance increase of the laser operation of QCLDs can be expected from lateral overgrowth, moving to continuous wave operation.

4.8.2 Fabry-Perót Cavity

The simplest case of a laser resonator is the Fabry-Perót cavity, which consists of two mirrors with the gain material in between. In the case of semiconductor lasers these two mirrors, commonly referred to as laser facets, can be formed by simply cleaving the laser waveguide along their crystallographic directions. Due to the high refractive index of semiconductor materials the mirror reflectivity is around 30 %. Although, this method is often used due to its simplicity, an asymmetric cavity consisting of a low and high

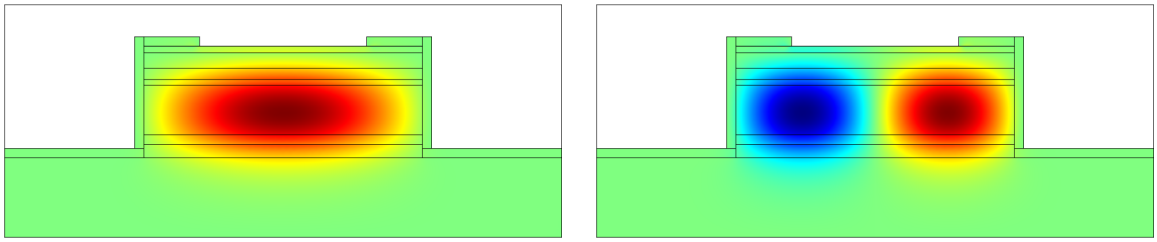

Figure 4.30: Mode simulation of a 14 µm wide ridge at $\lambda = 7\,\mu\text{m}$, showing the first (left) and secont (right) order lateral mode. The simulated effective mode indexes are $n_{\text{eff},1} = 3.22439 - j4.06177\times10{-}4$ and $n_{\text{eff},2} = 3.20114 - j3.90535\times10{-}4$, respectively

reflectivity mirror is preferred. This can be achieved by depositing one or multiple layers of low and high refractive index materials onto the facets. An alternative approach is the fabrication of tilted facets [173]. Alternatively, the mirrors can be fabricated by anisotropic etching, e.g. with the same dry etch step used to fabricate the lateral waveguide. A high reflectivity coating can then be obtained by covering the etched facet with the same insulation and gold layer as used for the electric contacts.

Typical Fabry-Perót Cavities have a length of a few millimeters in order to give a reasonable threshold current and optical output power. The allowed modes in the cavity have to fulfill the condition

$$m\lambda = 2n_{\text{eff}}L, \tag{4.56}$$

where m is the mode number, n_{eff} the effective refractive index of the waveguide and L the length of the cavity.

Considering a wavelength dependent refractive index, this leads to a spacing between adjacent Fabry-Perót modes of

$$\Delta\lambda = \frac{\lambda^2}{2n_{\text{g}}L} \tag{4.57}$$

and in terms of wavenumbers $\tilde{\nu} = 1/\lambda$

$$\Delta\tilde{\nu} = \frac{1}{2n_{\text{g}}L}, \tag{4.58}$$

with the group refractive index

$$n_{\text{g}} = n_{\text{eff}} - \lambda\frac{\partial n_{\text{eff}}}{\partial\lambda} = n_{\text{eff}} + \nu\frac{\partial n_{\text{eff}}}{\partial\nu}. \tag{4.59}$$

For a typical cavity length of $L \approx 2\,\text{mm}$ the spacing is $\Delta\nu \approx 0.8\,\text{cm}^{-1}$. Typical gain bandwidth of QCLs are around 80–120 cm^{-1} or even higher for broad-band designs.

Figure 4.31 illustrates the longitudinal modes and emission spectrum in a Fabry-Perót cavity QCL. It has to be noted, that multiple allowed cavity modes do not automatically result in multi-mode emission. The strong tendency of QCLs to form multi-mode spectra is utilized in the so called frequency combs [10]. By dispersion compensation, one can obtain

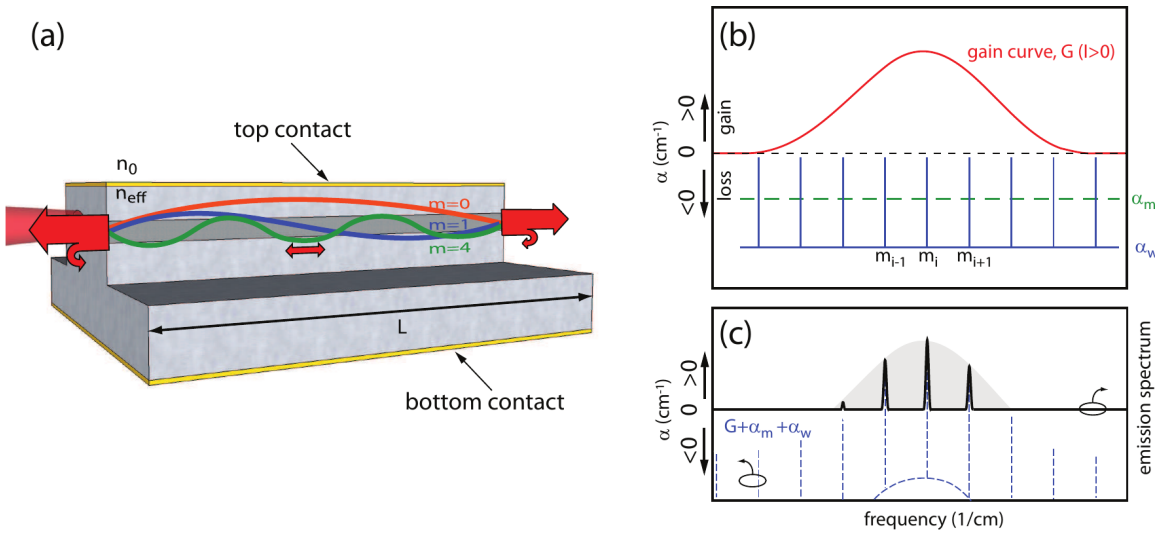

Figure 4.31: Sketch of a Fabry-Perót cavity QCL with its longitudinal modes (a) and the resulting emission spectrum (b). It has to be noted, that several additional effects are responsible for typical multi-mode emission spectra of QCL, e.g. short gain recovery time and four-wave mixing. Taken from [144].

equally spaced Fabry-Perót modes forming a comb in the frequency domain. Different to traditional frequency combs, QCL based combs do not show pulsed emission. Their very short gain recovery time preferences a fixed phase relation, which results in a frequency modulation like behavior instead of an amplitude modulation.

Model without spatial hole burning

In order to model the Fabry-Perót cavity more accurately, one has to consider a non constant gain saturation. In the following we do not consider the full coupled problem between the electronic and optical part, as can be done by Maxwell-Bloch's equations. Thereof, we cannot predict multi-mode behavior, such as mode competition and frequency mixing. The presented approach aims for cavity optimization and an accurate prediction of the output power of the laser. The transport and the cavity model can be uncoupled by parameterizing the active region with appropriate analytic expressions. These parameters can be obtained from transport simulations or alternatively from measurements.

The gain of the active region is commonly approximated by the relation

$$g(I) = \frac{g_0}{1 + I/I_{\mathrm{sat}}}, \tag{4.60}$$

where g_0 is the unsaturated gain and I_{sat} the so called saturation intensity. However, a slightly modified version adding an additional loss parameter α_{ar} gives a better correspondence to the simulation results of the the Monte-Carlo transport model

$$g(I) = \frac{g_0}{1 + I/I_{\mathrm{sat}}} - \alpha_{\mathrm{ar}}. \tag{4.61}$$

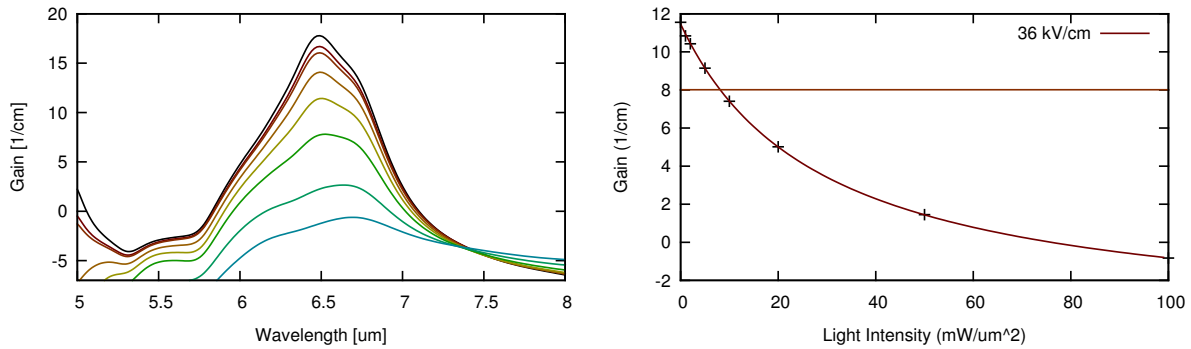

Figure 4.32: Saturation of the spectral gain with increasing intensity (left). The simulated peak gain values, obtained with the Monte-Carlo transport model (crosses), can be fitted to the analytic function. The obtained parameters are then used to solve the cavity problem independently from the electron transport.

In this case, the waveguide loss is split into $\alpha'_{\mathrm{w}} = \alpha_{\mathrm{w}} + \Gamma\alpha_{\mathrm{ar}}$. α_{w} denotes all waveguide losses despite those of the active region. This includes the free carrier losses of the cladding layers, but also loss due to roughness of the waveguide. The parameters g_0, α_{ar} and I_{sat} can be obtained via a least squares fit to the simulated gain-intensity relation, as shown in Figure 4.32.

To obtain stimulated emission from the laser resonator, the laser gain has to overcome the total loss within the cavity

$$g = \frac{1}{\Gamma}\left(\alpha_{\mathrm{w}} + \frac{1}{2L}\ln(R_1 R_2)\right), \tag{4.62}$$

as presented in section 4.1.2. The last term is commonly referred to as mirror loss α_{m}

Above threshold the cavity problem is non-linear, due to gain saturation. Neglecting the fast modulation of the light field due to interference of the right and left propagating waves as well as other longitudinal modes, we can write the cavity problem in terms of intensities following the relation

$$\frac{dI(x)}{dx} = \left(\Gamma g(I(x)) - \alpha_{\mathrm{w}}\right)\ I(x) \tag{4.63}$$

where Γ is the mode confinement factor and α_{w} the waveguide loss. This leads to the discretized equation for a slice i

$$\frac{I_i - I_{i-1}}{x_i - x_{i-1}} = \left(\Gamma g(\frac{I_i + I_{i-1}}{2}) - \alpha_{\mathrm{w}}\right)\ \frac{I_i + I_{i-1}}{2}. \tag{4.64}$$

For a fine discretization one can use the left (or right) sided discretization assuming $I_i - I_{i-1} \ll I_{i-1}$, resulting in the explicit form

$$\frac{I_i - I_{i-1}}{x_i - x_{i-1}} = \left(\Gamma g(I_{i-1}) - \alpha_{\mathrm{w}}\right)\ I_{i-1}. \tag{4.65}$$

For the right and left propagating waves, I_i^{R} and I_i^{L}, this results in

$$I_i^{\mathrm{R}} = \left[1 + \left(\Gamma g(I_{i-1}^{\mathrm{R}} + I_{i-1}^{\mathrm{L}}) - \alpha_{\mathrm{w}}\right)\ (x_i - x_{i-1})\right] I_{i-1}^{\mathrm{R}}, \tag{4.66}$$

$$I_i^{\mathrm{L}} = \left[1 + \left(\Gamma g(I_{i+1}^{\mathrm{R}} + I_{i+1}^{\mathrm{L}}) - \alpha_{\mathrm{w}}\right)\ (x_i - x_{i+1})\right] I_{i+1}^{\mathrm{L}}, \tag{4.67}$$

The advantage of this representation is that it does not require to spatially resolve the fast modulation of the light field. Thus the grid can be much coarser and the knowledge of the phases of the different modes is not required. Obviously, spatial hole burning, mode competition, etc. is not described at all.

The intensities I^{R} and I^{L} are connected at the facets via the relations

$$I_0^{\mathrm{R}} = R_1 I_0^{\mathrm{L}}, \tag{4.68}$$

$$I_M^{\mathrm{L}} = R_2 I_M^{\mathrm{R}}, \tag{4.69}$$

where R_1 and R_2 are the reflectivities of the front and back facets and M the index of the last slide.

Figure 4.33 shows the intensity envelope in terms of optical power and the saturated net gain in an asymmetric FP cavity.

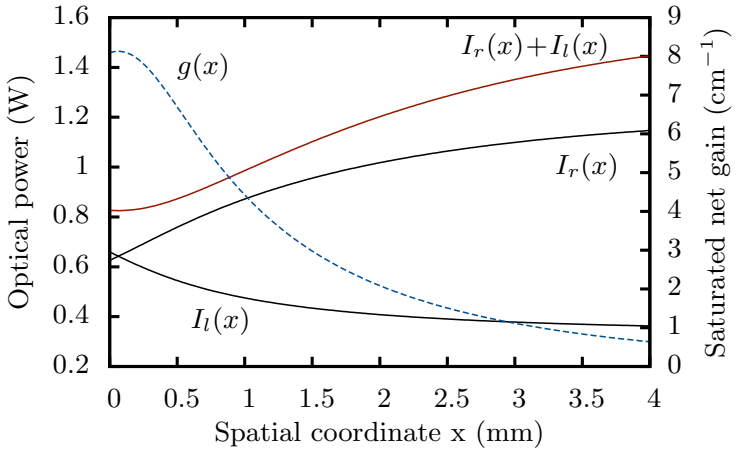

Figure 4.33: Optical power and saturated net gain in an asymmetric FP cavity.

The output power P_1 and P_2 at the facets 1 and 2 can then be expressed by

$$P_1 = (1 - R_1) I_0^{\mathrm{L}} A_{\mathrm{mode}}, \tag{4.70}$$

$$P_2 = (1 - R_2) I_M^{\mathrm{R}} A_{\mathrm{mode}}, \tag{4.71}$$

where A_{mode} is the mode area.

Constant intensity approximation

In order to give a simplified model, as also used in section 4.1.2 to sketch the relevant mechanisms, it is convenient to assume the total intensity $I(x)$ to be constant over x.

In this case the intensities of the right and left propagating waves follow exactly an exponential behavior and the equation system can be solved analytically.

The output power can then be expressed as

$$P_1 = \frac{1-R_1}{1+R_1} I_{\text{sat}} A_{\text{mode}} \left(\frac{\Gamma g_0}{\alpha} - 1 \right), \tag{4.72}$$

$$P_2 = \frac{1-R_2}{1+R_2} I_{\text{sat}} A_{\text{mode}} \left(\frac{\Gamma g_0}{\alpha} - 1 \right) \tag{4.73}$$

with

$$\alpha = \left(\alpha_{\text{w}} + \frac{1}{2L} \ln(R_1 R_2) \right). \tag{4.74}$$

4.9 Laser and detector on a chip

This section is based on the publication "Monolithically Integrated Mid-Infrared Quantum Cascade Laser and Detector", Sensors 13, 2196 (2013) [135].

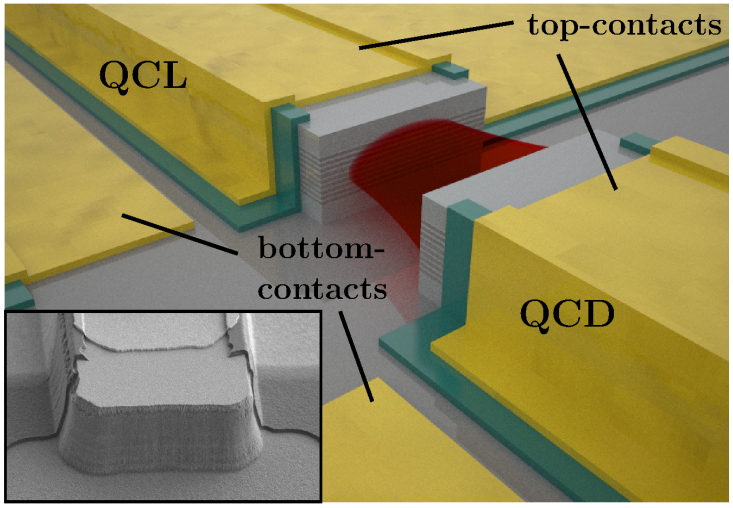

Figure 4.34: Sketch of the monolithic integrated QCL and QCD. The inset shows a SEM image of the etched laser facet of the 15 µm wide ridge. The gap between the laser and the detector is 10 µm. Published in [135].

Bi-functional quantum cascade laser and detector active regions allow a straightforward integration of lasers and detectors on the same chip. Once the layer structure is grown on top of the substrate, parts of the chip can be patterned with standard semiconductor fabrication techniques (optical lithography, etching, metal and dielectric layer deposition) to form lasers and others to form detectors. Our prototype device was build similar to a standard FP ridge laser, but with two sections separated by a small air gap. A 2 mm long section is used as FP QCL and a 0.5 mm long section as a detector. Figure 4.34

shows a sketch of the prototype device and an SEM image of the etched laser facet. The 15 µm wide ridges as well as the 10 µm gap between the laser and the detector were etched via reactive ion etching with $SiCl_4$/Ar using a SiN hardmask. In order to prevent electric crosstalk the device has been fabricated with separated bottom contacts.

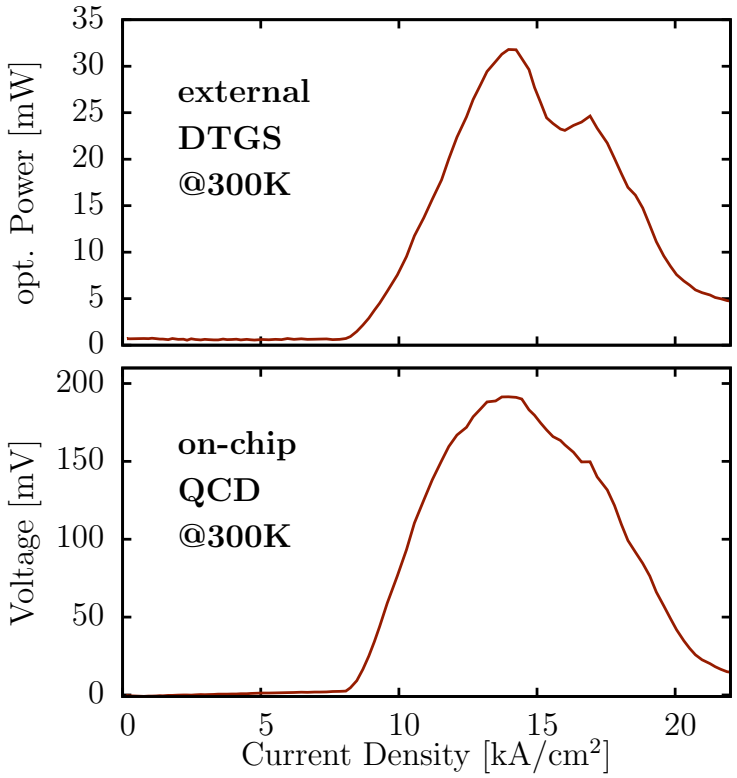

Figure 4.35: Optical power versus current density of the laser measured with a calibrated external triglycine sulfate pyroelectric detector (DTGS) at the front-facet and the on-chip QCD at the back-facet. All components were operating at room temperature in atmosphere. The laser was operated in pulsed mode with 40 ns pulses at 5 kHz. Published in [135].

Figure 4.35 shows the light power versus current density plot of the laser, comparing an external deuterated triglycine sulfate pyroelectric detector (DTGS) and the on-chip detector. We have observed a detector signal of 191.5 mV at a pulsed peak power of around 30 mW for the on-chip QCD located at the other facet of the laser ridge. The signal was measured with a standard digital oscilloscope without any additional amplifiers. This reduces the need of complex measurement circuits, which allows to reduce the size and costs. Due to the fast response of the QCD the laser pulse duration can be reduced to 40 ns without decreasing the peak detector signal. At a laser bias of around 10 V our device consumes an average power of around 4 mW, which is ideal for portable sensors. This results were obtained with the first generation of QCLDs. The second generation with the horizontal-vertical extraction scheme have a significant higher optical output power and wall-plug efficiency. Photocurrents as high as 9mA have been measured with the new generation.

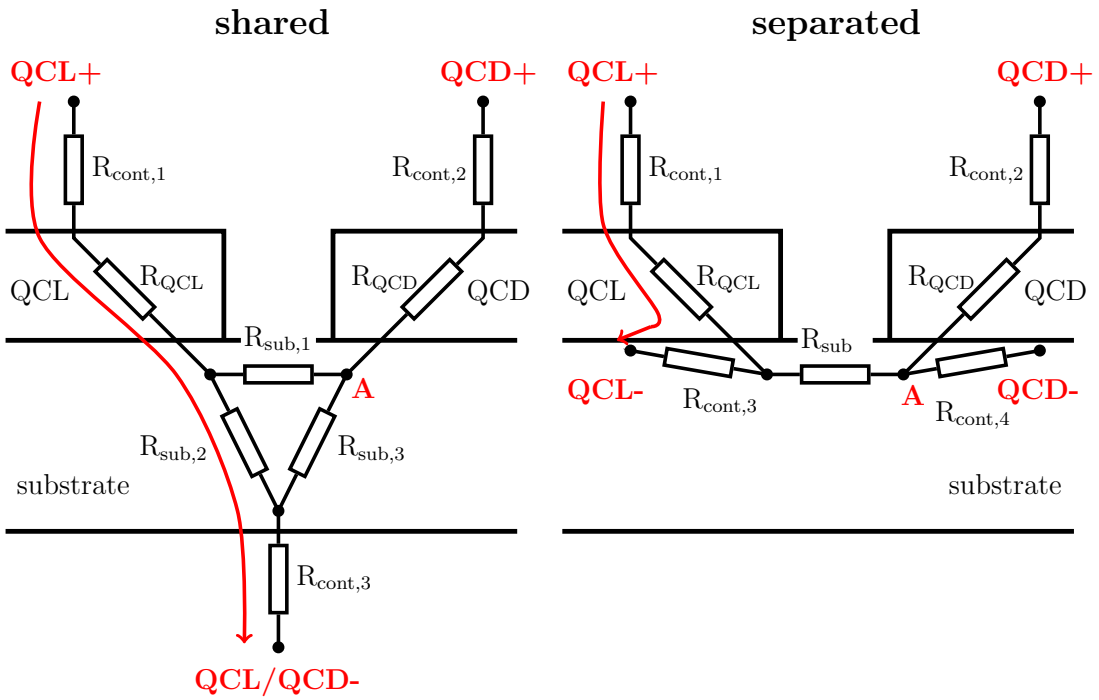

Figure 4.36: Schematic DC circuit diagram of the device with a shared bottom-side contact (left) and separated bottom contacts (right). The laser bias voltage is indicated by a red arrow. Separated bottom contacts allow to minimize electrical crosstalk to the detector, as both detector contacts are affected in the same manner. Thus a potential fluctuation at node "A" cancel out. Published in [135].

4.9.1 Separated bottom contacts

When using a large area contact on the bottom-side of the substrate, both the laser and the detector would be connected via this contact, leading to electrical crosstalk. As depicted in Fig. 4.36 (left), an applied voltage between the laser top contact and the shared bottom-side contact, would result in a change of the electric potential at node "A" and thus of the potential at the detectors top contact. Even a small voltage drop at the substrate and the shared bottom-contact would have a significant impact as the detector signal is a factor of hundred smaller than the laser bias. To minimize this effect, we have reduced the shared series resistance by separating the bottom-contact of the laser and the detector. As illustrated in Fig. 4.36 (right) an applied voltage again affects the potential at node "A". Different to before, a potential fluctuation at node "A" changes the potential of both QCD contacts in the same way and thus cancel out.

With the separation of the bottom contacts we were able to reduce the electric cross-talk from the laser to the detector below 2 mV at laser threshold. The remaining cross-talk is mainly due to the external measurement setup and can be eliminated by using a differential measurement approach or by signal post processing, as the crosstalk does not change from pulse to pulse. The DTGS signal was measured with lock-in technique collecting

the light of the front-facet of the same laser ridge. In contrast to the lock-in technique and the slow response of the DTGS, where the average pulse power is observed, the pulse peak power was measured with the fast QCD. This and the different reflectivity of the two laser facets results in different shapes for both curves depicted in Figure 4.35. The drop between 14 to 17 $\mathrm{kA/cm^2}$ is mainly due to atmospheric absorption within the optical path between the laser, the lenses and the DTGS detector. The emission wavelength shifts to longer wavelengths with increasing bias and passes several atmospheric absorption lines.

Chapter 5

Surface plasmon polaritons

This chapter is based on the publication "Monolithically integrated mid-infrared lab-on-a-chip using plasmonics and quantum cascade structures", Nature Communications 5, 4085 (2014) [25].

Plasmon polaritons are resonant interactions between a light field and quantized collective oscillations of the charge density, e.g. in metals or highly doped semiconductors. They play an important role in confinement, guiding and strong local enhancement of electromagnetic waves, which may be difficult or impossible using other technologies [174]. This is an enormous benefit for many applications and has already solved many fundamental problems in sensing [175, 176], imaging [177] and on-chip communication [178]. The field of plasmonics was first studied in the visible and near-infrared, with increasing interest in the mid-infrared spectral region [179, 180].

Surface plasmons are hybrid modes of electromagnetic waves and collective electron oscillations at the interface between a metal and a dielectric [181]. They are usually split into two schemes: those which propagate along a planar interface, commonly referred to as surface plasmon polaritons (SPPs) and those localized at metallic nanoparticles, referred to as localized surface plasmons (LSPs). SPPs are transverse magnetic (TM) polarized electromagnetic waves, with an evanescent decay in both neighboring media (see Figure 5.1). With this exponential decay, SPPs enable deep sub-wavelength confinement.

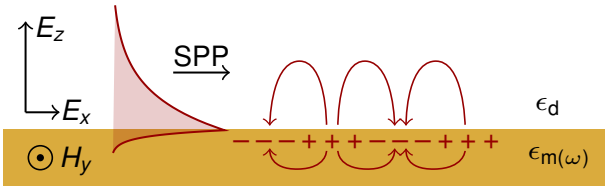

Figure 5.1: Schematic of a surface plasmon polariton propagating on a planar metal/dielectric interface.

5.1 Localized surface plasmons

In 1904, Maxwell-Garnett [182] developed a theory of effective dielectric media to describe the color of glasses that contain metallic particles. Later in 1908, Mie [183] described the absorption of light by spherical particles of arbitrary size and thereby explained the color of metallic particles [184]. One century later, localized surface plasmons on metallic nanoparticles emerged as an interesting research field showing many interesting phenomena [185]. The confined charge density oscillations give rise to highly enhanced electric fields at the particle surface. The particles optical extinction has a maximum at the plasmon resonant frequency, which occurs at visible wavelengths for noble metal nanoparticles. Incident light near the resonance frequency is strongly scattered or absorbed. As an example, this effect is particularly useful to enhance the absorption of solar cells [186]. The extinction peak depends on the refractive index of the surrounding medium, which is the basis for sensing applications [187].

5.2 From perfect metals to plasmonics

The propagation of optical waves in dielectrics and metals can be described with the classical framework given by Maxwell's equations, following [181]. The classical treatment is justified, as the high free carrier density leads to a small energy spacing between the electronic states in the system, which are much smaller compared to $\mathrm{k_B}\,T$. The strong frequency dependence of the optical properties of metals makes plasmonics a very interesting and diverse field with many different aspects and sometimes unexpected phenomena, e.g. extraordinary transmission through a sub-wavelength aperture [188].

In classical electromagnetics at microwave or THz frequencies, metals are often treated as perfect conductors that do not allow the propagation of electromagnetic waves within the media. At these frequencies metals are widely used as cladding material for waveguides and resonators. The assumption of a infinite or very high conductivity remains valid even in the near-infrared and visible part of the spectra. Going further in frequency to the ultraviolet regime, metals can appear transparent like dielectrics, depending on their particular electronic bandstructure. Alkali metals are almost transparent, where gold or silver show a strong attenuation. The frequency dependent properties of metals (as well as dielectrics) can be described with the complex dielectric function $\varepsilon(\omega)$, the macroscopic average of the material response in amplitude and phase. It is the change of the phase, which leads to the significant change of the material properties at optical frequencies.

Optical propagation in metals and dielectrics is governed by Maxwell's equations for

matter or sometimes called macroscopic Maxwell's equations [189]

$$\vec{\nabla} \cdot \vec{D} = \varrho_{\mathrm{f}} \tag{5.1}$$
$$\vec{\nabla} \cdot \vec{B} = 0 \tag{5.2}$$
$$\vec{\nabla} \times \vec{E} = -\partial_t \vec{B} \tag{5.3}$$
$$\vec{\nabla} \times \vec{H} = \vec{J}_{\mathrm{f}} + \partial_t \vec{D}. \tag{5.4}$$

The macroscopic Maxwell's equations ignore the microscopic details and uses averaged fields. Compared to the general Maxwell's equations, it separates free and bound charges and currents, where the total charge and current density is

$$\varrho = \varrho_{\mathrm{f}} + \varrho_{\mathrm{b}} \tag{5.5}$$
$$J = J_{\mathrm{f}} + J_{\mathrm{b}} \tag{5.6}$$

The four macroscopic fields are linked via the density of free charges ϱ_{f}, which describes a macroscopic charge imbalance due to free charged carriers and the current density $\vec{J}_{\mathrm{f}}$ due to free charged carriers. The flux densities $\vec{D}$ and $\vec{B}$ are linked to the field amplitudes $\vec{E}$ and $\vec{H}$ via the polarization $\vec{P}$ and the magnetization $\vec{M}$ by

$$\vec{D} = \varepsilon_0 \vec{E} + \vec{P} \tag{5.7}$$
$$\vec{B} = \mu_0 \vec{H} - \vec{M}, \tag{5.8}$$

where ε_0 is the dielectric permittivity and μ_0 the magnetic permeability of vacuum. The polarization $\vec{P}$ describes the macroscopic average of the microscopic dipole moments formed due to the external electric field $\vec{E}$. In a linear, isotropic and nonmagnetic media, the relation can be described via

$$\vec{D} = \varepsilon \vec{E} \tag{5.9}$$
$$\vec{B} = \mu_0 \vec{H} \tag{5.10}$$

Finally, the current density is related to the electric field via the conductivity σ

$$\vec{J} = \sigma \vec{E}. \tag{5.11}$$

Historically, the conductivity has been used to describe metals at low frequencies and the dielectric permittivity has been used to describe their optical response. However, electromagnetic phenomena with metals can be described with either of these quantities. Furthermore, the relations 5.10 and 5.11 are only correct for linear isotropic media without temporal or spatial dispersion. At optical frequencies also the phase of the response has to be considered, leading to the generalized relations that describe the impulse response of the linear relations decomposed into plane-wave components of wavevector $\vec{k}$

$$\vec{D}(\vec{k}, \omega) = \varepsilon_0 \varepsilon(\vec{k}, \omega) \vec{E}(\vec{k}, \omega) \tag{5.12}$$
$$\vec{J}(\vec{k}, \omega) = \sigma(\vec{k}, \omega) \vec{E}(\vec{k}, \omega). \tag{5.13}$$

In complex notation $\partial_t = -j\omega$ and the charge conservation for bound charges

$$\vec{\nabla} \cdot \vec{J}_\mathrm{b} = -\partial_t \varrho_\mathrm{b}, \tag{5.14}$$

as well as the relation between the charge density of bound charges and the polarization

$$\vec{\nabla} \cdot \vec{P} = -\varrho_\mathrm{b}, \tag{5.15}$$

one can obtain the relation between the relative electric permittivity and the conductivity

$$\varepsilon(\vec{k}, \omega) = 1 + \frac{j\sigma(\vec{k}, \omega)}{\varepsilon_0 \omega}. \tag{5.16}$$

The general form of the relative dielectric permittivity can be further simplified to a spatially local response with $\varepsilon(\vec{k} = \vec{0}, \omega) = \varepsilon(\omega)$, when restricting to characteristic dimensions (unit cell or mean free path or electrons) significantly smaller than the wavelength in the material. This is usually the case even at ultraviolet frequencies, but can lead to small errors at very small nanostructures such as sharp tips [181].

At optical frequencies the dielectric permittivity ε is commonly expressed using the complex refractive index $\tilde{n}(\omega) = n(\omega) + jk(\omega)$, defined as

$$n = \sqrt{\varepsilon} \tag{5.17}$$

or

$$\varepsilon_1 = n^2 - k^2 \tag{5.18}$$

$$\varepsilon_2 = 2nk \tag{5.19}$$

$$n = \sqrt{\frac{\varepsilon_1}{2} + \frac{1}{2}\sqrt{\varepsilon_1^2 + \varepsilon_2^2}} \tag{5.20}$$

$$k = \frac{\varepsilon_2}{2n}. \tag{5.21}$$

The exponential attenuation of an optical wave is related to the extinction coefficient k via Beer's law

$$\alpha(\omega) = \frac{2k(\omega)\omega}{c} = \frac{4\pi k(\omega)}{\lambda}. \tag{5.22}$$

The real part of the conductivity is thus related to optical absorption and the imaginary part to the amount of polarization.

5.2.1 Optical properties of a free electron gas

Electromagnetic properties of metals and highly doped semiconductors can be described over a wide frequency range using the Drude-Lorentz model. The Drude model is often

referred to as plasma model. It describes the collective movement of free electrons, referred to as free electron gas, against the fixed positive ion cores. Extended to multiple resonances (the Drude-Lorentz model) it can describe the dielectric constants over a wide frequency range. In the plasma model, the microscopic details, e.g. lattice potential or electron-electron interaction are not considered. Similar to the treatment of semiconductors, theses details are included via an effective electron mass and their oscillation is damped through collisions occurring at characteristic time scales described by the so called relaxation time τ (typically $\tau \approx 10\,\mathrm{fs}$). The equation of motion for an electron in the plasma is

$$m_\mathrm{e}^* \partial_t^2 \vec{x} + m_\mathrm{e}^* \gamma \partial_t \vec{x} = -e\vec{E} \tag{5.23}$$

In a harmonic field $\vec{E}(t) = \vec{E}_0 \exp(-j\omega t)$ the electrons oscillate with

$$\vec{x}(t) = \frac{e}{m_\mathrm{e}^*(\omega^2 + j\gamma\omega)} \vec{E}(t). \tag{5.24}$$

The macroscopic polarization induced by the electric dipole of the displaced electrons is

$$\vec{P} = -_\mathrm{e} e\vec{x} = -\frac{ne}{m_\mathrm{e}^*(\omega^2 + j\gamma\omega)} \vec{E} \tag{5.25}$$

where n_e is the electron density. Equally in terms of electric permittivity this reads

$$\varepsilon = \varepsilon_0 \left(1 - \frac{\omega_\mathrm{p}^2}{\omega^2 + j\gamma\omega}\right), \tag{5.26}$$

using the so called plasma frequency

$$\omega_\mathrm{p}^2 = \frac{n_\mathrm{e} e^2}{\varepsilon_0 m_\mathrm{e}^*}. \tag{5.27}$$

The damping γ is connected to the relaxation time via $\gamma = 1/\tau$. The complex dielectric can be split into their real and imaginary part

$$\varepsilon_1 = \varepsilon_0 \left(1 - \frac{\omega_\mathrm{p}^2 \tau^2}{1 + \omega^2\tau^2}\right) \tag{5.28}$$

$$\varepsilon_2 = \varepsilon_0 \left(\frac{\omega_\mathrm{p}^2 \tau}{\omega(1 + \omega^2\tau^2)}\right) \tag{5.29}$$

At very low frequencies, $\omega\tau \ll 1$, the imaginary dominates the permittivity $\varepsilon_2 \gg \varepsilon_1$. There, metals are mainly absorbing and the electric field inside the metal is strongly damped following $\exp(-z/\delta)$, where $\delta = \sqrt{\frac{2}{\sigma_0 \omega \mu_0}}$ is the so called skin depth. The mainly imaginary permittivity is connected to a predominantly real conductivity σ, meaning that the charges respond in phase with an external field.

At higher frequencies (optical frequencies), where $1 < \omega\tau < \omega_\mathrm{p}\tau$, σ approaches more and more complex character and the refractive index is predominantly imaginary. There, metals are mainly reflective.

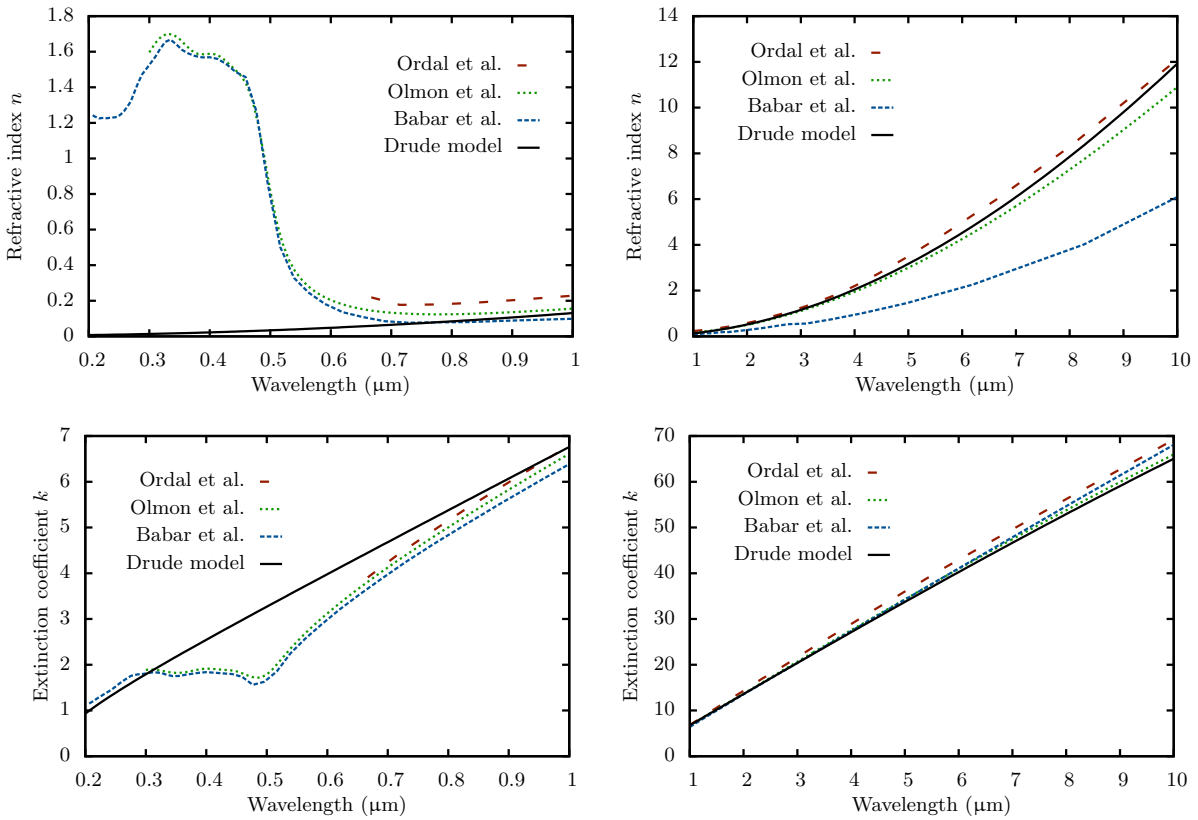

Figure 5.2: Refractive index and extinction coefficient of gold from different sources [190–192]. At near- and mid-infrared frequencies it is well described using the Drude model.

For $\omega \gg \omega_\mathrm{p}$, the free-electron model leads to $\varepsilon \to 1$. However, in noble metals, the optical fields induce interband transitions. Real metals are often described by introducing a remaining high frequency permittivity, resulting in a slight modification of equation 5.26

$$\varepsilon = \varepsilon_0 \left(\varepsilon_{r,\infty} - \frac{\omega_\mathrm{p}^2}{\omega^2 + j\gamma\omega} \right) \tag{5.30}$$

Figure 5.2 shows the real and imaginary part of the refractive index of gold from multiple literature sources and the fitted Drude model. The model accurately describes the refractive index in the mid- and near-infrared, but is not applicable at visible wavelength or beyond, due to interband transitions. The parameters from different sources deviate.

5.2.2 Surface plasmon polaritons on metal/dielectric interfaces

Starting from Maxwell's equations 5.4, one can obtain the wave equation using a harmonic time dependence $\delta_t = -j\omega$ for transversal magnetic (TM) and transversal electric (TE) modes. A more detailed description can be found in various text books, e.g. [181, 193].

TM polarized guided modes can be described by the following set of equations

$$E_x = -j\frac{1}{\omega\varepsilon}\partial_z H_y \tag{5.31}$$

$$E_z = -\frac{\beta}{\omega\varepsilon}H_y \tag{5.32}$$

$$\partial_z^2 H_y + (k_0^2\varepsilon_r - \beta)H_y = 0, \tag{5.33}$$

and analogously for TE modes

$$H_x = j\frac{1}{\omega\mu_0}\partial_z E_y \tag{5.34}$$

$$H_z = \frac{\beta}{\omega\mu_0}E_y \tag{5.35}$$

$$\partial_y^2 E_y + (k_0^2\varepsilon_r - \beta)E_y = 0, \tag{5.36}$$

where β is the complex propagation constant in propagation direction. Surface plasmon polaritons are TM modes, that propagate along a metal/dielectric interface. As required due to normalization, the fields decay exponentially on both sides. Using the set of equations describing TM modes one can specify the problem using the ansatz

$$H_y(z) = B_2 \mathrm{e}^{-k_2 z}\mathrm{e}^{j\beta z} \tag{5.37}$$

$$E_x(z) = jB_2\frac{1}{\omega\varepsilon_2}k_2\mathrm{e}^{-k_2 z}\mathrm{e}^{j\beta z} \tag{5.38}$$

$$E_z(z) = -B_2\frac{\beta}{\omega\varepsilon_2}\mathrm{e}^{-k_2 z}\mathrm{e}^{j\beta z} \tag{5.39}$$

for the dielectric ($z > 0$) and

$$H_y(z) = A_1 \mathrm{e}^{k_1 z}\mathrm{e}^{j\beta z} \tag{5.40}$$

$$E_x(z) = -jA_1\frac{1}{\omega\varepsilon_1}k_1\mathrm{e}^{k_1 z}\mathrm{e}^{j\beta z} \tag{5.41}$$

$$E_z(z) = A_1\frac{\beta}{\omega\varepsilon_1}\mathrm{e}^{k_1 z}\mathrm{e}^{j\beta z} \tag{5.42}$$

for the metal ($z < 0$). Continuity of H_y and E_x and the wave equation require

$$A_1 = B_2 \tag{5.43}$$

$$\frac{k_2}{k1} = -\frac{\varepsilon_2}{\varepsilon_1} \tag{5.44}$$

and the wave equation (5.33)

$$k_1^2 = \beta - k_0^2\varepsilon_{r,1} \tag{5.45}$$

$$k_2^2 = \beta - k_0^2\varepsilon_{r,2}. \tag{5.46}$$

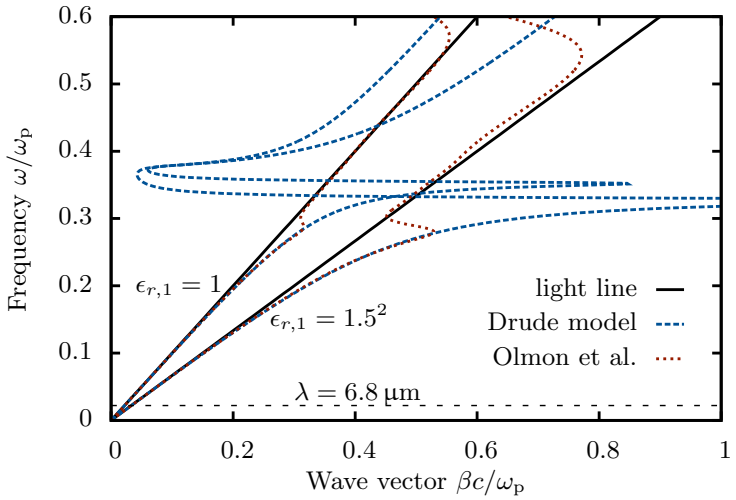

Figure 5.3: Dispersion relation of a SPP on a gold/dielectric surface. The dispersion relation is calculated using the Drude model with the high frequency permittivity $\varepsilon_\infty = 7$ and data from Olmon et al. [191]. The wavelength of interest ($\lambda = 6.8\,\mu m$) is highlighted with the black dashed line.

Solving this equation system leads to the dispersion relation for SPPs on a metal/dielectric interface

$$\beta = k_0 \sqrt{\frac{\varepsilon_{r,1}\varepsilon_{r,2}}{\varepsilon_{r,1} + \varepsilon_{r,2}}}. \tag{5.47}$$

The same approach can be followed for TE modes, with the result, that propagating TE modes are not allowed on a metal/dielectric interface.

Figure 5.3 shows the calculated dispersion relation for an SPP on a gold/air, as well as a gold/dielectric interface. For ideal conductors, where $\mathrm{Im}(\varepsilon_1) = 0$, the SPP dispersion approaches an asymptotic limit at higher frequencies. At the so called surface plasmon frequency

$$\omega_{sp} = \frac{\omega_p}{\sqrt{1 + \varepsilon_{r,2}}}, \tag{5.48}$$

the wave vector approaches infinity. At this frequency, the mode has electrostatic character and is referred to as surface plasmon. The damping in real metals leads to a complex ε_1 and thus also for the propagation constant β. The resulting attenuation of SPP is described via the propagation length

$$L_{SPP} = \frac{1}{2\mathrm{Im}(\beta)}. \tag{5.49}$$

Below this surface plasmon frequency, the dispersion of SPP lies on the right side of the light line and thus leads to bound modes, that can propagate along the metal/dielectric interface. However, at low frequencies, the SPP approaches the character of Sommerfeld-Zenneck waves [181]. There, the propagation constant β is very close to the light line,

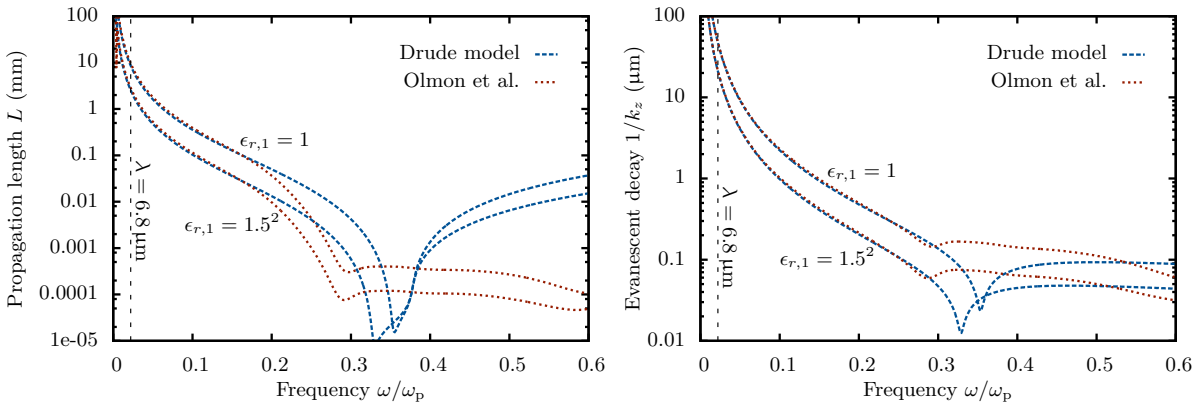

Figure 5.4: Propagation length and evanescent decay into the dielectric media versus frequency of SPPs propagating on a gold/air interface.

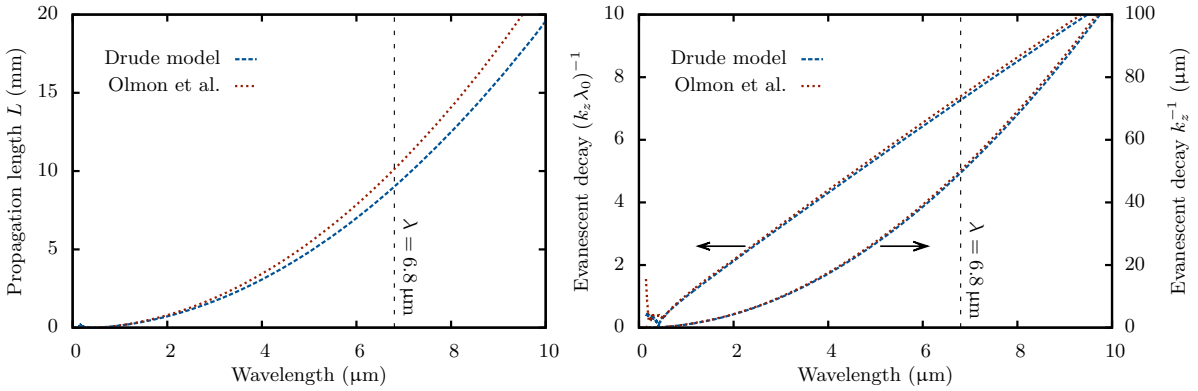

Figure 5.5: Propagation length and evanescent decay into the dielectric media of SPPs propagating on a gold/air interface in the mid-infrared. SPPs in the mid-infrared show relatively long propagation length but are weakly bound and extend widely into the dielectric media. At the target wavelength, the SPP is weakly confined and extends over 50 µm into air.

k_0 and the SPP mode extends over a large distance into the dielectric media, following $e^{-k_z z}$ with $k_z = \sqrt{\beta^2 - \varepsilon_{r,2} k_0}$, leading to weakly bound modes. This work is focused on the mid-infrared properties of surface plasmon polaritons, which is exactly in this regime. The target wavelength of $\lambda \approx 6.8\,\mu m$ used in this work is highlighted in the figures as a dashed line. Figure 5.4 shows the calculated propagation length and evanescent decay length corresponding to the dispersion relation shown in figure 5.3. Both the propagation length, as well as the evanescent decay is very large in the mid-infrared and decrease rapidly with increasing frequency, approaching very small values at the surface plasmon frequency.

5.3 Plasmonics in the mid-infrared

Often overlooked, plasmonics are gaining interest in the mid-infrared spectral region. Due to the strong frequency dependent material response of metals, the knowledge about visible and near-infrared plasmonics cannot be directly transferred to the mid-infrared [179, 194]. As shown in the previous section, in the visible and near-infrared, noble metals have a relatively small negative permittivity, comparable to the permittivity of dielectrics, enabling deep subwavelength confinement. In contrast, the negative permittivity in the mid-infrared is much larger, leading to the fact that surface waves are weakly bound to the metal-dielectric interface with an evanescent decay penetrating deep into the dielectric medium. Figure 5.5 shows the propagation length and the evanescent decay into the dielectric for infrared SPPs on a gold/air interface. The weak confinement and the lack of efficient sources and detectors are the main issues, as to why mid-infrared plasmonics have not been as broadly adopted. Despite these challenges, mid-infrared plasmonics have been demonstrated for some very promising applications during the last years, such as beam-shaping [195], detectivity enhancement [169, 196] and sensing [197].

Due to the higher conductivity at longer wavelength, the field inside metallic nanoparticles becomes vanishingly small [194]. This prevents subwavelength metallic particles from supporting localized surface plasmons in the mid-infrared. However, localized modes can be achieved either with highly doped semiconductors or with antenna-like metallic nanostructures. Compared to LSPs, these structures scale linearly with its dimensions. Schnell *et al.* have demonstrated mid-infrared subwavelength nanofocusing to $\lambda/150$ by propagating a mid-infrared surface wave along a tapered two-wire transmission line [198]. An SPP is excited on the transmission line with an optical antenna. The mode of this asymmetric SPP on the transmission line is then converted to a nanofocused mode inside the narrow gap between the two metal strips, showing extremely high intensities.

5.3.1 Spoof plasmon polaritons

In the mid-infrared, SPPs propagating on a metal-air interface are weakly confined and penetrate deeply into the dielectric material. Pendry *et al.* [199] proposed patterning the metal surface with resonant grooves to modify the propagation properties in such a way that electromagnetic waves are strongly bound to the interface. These so called spoof or designer SPPs are collective excitations of optical modes in the grooves with subwavelength periodicity resulting in an effective media with a plasma-like response. Considering the finite conductivity of noble metals, the effective medium theory results in propagation losses, similar to visible frequencies [194, 200, 201].

5.3.2 New materials for mid-infrared plasmonics

In order to transfer the advantages of plasmonics to longer wavelength, new approaches or materials have to be developed. The negative permittivity of plasmonic materials results from the collective oscillation of free carriers. Alternatively, lattice vibrations in polar dielectrics can also lead to a negative permittivity. So called surface phonon polaritons have been demonstrated in SiC around 11 µm. They have the advantage of strong confinement and low damping [202, 203], but are limited to a narrow spectral range.

Since their first experimental demonstration, graphene and 2D-materials have become a major research field during the last years [204]. While most work is focused on the electronic and mechanical properties, the interest on its unique optical properties is growing. For mid-infrared plasmonics, graphene has been studied as an alternative material serving strong confinement and electrostatic tunability of the plasma-frequency through the carrier concentration [205–207].

An alternative material class for mid-infrared plasmonics are highly doped semiconductors, often referred to as designer metals due to their Drude like behavior [208, 209]. Highly doped semiconductors allow a wide control of plasma frequency via the carrier density. High doping and low effective carrier masses can lead to plasma frequencies in the mid-infrared, which makes especially the III/V semiconductors particularly interesting [210, 211].

5.4 Dielectric-loaded surface plasmon polaritons

Dielectric-loading is an interesting and straightforward alternative to increase the confinement of mid-infrared plasmons. By applying a thin dielectric strip on top of an unpatterned metal surface, propagation properties similar to spoof plasmons can be achieved without the need for sub-wavelength patterning. The dielectric layer produces an increase of the effective modal index, enabling the support of well confined mid-infrared plasmon waves on noble metals.

To calculate the propagation properties of such dielectric loaded SPPs, we consider three layers. The cross section in z direction is as follows: Layer I ($z < 0$) is a metal with $\varepsilon_{r,1} < 0$, layer II ($0 < z < D$) is a dielectric with $\varepsilon_{r,2}$ and layer III ($z > D$) is a dielectric with $\varepsilon_{r,3} > \varepsilon_{r,3} > 1$. Layer I and III extend infinitely in the other directions and because of normalization requires that the mode approaches zero. For layer I and III one can use the same ansatz as for SPPs on a metal/air interface, equations 5.38–5.39 and 5.41–5.42, respectively. For layer II, the additional dielectric, we have to consider the general version

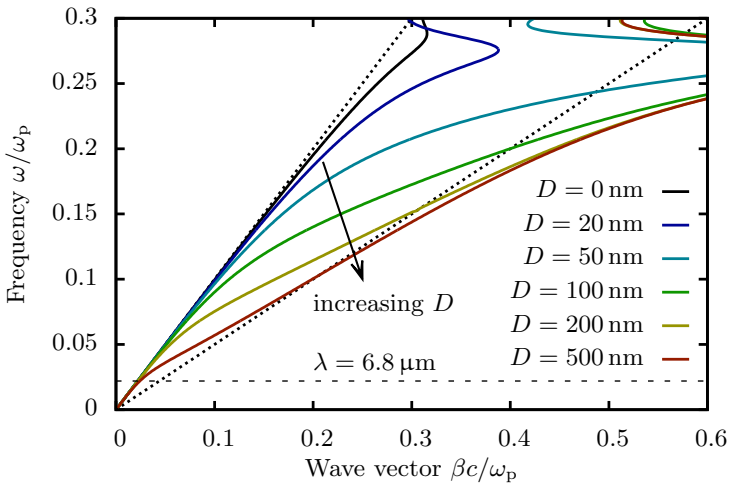

Figure 5.6: Dispersion relation of dielectric loaded SPPs for various layer thicknesses. The straight dotted lines indicate the light lines of air and the dielectric material with $\varepsilon_{r,2} = 4$.

for TM modes

$$H_y^{\mathrm{II}}(z) = (A_2 \mathrm{e}^{k_2 z} + B_2 \mathrm{e}^{-k_2 z}) \mathrm{e}^{j\beta z} \tag{5.50}$$

$$E_x^{\mathrm{II}}(z) = -j\frac{1}{\omega\varepsilon_1} k_1 (A_2 \mathrm{e}^{k_2 z} - B_2 \mathrm{e}^{-k_2 z}) \mathrm{e}^{j\beta z} \tag{5.51}$$

$$E_z^{\mathrm{II}}(z) = \frac{\beta}{\omega\varepsilon_1} (A_2 \mathrm{e}^{k_2 z} + B_2 \mathrm{e}^{-k_2 z}) \mathrm{e}^{j\beta z}. \tag{5.52}$$

The continuity at the interfaces at $z = 0$ and $z = D$ leads to an equation system for A_1,A_2,B_2 and A_3. A distinct solution requires that the determinant of the equation system equals zero, leading to the condition

$$\frac{\left(\frac{k_2}{\varepsilon_2} + \frac{k_3}{\varepsilon_3}\right)\left(\frac{k_2}{\varepsilon_2} + \frac{k_1}{\varepsilon_1}\right)}{\left(\frac{k_2}{\varepsilon_2} - \frac{k_3}{\varepsilon_3}\right)\left(\frac{k_2}{\varepsilon_2} - \frac{k_1}{\varepsilon_1}\right)} = \mathrm{e}^{-2k_2 D}, \tag{5.53}$$

with $k_i = \sqrt{\beta^2 - k_0^2 \varepsilon_{r,i}}$. Different to the much simpler case of SPP on a single metal/dielectric interface, equation 5.53 cannot be solved analytically.

Figure 5.6 shows the numerically calculated dispersion relation of a DL-SPP on an metal/dielectric/air structure, for different thickness of the dielectric layer. At very low frequencies the SPP mode extends widely into air. There, the thin dielectric layer barely influences the dispersion relation. Going to slightly higher frequencies the part of the mode inside the dielectric layer becomes more and more relevant and the DL-SPP dispersion approaches the dispersion of an SPP on a metal/dielectric with ε_2.

The higher propagation constant of DL-SPPs is connected to an increased confinement, which is particularly useful at longer wavelength. Figure 5.7 shows evanescent decay of

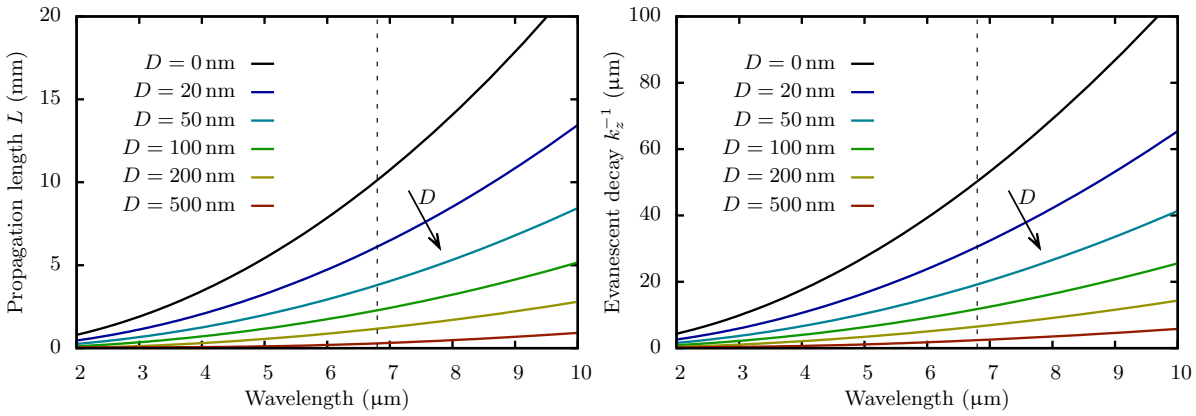

Figure 5.7: Propagation length and evanescent decay of DL-SPPs with different layer thickness. A thicker dielectric layer leads to an increased mode confinement, but a higher attenuation due to ohmic losses in the metal.

DL-SPPs compared to SPPs in the infrared. Even at very long wavelength, where the difference in the dispersion relation can be barely seen, a very thin dielectric layer has a huge impact on the confinement. As an example, an SPP at $\lambda = 6.8\,\mu\text{m}$ extents approximately 50 µm into air. By putting just a 50 nm thin dielectric layer with small $\varepsilon_2 = 4$, the evanescent decay is reduced by 50%. A higher confinement is always connected with stronger attenuation due to ohmic losses in the metal. However, the propagation length is still in the millimeter range, which is sufficient for many on-chip applications. The adjustment of the propagation properties with the layer thickness gives a very flexible tool to optimize for either confinement or maximal propagation length and further to optimize for spatial mode matching to the QCL mode as will be discussed in section 5.6.

5.5 Lateral confinement

Although loss due to the dielectric layer can be neglected by choosing the right material, increased vertical confinement is always connected to an increase in ohmic loss, due to the higher field intensity at the metal interface. However, in narrow metal strips, the waveguide loss is dominated by scattering on the metal edges and leakage into the substrate.

The so called dielectric loaded surface plasmon polaritons (DL-SPPs) have already been investigated both theoretically and experimentally for telecommunication wavelengths [212, 213]. There, the increased vertical confinement plays a minor role, as the SPPs are already well confined. The main advantage is the increased propagation length for SPPs with high lateral confinement. In the mid-infrared, dielectric loading solves both issues. It enables the propagation of surface plasmons that are strongly bound to the interface and it significantly increases the propagation length for narrow waveguides.

The obvious solution is to eliminate these metal edges, which is possible with dielec-

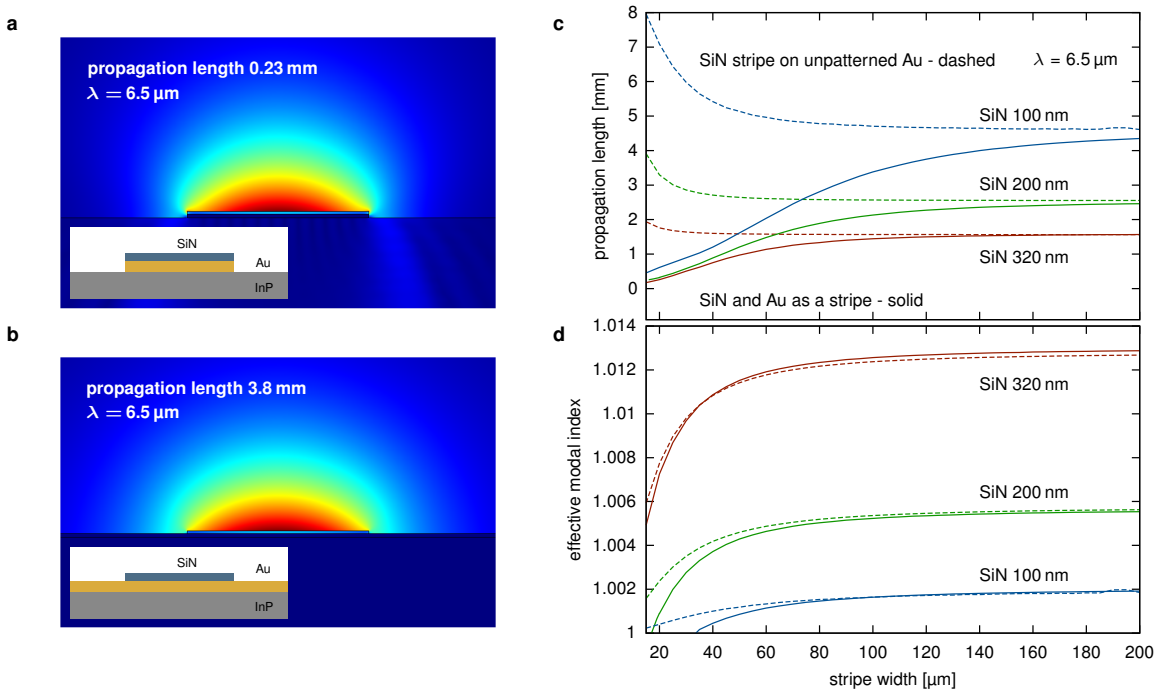

Figure 5.8: Simulated 2D mode profile of the dielectric loaded SPP waveguide with a 200 nm thick and 15 µm wide SiN_x strip on top of a gold strip (a) and on an unpatterned gold surface (b). Influence of the strip width and the SiN_x layer thickness on the propagation length (c) and the effective modal index (d) for the two waveguide configurations. Gold strip as solid and gold surface as dashed lines. For narrow waveguides the additional loss due to the metal edges leads to a dramatic reduction of the propagation length. In this case dielectric loading can improve not only the confinement, but also the propagation length significantly. Published in [25].

tric loading. To achieve this, the dielectric layer is patterned as a strip on top of an unpatterned gold surface. Figure 5.8a&b show the 2D mode simulation of a DL-SPP waveguide, where the metal and the dielectric are patterned as a strip or just the dielectric is patterned as a strip and the gold layer remains unpatterned. For a 15 µm wide plasmonic waveguide, the lateral dielectric guiding yields an increased propagation length of one order of magnitude, while providing the same lateral and enhanced vertical confinement. For the fabricated test structures (15 µm wide with 200 nm SiN_x), our simulations show a propagation length of 2–4 mm, depending on the material parameters [190, 214]. Figure 5.8c depicts the influence of the strip width on the propagation length and figure 5.8d the modal index for both waveguide configurations (gold strip as solid lines and SiN strip atop gold surface as dashed lines). When gold is used for lateral confinement, the propagation length dramatically reduced with decreasing waveguide width. The situation changes, when the dielectric layer is used to laterally confine the SPP. There, a decreased waveguide width leads to a slight increase of the propagation length.

In conclusion, for narrow, laterally single mode SPP waveguides the concept of dielectric loading allows an increase of the mode confinement and at the same time an increase

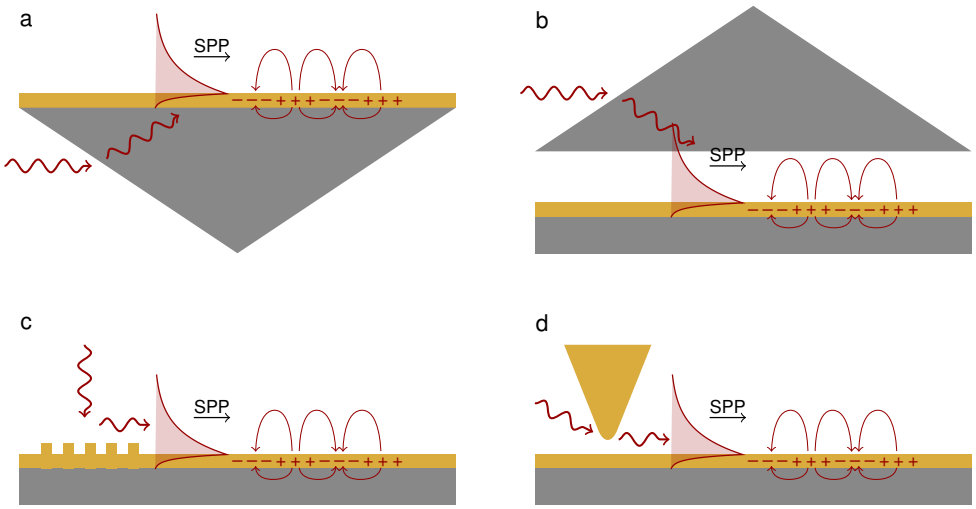

Figure 5.9: Different methods to excite SPPs from free space, including prism coupling in Kretschmann (a) and Otto (b) configuration, as well as grating (c) and near-field coupling (d).

of the propagation loss due to the elimination of the metal edges.

5.6 Excitation and detection

The condition for bound modes is, that the wave wavevector β is larger than the wavevector of its surrounding dielectric material $\sqrt{\varepsilon r}k$. The phase matching condition of direct coupling through an angle $\beta = \sqrt{\varepsilon r}k_0 \sin\theta$ has no real solution for k_0 and is thus prohibited. Special techniques are required to achieve coupling to and from SPPs. Figure 5.9 illustrates the most common methods to excite SPPs from free space.

Phase matching can be achieved using a higher refractive index material, commonly in the form of a prism. This techniques allows the excitation of SPPs on the low-index side of the interface with the condition $\beta = k\sqrt{\varepsilon}\sin\theta$. Obviously, the condition is also fulfilled for outcoupling, leading to leaky modes. This coupling scheme is also referred to as attenuated total internal reflection, as coupling is achieved through the evanescent decay on the low-index side of the interface. In the Kretschmann configuration [215], SPPs are excited from the other side of the metal. A thin metal film is required to enable coupling through the metal layer. In the Otto configuration [216], the prism is placed on the same side with a small separation.

In grating coupling the wave vector mismatch is compensated by patterning the surface with a periodic structure. This periodic structure induces an additional phase term and modifies the phase matching condition to

$$\beta = k\sin\theta + m\frac{2\pi}{a}, \tag{5.54}$$

where a is the grating period and m a positive integer number.

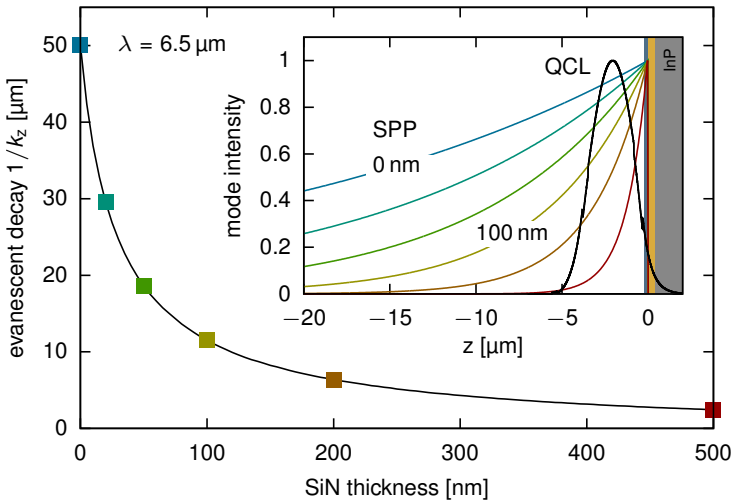

Figure 5.10: Spatial mode matching with the dielectric layer thickness and the etch depth. Vertical confinement due to dielectric loading. A thicker dielectric layer leads to a better confinement of the SPP. The inset shows the modal intensity profile of the SPP for different SiN_x thickness, corresponding to the points at 0, 20, 50, 100, 200, 500 nm, as well as the mode of the QCL/QCD ridge waveguide. Published in [25].

Different to all other techniques, near-field coupling allows a local excitation of SPPs far below the diffraction limit. A sharp tip or a defect acts as a sub-wavelength point source for SPPs [217]. This technique is utilized in near-field spectroscopy using an AFM tip, which is scanned over the sample surface. Near-field imaging of SPPs is described in more detail in section 5.7.

5.6.1 On-Chip excitation and detection

An alternative way to excite guided modes is spatial mode matching, commonly referred to as end-fire coupling. This can be achieved either by precisely focusing light onto the end of the waveguide, or by direct coupling between two waveguides. As discussed previously, SPPs require TM polarization. Further, also intersubband transitions interact with light polarization into growth direction, which matches the TM polarization of SPPs. Thus, it is possible to directly excite SPPs from a QCL via end-fire coupling, as has been demonstrated by Tetienne et al. [218]. The coupling efficiency strongly depends on the spatial overlap between the QCL and the SPP modes.

The coupling efficiency from the QCL to the SPP can be calculated using the transmission coefficient due to the effective mode indexes n_{QCL} and n_{SPP} as well as the spatial mode overlap. For the TM modes of the QCL waveguide and the SPPs, described by

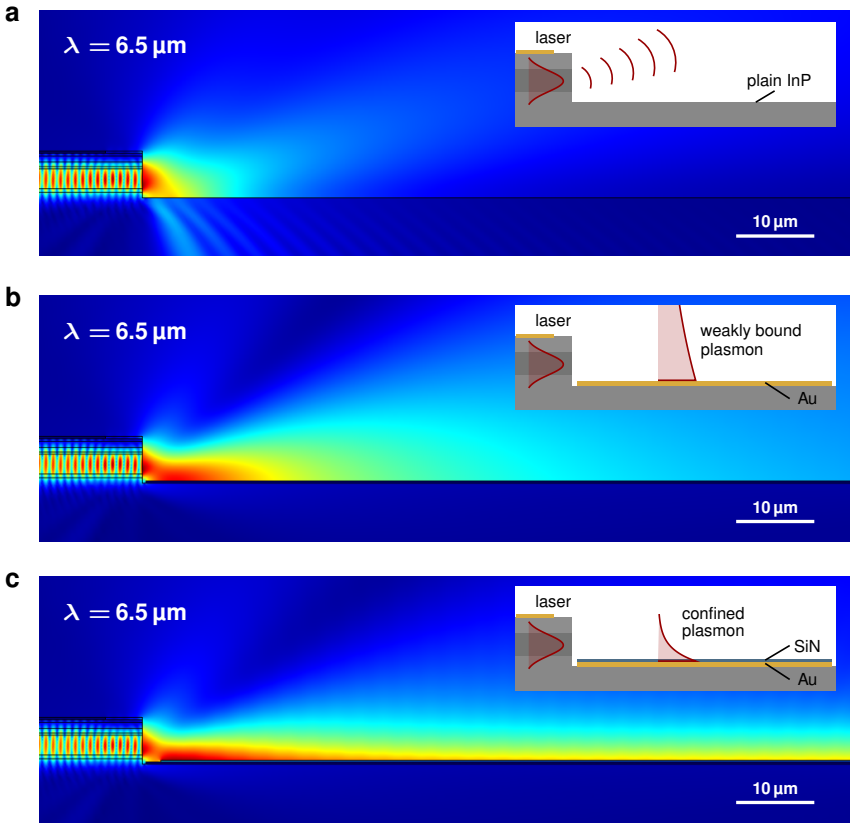

Figure 5.11: Excitation and detection of SPPs a, Without waveguide light couples to free space and partially into the substrate. **b,** An SPP can be excited on the gold surface, but is weakly bound to the interface. **c,** The 200 nm thick SiN_x layer on top of the gold surface, leads to an increased confinement. Due to the high confinement, this SPP can be coupled directly to a detector. Published in [25].

$H_{y,\mathrm{QCL}}(y,z)$ and $H_{y,\mathrm{SPP}}(y,z)$, the coupling efficiency is

$$\eta_c = \frac{4 n_{\mathrm{QCL}} n_{\mathrm{SPP}}}{(n_{\mathrm{QCL}} + n_{\mathrm{SPP}})^2} \frac{\left| \int_{-\infty}^{\infty} \int_{-\infty}^{\infty} H_{y,\mathrm{QCL}}(y,z) H_{y,\mathrm{SPP}}(y,z)\, dydz \right|^2}{\int_{-\infty}^{\infty} \int_{-\infty}^{\infty} |H_{y,\mathrm{QCL}}(y,z)|^2 \int_{-\infty}^{\infty} \int_{-\infty}^{\infty} |H_{y,\mathrm{SPP}}(y,z)|^2 dydz}. \tag{5.55}$$

The part due to the mode index mismatch leads to a reflection, which is desired to form the laser cavity. If required, it can be reduced by applying an anti-reflection coating. Dielectric-loading allows a straightforward optimization of the overlap via the evanescent decay length, which can be adjusted by the dielectric layer thickness. Another knob is the choice of the etch depth, which should be below but close to the lower end of the active region. Figure 5.10 shows the evanescent decay length versus the dielectric layer thickness and the vertical confinement of the DL-SPPs compared to the QCL mode.

Figure 5.11a–c show the finite element simulation result of the coupling between the laser and the SPP waveguide. In the case of an etched faced without any waveguide, the QCL just emits into free space and the substrate. Due to the large divergence of typical

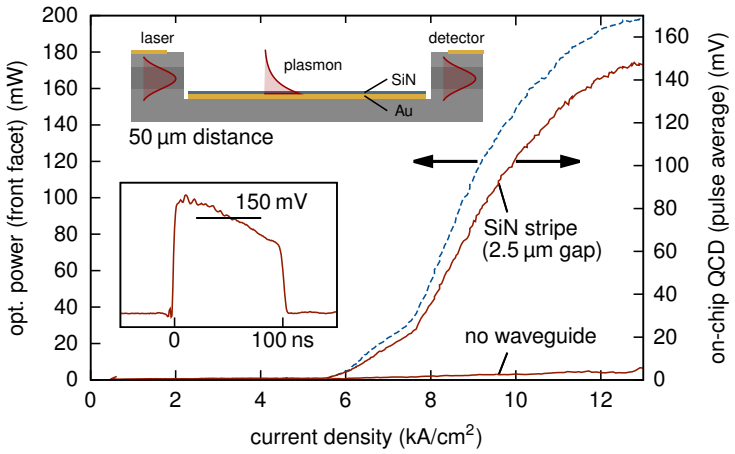

Figure 5.12: Detector signal into 50 Ω compared to the laser power (front facet) over the laser current density for a distance of 50 µm. The inset shows the time resolved detector signal. Published in [25].

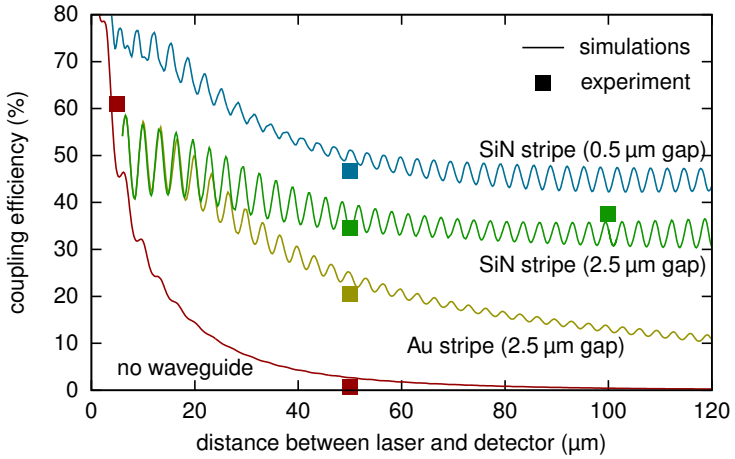

Figure 5.13: Coupling efficiency from the laser to detector facet over the distance between them, with the simulation as curves and the experiment as points. Published in [25].

QCLs ($> 30°$) the light intensity decreases rapidly. By depositing a gold layer in front of the QCL facet, an SPP can be excited. Due to the weak confinement of the SPP at mid-infrared frequencies the mode extends more and more into air approaching $1/k_z \approx 50\,\mu\text{m}$ for $\lambda = 6.5\,\mu\text{m}$. The deposition of another 200 nm thick silicon nitrite layer is sufficient to squeeze the SPP by an order of magnitude to provide a large spatial overlap, as well as well confined plasmon propagation. The DL-SPP plasmon is much stronger bound to the interface. The required thickness for mode matching lies in the same range as desired for well confined propagation.

End-fire coupling can also be used to couple an SPP into a dielectric waveguide, e.g. into a QCD fabricated as ridge waveguide. The bi-functional active region presented in chapter 4, enable a straightforward integration of lasers with detectors on the same chip. Together with DL-SPP waveguides, it can serve as a flexible monolithic platform

for mid-infrared photonics. For an experimental analysis, several devices combining a QCL, a DL-SPP and a QCD have been fabricated. Figure 5.12 shows the light-current characteristic of a QCL measured with the on-chip detector coupled through a 50 µm long DL-SPP waveguide compared to an external detector, which collects the light from the other laser facet. The particular device structure is sketched in the inset. The on-chip detector has been measured with an oscilloscope without additional amplifier and terminated with 50 Ω in order to resolve the pulse shape in time. A laser pulse power of approximately 200 mW leads to a signal as high as 150 mV on the on-chip detector, which corresponds to a photocurrent of 3 mA. This corresponds to a coupling efficiency of 35%. Without any waveguide between the laser and the detector, the signal on the detector can be barely seen. The detector voltage signal can be increased to 3 V by terminating it with 1 MΩ rather than 50 Ω. To maintain the bandwidth required to observe 100 ns pulses, the measurement electronics or amplifier should be placed close or in the direct vicinity of the device. This first experiment demonstrates the huge potential of the presented concept. Figure 5.13 shows the coupling efficiencies of the fabricated devices compared to the simulations. Here, the coupling efficiency describes the ratio between the power through the detector facet and the power emitted from the laser facet. Without any waveguide, the coupling efficiency drops immediately with increasing distance. With a gold strip between the laser and the detector the coupling is improved, but still shows a significant drop at larger waveguide lengths. For the dielectric loaded SPP waveguide, the coupling efficiency also initially drops due to additional free space coupling, but then approaches a constant slope determined by the waveguide loss. In the simulations, as well as in the experiments, we see a significant dependency on the gap between the ridge facets and the SPP waveguide. For a 50 µm DL-SPP waveguide and a gap between the gold surface and the ridge facets of 0.5 µm and 2.5 µm, we have calculated the coupling efficiency to be 47% and 35%, respectively. All curves show an oscillation because of the presence of longitudinal modes within the SPP waveguide. To minimize coupled cavity effects, the detector facet can be etched with a small lateral angle preventing back reflection into the laser.

Due to the strong dependence of the coupling efficiency on the gap between the facets and the metal, an optimized device fabrication is required. The gap between the facet and the dielectric strip is minor. An important improvement has obtained by a refined etching recipe. The isotropic etching of the hardmask (SiN) lead to a significant angle for the facets, as shown in the inset of figure 4.34. By using CHF_3 instead of SF_6, the hard-mask is etched anisotropic, leading to vertical edges. This results in vertical etching of the heterostructure and claddings with $SiCl_4$. An etched facet obtained with the refined recipe is shown in figure 5.14. Furthermore, a precise alignment of the plasmonic metal mask and perfectly matched exposure and development times are required to obtain such a small gap as shown in the figure. A slight misalignment or over development immediately leads to a coverage of the facets, but larger tolerances lead to a lower coupling efficiency.

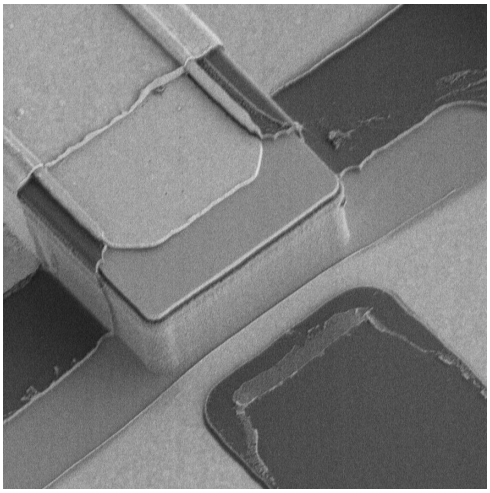

Figure 5.14: Scanning electron microscope image of the vertically etched laser ridge with top contact metal and the DL-SPP plasmonic waveguide in front of the facet. The ridge is 15 µm wide.

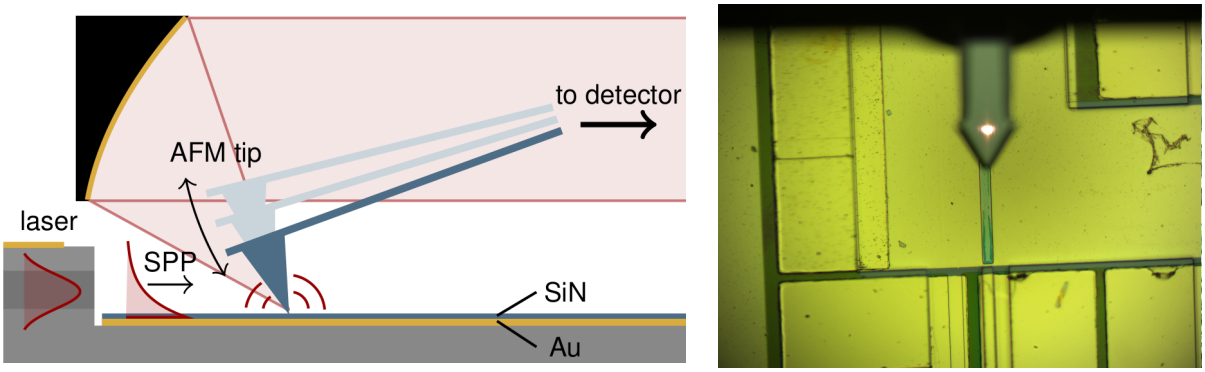

Figure 5.15: Sketch of a scattering near-field measurement of the DL-SPP directly excited from a QCL (left) and microscope image of the scanning cantilever on the DL-SPP.

5.7 Near-field imaging of DL-SPPs

Classical optical microscopy is one of the most important instruments in science, but is limited in its resolution by the diffraction limit of one half of the wavelength ($\lambda/2$). Aperture-based scanning near-field optical microscopy (SNOM) allows a dramatic improvement of the optical resolution [219]. In practice, however, the geometry of a metalized tapered glass fiber causes the well-known waveguide cut-off effect. Light propagation becomes evanescent when the diameter is below the critical cut-off diameter, which practically limits the achievable resolution to minimal apertures around $\lambda/10$ [220]. Especially at longer wavelengths the coupling becomes very inefficient.

Aperture-less SNOMs use a scatterer and are therefore commonly referred to as scattering-type SNOM (s-SNOM). They can achieve a much better relative resolution compared to the wavelength [221, 222]. Although the illumination of the scatterer obeys

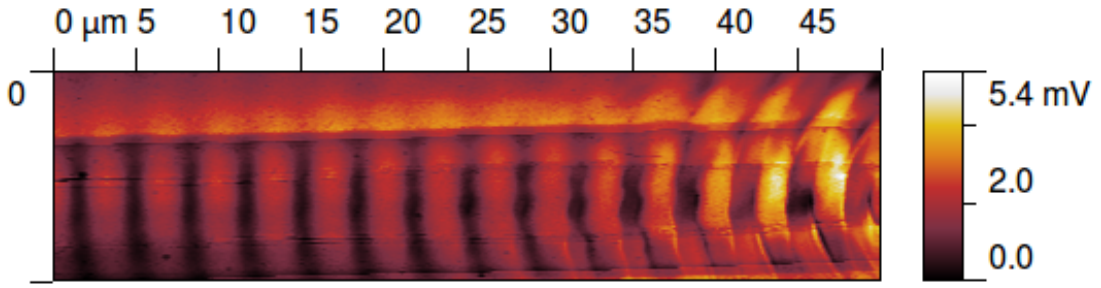

Figure 5.16: 2D scan of the directly excited SPP (QCL facet on the right). The strong divergence due to the narrow ridge width leads to leakage.

the diffraction limit, the signal can be modulated by moving the scatterer, enabling deep sub-wavelength resolution. In practice, a metallized tip of an AFM is used and the radius its apex determines the mechanical and optical resolution [220].

In a first near-field experiment during the visit at Harvard University, a directly excited surface plasmon polariton on a DL-SPP structure has been measured. The presented results are preliminary but give an impression of the plasmon propagation. Several more measurements are required to give an absolute statement on the parameters such as propagation loss, evanescent decay, etc. Figure 5.15 shows a sketch of the experiment and a microscope image of the AFM cantilever on the sample. The SPP excited from the QCL is locally scattered by the AFM tip. The scattered light is collected with a parabolic mirror and focused onto a liquid nitrogen cooled MCT detector. The first, second and third harmonic of the detector signal are measured using a lock-in amplifier, locked to the vertical oscillation of the cantilever in tapping mode.

The image is obtained by moving the sample below the cantilever with a piezo scanning stage. The vertical position of the cantilever is controlled to a fixed distance via its resonance frequency. Figure 5.16 shows the image constructed from the second harmonic. Some residuals from fabrication on the dielectric strip disturb the propagation slightly. In the coupling region, a part of the light from the QCL is emitted at higher lateral angles and is not coupled to the detector. Figure 5.17 shows a longitudinal scan along the center of the dielectric strip. The fast oscillation is due to interference between the different Fabry-Perót modes. The black curve shows the average value. The signal drops relatively fast during the first 20 µm. This decrease might be due to lateral coupling loss, but can also be attributed to the larger scattering cross section of the AFM tip for the QCL mode. One possibility to distinguish both effects might be the reduction of the oscillation amplitude. A smaller amplitude or using higher harmonics should lead to a stronger signal from fast decaying fields and thus would increase the scattering from SPP like modes. At longer distances > 100 µm the signal remains nearly constant. This indicates a very long

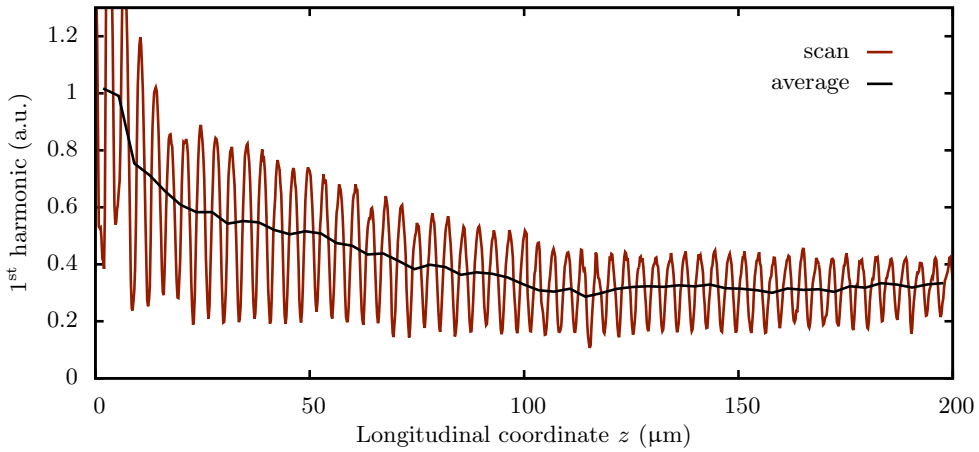

Figure 5.17: 1D scan along the DL-SPP waveguide (QCL facet on the left). The oscillation is due to the interference of the direct light from the QCL and the scattered light from the tip and corresponds to the wavelength of the light. The intensity drops in the coupling region, but then stays nearly constant. Two sections, each 100 µm long are stacked.

propagation length in the millimeter range, as predicted from the models. However, a refined measurement over a longer distance and multiple devices is required to give an absolute statement. Due to the maximal scan range of 100 µm of the piezo-stage the total was stacked. A small correction factor was used to match the amplitudes. This might be due to a misalignment of the scanning direction from the center of the strip. A full 2D scan has to be used to correct such misalignments.

Chapter 6

A mid-infrared lab-on-a-chip

This chapter introduces the first monolithically integrated lab-on-a-chip via mid-infrared absorption and is based on the publication "Monolithically integrated mid-infrared lab-on-a-chip using plasmonics and quantum cascade structures", Nature Communications 5, 4085 (2014) [25]. It further includes the considerations to improve the sensitivity and selectivity, showing results published by Ristanic et al. in "Monolithically integrated mid-infrared sensor using narrow mode operation and temperature feedback", Applied Physics Letters 106, 041101 (2015).

A challenging task is to make mid-infrared spectroscopy accessible to remote areas, where conventional power supply and laboratory equipment is not available or possible [223]. The steadily increasing demand for more compact and cost-effective sensing solutions requires monolithic integration to replace table-top systems with portable devices that incorporate all necessary optical components and functionality onto a single chip. The presented integration approach solves two major issues, which previously inhibited the integration and downscaling of the laser, waveguide and detector. First, the bi-functional active region serves as a coherent light source and as a detector, allowing a compact yet fully functional sensing device. Second, the interaction between the electromagnetic wave and the analyte is managed through a dielectric-loaded SPP waveguide. This waveguide offers both a high coupling efficiency, as well as a strong interaction with the environment.

Figure 6.1 shows a sketch and an scanning electron microscope (SEM) image of the fabricated device. With the bi-functional QCLD and the dielectric loaded SPP waveguide, two technologies are combined that are ideally suited for on-chip sensing applications and are fully compatible with each other. Both give rise to the same polarization (electric field perpendicular to the surface) and can be fabricated onto the same substrate without any hybrid integration approaches. The presented on-chip sensor can be fabricated for basically the same cost as the mid-infrared laser (QCL) alone.

A main challenge in the integration is to compensate for the limitation that arises

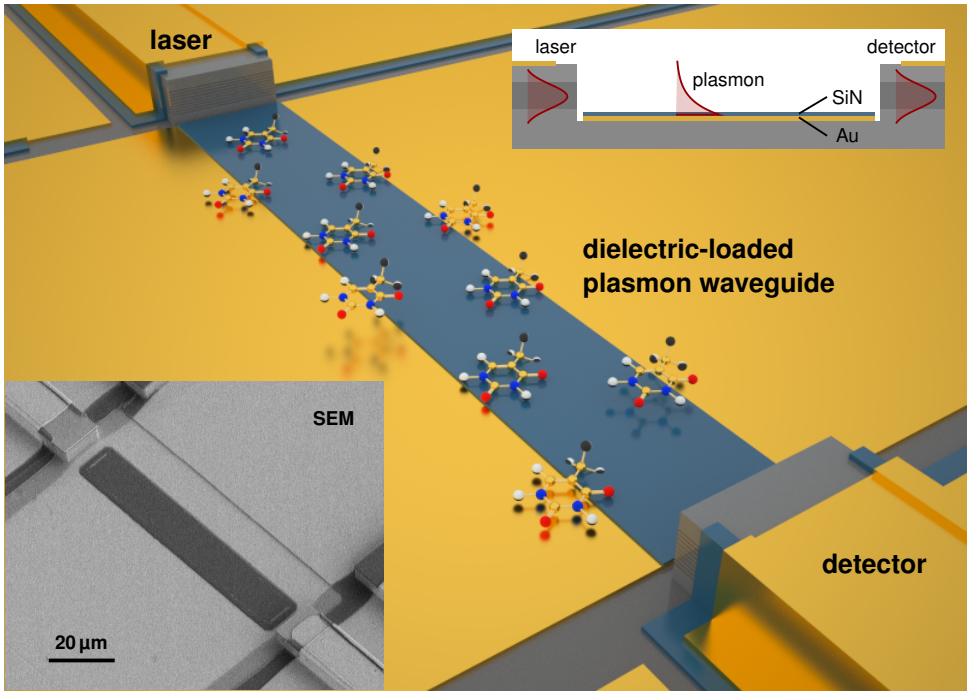

Figure 6.1: Monolithic mid-infrared on-chip sensor. The device comprised of a laser, a surface plasmon polariton waveguide and a detector, monolithically integrated on the same substrate. The upper inset shows the cross section of the structure and the lower inset the corresponding SEM image of the fabricated device.

from the difficulty to optimize all optical components individually. Different to dielectric waveguides, the mode in an SPP waveguide is mainly located outside (96%), providing a high interaction with chemical substances. The end-fire coupling is very efficient compared to conventional optics, and enables the use of ridge waveguide detectors. Compared to a discrete QCD, this leads to a signal enhancement due to the much higher absorption efficiency and lower thermal noise. Furthermore, the saturation threshold of the detector increases due to the reduced sensitivity on the absorption coefficient. Overall, the waveguide coupled detector leads to an improvement of about a factor 50 compared to a detector coupled through traditional free space optics. This is mainly due to geometrical aspects and the much higher coupling and absorption efficiency. As a result, the optimized intersubband on-chip detector can easily compete with available discrete detectors in terms of signal-to-noise and outperforms them in terms of saturation intensity. The high saturation threshold of the detector is particularly important due to the high optical peak power of the laser.

On-chip sensing of chemicals in liquid phase.

In order to prove the functionality of the on-chip sensor, the entire unpassivated devices has been submerged into a testing fluid consisting of two substances with a low and a high

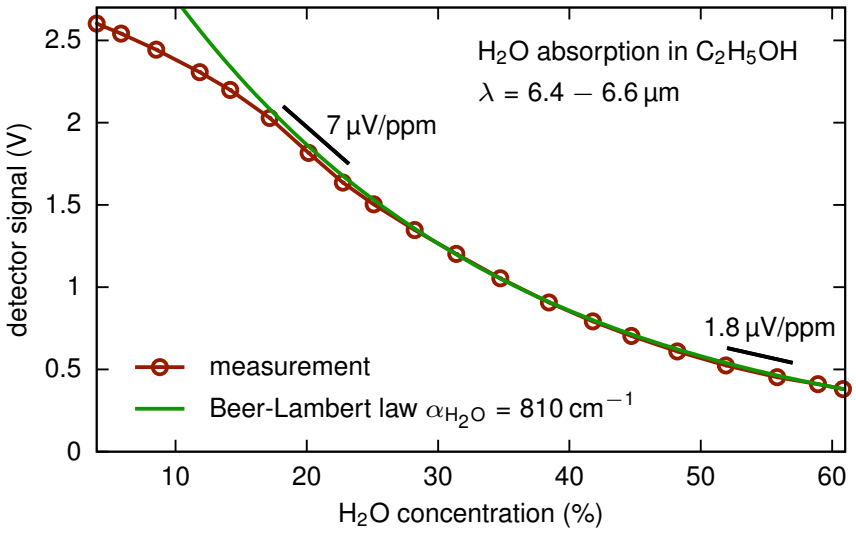

Figure 6.2: On-chip absorption measurement. The entire unpassived sensor device is submerged in a H_2O/C_2H_5OH solution with H_2O concentration from 0 to 60%. The detector signal fits to Beer-Lambert law, with a deviation at low concentrations due to detector saturation.

absorption coefficient. For the model experiment, ethanol (low absorption at $\lambda = 6.5\,\mu m$) and distilled water (high absorption at $\lambda = 6.5\,\mu m$) has been used. Figure 6.2 shows the detector signal versus the H_2O concentration of the fluid. A waveguide length of $50\,\mu m$ is used to cover a high dynamic range of concentrations from 0–60% with a slope of 1.8–$7\,\mu V ppm^{-1}$, which can be easily analyzed with state-of-the-art electronics. While longer waveguides are preferable to increase the sensitivity for low concentrations, short interaction length are beneficial if the background absorption is high, e.g. water containing liquids or high concentrations of the chemicals.

The absorption coefficient of H_2O obtained by fitting to Beer-Lamberts law agrees well with literature data [224]. At small concentrations the slope is slightly smaller due to detector saturation. Detector saturation occurs in voltage mode, when a voltage amplifier with a high input impedance ($1\,M\Omega$) is used (see section 4.2.6). In this case, the photocurrent leads to a voltage drop $V_{QCD} \approx R_{QCD} I_{ph}$ across the heterostructure, which significantly alters the bandstructure. As the detector was designed for operation near zero bias, the high reverse bias affects the absorption peak position, the extraction efficiency and the differential resistance. The laser power can be reduced, which would lead to a higher resolution at low concentrations, but a lower resolution at high concentrations. In current mode, the QCD is terminated with a small resistance which decreases the voltage drop across the heterostructure and guaranties the operating condition near zero bias. In this case, no detector saturation has been observed, which allows a better resolution at low concentrations but would require a proper transimpedance amplifier.

When the entire device is submerged into the fluid, the refractive index of the carrier fluid alters the reflectivity of the facets and the waveguide properties, but all components remain functional. The confinement of the dielectric loaded SPP is only slightly modified.

For sensing operation the change of the reflectivity due to the analyte in the carrier fluid can be neglected compared to the more pronounced absorption features. A small remaining effect may be corrected using a calibration curve. Although not necessarily required, a high-reflectivity coating was applied during the contact fabrication to minimise the impact of the fluid onto the back facet. Due to the typical relatively low conductivity of fluids, an insulation is not necessarily required. To insulate the device or to improve its chemical stability over the solvent or analyte, the device can be passivated with a thin dielectric layer, e.g. SiO_2 or CaF_2. Regular purging, e.g. with acetone or isopropyl alcohol, can be used to prevent false positives due to waveguide or detector poisoning. A 150 nm thick SiO_2 passivation layer was applied, covering the entire wire-bonded device and the bond wires were reinforced with polyimide, without a significant performance reduction. Certainly, the passivation layer should have a small refractive index to maintain the lateral index contrast of the SPP waveguide ($n_{SiO_2} = 1.2 < n_{SiN} = 1.85$) [225] and has to be considered in the waveguide design. Another possible passivation material would be CaF_2 with a refractive index of $n_{CaF_2} = 1.38$, which is known to be chemically stable. For practical applications, the sensor can be combined with microfluidics, fabricating a fluidic channel on top of the waveguide.

6.1 Noise and crosstalk

A common way to express the resolution of chemical sensors is the limit of detection, which denotes the smallest detectable concentration Δc. One has to include all other noise sources, such as laser power fluctuations, detector noise, temperature drift, etc., as well as the particular device configuration.

Pulse-to-pulse fluctuations

One main source of noise is the fluctuation of the laser intensity and spectrum from pulse-to-pulse. Each spectrum of a pulse emitted from a Fabry-Perót QCL consists of multiple longitudinal modes with an intensity distribution different from the other pulses. For the particular FP-laser this resulted in a fluctuation from pulse to pulse described by the normalized standard deviation $\sigma_P/P = 2\%$. The limit of detection with a 3σ criteria can be calculated to be

$$\Delta c = 3\,\sigma_P\,(P\alpha L_{\text{eff}}\sqrt{N})^{-1} = 1.5\%\,N^{-\frac{1}{2}}, \tag{6.1}$$

where $L_{\text{eff}} = 0.96 \cdot 50\,\mu\text{m}$ is the effective interaction length and N the number of averaged pulses. In the prototype test setup, $N = 512$ pulses were averaged, which results in a limit of detection of $\Delta c = 0.06\%$, which is independent of the concentration and thus is the limit over the entire range from 0 to 60% and beyond. The accuracy can be further increased by even longer averaging. At a certain point, other effects limit the performance, such

as drift due to temperature fluctuations of the device and the measurement electronics. As a common solution in chemical sensing, pulse-to-pulse intensity fluctuations can be accounted for by using a second reference detector [226], which can be integrated at the back facet of the laser.

Temperature fluctuations

In every laser based optical absorption measurement system, a fluctuation of the laser and detector temperature results in a fluctuation of the detected signal. The temperature sensitivity of the entire system can be characterize by the sensitivity of the laser output power and the detector responsivity. Around room temperature, the entire device shows a sensitivity of

$$\frac{dI_{ph}}{I_{ph}\,dT} = 2.45\%/\mathrm{K} \tag{6.2}$$

The device temperature is thermoelectrically controlled to $22 \pm 0.01\,^{\circ}\mathrm{C}$, which results in a limit of detection of

$$\Delta c = 3\,\sigma_{I_{ph}}\,(I_{ph}\alpha L_{\mathrm{eff}})^{-1} = 0.02\% \tag{6.3}$$

Similar to pulse-to-pulse intensity fluctuations, also the fluctuation due to temperature can be corrected using a second reference detector.

Detector noise

Due to the operation at zero bias, the noise of QCDs is commonly dominated by thermal noise (see section 4.2.4). With the high device resistance of $R_0 = 1.7\,\mathrm{k}\Omega$, the thermal noise can be calculated to be

$$i_{\mathrm{n,therm}} = \sqrt{4k_{\mathrm{B}}T\Delta f/R_0} = 3\,\mathrm{pA\,Hz^{-\frac{1}{2}}}. \tag{6.4}$$

Rather unexpected, this is not the limiting noise mechanism of the detector. Due to the very large laser intensity, the detector noise is dominated by shot noise due to the signal itself. This means, that for the particular device, a higher resistance of the detector does not improve the performance. However, for longer interaction length or large background absorption, the optical power impinging the detector can be much smaller. In this case the detector noise is again thermal noise limited, making the optimization of the detector again an important part for the optimization of the entire device. Furthermore, a higher device resistance allows a higher bandwidth or transimpedance gain of the first amplifier stage. Due to the discrete nature of electrons, the signal current $\overline{i_{\mathrm{s}}} = 2.6\mathrm{mA}$ is overlayed by the noise current

$$i_{\mathrm{n,shot}} = \sqrt{2\mathrm{e}\overline{i_{\mathrm{s}}}\Delta f} = 30\,\mathrm{pA\,Hz^{-\frac{1}{2}}}. \tag{6.5}$$

The 3σ limit of detection for 100 ns pulses is

$$\Delta c = 3\, i_{\mathrm{n,shot}}\, (\mathcal{R} P \alpha L_{\mathrm{eff}} \sqrt{2\, T_{\mathrm{average}}})^{-1} = 20\,\mathrm{ppm}\, N^{-\frac{1}{2}}, \tag{6.6}$$

where P is the optical power impinging the detector. Obviously, this limit is much lower compared to the limit due to pulse-to-pulse and temperature fluctuations.

Other sources

In the presented prototype experiment, the contribution of other noise sources were not limiting the performance. However, further pushing the limits, e.g. with a second reference detector, other noise sources will become relevant. In particular, the setup can be limited by noise or drift of the measurement electronics. The noise of the measurement electronics is mainly dominated by the first amplifier stage of the detector. This noise can be significantly reduced by averaging but the drift of the electronics, e.g. the offset voltages of operational amplifiers, has to be considered as a possible limiting factor. These considerations also apply for discrete laser based sensing systems and are not specific to the presented concept. An important additional limitation due to integration can be electric crosstalk. As discussed in section 4.9.1, separating the electric contacts of the laser and the detector is a crucial step. Further, the gold layer of the plasmonic waveguide has been used to shield the detector. In particular, the gold layer forms a closed circle around both detector contacts, which in electronics is commonly referred to as guard ring. Due to this additional shielding, the crosstalk has been significantly reduced. The small remaining crosstalk is due to the external measurement equipment, which can be reduced using custom electronics that consider this issue.

6.2 A multi-wavelength chip

The first prototype sensor demonstrated the huge potential of the presented monolithic integration approach combining the bi-functional active region and dielectric loaded plasmonics. It is capable to detect the composition of a binary liquid composed of ethanol and water within a broad range of concentrations. In order to extend this concept to detect chemicals in a complex mixture of multiple spices, an additional element is required to provide sufficient selectivity over other chemicals. This can be realized by identifying the individual and unique spectra of the different chemicals. In order to realize this, a first order distributed feedback (DFB) grating has been incorporated on the laser waveguide. The distributed grating induces a wavelength dependent reflection and allows single mode emission at specified wavelength by choosing the right grating period. Depending on the coupling strength of the grating (defined by the duty cycle and the etch depth) the laser emits multi, narrow or single mode. Narrow mode emission is sufficient for liquid sensing, where single mode emission is required for gas sensing, due to the narrow absorption lines.

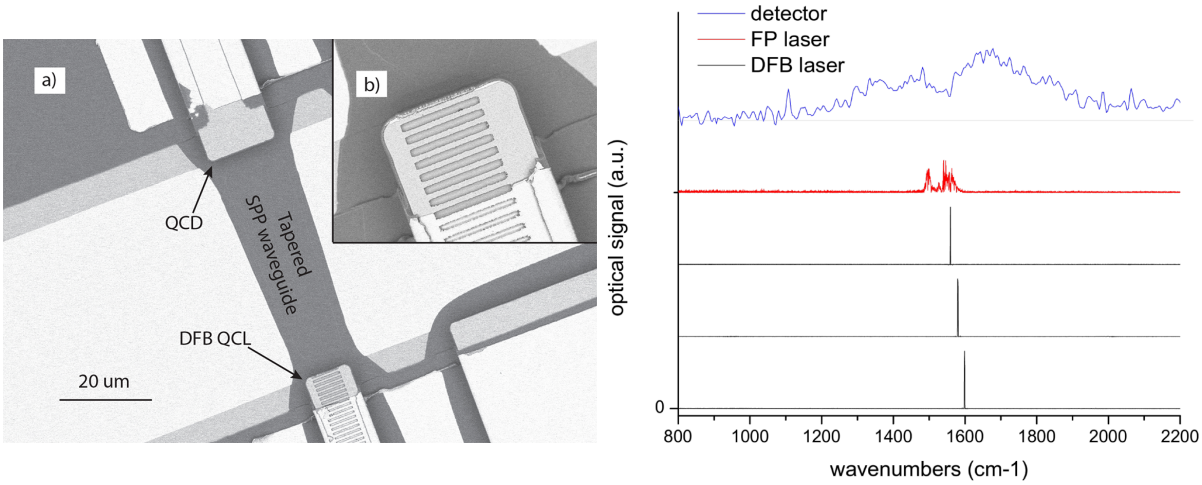

Figure 6.3: (a) Scanning electron microscopy image of the monolithic mid-infrared on-chip sensor and (b) the DFB grating (left). The emission spectra of three DFB lasers and one FP laser, as well as the photocurrent spectrum of the detector (right). Taken from [227].

Figure 6.3(left) shows a SEM image of one element consisting of a DFB laser, a DL-SPP waveguide and a detector. The DL-SPP waveguide was tapered to increase the lateral coupling and the fabrication has been further improved in terms of surface roughness. The entire sensor chip consists of an array of such elements, where each element probes a different wavelength. Figure 6.3(right) shows the corresponding emission spectra of different DFB lasers compared to a FP laser with the same active region. This experiment was based on a first generation bi-functional material. A much higher performance can be expected using the high performance active region or by further optimization for broadband operation. A coverage of around $200\,\mathrm{cm}^{-1}$ can be expected with a broadband QCLD based DFB array in the near future.

Single or narrow mode emission has a second important advantage, it leads to a significant reduction of the pulse-to-pulse intensity fluctuation of the laser. The multi mode emission of FP QCLs leads to strong competition between individual modes and due to its randomness, to a strong variation of the emission spectra between individual pulses. In a DFB laser, this mode competition is suppressed due to single or narrow mode emission. Due to the significant reduction of pulse-to-pulse fluctuations, the multi-wavelength sensor chip was limited by temperature induced fluctuations. This can be solved by a second reference detector at the back facet. As an alternative approach, a real time on-chip temperature sensor has been incorporated. This has been realized by using the strongly temperature dependent differential resistance of the bi-functional material. In particular the detector of an adjacent sensor element (DFB-laser/DL-SPP waveguide/detector) has been used for this purpose. A sketch of the measurement setup is shown in figure 6.4 (left). Due to the short spatial distance, the temperature fluctuation of the QCL, the QCD and the integrated temperature sensor are strongly correlated. It has to be noted, that no

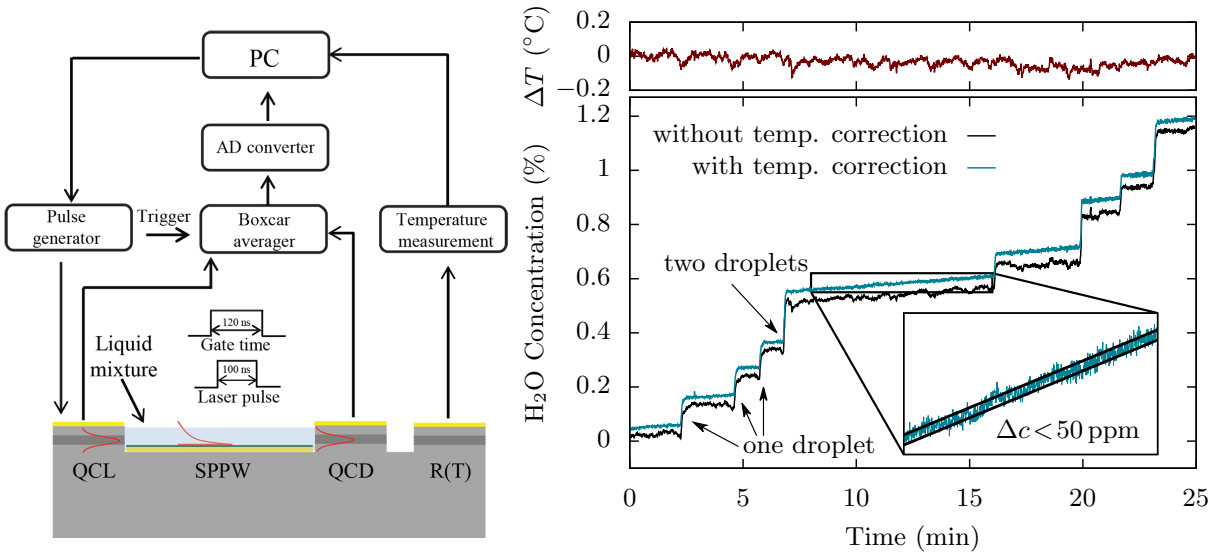

Figure 6.4: Real-time on chip absorption measurement, with the setup (left) and the result (right). The voltage signal on the detector is shown in black. The temperature fluctuation measured with the on-chip resistive temperature sensor in depicted in red. The blue line represents the corrected detector signal where the temperature fluctuations are removed from the original signal. The inset shows an enlarged view of the refined signal. The fluctuations remain within a range of approximately 50 ppm. The drift is due to the different evaporation and adsorption rate of water and isopropyl alcohol. Taken from [227].

correlation was observed between the temperature induced fluctuation of the sensor and the sub-mount temperature used for thermo-electric control.

Figure 6.4 (right) shows result of the real-time experiment, measuring the concentration of water in an water/isopropyl alcohol mixture. The concentration was stepwise increased by adding droplets of water. A homogeneous solution was ensured using a magnetic mixer. The sensor immediately response to the signal, when a droplet is added. However, temperature fluctuation of the sub-mount and the liquid mixture induce a significant fluctuation of the chip temperature and further of the detected signal. The red curve shows the temperature fluctuation measured with the on-chip temperature sensor. The blue curve shows the sensor signal, corrected for temperature fluctuation, which remains within a range of 50 ppm. The small drift in the measurement is due to different evaporation and adsorption rates of isopropyl alcohol and water. This has been checked by adding a mixture with the same initial concentration ratio, but stored in a closed environment. This is clearly an impressive first result of the presented multi-wavelength sensor chip and the concept is ready to be adapted for a particular application. This involves the design of a new QCLD active region for the particular wavelength range, the choice of the particular DFB wavelength as well as the fabrication of a fluidic channel on top of the plasmonic waveguides.

Chapter 7

Conclusion and outlook

The work described in this thesis involved the full range and variety from the initial idea and the concept development over the design and modelling of the individual components to the fabrication and experimental demonstration of the first monolithically integrated sensor based on mid-infrared absorption spectroscopy. Moving from the state-of-the-art to the monolithic integration of all necessary optical components on a single chip involved several important steps.

Quantum cascade lasers are one of the most important compact coherent light sources in the mid-infrared. Moving one step further, a device was presented, which provides additional detection functionality for the same spectral range. Simply by changing the applied bias, the bi-functional device switches between laser and detector operation. This so called quantum cascade laser and detector (QCLD) enables a straightforward and cost-effective monolithic integration. Matching the wavelength requires specific design approaches. The introduction of the horizontal-vertical extraction scheme allowed to push the laser performance significantly. Recent results show that a bi-functional operation is not necessarily connected with a high performance drawback and a similar performance can be achieved. The on-chip integrated detector from the same material serves as an ideal counterpart to the high peak power laser. Owing to direct coupling and the optimized quantum design, it provides a better performance than available uncooled detectors.

The lasers and the detectors were connected via a surface plasmon polariton (SPP) waveguide. However, the typical high conductivity of metals at mid-infrared frequencies leads to SPPs that are weakly bound to the interface. This issue previously has been solved with subwavelength patterning of grooves into the metal layer. With the introduction of dielectric loading at mid-infrared frequencies, an alternative, much simpler solution was presented, which does not require subwavelength patterning. An additional dielectric layer was used to squeeze the weakly confined SPPs providing the propagation of strongly bound modes, as well as the efficient coupling from the laser and to the detector. Depending on the thickness of the dielectric layer the evanescent decay length into the air can be adjusted over a broad range, typically in the range of 2–50 µm. Fabricated as a dielectric

strip on an unpatterned gold surface they further reduced the attenuation of narrow single mode waveguides by one order of magnitude. In particular, the dielectric strip enabled the elimination of the metal edges that lead to additional scattering and leakage into the substrate.

In an first prototype experiment the entire device comprising a laser, a 50 µm long waveguide and a detector was submerged into a binary mixture of ethanol and water. Owing to the evanescent nature of SPPs, 96% of the mode is located outside and interacts with the chemicals. A resolution of $\Delta c = 0.06\%$ was achieved over a large dynamic range from 0 to 60%. This first experiment already demonstrated the huge potential of the presented integration concept, but was limited to a binary mixture. Selectivity over other chemicals is required when analysing complex mixtures of multiple chemicals with unknown concentrations. Distributed feedback gratings were incorporated on the laser waveguide to achieve spectrally resolved measurements. The multi-wavelength chip consists of several sensor elements, each comprising a DFB laser at a different wavelength, a DLSPP waveguide and a detector. Single or narrow mode emission further reduces the pulse-to-pulse fluctuation, which limited the previous monolithic sensor. Together with temperature fluctuation compensation using an on-chip resistive temperature sensor, a limit of detection in the ppm range was demonstrated.

The presented on-chip concept is now at a stage, where it can be adapted to particular applications. This involves the selection of the target wavelength, the design of a proper bi-functional active region, the fabrication of the mulit-wavelength chip. This thesis provides the required information and background for this steps. A microfluidic channel would enable a higher reproducibly for the characterization of the limit of detection, including long term drift and degradation.

The DLSPP waveguide provides a superior surface sensitivity compared to dielectric waveguides and first near-field experiments indicate their potential to achieve much longer interaction length. The presented sensor concept is perfectly suitable for biochemical sensing applications utilizing functionalized surfaces, e.g with receptors. Polymers may be used to enrich the local concentration of gas molecules near the surface. However, more interesting is the combination with waveguide based cavity enhanced techniques, e.g. ring resonators, as such techniques make use of the inherent selectivity of mid-infrared spectroscopy. This prevents issues connected to chemical extraction methods. Further optimization of the QCLD active region and the waveguide will most probably lead to room temperature continuous wave operation. Even more broadband, tunable or multiple wavelength QCLDs will enable the detection of multiple chemical species in a complex matrix. Another interesting alternative for bi-functional devices at shorter wavelength might be the interband cascade technology, combining ICLs and ICDs in the same active region.

It took several years from the first demonstration of a QCL, till the technology started

to be available for commercial use. Still, the main costumers are people working in research and development. These years, the situation is changing: QCLs are commercially available from various sources and are gaining interest in analytical chemistry. Although the QCL technology is still too expensive for killer applications, e.g. a chemical sensor chips for smartphones, products for specific industrial applications are emerging[228]. The presented work initializes a new class of miniaturization, which was possible due to the achievements and developments in the research areas on QCLs and plasmonics during the last years. It is the right time to move towards monolithically integrated optical systems and one can be curious about the progress in research as well as industry during the next years.

Appendix A

Device fabrication

All quantum cascade devices where grown with the in-house molecular beam epitaxy system. At this point, I want to acknowledge the excellent work of our MBE team, in particular: Donald McFarland, Tobias Zederbauer, Hermann Detz, Werner Schrenk and Aaron Maxwell Andrews. They provided all samples cleaved to $\sim 10\,\mathrm{mm} \times 10\,\mathrm{mm}$.

A.1 Basic recipes

A.1.1 Initial sample cleaning

This step is required to remove dust from sample cleaving.

- acetone in ultrasonic bath: 1 min @ 10% power
- rinsing in isoproanol, drying with N_2

A.1.2 Oxide removal

Oxide removal is a crucial step, before metal contact deposition.
For InP based samples

- KOH (20%) 1 min
- rinsing in H_2O, drying with N_2

For GaAs based samples

- HCl:H_2O (1:1) 1 min
- rinsing in H_2O; drying with N_2

A.1.3 Removal of residual photoresist

Mostly, the photoresist can be removed with acetone. However, in some cases (e.g. after dry etching) parts of the resist harden and will not be removed with simple acetone cleaning. In this case, the residual resist can be burned with an oxygen plasma followed by acetone cleaning. In some cases additional ultrasonic cleaning can help, e.g. for lift-off processes. Some resists, e.g. nLof2070, do not dissolve well in acetone when they are hardened. Alternative solvents can be used in this case. It has to be noted, that alternative solvents are often much more toxic, e.g. NEP or NMP.

Hardend photoresist removal

- PLOX (oxygen plasma): 5–15 min @ 300 W
- acetone or other solvent (maybe in ultrasonic bath with 60 s @ 10%)
- rinsing in isopropanol, drying with N_2

A.1.4 SiN deposition with PECVD

SiN deposition has been realized by plasma enhanced chemical vapour deposition (PECVD). The gas mixture of the precursor gases is transformed into reactive radicals, which diffuse to the sample surface and form a layer via a surface reaction. Remaining products of the surface reaction diffuse from the surface and are removed together with the remaining precursor gases. The main advantage of the PECVD over CVD is the low temperature operation. The energy for the reaction is supplied by the plasma and allows very low substrate temperatures, even room-temperature. The chemical reaction of the particular process is the following:

$$3SiH_4 + 4NH_3 \rightarrow Si_3N_4 + 12H_2 \tag{A.1}$$

After film deposition, the thickness is tested by spectral reflection measurements using a tool from Filmmetrics. In this work, SiN layers were used as a hardmask, as electric insulation layer and as dielectric layer for the plasmonic waveguides.

Recipe:

Oxford Plasmalab 80 plus
p_{work} = 1.33 mbar,
p_{base} = 0.08 mbar,
gas flow 700 sccm SiH_4N_2 (2%), 18 sccm NH_3,
10 W RF power, $T = 300\,°C$,
typ. deposition rate 10 nm/min

A.1.5 Metal deposition

Sputtering and electron-beam evaporation was used to deposit metals for the contacts, the high reflection facet coating and the SPP waveguides. In the sputter process, solid materials are deposited by ejecting particles with high energetic ions. In the electron beam evaporation process, the material is heated with the electron beam and the evaporated material is deposited on the sample surface. Sputtering has higher deposition rates and due to resputtering leads to deposition on vertical sidewalls. Both, extended contact and facet coatings require sidewall deposition. Alternatively, sidewall deposition can be achieved with evaporation by mounting the sample at an angle. The metal layer for the SPP waveguide can be deposited with either of these methods. A thin Ti layer acts as additional adhesion layer, which is crucial for extended contacts on the SiN insulation layer.

Sputter recipe for Ti/Au contacts: pbase=2e-5mbar pwork=8e-3mbar

- Ti oxide removal 60s @ 100W RF
- Ti 4x30s @ 25W RF ($\sim 5\,\mathrm{nm/min}$)
- Au 12x40s @ 25W RF ($\sim 30\,\mathrm{nm/min}$)

E-beam evaporation recipe for ohmic contacts:

- 4-5 h pumping to $p \approx 8e-7\,\mathrm{mbar}$
- Ti evaporation with closed shutter, $p \approx 2-3e-7\,\mathrm{mbar}$
- Ge evaporation, 15 nm with 0.05 nm/s
- Au evaporation, 30 nm with 0.08 nm/s
- Ni evaporation, 30 nm with 0.05 nm/s
- Au evaporation, 100–200 nm with 0.08–0.12 nm/s

A.1.6 UV lithography

All lithography recipes are based on the mask aligner SÜSS MicroTec MJB-4. For the MJB-3 all exposure times have to be modified ($t_{\mathrm{exp}}^{\mathrm{MJB3}} \approx 2t_{\mathrm{exp}}^{\mathrm{MJB4}}$).

Resist AZ5214

standard recipe

- sample cleaning: aceton, rinsing in isoproanol, drying with N_2
- spin coating: photoresist AZ5214 (1:0), 35 s @ 4000 rpm

- baking: 2 min @ 100 °C
- exposure: removing of the edges, 40 s
- developing: AZ726MIF, 60 s, rinsing in H_2O, drying with N_2
- exposure: particular structure, 3.5 s
- developing: AZ726MIF, 25–30 s, rinsing in H_2O, drying with N_2

For 8000 rpm the development time reduces to $\sim$ 2 s. Also the developer AZ351 (1:4) can be used with the given development times divided by two.

image reversal recipe

- sample cleaning: aceton, rinsing in isoproanol, drying with N_2
- spin coating: photoresist AZ5214 (1:0), 35 s @ 4000 rpm
- baking: 2 min @ 100 °C
- exposure: removing of the edges, 20 s
- developing: AZ726MIF, 40 s, rinsing in H_2O, drying with N_2
- exposure: particular structure, 1.5 s
- reverse baking: 50 s @ 120 °C
- flood exposure: 15 s
- developing: AZ726MIF, 15-20 s, rinsing in H_2O, drying with N_2

for wet-chemical etching

- sample cleaning: aceton, rinsing in isoproanol, drying with N_2
- to prevent H_2O adsorption: store on hotplate @ 120 °C
- spin coating: adhesion layer HDMS (1:0), 35 s @ 9000 rpm
- baking: 1 min @ 100 °C
- spin coating: photoresist AZ5214 (1:0), 35 s @ 8000 rpm
- baking: 1 min @ 100 °C
- exposure: removing of the edges, 20 s
- developing: AZ726MIF, 40 s, rinsing in H_2O, drying with N_2
- exposure: particular structure, 2 s
- developing: AZ726MIF, 20–25 s, rinsing in H_2O, drying with N_2
- hard-baking: 5 min @ 100 °C

Resist maP1275

- sample cleaning: aceton, rinsing in isoproanol, drying with N_2
- spin coating: photoresist maP1275 (1:0), 35 s @ 8000 rpm
- baking: 5 min @ 100 °C
- exposure: removing of the edges, 50 s
- developing: maD331 (1:0), 100 s, rinsing in H_2O, drying with N_2
- exposure: particular structure, 10 s
- developing: maD331 (1:0), 40–60 s, rinsing in H_2O, drying with N_2

Resist nlof2070

- sample cleaning: aceton, rinsing in isoproanol, drying with N_2
- spin coating: photoresist nLof2070 (1:0), 35 s @ 8000 rpm
- baking: 5 min @ 100 °C
- exposure: particular structure, 7 s
- baking: 1 min @ 110 °C
- developing: AZ726MIF, 50–100 s, rinsing in H_2O, drying with N_2

A.1.7 Lift-off process

The lift-off process is often used to deposit thin structured layers. A photoresist acts as sacrificial layer, which is patterned with the inverted structure. The target material layer, e.g. metal contact, is deposited on top of the patterned sacrificial layer. By removing the rest of the sacrificial layer, the target material is partly lifted off and remains only in the regions, where it has a direct contact to the sample surface. A main issue is the sidewall deposition of the target layer, which can prevent the lift-off or can lead to remaining edges. For thicker layers, it is common to use negative or dual resist recipes to enable an undercut to prevent sidewall deposition, e.g. in the sputter process.

A.1.8 Reactive ion etching

Reactive ion etching (RIE) is a dry etching technique and uses a chemically reactive plasma. The plasma typically generated at a low pressure with a strong radio frequency electromagnetic field. The high energy ions generated by the plasma are accelerated towards the sample surface and result can result in anisotropic etching, due to a physical and chemical compound. Higher plasma densities can be achieved using an inductively coupled plasma (ICP). Two systems were available. First an Oxford Plasmalab 80 plus,

with a 13.56 MHz driven parallel plate reactor. The second system is an Oxford Systems PlasmaLab 100, which is a RIE-ICP system providing separate control of RF and ICP, as well as adjustable temperature control from −150 °C to 400 °C and a transfer chamber.

Both machines are equipped with in-situ interferometric process monitoring.

SiN dry etching

The following recipe provides an isotropic etching of SiN. It is ideal for removing the hardmask. Further it is used for passivation opening, as it also etches the SiN layer on the sidewalls (e.g. laser facets) with a similar rate.

Isotropic etching recipe:

Oxford Systems PlasmaLab 100
quartz carrier
$p_{\text{work}} = 2 \times 10^{-2}$ mbar,
gas flow 40 sccm SF_6,
60 W RF power, $T = 30\,^{\circ}\text{C}$,
typ. etch rate 100–170 nm/min

A higher anisotropy is provides by the following recipe. It is used for the hardmask and together with anisotropic InGaAs/InAlAs/InP etching it leads to vertically etched laser facets.

Anisotropic etching recipe:

Oxford Systems PlasmaLab 80 plus
p_{work} = 1.33 mbar,
p_{base} = 0.08 mbar,
gas flow 2 sccm O_2, 20 sccm CHF_3
120 W RF power, $T = 30\,^{\circ}\text{C}$,

InGaAs/InAlAs/InP dry etching

This recipe provides anisotropic etching of InGaAs, InAlAs and InP, but requires a hardmask (e.g. SiN or chromium).

Oxford Systems PlasmaLab 100
silicon carrier
$p_{\text{work}} = 5 \times 10^{-3}$ mbar,
gas flow 5 sccm $SiCl_4$, 40 sccm Ar
200 W RF power, $T = 240\,^{\circ}\text{C}$,
typ. etch rate 90–160 nm/min typ. etch rate of SiN hardmask 15 nm/min

A.1.9 Wet chemical etching

InGaAs/InAlAs/InP wet chemical etching

Isotropic etching of InGaAs, InAlAs and InP can be achieved with wet chemical etching. A hardmask is not necessarily required, but leads to much lower roughness of the etches and more reliable results. For Mesa etching a hard baked resist is sufficient, but for laser ridge etching, a hardmask might lead to better results. Hard-baking of the resist and specific pretreatment is essential to provide sufficient adhesion. The particular recipe is given in section A.3.

Recipe:

H_3PO_4:H_2O_2:H_2O (1:4:1)
typical etch rate $\sim 30\,\mathrm{nm/s}$
rinsing twice in H_2O
drying with N_2

The etch depth is checked using a Dektak profilometer.

A.2 Laser ridge fabrication

- initial sample cleaning

- trenches/ridge waveguide:
  1.2–1.5 µm SiN hardmask deposition
  AZ5214 standard lithography
  SiN hardmask dry etching with CHF_3
  photoresist removal
  InAlAs/InGaAs/InP dry etching with SiCl4
  SiN hardmask removal with SF_6

- electric insulation:
  400 nm SiN depostition
  maP 1275 standard lithography
  SiN dry etching with SF_6
  photoresist removal

- top contact:
  oxide removal
  maP1275 standard lithography (neg. mask)
  Ti/Au (10 nm/300 nm) sputter deposition
  lift-off

- sample cleaving (typically 2-4 mm long)
- mounting on copper plates with InP
- wire bonding

A.3 Double-pass mesa processing

- initial sample cleaning
- mesa definition:AZ5214 lithography for wet chemical etching
  InAlAs/InGaAs/InP wet etching
  photoresist removal
- contacts:
  oxide removal
  maP1275 standard lithography (neg. mask)
  Ge/Au/Ni/Au (15/30/14/150 nm) sputtering or evaporation
  lift-off
- sample cleaving (typically 2-4 mm long)
- 45 ° facet polishing
- mounting on copper plates with indium or epoxy glue
- wire bonding

A.4 Fabry-Perót sensor-chip fabrication recipe I

- initial sample cleaning
- trenches/ridge waveguide:
  1.2–1.5 µm SiN hardmask deposition
  AZ5214 standard lithography
  SiN hardmask dry etching with CHF_3
  photoresist removal
  InAlAs/InGaAs/InP dry etching with SiCl4
  SiN hardmask removal with SF_6
- electric insulation:
  400 nm SiN depostition
  maP 1275 standard lithography

SiN dry etching with SF_6
photoresist removal

- top contact and SPP metalization/:
  oxide removal
  nLof2070 standard lithography
  Ti/Au (10 nm/300 nm) sputter deposition
  lift-off with NEP
- dielectric layer for SPP:
  200 nm SiN depostition
  AZ5214 standard lithography
  SiN dry etching with SF_6
  photoresist removal
- sample cleaving (typically 2-4 mm long)
- mounting on copper plates with InP
- wire bonding

A.5 Fabry-Perót sensor-chip fabrication recipe II

One metallization step requires precise alignment and lithography optimization, such that narrow gaps between the facets and the SPP metal layer are possible, but no metal is deposited onto the facets. Alternatively the metallization can be split into contact and SPP metallization. This requires one additional evaporation step, but is more robust.

- top contact:
  oxide removal
  maP1275 standard lithography (neg. mask)
  Ti/Au (10 nm/300 nm) sputter deposition
  lift-off
- SPP metalization:
  nLof2070 standard lithography
  Ti/Au (10 nm/100 nm) evaporation
  lift-off

A.6 Multi-wavelength sensor-chip fabrication

The fabrication of the multi-wavelength sensor-chip requires the additional etching of the DFB gratings after the initial cleaning step, followed by the fabrication steps of the

Fabry-Perót sensor-chip (A.4 or A.5).

- DFB grating:
  400 nm SiN deposition
  electron-beam lithography
  SiN hardmask dry etching with CHF_3
  photoresist removal
  InAlAs/InGaAs/InP dry etching with SiCl4
  SiN hardmask removal with SF_6

Appendix B

Device characterization

All spectral characterizations of the lasers and the detectors were performed with different FTIR spectrometers from Bruker. The laser emission spectra were obtained in pulsed mode with the internal DTGS detector and the electroluminescence spectra below threshold with an external MCT detector. The detector spectra were measured using a Globar broadband source and the Stanford research SR-570 transimpedance amplifier. The input resistance of the amplifier was considered to obtain an accurate temperature dependent photoresonse. Furthermore, the mirror oscillation of the FTIR spectrometer was set to the lowest possible value. This is important, as the frequency response of the amplifier depends on the device resistance.

The light-current-voltage (LIV) characteristics of the lasers were measured in pulsed mode (100 ns or 200 ns pulses with 5 kHz or 10 kHz repetition rates.) using an Avtech pulser, a current probe, a standard oscilloscope and a calibrated detector. Three different setups were used. The first setup used the internal DTGS of the FTIR spectrometer, which was calibrated to an external powermeter for the same laser at a higher repetition rate. This was required due to the low emission power of the first QCLD generation. The horizontal-vertical transition QCLD was measured directly with a calibrated powermeter. Two coupling schemes were used, which gave similar results: Direct coupling without any optical element by putting the QCL close to the detector area (3 mm distance, 10 mm detector area) and coupling with a polished aluminium tube.

The responsivity of the detector was obtained with two different setups. The first used a continuous wave narrow emission QCL at the detector wavelength calibrated with the power meter and considering the incident radiation through the beam profile and the detector area. The calculation of the incident radiation through the beam profile is described in more detail in [229]. The second was based on the FTIR spectrometer using the Glowbar source, calibrated for spectral intensity and considering the beam profile. The responsivity measurement approach using the FTIR spectrometer is described in more detailed in [163].

The differential resistance of the detector near zero bias was extracted from the current-

voltage characteristics measured with a Keithley source-meter.

The on-chip detector signal was measured with a standard oscilloscope without additional amplifier. In the sensing experiment of the multi-wavelength chip, a boxcar averager was used to measure the signal of the on-chip detector. The particular setup is described in more detail in the corresponding section 6.2.

Appendix C

Growth sheets

This thesis involved the design, fabrication and characterization of 5 QCLs, 16 QCDs and 7 QCLDs. Some devices have been fabricated in close cooperation with D. Ristanic, A. Harrer, and P. Reininger. In this section the growth sheets of selected devices are listed.

C.1 Quantum cascade detectors

C0115 - 4.5 µm QCD

High performance 4.5 µm QCD for a QCD focal plane array. The high doping in the contact layer is required to provide sufficient carrier injection into the ground level of the first stage.

C0115 - 4.5 µm QCD			
Material	**x (%)**	**thickness**	**Doping**
InP substrate			semi-insulating
$In_xGa_{1-x}As$	53	500	$1.5\times10^{18}\,cm^{-3}$
20 × active region			
$In_xAl_{1-x}As$	52	5.0	
$In_xGa_{1-x}As$	53	800	$1.5\times10^{18}\,cm^{-3}$

Active region			
Material	**x (%)**	**thickness**	**Doping**
$In_xAl_{1-x}As$	52	3.0	
$In_xGa_{1-x}As$	53	2.85	
$In_xAl_{1-x}As$	52	4.0	
$In_xGa_{1-x}As$	53	2.4	
$In_xAl_{1-x}As$	52	4.0	

$In_xGa_{1-x}As$	53	2.05	
$In_xAl_{1-x}As$	52	4.5	
$In_xGa_{1-x}As$	53	1.7	
$In_xAl_{1-x}As$	52	4.5	
$In_xGa_{1-x}As$	53	1.45	
$In_xAl_{1-x}As$	52	4.5	
$In_xGa_{1-x}As$	53	1.2	
$In_xAl_{1-x}As$	52	6.5	
$In_xGa_{1-x}As$	53	1.1	
$In_xAl_{1-x}As$	52	6.5	
$In_xGa_{1-x}As$	53	1.05	
$In_xAl_{1-x}As$	52	6.5	
$In_xGa_{1-x}As$	53	4.7	$8\times10^{17}\,\mathrm{cm}^{-3}$

C0116 - 4.5 µm QCD

Similar to C0115, but with super-lattice contact regions instead of the highly doped contact layers. As expected, the performance is very similar. This approach is very useful for ridge waveguide detectors, where contact regions act as claddings and thus require much lower doping densities.

C0116 - 4.5 µm QCD			
Material	**x (%)**	**thickness**	**Doping**
InP substrate			semi-insulating
$In_xGa_{1-x}As$	53	500	$1\times10^{17}\,cm^{-3}$
Contact region 1			
20 × active region			
Contact region 2			
$In_xAl_{1-x}As$	52	5.0	
$In_xGa_{1-x}As$	53	750	$1\times10^{17}\,cm^{-3}$
$In_xGa_{1-x}As$	53	50	$5\times10^{18}\,cm^{-3}$

Contact region 1			
Material	**x (%)**	**thickness**	**Doping**
$In_xAl_{1-x}As$	52	2.0	$1\times10^{17}\,cm^{-3}$
$In_xGa_{1-x}As$	53	7.5	$1\times10^{17}\,cm^{-3}$
$In_xAl_{1-x}As$	52	2.0	$1\times10^{17}\,cm^{-3}$
$In_xGa_{1-x}As$	53	7.	$1\times10^{17}\,cm^{-3}$
$In_xAl_{1-x}As$	52	2.0	$1\times10^{17}\,cm^{-3}$
$In_xGa_{1-x}As$	53	6.5	$1\times10^{17}\,cm^{-3}$
$In_xAl_{1-x}As$	52	2.0	$1\times10^{17}\,cm^{-3}$
$In_xGa_{1-x}As$	53	6.0	$1\times10^{17}\,cm^{-3}$
$In_xAl_{1-x}As$	52	2.0	$1\times10^{17}\,cm^{-3}$
$In_xGa_{1-x}As$	53	5.5	$1\times10^{17}\,cm^{-3}$
$In_xAl_{1-x}As$	52	2.0	$1\times10^{17}\,cm^{-3}$
$In_xGa_{1-x}As$	53	5.0	$1\times10^{17}\,cm^{-3}$
$In_xAl_{1-x}As$	52	2.0	$1\times10^{17}\,cm^{-3}$
$In_xGa_{1-x}As$	53	4.5	$1\times10^{17}\,cm^{-3}$
$In_xAl_{1-x}As$	52	2.0	$1\times10^{17}\,cm^{-3}$
$In_xGa_{1-x}As$	53	4.0	$1\times10^{17}\,cm^{-3}$
$In_xAl_{1-x}As$	52	2.0	$1\times10^{17}\,cm^{-3}$
$In_xGa_{1-x}As$	53	3.5	$1\times10^{17}\,cm^{-3}$
$In_xAl_{1-x}As$	52	2.0	$1\times10^{17}\,cm^{-3}$

$In_xGa_{1-x}As$	53	3.0	$1\times10^{17}\,cm^{-3}$
$In_xAl_{1-x}As$	52	2.0	$1\times10^{17}\,cm^{-3}$
$In_xGa_{1-x}As$	53	3.0	$1\times10^{17}\,cm^{-3}$

Contact region 2			
Material	**x (%)**	**thickness**	**Doping**
$In_xAl_{1-x}As$	52	4.5	$5\times10^{17}\,cm^{-3}$
$In_xGa_{1-x}As$	53	6.0	$5\times10^{17}\,cm^{-3}$
$In_xAl_{1-x}As$	52	3.0	$5\times10^{17}\,cm^{-3}$
$In_xGa_{1-x}As$	53	6.5	$5\times10^{17}\,cm^{-3}$
$In_xAl_{1-x}As$	52	3.0	$5\times10^{17}\,cm^{-3}$
$In_xGa_{1-x}As$	53	7.0	$5\times10^{17}\,cm^{-3}$
$In_xAl_{1-x}As$	52	3.0	$5\times10^{17}\,cm^{-3}$
$In_xGa_{1-x}As$	53	7.5	$5\times10^{17}\,cm^{-3}$
$In_xAl_{1-x}As$	52	3.0	$5\times10^{17}\,cm^{-3}$
$In_xGa_{1-x}As$	53	8.0	$5\times10^{17}\,cm^{-3}$
$In_xAl_{1-x}As$	52	3.0	$5\times10^{17}\,cm^{-3}$

C0119 - 4.5 µm QCD

Similar to C0116, but with a diagonal-transition active region.

Active region			
Material	**x (%)**	**thickness**	**Doping**
$In_xAl_{1-x}As$	52	3.0	
$In_xGa_{1-x}As$	53	2.5	
$In_xAl_{1-x}As$	52	4.0	
$In_xGa_{1-x}As$	53	2.15	
$In_xAl_{1-x}As$	52	4.5	
$In_xGa_{1-x}As$	53	1.8	
$In_xAl_{1-x}As$	52	4.5	
$In_xGa_{1-x}As$	53	1.55	
$In_xAl_{1-x}As$	52	4.8	
$In_xGa_{1-x}As$	53	1.25	
$In_xAl_{1-x}As$	52	4.5	
$In_xGa_{1-x}As$	53	1.1	
$In_xAl_{1-x}As$	52	4.8	
$In_xGa_{1-x}As$	53	0.85	
$In_xAl_{1-x}As$	52	3.0	
$In_xGa_{1-x}As$	53	3.9	$1.5\times10^{18}\,\mathrm{cm}^{-3}$

C.2 Bi-functional quantum cascade laser/detectors

H853 - 6.5 µm QCLD

H853 - 6.5 µm QCLD			
Material	**x (%)**	**thickness**	**Doping**
InP substrate			$2–4\times10^{17}\,\mathrm{cm}^{-3}$
grading 1			
$In_xGa_{1-x}As$	53	500	$5\times10^{16}\,\mathrm{cm}^{-3}$
35 × active region			
contact region			
$In_xGa_{1-x}As$	53	300	$5\times10^{16}\,\mathrm{cm}^{-3}$
grading 2			
$In_xAl_{1-x}As$	52	1500	$1\times10^{17}\,\mathrm{cm}^{-3}$
$In_xAl_{1-x}As$	52	800	$2\times10^{17}\,\mathrm{cm}^{-3}$
grading 3			
$In_xGa_{1-x}As$	53	350	$8\times10^{18}\,\mathrm{cm}^{-3}$
$In_xGa_{1-x}As$	53	10	$1\times10^{19}\,\mathrm{cm}^{-3}$

Active region			
Material	**x (%)**	**thickness**	**Doping**
$In_xGa_{1-x}As$	53	4.4	
$In_xAl_{1-x}As$	52	2.6	
$In_xGa_{1-x}As$	53	3.7	
$In_xAl_{1-x}As$	52	2.8	
$In_xGa_{1-x}As$	53	3.2	
$In_xAl_{1-x}As$	52	3.0	$2\times10^{17}\,\mathrm{cm}^{-3}$
$In_xGa_{1-x}As$	53	2.6	$2\times10^{17}\,\mathrm{cm}^{-3}$
$In_xAl_{1-x}As$	52	2.8	$2\times10^{17}\,\mathrm{cm}^{-3}$
$In_xGa_{1-x}As$	53	2.1	$2\times10^{17}\,\mathrm{cm}^{-3}$
$In_xAl_{1-x}As$	52	3.4	
$In_xGa_{1-x}As$	53	2.1	
$In_xAl_{1-x}As$	52	2.8	
$In_xGa_{1-x}As$	53	1.9	
$In_xAl_{1-x}As$	52	4.4	
$In_xGa_{1-x}As$	53	1.4	
$In_xAl_{1-x}As$	52	1.5	
$In_xGa_{1-x}As$	53	5.6	

$In_xAl_{1-x}As$	52	2.5	

Grading 1			
Material	**x (%)**	**thickness**	**Doping**
$In_xGa_{1-x}As$	53	2.5	$1\times10^{17}\,cm^{-3}$
$In_xAl_{1-x}As$	52	2.5	$1\times10^{17}\,cm^{-3}$
$In_xGa_{1-x}As$	53	3.0	$1\times10^{17}\,cm^{-3}$
$In_xAl_{1-x}As$	52	2.0	
$In_xGa_{1-x}As$	53	3.5	
$In_xAl_{1-x}As$	52	1.5	
$In_xGa_{1-x}As$	53	4.0	
$In_xAl_{1-x}As$	52	1.0	
$In_xGa_{1-x}As$	53	4.5	
$In_xAl_{1-x}As$	52	0.5	

Contact region			
Material	**x (%)**	**thickness**	**Doping**
$In_xGa_{1-x}As$	53	4.4	
$In_xAl_{1-x}As$	52	2.6	
$In_xGa_{1-x}As$	53	3.7	
$In_xAl_{1-x}As$	52	2.8	

Grading 2			
Material	**x (%)**	**thickness**	**Doping**
$In_xAl_{1-x}As$	52	0.8	$1\times10^{17}\,cm^{-3}$
$In_xGa_{1-x}As$	53	4.2	$1\times10^{17}\,cm^{-3}$
$In_xAl_{1-x}As$	52	1.6	$1\times10^{17}\,cm^{-3}$
$In_xGa_{1-x}As$	53	3.4	$1\times10^{17}\,cm^{-3}$
$In_xAl_{1-x}As$	52	2.5	$1\times10^{17}\,cm^{-3}$
$In_xGa_{1-x}As$	53	2.5	$1\times10^{17}\,cm^{-3}$
$In_xAl_{1-x}As$	52	3.4	$1\times10^{17}\,cm^{-3}$
$In_xGa_{1-x}As$	53	1.6	$1\times10^{17}\,cm^{-3}$
$In_xAl_{1-x}As$	52	4.2	$1\times10^{17}\,cm^{-3}$
$In_xGa_{1-x}As$	53	0.8	$1\times10^{17}\,cm^{-3}$

Grading 3			
Material	**x (%)**	**thickness**	**Doping**
$In_xGa_{1-x}As$	53	0.8	$2\times10^{17}\,cm^{-3}$
$In_xAl_{1-x}As$	52	4.2	$2\times10^{17}\,cm^{-3}$
$In_xGa_{1-x}As$	53	1.6	$2\times10^{17}\,cm^{-3}$
$In_xAl_{1-x}As$	52	3.4	$2\times10^{17}\,cm^{-3}$
$In_xGa_{1-x}As$	53	2.5	$2\times10^{17}\,cm^{-3}$
$In_xAl_{1-x}As$	52	2.5	$2\times10^{17}\,cm^{-3}$
$In_xGa_{1-x}As$	53	3.4	$2\times10^{17}\,cm^{-3}$
$In_xAl_{1-x}As$	52	1.6	$2\times10^{17}\,cm^{-3}$
$In_xGa_{1-x}As$	53	4.2	$2\times10^{17}\,cm^{-3}$
$In_xAl_{1-x}As$	52	0.8	$2\times10^{17}\,cm^{-3}$

K000 - 6.5 µm QCLD

Slighly improved version of H853 with 6 kA/cm^2 threshold instead of 8 kA/cm^2 as well as 200 mW instead of 45 mW peak output power at room-temperature. Similar waveguide but with thinner top cladding, which are required for DFB lasers.

K000 - 6.5 µm QCLD			
Material	**x (%)**	**thickness**	**Doping**
InP substrate			2–4×10^{17} cm^{-3}
grading 1			
$In_xGa_{1-x}As$	53	500	5×10^{16} cm^{-3}
37 × active region			
$In_xGa_{1-x}As$	53	300	5×10^{16} cm^{-3}
grading 2			
$In_xAl_{1-x}As$	52	600	1×10^{17} cm^{-3}
$In_xAl_{1-x}As$	52	800	2×10^{17} cm^{-3}
grading 3			
$In_xGa_{1-x}As$	53	350	8×10^{18} cm^{-3}
$In_xGa_{1-x}As$	53	10	1×10^{19} cm^{-3}

Active region			
Material	**x (%)**	**thickness**	**Doping**
$In_xGa_{1-x}As$	53	3.5	
$In_xAl_{1-x}As$	52	2.6	
$In_xGa_{1-x}As$	53	4.2	
$In_xAl_{1-x}As$	52	2.5	
$In_xGa_{1-x}As$	53	5.2	
$In_xAl_{1-x}As$	52	1.5	
$In_xGa_{1-x}As$	53	1.3	
$In_xAl_{1-x}As$	52	4.3	
$In_xGa_{1-x}As$	53	1.7	
$In_xAl_{1-x}As$	52	2.7	
$In_xGa_{1-x}As$	53	1.9	
$In_xAl_{1-x}As$	52	3.4	
$In_xGa_{1-x}As$	53	1.9	
$In_xAl_{1-x}As$	52	2.7	
$In_xGa_{1-x}As$	53	2.2	2×10^{17} cm^{-3}
$In_xAl_{1-x}As$	52	2.7	2×10^{17} cm^{-3}
$In_xGa_{1-x}As$	53	2.4	2×10^{17} cm^{-3}

$In_xAl_{1-x}As$	52	2.7	$2\times10^{17}\,cm^{-3}$
$In_xGa_{1-x}As$	53	2.6	
$In_xAl_{1-x}As$	52	2.7	
$In_xGa_{1-x}As$	53	2.7	
$In_xAl_{1-x}As$	52	2.7	
$In_xGa_{1-x}As$	53	2.8	
$In_xAl_{1-x}As$	52	3.0	
$In_xGa_{1-x}As$	53	3.1	
$In_xAl_{1-x}As$	52	2.8	

C0120 - 6.7 µm QCLD

High-performance QCLD using the horizontal-vertical extractor scheme.

C0120 - 6.7 µm QCLD			
Material	**x (%)**	**thickness**	**Doping**
InP substrate			$2–4\times10^{17}\,\mathrm{cm}^{-3}$
grading 1			
$In_xGa_{1-x}As$	53	550	$5\times10^{16}\,\mathrm{cm}^{-3}$
contact region 1			
35 × active region			
contact region 2			
$In_xGa_{1-x}As$	53	400	$5\times10^{16}\,\mathrm{cm}^{-3}$
grading 2			
$In_xAl_{1-x}As$	52	1200	$1\times10^{17}\,\mathrm{cm}^{-3}$
$In_xAl_{1-x}As$	52	800	$2\times10^{17}\,\mathrm{cm}^{-3}$
grading 3			
$In_xGa_{1-x}As$	53	350	$8\times10^{18}\,\mathrm{cm}^{-3}$
$In_xGa_{1-x}As$	53	10	$1\times10^{19}\,\mathrm{cm}^{-3}$

Active region			
Material	**x (%)**	**thickness**	**Doping**
$In_xAl_{1-x}As$	52	2.4	
$In_xGa_{1-x}As$	53	5.6	
$In_xAl_{1-x}As$	52	1.7	
$In_xGa_{1-x}As$	53	1.8	
$In_xAl_{1-x}As$	52	4.4	
$In_xGa_{1-x}As$	53	2.1	
$In_xAl_{1-x}As$	52	2.8	
$In_xGa_{1-x}As$	53	2.2	
$In_xAl_{1-x}As$	52	3.1	
$In_xGa_{1-x}As$	53	2.4	$1.5\times10^{17}\,\mathrm{cm}^{-3}$
$In_xAl_{1-x}As$	52	2.8	$1.5\times10^{17}\,\mathrm{cm}^{-3}$
$In_xGa_{1-x}As$	53	2.6	$1.5\times10^{17}\,\mathrm{cm}^{-3}$
$In_xAl_{1-x}As$	52	2.6	$1.5\times10^{17}\,\mathrm{cm}^{-3}$
$In_xGa_{1-x}As$	53	3.0	$1.5\times10^{17}\,\mathrm{cm}^{-3}$
$In_xAl_{1-x}As$	52	2.2	
$In_xGa_{1-x}As$	53	3.2	
$In_xAl_{1-x}As$	52	2.0	

$In_xGa_{1-x}As$	53	3.4	
$In_xAl_{1-x}As$	52	1.9	
$In_xGa_{1-x}As$	53	3.5	
$In_xAl_{1-x}As$	52	1.8	
$In_xGa_{1-x}As$	53	3.7	
$In_xAl_{1-x}As$	52	2.6	
$In_xGa_{1-x}As$	53	4.3	
$In_xAl_{1-x}As$	52	2.6	
$In_xGa_{1-x}As$	53	4.8	

Contact region 1			
Material	**x (%)**	**thickness**	**Doping**
$In_xAl_{1-x}As$	52	2.8	$5\times10^{17}\,cm^{-3}$
$In_xGa_{1-x}As$	53	4.3	$5\times10^{17}\,cm^{-3}$
$In_xAl_{1-x}As$	52	2.6	$5\times10^{17}\,cm^{-3}$
$In_xGa_{1-x}As$	53	4.3	$5\times10^{17}\,cm^{-3}$
$In_xAl_{1-x}As$	52	2.2	
$In_xGa_{1-x}As$	53	3.2	
$In_xAl_{1-x}As$	52	2.0	
$In_xGa_{1-x}As$	53	3.4	
$In_xAl_{1-x}As$	52	1.9	
$In_xGa_{1-x}As$	53	3.5	
$In_xAl_{1-x}As$	52	1.8	
$In_xGa_{1-x}As$	53	3.7	
$In_xAl_{1-x}As$	52	2.6	
$In_xGa_{1-x}As$	53	4.3	
$In_xAl_{1-x}As$	52	2.6	
$In_xGa_{1-x}As$	53	4.8	

Contact region 2			
Material	**x (%)**	**thickness**	**Doping**
$In_xAl_{1-x}As$	52	2.0	$1.5\times10^{17}\,cm^{-3}$
$In_xGa_{1-x}As$	53	5.0	$1.5\times10^{17}\,cm^{-3}$
$In_xAl_{1-x}As$	52	2.0	$1.5\times10^{17}\,cm^{-3}$
$In_xGa_{1-x}As$	53	6.0	$1.5\times10^{17}\,cm^{-3}$
$In_xAl_{1-x}As$	52	2.0	$1.5\times10^{17}\,cm^{-3}$
$In_xGa_{1-x}As$	53	7.0	$1.5\times10^{17}\,cm^{-3}$
$In_xAl_{1-x}As$	52	2.0	$1.5\times10^{17}\,cm^{-3}$

Appendix D

Material parameters for bandstructure calculation

D.1 Binary compounds

As a generalization of the k · p - Theory, the envelop function theory only relies on the knowledge of the band offsets, the effective masses and the interband matrix elements. In the device simulator VSP2 all band offsets are referenced to the light hole valence band, to be compatible to the work of Vurgaftman et al. [128]. The Poisson's equation requires the low frequency dielectric constant ϵ_r as an additional parameter.

GaAs

Here we discuss the required material parameters to calculate the energy levels in a quantum cascade structure. For illustration we use the material parameters for gallium arsenide, taken from Vurgaftman et al. [128]. The parameters for other materials, e.g. AlAs,InAs,GaSb and their compositions can be found in the attachments.

T the temperature dependence

$$E_{\mathrm{v},0} = E_{\mathrm{v,ref}} - 0.8\,\mathrm{eV} \tag{D.1}$$

$$E_i = E_{\mathrm{v}} + E_{\mathrm{g}}^i \text{ with } i = \Gamma, X, L \tag{D.2}$$

$$E_{\mathrm{g}}^i = E_{\mathrm{g},0}^i - \frac{\alpha^i T^2}{T + \beta^i} \tag{D.3}$$

$$\begin{array}{lllll} E_{\mathrm{g},0}^{\Gamma} = 1.51\,\mathrm{eV} & \alpha^{\Gamma} = 0.5405\,\mathrm{meV/K} & \beta^{\Gamma} = 204\,\mathrm{K} & m_{\perp}^{\Gamma} = 0.067 m_0 & m_{\parallel}^{\Gamma} = 0.067 m_0 \\ E_{\mathrm{g},0}^{X} = 1.981\,\mathrm{eV} & \alpha^{X} = 0.460\,\mathrm{meV/K} & \beta^{X} = 204\,\mathrm{K} & m_{\perp}^{X} = 1.3 m_0 & m_{\parallel}^{X} = 0.23 m_0 \\ E_{\mathrm{g},0}^{L} = 1.815\,\mathrm{eV} & \alpha^{L} = 0.605\,\mathrm{meV/K} & \beta^{L} = 204\,\mathrm{K} & m_{\perp}^{L} = 1.9 m_0 & m_{\parallel}^{L} = 0.0754 m_0 \end{array} \tag{D.4}$$

$$E_\mathrm{p} = 28.8\,\mathrm{eV} \quad F = -1.94 \quad \Delta_\mathrm{so} = 0.341\,\mathrm{eV} \tag{D.5}$$

For the strain model, we need the lattice constant

$$a_\mathrm{lc} = 5.65325\,\text{Å} + 3.88\times10^{-5}\,\text{Å/K}\,(T - 300\,\mathrm{K}) \tag{D.6}$$

the hydrostatic deformation potentials

$$a_\mathrm{c} = -7.17\,\mathrm{eV} \quad a_\mathrm{v} = -1.16\,\mathrm{eV} \quad b = -2.0\,\mathrm{eV} \tag{D.7}$$

and the elastic constants of the material

$$c_{11} = 122.1\,\mathrm{GPa} \quad c_{12} = 56.6\,\mathrm{GPa}. \tag{D.8}$$

For Poisson's equation we additionally need the static dielectric constant of the material [127]

$$\epsilon_\mathrm{r} = 12.9 \tag{D.9}$$

AlAs

Valence band offset

$$E_{\mathrm{v},0} = E_{\mathrm{v,ref}} - 1.33\,\mathrm{eV}$$

Bandgab energies

$$\begin{array}{lllll}
E^\Gamma_{\mathrm{g},0} = 3.099\,\mathrm{eV} & \alpha^\Gamma = 0.885\,\mathrm{meV/K} & \beta^\Gamma = 530\,\mathrm{K} & m^\Gamma_\perp = 0.15m_0 & m^\Gamma_\parallel = 0.15m_0 \\
E^X_{\mathrm{g},0} = 2.24\,\mathrm{eV} & \alpha^X = 0.70\,\mathrm{meV/K} & \beta^X = 530\,\mathrm{K} & m^X_\perp = 0.97m_0 & m^X_\parallel = 0.22m_0 \\
E^L_{\mathrm{g},0} = 2.46\,\mathrm{eV} & \alpha^L = 0.605\,\mathrm{meV/K} & \beta^L = 204\,\mathrm{K} & m^L_\perp = 1.9m_0 & m^L_\parallel = 0.0754m_0
\end{array}$$

Kane parameters and spin-orbit coupling

$$E_\mathrm{p} = 21.1\,\mathrm{eV} \quad F = -0.48 \quad \Delta_\mathrm{so} = 0.28\,\mathrm{eV}$$

Lattice constant

$$a_\mathrm{lc} = 5.6611\,\text{Å} + 2.9\times10^{-5}\,\text{Å/K}\,(T - 300\,\mathrm{K})$$

Hydrostatic deformation potentials

$$a_\mathrm{c} = -5.64\,\mathrm{eV} \quad a_\mathrm{v} = -2.47\,\mathrm{eV} \quad b = -2.30\,\mathrm{eV}$$

Elastic constants

$$c_{11} = 125.0\,\mathrm{GPa} \quad c_{12} = 53.4\,\mathrm{GPa}.$$

Static dielectric constant

$$\epsilon_\mathrm{r} = 10.1$$

InAs

Valence band offset

$$E_{\mathrm{v},0} = E_{\mathrm{v,ref}} - 0.59\,\mathrm{eV}$$

Bandgab energies

$$\begin{array}{lllll} E_{\mathrm{g},0}^{\Gamma} = 0.417\,\mathrm{eV} & \alpha^{\Gamma} = 0.276\,\mathrm{meV/K} & \beta^{\Gamma} = 93\,\mathrm{K} & m_{\perp}^{\Gamma} = 0.026 m_0 & m_{\parallel}^{\Gamma} = 0.026 m_0 \\ E_{\mathrm{g},0}^{X} = 1.433\,\mathrm{eV} & \alpha^{X} = 0.276\,\mathrm{meV/K} & \beta^{X} = 93\,\mathrm{K} & m_{\perp}^{X} = 1.13 m_0 & m_{\parallel}^{X} = 0.16 m_0 \\ E_{\mathrm{g},0}^{L} = 1.133\,\mathrm{eV} & \alpha^{L} = 0.276\,\mathrm{meV/K} & \beta^{L} = 93\,\mathrm{K} & m_{\perp}^{L} = 0.64 m_0 & m_{\parallel}^{L} = 0.05 m_0 \end{array}$$

Kane parameters and spin-orbit coupling

$$E_{\mathrm{p}} = 21.5\,\mathrm{eV} \quad F = -2.90 \quad \Delta_{\mathrm{so}} = 0.390\,\mathrm{eV}$$

Lattice constant

$$a_{\mathrm{lc}} = 6.05831\,\text{Å} + 2.74e-5\times10^{-5}\,\text{Å/K}\,(T - 300\,\mathrm{K})$$

Hydrostatic deformation potentials

$$a_{\mathrm{c}} = -5.08\,\mathrm{eV} \quad a_{\mathrm{v}} = -1.0\,\mathrm{eV} \quad b = -1.8\,\mathrm{eV}$$

Elastic constants

$$c_{11} = 83.29\,\mathrm{GPa} \quad c_{12} = 45.26\,\mathrm{GPa}.$$

Static dielectric constant

$$\epsilon_{\mathrm{r}} = 14.6$$

InP

Valence band offset

$$E_{\mathrm{v},0} = E_{\mathrm{v,ref}} - 0.94\,\mathrm{eV}$$

Bandgab energies

$$\begin{array}{lllll} E_{\mathrm{g},0}^{\Gamma} = 1.4236\,\mathrm{eV} & \alpha^{\Gamma} = 0.363\,\mathrm{meV/K} & \beta^{\Gamma} = 162\,\mathrm{K} & m_{\perp}^{\Gamma} = 0.0795 m_0 & m_{\parallel}^{\Gamma} = 0.0795 m_0 \\ E_{\mathrm{g},0}^{X} = 2.384\,\mathrm{eV} & \alpha^{X} = 0.37\,\mathrm{meV/K} & \beta^{X} = 0.\,\mathrm{K} & m_{\perp}^{X} = 1.13 m_0 & m_{\parallel}^{X} = 0.16 m_0 \\ E_{\mathrm{g},0}^{L} = 2.014\,\mathrm{eV} & \alpha^{L} = 0.363\,\mathrm{meV/K} & \beta^{L} = 162\,\mathrm{K} & m_{\perp}^{L} = 0.64 m_0 & m_{\parallel}^{L} = 0.05 m_0 \end{array}$$

Kane parameters and spin-orbit coupling

$$E_{\mathrm{p}} = 20.7\,\mathrm{eV} \quad F = -1.31 \quad \Delta_{\mathrm{so}} = 0.108\,\mathrm{eV}$$

Lattice constant

$$a_{\mathrm{lc}} = 5.8697\,\text{Å} + 2.79e-5\times10^{-5}\,\text{Å/K}\,(T - 300\,\mathrm{K})$$

Hydrostatic deformation potentials

$$a_{\mathrm{c}} = -6.0\,\mathrm{eV} \quad a_{\mathrm{v}} = -0.6\,\mathrm{eV} \quad b = -2.0\,\mathrm{eV}$$

Elastic constants

$$c_{11} = 1011\,\mathrm{GPa} \quad c_{12} = 561\,\mathrm{GPa}.$$

Static dielectric constant

$$\epsilon_{\mathrm{r}} = 14.6$$

D.1.1 Ternary compounds

The material parameters of ternary compounds AB are calculated using the parameters of the binary compounds A and B with a quadratic from [128].

$$P_{AB} = (1-x)P_A + x\,P_B - x\,(1-x)\,C_P,$$

where C is the so called bowing parameter. The following parameters denote the non-zero bowing parameters, all other parameters are calculated with a linear relation ($C = 0$).

$\mathsf{Al_xGa_{1-x}As}$

Bandgab energies

$$\begin{aligned} C_{E^{\Gamma}_{\mathrm{g},0}} &= -0.127\,\mathrm{eV} + x1.310\,\mathrm{eV} \\ C_{E^{X}_{\mathrm{g},0}} &= 0.055\,\mathrm{eV} \end{aligned}$$

$\mathsf{In_xGa_{1-x}As}$

Valence band offset

$$C_{E_{\mathrm{v},0}} = -0.38\,\mathrm{eV}$$

Bandgab energies

$$\begin{aligned} C_{E^{\Gamma}_{\mathrm{g},0}} &= 0.477\,\mathrm{eV} \quad C_{m^{\Gamma}_{\perp}} = 0.0091 m_0 \quad C_{m^{\Gamma}_{\parallel}} = 0.0091 m_0 \\ C_{E^{X}_{\mathrm{g},0}} &= 1.4\,\mathrm{eV} \\ C_{E^{L}_{\mathrm{g},0}} &= 0.33\,\mathrm{eV} \end{aligned}$$

Kane parameters and spin-orbit coupling

$$C_{E_{\mathrm{p}}} = -1.48\,\mathrm{eV} \quad C_{\Delta_{\mathrm{so}}} = -0.38\,\mathrm{eV}$$

For InGaAs/InAlAs, we found be best parameter set for the three-band $\mathrm{k}\cdot\mathrm{p}$ - Theory of VSP2 using a Kane parameter F derived from the effective mass.

$$F = \frac{1}{2}\left[\frac{m_0}{m^{\Gamma}_{\perp}} - 1 - E_{\mathrm{p}}\frac{E^{\Gamma}_{\mathrm{g},0} + \frac{2}{3}\Delta_{\mathrm{so}}}{E^{\Gamma}_{\mathrm{g},0}(E^{\Gamma}_{\mathrm{g},0} + \Delta_{\mathrm{so}})}\right]$$

Hydrostatic deformation potentials

$$C_{a_\mathrm{c}} = 2.61\,\mathrm{eV}$$

Static dielectric constant

$$C_{\epsilon_\mathrm{r}} = -0.67$$

$In_xAl_{1-x}As$

Valence band offset

$$C_{E_{\mathrm{v},0}} = -0.64\,\mathrm{eV}$$

Bandgab energies

$$C_{E^\Gamma_{\mathrm{g},0}} = 0.70\,\mathrm{eV} \quad C_{m^\Gamma_\perp} = 0.049 m_0 \quad C_{m^\Gamma_\parallel} = 0.049 m_0$$

Kane parameters and spin-orbit coupling

$$C_{E_\mathrm{p}} = -4.81\,\mathrm{eV} \quad C_{\Delta_\mathrm{so}} = 0.15\,\mathrm{eV}$$

Similarly to InGaAs, the Kane parameter F was derived from the effective electron mass. However, the influence of F of the barrier is minor.

Hydrostatic deformation potentials

$$C_{a_\mathrm{c}} = -1.4\,\mathrm{eV}$$

References

[1] S.-S. Kim, C. Young, and B. Mizaikoff. "Miniaturized mid-infrared sensor technologies". *Analytical and Bioanalytical Chemistry* **390** (2007) pp. 231–237. doi: 10.1007/s00216-007-1673-5.

[2] L. Rothman et al. "The HITRAN 2008 molecular spectroscopic database". *Journal of Quantitative Spectroscopy and Radiative Transfer* **110** (2009) pp. 533–572. doi: 10.1016/j.jqsrt.2009.02.013.

[3] B. Mizaikoff. "Waveguide-enhanced mid-infrared chem/bio sensors". *Chemical Society Reviews* **42** (2013) p. 8683. doi: 10.1039/c3cs60173k.

[4] A. Kosterev and F. Tittel. "Chemical sensors based on quantum cascade lasers". *IEEE Journal of Quantum Electronics* **38** (2002) pp. 582–591. doi: 10.1109/jqe.2002.1005408.

[5] A. Hugi, R. Terazzi, Y. Bonetti, A. Wittmann, M. Fischer, M. Beck, J. Faist, and E. Gini. "External cavity quantum cascade laser tunable from 7.6 to 11.4 µm". *Applied Physics Letters* **95** (2009) p. 061103. doi: 10.1063/1.3193539.

[6] B. Lee, M. Belkin, C. Pflugl, L. Diehl, H. Zhang, R. Audet, J. MacArthur, D. Bour, S. Corzine, G. Hufler, and F. Capasso. "DFB Quantum Cascade Laser Arrays". *IEEE Journal of Quantum Electronics* **45** (2009) pp. 554–565. doi: 10.1109/jqe.2009.2013175.

[7] B. G. Lee, J. Kansky, A. K. Goyal, C. Pflügl, L. Diehl, M. A. Belkin, A. Sanchez, and F. A. Capasso. "Beam combining of quantum cascade laser arrays". *Optics Express* **17** (2009) p. 16216. doi: 10.1364/oe.17.016216.

[8] M. Carras, G. Maisons, B. Simozrag, V. Trinite, M. Brun, G. Grand, P. Labeye, and S. Nicoletti. "Monolithic tunable single source in the mid-IR for spectroscopy". *Quantum Sensing and Nanophotonic Devices X*. Ed. by M. Razeghi. SPIE-Intl Soc Optical Eng, 2013. doi: 10.1117/12.2009282.

[9] T. S. Mansuripur, S. Menzel, R. Blanchard, L. Diehl, C. Pflügl, Y. Huang, J.-H. Ryou, R. D. Dupuis, M. Loncar, and F. Capasso. "Widely tunable mid-infrared quantum cascade lasers using sampled grating reflectors". *Optics Express* **20** (2012) p. 23339. doi: 10.1364/oe.20.023339.

[10] A. Hugi, G. Villares, S. Blaser, H. C. Liu, and J. Faist. "Mid-infrared frequency comb based on a quantum cascade laser". *Nature* **492** (2012) pp. 229–233. doi: 10.1038/nature11620.

[11] G. Villares, A. Hugi, S. Blaser, and J. Faist. "Dual-comb spectroscopy based on quantum-cascade-laser frequency combs". *Nature Communications* **5** (2014) p. 5192. doi: 10.1038/ncomms6192.

[12] S. A. Diddams, D. J. Jones, J. Ye, S. T. Cundiff, J. L. Hall, J. K. Ranka, R. S. Windeler, R. Holzwarth, T. Udem, and T. W. Hänsch. "Direct Link between Microwave and Optical Frequencies with a 300 THz Femtosecond Laser Comb". *Physical Review Letters* **84** (2000) pp. 5102–5105. doi: 10.1103/physrevLetters84.5102.

[13] Wikimedia Commons. *Illustration of a Herriott cell*. web link (visited on 10/19/2015).

[14] J. Wojtas, J. Mikolajczyk, and Z. Bielecki. "Aspects of the Application of Cavity Enhanced Spectroscopy to Nitrogen Oxides Detection". *Sensors* **13** (2013) pp. 7570–7598. doi: 10.3390/s130607570.

[15] P. Patimisco, G. Scamarcio, F. Tittel, and V. Spagnolo. "Quartz-Enhanced Photoacoustic Spectroscopy: A Review". *Sensors* **14** (2014) pp. 6165–6206. doi: 10.3390/s140406165.

[16] A. A. Kosterev, R. F. Curl, F. K. Tittel, C. Gmachl, F. Capasso, D. L. Sivco, J. N. Baillargeon, A. L. Hutchinson, and A. Y. Cho. "Effective Utilization of Quantum-Cascade Distributed-Feedback Lasers in Absorption Spectroscopy". *Applied Optics* **39** (2000) p. 4425. doi: 10.1364/ao.39.004425.

[17] L. Dong, Y. Yu, C. Li, S. So, and F. K. Tittel. "Ppb-level formaldehyde detection using a CW room-temperature interband cascade laser and a miniature dense pattern multipass gas cell". *Optics Express* **23** (2015) p. 19821. doi: 10.1364/oe.23.019821.

[18] G. Berden, R. Peeters, and G. Meijer. "Cavity ring-down spectroscopy: Experimental schemes and applications". *International Reviews in Physical Chemistry* **19** (2000) pp. 565–607. doi: 10.1080/014423500750040627.

[19] D. Hofstetter, M. Beck, J. Faist, M. Nägele, and M. W. Sigrist. "Photoacoustic spectroscopy with quantum cascade distributed-feedback lasers". *Optics Letters* **26** (2001) p. 887. doi: 10.1364/ol.26.000887.

[20] C. B. Hirschmann, J. Lehtinen, J. Uotila, S. Ojala, and R. L. Keiski. "Sub-ppb detection of formaldehyde with cantilever enhanced photoacoustic spectroscopy using quantum cascade laser source". *Applied Physics B* **111** (2013) pp. 603–610. doi: 10.1007/s00340-013-5379-4.

[21] J. Hu, V. Tarasov, A. Agarwal, L. Kimerling, N. Carlie, L. Petit, and K. Richardson. "Fabrication and testing of planar chalcogenide waveguide integrated microfluidic sensor". *Optics Express* **15** (2007) p. 2307. doi: 10.1364/oe.15.002307.

[22] M.-L. Anne, J. Keirsse, V. Nazabal, K. Hyodo, S. Inoue, C. Boussard-Pledel, H. Lhermite, J. Charrier, K. Yanakata, O. Loreal, J. L. Person, F. Colas, C. Compère, and B. Bureau. "Chalcogenide Glass Optical Waveguides for Infrared Biosensing". *Sensors* **9** (2009) pp. 7398–7411. doi: 10.3390/s90907398.

[23] Y.-C. Chang, P. Wägli, V. Paeder, A. Homsy, L. Hvozdara, P. van der Wal, J. D. Francesco, N. F. de Rooij, and H. P. Herzig. "Cocaine detection by a mid-infrared waveguide integrated with a microfluidic chip". *Lab on a Chip* **12** (2012) p. 3020. doi: 10.1039/c2lc40601b.

[24] M. Sieger, F. Balluff, X. Wang, S.-S. Kim, L. Leidner, G. Gauglitz, and B. Mizaikoff. "On-Chip Integrated Mid-Infrared GaAs/AlGaAs Mach–Zehnder Interferometer". *Analytical Chemistry* **85** (2013) pp. 3050–3052. doi: 10.1021/ac302551s.

[25] B. Schwarz, P. Reininger, D. Ristanić, H. Detz, A. M. Andrews, W. Schrenk, and G. Strasser. "Monolithically integrated mid-infrared lab-on-a-chip using plasmonics and quantum cascade structures". *Nature Communications* **5**, 4085 (2014). doi: 10.1038/ncomms5085.

[26] W. Herschel. "Experiments on the Refrangibility of the Invisible Rays of the Sun. By William Herschel, LL. D. F. R. S." *Philosophical Transactions of the Royal Society of London* **90** (1800) pp. 284–292. doi: 10.1098/rstl.1800.0015.

[27] E. S. Barr. "Historical Survey of the Early Development of the Infrared Spectral Region". *American Journal of Physics* **28** (1960) p. 42. doi: 10.1119/1.1934975.

[28] E. Barr. "The infrared pioneers—I. Sir William Herschel". *Infrared Physics* **1** (1961) 1–IN6. doi: 10.1016/0020-0891(61)90037-9.

[29] S. G. Brush. "The Wave Theory of Heat: A Forgotten Stage in the Transition from the Caloric Theory to Thermodynamics". *The British Journal for the History of Science* **5** (1970) pp. 145–167. web link.

[30] W. Commons. *BlackbodySpectrum*. web link (visited on 09/14/2015).

[31] M. Planck. "Über eine Verbesserung der Wienschen Spektralgleichung". *Von Kirchhoff bis Planck*. Springer Science + Business Media, 1978 pp. 175–178. doi: 10.1007/978-3-663-13885-3_15.

[32] I. T. Sorokina and K. L. Vodopyanov, eds. *Solid-State Mid-Infrared Laser Sources*. Springer Berlin Heidelberg, 2003. doi: 10.1007/3-540-36491-9.

[33] H. K. Choi, ed. *Long-Wavelength Infrared Semiconductor Lasers*. Wiley-Blackwell, 2004. doi: 10.1002/0471649813.

[34] I. Melngailis. “Maser action in InAs diodes”. *Applied Physics Letters* **2** (1963) p. 176. doi: 10.1063/1.1753832.

[35] R. J. Phelan, A. R. Calawa, R. H. Rediker, R. J. Keyes, and B. Lax. “Infrared InSb laser diode in high magnetic fields”. *Applied Physics Letters* **3** (1963) p. 143. doi: 10.1063/1.1753905.

[36] J. F. Butler, A. R. Calawa, R. J. Phelan, T. C. Harman, A. J. Strauss, and R. H. Rediker. “PbTe diode laser”. *Applied Physics Letters* **5** (1964) p. 75. doi: 10.1063/1.1754062.

[37] H. Kroemer. “A proposed class of hetero-junction injection lasers”. *Proceedings of the IEEE* **51** (1963) pp. 1782–1783. doi: 10.1109/proc.1963.2706.

[38] Z. I. Alferov. “Nobel Lecture: The double heterostructure concept and its applications in physics, electronics, and technology”. *Reviews of Modern Physics* **73** (2001) pp. 767–782. doi: 10.1103/revmodphys.73.767.

[39] G. G. Zegrya and A. D. Andreev. “Mechanism of suppression of Auger recombination processes in type-II heterostructures”. *Applied Physics Letters* **67** (1995) p. 2681. doi: 10.1063/1.114291.

[40] J. R. Meyer, C. A. Hoffman, F. J. Bartoli, and L. R. Ram-Mohan. “Type-II quantum-well lasers for the mid-wavelength infrared”. *Applied Physics Letters* **67** (1995) p. 757. doi: 10.1063/1.115216.

[41] Wikimedia Commons. *Cascade transitions*. web link (visited on 10/21/2015).

[42] Wikimedia Commons. *QCL wavefunctions in 3QW active region*. web link (visited on 10/21/2015).

[43] R. F. Kazarinov and R. A. Suris. “Possibility of amplification of electromagnetic waves in a semiconductor with a superlattice”. *Soviet physics: Semiconductors* **5** (1971) p. 707.

[44] J. Faist, F. Capasso, D. L. Sivco, C. Sirtori, A. L. Hutchinson, and A. Y. Cho. “Quantum Cascade Laser”. *Science* **264** (1994) pp. 553–556. doi: 10.1126/science.264.5158.553.

[45] Y. Yao, A. J. Hoffman, and C. F. Gmachl. “Mid-infrared quantum cascade lasers”. *Nature Photonics* **6** (2012) pp. 432–439. doi: 10.1038/nphoton.2012.143.

[46] B. S. Williams. “Terahertz quantum-cascade lasers”. *Nature Photonics* **1** (2007) pp. 517–525. doi: 10.1038/nphoton.2007.166.

[47] Y. Bai, S. Slivken, S. R. Darvish, A. Haddadi, B. Gokden, and M. Razeghi. “High power broad area quantum cascade lasers”. *Applied Physics Letters* **95** (2009) p. 221104. doi: 10.1063/1.3270043.

[48] P. Q. Liu, A. J. Hoffman, M. D. Escarra, K. J. Franz, J. B. Khurgin, Y. Dikmelik, X. Wang, J.-Y. Fan, and C. F. Gmachl. "Highly power-efficient quantum cascade lasers". *Nature Photonics* **4** (2010) pp. 95–98. doi: 10.1038/nphoton.2009.262.

[49] Y. Bai, S. Slivken, S. Kuboya, S. R. Darvish, and M. Razeghi. "Quantum cascade lasers that emit more light than heat". *Nature Photonics* **4** (2010) pp. 99–102. doi: 10.1038/nphoton.2009.263.

[50] A. Wittmann, A. Hugi, E. Gini, N. Hoyler, and J. Faist. "Heterogeneous High-Performance Quantum-Cascade Laser Sources for Broad-Band Tuning". *IEEE Journal of Quantum Electronics* **44** (2008) pp. 1083–1088. doi: 10.1109/jqe.2008.2001928.

[51] Wikimedia Commons. *Schematic of single stage of a typical interband cascade laser*. web link (visited on 10/21/2015).

[52] R. Q. Yang. "Infrared laser based on intersubband transitions in quantum wells". *Superlattices and Microstructures* **17** (1995) p. 77. doi: 10.1006/spmi.1995.1017.

[53] C.-H. Lin, R. Q. Yang, D. Zhang, S. Murry, S. Pei, A. Allerman, and S. Kurtz. "Type-II interband quantum cascade laser at 3.8 [micro sign]m". *Electronics Letters* **33** (1997) p. 598. doi: 10.1049/el:19970421.

[54] M. Kim, W. W. Bewley, C. L. Canedy, C. S. Kim, C. D. Merritt, J. Abell, I. Vurgaftman, and J. R. Meyer. "High-power continuous-wave interband cascade lasers with 10 active stages". *Optics Express* **23** (2015) p. 9664. doi: 10.1364/oe.23.009664.

[55] I. Vurgaftman, R. Weih, M. Kamp, J. R. Meyer, C. L. Canedy, C. S. Kim, M. Kim, W. W. Bewley, C. D. Merritt, J. Abell, and S. Höfling. "Interband cascade lasers". *Journal of Physics D: Applied Physics* **48** (2015) p. 123001. doi: 10.1088/0022-3727/48/12/123001.

[56] R. Paschotta. *Encyclopedia of Laser Physics and Technology*. Wiley-VCH, 2008.

[57] D. A. G. Deacon, L. R. Elias, J. M. J. Madey, G. J. Ramian, H. A. Schwettman, and T. I. Smith. "First Operation of a Free-Electron Laser". *Physical Review Letters* **38** (1977) pp. 892–894. doi: 10.1103/physrevLetters38.892.

[58] T. J. Seebeck. "Über die magnetische Polarisation der Metalle und Erze durch Temperatur-Differenz". *Annalen der Physik* **82** (1826) pp. 133–160. doi: 10.1002/andp.18260820202.

[59] P. L. Richards. "Bolometers for infrared and millimeter waves". *Journal of Applied Physics* **76** (1994) p. 1. doi: 10.1063/1.357128.

[60] M. J. Griffin et al. "The Herschel -SPIRE instrument and its in-flight performance". *Astronomy and Astrophysics* **518** (2010) p. L3. doi: 10.1051/0004-6361/201014519.

[61] R. Bhan, R. Saxena, C. Jalwani, and S. Lomash. "Uncooled Infrared Microbolometer Arrays and their Characterisation Techniques". *Defence Science Journal* **59** (2009) pp. 580–589. doi: 10.14429/dsj.59.1562.

[62] A. Hossain and M. Rashid. "Pyroelectric detectors and their applications". *IEEE Transactions on Industry Applications* **27** (1991) pp. 824–829. doi: 10.1109/28.90335.

[63] W. Commons. *Internal photoelectric effect*. web link (visited on 09/14/2015).

[64] A Rogalski. "HgCdTe infrared detector material: history, status and outlook". *Reports on Progress in Physics* **68** (2005) pp. 2267–2336. doi: 10.1088/0034-4885/68/10/r01.

[65] W. G. Adams and R. E. Day. "The Action of Light on Selenium". English. *Philosophical Transactions of the Royal Society of London* **167** (1877) pp. 313–349. web link.

[66] T. W. Case. "Notes on the Change of Resistance of Certain Substances in Light". *Physical Review* **9** (1917) pp. 305–310. doi: 10.1103/physrev.9.305.

[67] A. Rogalski. "Infrared detectors: status and trends". *Progress in Quantum Electronics* **27** (2003) pp. 59–210. doi: 10.1016/s0079-6727(02)00024-1.

[68] P. Capper and J. Garland, eds. *Mercury Cadmium Telluride*. Wiley-Blackwell, 2010. doi: 10.1002/9780470669464.

[69] J. V. Li, R. Q. Yang, C. J. Hill, and S. L. Chuang. "Interband cascade detectors with room temperature photovoltaic operation". *Applied Physics Letters* **86** (2005) p. 101102. doi: 10.1063/1.1875758.

[70] R. Q. Yang, Z. Tian, Z. Cai, J. F. Klem, M. B. Johnson, and H. C. Liu. "Interband-cascade infrared photodetectors with superlattice absorbers". *Journal of Applied Physics* **107** (2010) p. 054514. doi: 10.1063/1.3327415.

[71] N. Gautam, S. Myers, A. V. Barve, B. Klein, E. P. Smith, D. R. Rhiger, L. R. Dawson, and S. Krishna. "High operating temperature interband cascade midwave infrared detector based on type-II InAs/GaSb strained layer superlattice". *Applied Physics Letters* **101** (2012) p. 021106. doi: 10.1063/1.4733660.

[72] Wikimedia Commons. *Photoconductive gain in a quantum well infrared photodetector*. web link (visited on 10/21/2015).

[73] Wikimedia Commons. *Conduction band profile of a photoconductive QWIP*. web link (visited on 10/21/2015).

[74] L. L. Chang, L. Esaki, and G. A. Sai-Halasz. "Infrared Optical Devices of Layered Structures". *IBM Technical Disclosure Bulletin* **20** (1977) p. 2019.

[75] B. F. Levine, K. K. Choi, C. G. Bethea, J. Walker, and R. J. Malik. "New 10 µm infrared detector using intersubband absorption in resonant tunneling GaAlAs superlattices". *Applied Physics Letters* **50** (1987) p. 1092. doi: 10.1063/1.97928.

[76] H. Schneider and H. C. Liu. *Quantum Well infrared photodetectors*. Springer, Berlin, 2006.

[77] H. Schneider, C. Schönbein, G. Bihlmann, P. van Son, and H. Sigg. "High-speed infrared detection by uncooled photovoltaic quantum well infrared photodetectors". *Applied Physics Letters* **70** (1997) p. 1602. doi: 10.1063/1.118628.

[78] D. Hofstetter, M. Beck, and J. Faist. "Quantum-cascade-laser structures as photodetectors". *Applied Physics Letters* **81** (2002) p. 2683. doi: 10.1063/1.1512954.

[79] L. Gendron, M. Carras, A. Huynh, V. Ortiz, C. Koeniguer, and V. Berger. "Quantum cascade photodetector". *Applied Physics Letters* **85** (2004) p. 2824. doi: 10.1063/1.1781731.

[80] M. Graf, N. Hoyler, M. Giovannini, J. Faist, and D. Hofstetter. "InP-based quantum cascade detectors in the mid-infrared". *Applied Physics Letters* **88** (2006) p. 241118. doi: 10.1063/1.2210088.

[81] Y. Arakawa. "Multidimensional quantum well laser and temperature dependence of its threshold current". *Applied Physics Letters* **40** (1982) p. 939. doi: 10.1063/1.92959.

[82] J. Campbell and A. Madhukar. "Quantum-dot infrared photodetectors". *Proceedings of the IEEE* **95** (2007) pp. 1815–1827. doi: 10.1109/jproc.2007.900967.

[83] S. Raghavan, P. Rotella, A. Stintz, B. Fuchs, S. Krishna, C. Morath, D. A. Cardimona, and S. W. Kennerly. "High-responsivity, normal-incidence long-wave infrared ($\lambda \approx 7.2\,\mu m$) InAs/$In_{0.15}Ga_{0.85}As$ dots-in-a-well detector". *Applied Physics Letters* **81** (2002) p. 1369. doi: 10.1063/1.1498009.

[84] B. C. Smith. *Fundamentals of Fourier transform infrared spectroscopy*. CRC press, 2011.

[85] A. A. Michelson and E. W. Morley. "On the relative motion of the Earth and the luminiferous ether". *American Journal of Science* **s3-34** (1887) pp. 333–345. doi: 10.2475/ajs.s3-34.203.333.

[86] D. Ristanić. "Optoelectonics integration: On-Chip Infrared Sensors". PhD thesis. Institut of Solid State Electronics, TU Wien, Vienna, Austria, 2015.

[87] L. Esaki and R. Tsu. "Superlattice and Negative Differential Conductivity in Semiconductors". *IBM Journal of Research and Development* **14** (1970) pp. 61–65. doi: 10.1147/rd.141.0061.

[88] C. H. Henry. "The origin of quantum wells and the quantum well laser". *Quantum Well Lasers*. Elsevier BV, 1993 pp. 1–16. doi: 10.1016/b978-0-08-051558-8.50006-3.

[89] A. Cho and J. Arthur. "Molecular beam epitaxy". *Progress in Solid State Chemistry* **10** (1975) pp. 157–191. doi: 10.1016/0079-6786(75)90005-9.

[90] R. Dingle, W. Wiegmann, and C. H. Henry. "Quantum States of Confined Carriers in Very Thin $Al_xGa_{1-x}As$-GaAs-$Al_xGa_{1-x}As$ Heterostructures". *Physical Review Letters* **33** (1974) pp. 827–830. doi: 10.1103/physrevLetters33.827.

[91] J. P. van der Ziel, R. Dingle, R. C. Miller, W. Wiegmann, and W. A. Nordland. "Laser oscillation from quantum states in very thin GaAs-$Al_{0.2}Ga_{0.8}As$ multilayer structures". *Applied Physics Letters* **26** (1975) p. 463. doi: 10.1063/1.88211.

[92] H. Detz. "Epitaxy of InGaAs/GaAsSb Heterostructures for Intersubband Optoelectronics". PhD thesis. Institut of Solid State Electronics, TU Wien, Vienna, Austria, 2011.

[93] T. Ando, A. B. Fowler, and F. Stern. "Electronic properties of two-dimensional systems". *Reviews of Modern Physics* **54** (1982) pp. 437–672. doi: 10.1103/revmodphys.54.437.

[94] E. Gornik and D. C. Tsui. "Voltage-Tunable Far-Infrared Emission from Si Inversion Layers". *Physical Review Letters* **37** (1976) pp. 1425–1428. doi: 10.1103/physrevLetters37.1425.

[95] L. C. West and S. J. Eglash. "First observation of an extremely large-dipole infrared transition within the conduction band of a GaAs quantum well". *Applied Physics Letters* **46** (1985) p. 1156. doi: 10.1063/1.95742.

[96] F. Capasso, K. Mohammed, and A. Cho. "Resonant tunneling through double barriers, perpendicular quantum transport phenomena in superlattices, and their device applications". *IEEE Journal of Quantum Electronics* **22** (1986) pp. 1853–1869. doi: 10.1109/jqe.1986.1073171.

[97] M. Helm, P. England, E. Colas, F. DeRosa, and S. J. Allen. "Intersubband emission from semiconductor superlattices excited by sequential resonant tunneling". *Physical Review Letters* **63** (1989) pp. 74–77. doi: 10.1103/physrevLetters63.74.

[98] J. Faist. *Quantum Cascade Lasers*. Oxford University press, 2013.

[99] J. Singh. *Electronic and Optoelectronic Properties of Semiconductor Structures*. Cambridge University Press (CUP), 2003. doi: 10.1017/cbo9780511805745.

[100] G. Bastard. *Wave Mechanics Applied to Semiconductor Heterostructures*. Wiley-Interscience, 1991. ISBN: 978-0470217085.

[101] M. Willatzen and L. C. L. Y. Voon. *The k p Method*. Springer Science + Business Media, 2009. doi: 10.1007/978-3-540-92872-0.

[102] Wikimedia Commons. *A zincblende unit cell*. web link (visited on 10/28/2015).

[103] G. Klimeck, R. C. Bowen, T. B. Boykin, and T. A. Cwik. "sp3s* Tight-binding parameters for transport simulations in compound semiconductors". *Superlattices and Microstructures* **27** (2000) pp. 519–524. doi: 10.1006/spmi.2000.0862.

[104] Nextnano. *1D tight binding bandstructure*. web link (visited on 09/28/2015).

[105] E. O. Kane. "Band structure of indium antimonide". *Journal of Physics and Chemistry of Solids* **1** (1957) pp. 249–261. doi: 10.1016/0022-3697(57)90013-6.

[106] O. Baumgartner, Z. Stanojevic, and H. Kosina. "Monte Carlo Simulation of Electron Transport in Quantum Cascade Lasers". *Monte Carlo Methods and Applications*. Ed. by K. K. Sabelfeld and I. Dimov. Vol. 59. De Gruyter Borovets, Bulgaria, 2012 p. 67. ISBN: 9783110293586.

[107] C. Jirauschek and T. Kubis. "Modeling techniques for quantum cascade lasers". *Applied Physics Reviews* **1** (2014) p. 011307. doi: 10.1063/1.4863665.

[108] M. Graf. "Design and characterisation of far- and mid-infrared quantum cascade detectors". PhD thesis. Faculté des Sciences de l'Université de Neuchâtel, Neuchâtel, Switzerland, 2006.

[109] P. Price. "Two-dimensional electron transport in semiconductor layers. I. Phonon scattering". *Annals of Physics* **133** (1981) pp. 217–239. doi: 10.1016/0003-4916(81)90250-5.

[110] H. Fröhlich. "Electrons in lattice fields". *Advances in Physics* **3** (1954) pp. 325–361. doi: 10.1080/00018735400101213.

[111] K. Huang and B. Zhu. "Dielectric continuum model and Fröhlich interaction in superlattices". *Physical Review B* **38** (1988) pp. 13377–13386. doi: 10.1103/physrevb.38.13377.

[112] T. P. Pearsall. "Single longitudinal-mode optical phonon scattering in Ga0.47In0.53As". *Applied Physics Letters* **42** (1983) p. 436. doi: 10.1063/1.93962.

[113] M. Franckié, D. O. Winge, J. Wolf, V. Liverini, E. Dupont, V. Trinité, J. Faist, and A. Wacker. "Impact of interface roughness distributions on the operation of quantum cascade lasers". *Optics Express* **23** (2015) p. 5201. doi: 10.1364/oe.23.005201.

[114] Y. Chiu, Y. Dikmelik, J. B. Khurgin, and C. Gmachl. "Engineering the Intersubband Lifetime with Interface Roughness in Quantum Cascade Lasers". *Conference on Lasers and Electro-Optics 2012*. Optical Society of America (OSA), 2012. doi: 10.1364/cleo_si.2012.cth3n.1.

[115] C. Deutsch, H. Detz, T. Zederbauer, A. M. Andrews, P. Klang, T. Kubis, G. Klimeck, M. E. Schuster, W. Schrenk, G. Strasser, and K. Unterrainer. "Probing scattering mechanisms with symmetric quantum cascade lasers". *Optics Express* **21** (2013) p. 7209. doi: 10.1364/oe.21.007209.

[116] J. B. Khurgin, Y. Dikmelik, A. Hugi, and J. Faist. "Coherent frequency combs produced by self frequency modulation in quantum cascade lasers". *Applied Physics Letters* **104** (2014) p. 081118. doi: 10.1063/1.4866868.

[117] G. Villares and J. Faist. "Quantum cascade laser combs: effects of modulation and dispersion". *Optics Express* **23** (2015) p. 1651. doi: 10.1364/oe.23.001651.

[118] P. Harrison, D. Indjin, and R. W. Kelsall. "Electron temperature and mechanisms of hot carrier generation in quantum cascade lasers". *Journal of Applied Physics* **92** (2002) p. 6921. doi: 10.1063/1.1517747.

[119] O. Baumgartner, Z. Stanojevic, and H. Kosina. "Efficient simulation of quantum cascade lasers using the Pauli master equation". *2011 International Conference on Simulation of Semiconductor Processes and Devices*. Institute of Electrical & Electronics Engineers (IEEE), 2011. doi: 10.1109/sispad.2011.6035057.

[120] C. Jirauschek and P. Lugli. "Monte-Carlo-based spectral gain analysis for terahertz quantum cascade lasers". *Journal of Applied Physics* **105** (2009) p. 123102. doi: 10.1063/1.3147943.

[121] H. Callebaut and Q. Hu. "Importance of coherence for electron transport in terahertz quantum cascade lasers". *Journal of Applied Physics* **98** (2005) p. 104505. doi: 10.1063/1.2136420.

[122] S. Kumar and Q. Hu. "Coherence of resonant-tunneling transport in terahertz quantum-cascade lasers". *Physical Review B* **80**, 24 (2009). doi: 10.1103/physrevb.80.245316.

[123] R. Terazzi and J. Faist. "A density matrix model of transport and radiation in quantum cascade lasers". *New Journal of Physics* **12** (2010) p. 033045. doi: 10.1088/1367-2630/12/3/033045.

[124] R. Bersohn. "Quantum Statistical Mechanics. L. P. Kadanoff and G. Baym. Benjamin, New York, 1962. 203 pp. Illus. Paper, 4.95; cloth, 6.95". *Science* **139** (1963) pp. 399–400. doi: 10.1126/science.139.3553.399-b.

[125] S.-C. Lee and A. Wacker. "Nonequilibrium Green's function theory for transport and gain properties of quantum cascade structures". *Physical Review B* **66**, 24 (2002). doi: 10.1103/physrevb.66.245314.

[126] M. Lindskog, J. M. Wolf, V. Trinite, V. Liverini, J. Faist, G. Maisons, M. Carras, R. Aidam, R. Ostendorf, and A. Wacker. "Comparative analysis of quantum cascade laser modeling based on density matrices and non-equilibrium Green's functions". *Applied Physics Letters* **105** (2014) p. 103106. doi: 10.1063/1.4895123.

[127] *NSM Archive, Physical Properties of Semiconductors.* web link (visited on 10/01/2015).

[128] I. Vurgaftman, J. R. Meyer, and L. R. Ram-Mohan. "Band parameters for III–V compound semiconductors and their alloys". *Journal of Applied Physics* **89** (2001) p. 5815. doi: 10.1063/1.1368156.

[129] M. Nobile, H. Detz, E. Mujagić, A. M. Andrews, P. Klang, W. Schrenk, and G. Strasser. "Midinfrared intersubband absorption in InGaAs/GaAsSb multiple quantum wells". *Applied Physics Letters* **95** (2009) p. 041102. doi: 10.1063/1.3189703.

[130] C. Deutsch, H. Detz, T. Zederbauer, M. Krall, M. Brandstetter, A. M. Andrews, P. Klang, W. Schrenk, G. Strasser, and K. Unterrainer. "InGaAs/GaAsSb/InP terahertz quantum cascade lasers". *Journal of Infrared, Millimeter, and Terahertz Waves* (2013) pp. 374–385. doi: 10.1007/s10762-013-9991-5.

[131] J. Devenson, R. Teissier, O. Cathabard, and A. N. Baranov. "InAs/AlSb quantum cascade lasers emitting below 3 µm". *Applied Physics Letters* **90** (2007) p. 111118. doi: 10.1063/1.2714098.

[132] C. G. V. de Walle. "Band lineups and deformation potentials in the model-solid theory". *Physical Review B* **39** (1989) pp. 1871–1883. doi: 10.1103/physrevb.39.1871.

[133] M. Sugawara, N. Okazaki, T. Fujii, and S. Yamazaki. "Conduction-band and valence-band structures in strained $In_{1-x}Ga_xAs$/InP quantum wells on (001) InP substrates". *Physical Review B* **48** (1993) pp. 8102–8118. doi: 10.1103/physrevb.48.8102.

[134] B. Schwarz, P. Reininger, H. Detz, T. Zederbauer, A. M. Andrews, S. Kalchmair, W. Schrenk, O. Baumgartner, H. Kosina, and G. Strasser. "A bi-functional quantum cascade device for same-frequency lasing and detection". *Applied Physics Letters* **101** (2012) p. 191109. doi: 10.1063/1.4767128.

[135] B. Schwarz, P. Reininger, H. Detz, T. Zederbauer, A. Andrews, W. Schrenk, and G. Strasser. "Monolithically Integrated Mid-Infrared Quantum Cascade Laser and Detector". *Sensors* **13** (2013) pp. 2196–2205. doi: 10.3390/s130202196.

[136] B. Schwarz, D. Ristanic, P. Reininger, T. Zederbauer, D. MacFarland, H. Detz, A. M. Andrews, W. Schrenk, and G. Strasser. "High performance bi-functional quantum cascade laser and detector". *Applied Physics Letters* **107** (2015) p. 071104. doi: 10.1063/1.4927851.

[137] Y. Bai, S. R. Darvish, S. Slivken, W. Zhang, A. Evans, J. Nguyen, and M. Razeghi. "Room temperature continuous wave operation of quantum cascade lasers with watt-level optical power". *Applied Physics Letters* **92** (2008) p. 101105. doi: 10.1063/1.2894569.

[138] J. Faist, C. Gmachl, F. Capasso, C. Sirtori, D. L. Sivco, J. N. Baillargeon, and A. Y. Cho. "Distributed feedback quantum cascade lasers". *Applied Physics Letters* **70** (1997) p. 2670. doi: 10.1063/1.119208.

[139] C. Gmachl, D. L. Sivco, J. N. Baillargeon, A. L. Hutchinson, F. Capasso, and A. Y. Cho. "Quantum cascade lasers with a heterogeneous cascade: Two-wavelength operation". *Applied Physics Letters* **79** (2001) p. 572. doi: 10.1063/1.1383806.

[140] A. Kosterev, G. Wysocki, Y. Bakhirkin, S. So, R. Lewicki, M. Fraser, F. Tittel, and R. Curl. "Application of quantum cascade lasers to trace gas analysis". *Applied Physics B* **90** (2007) pp. 165–176. doi: 10.1007/s00340-007-2846-9.

[141] M. Brandstetter, L. Volgger, A. Genner, C. Jungbauer, and B. Lendl. "Direct determination of glucose, lactate and triglycerides in blood serum by a tunable quantum cascade laser-based mid-IR sensor". *Applied Physics B* **110** (2012) pp. 233–239. doi: 10.1007/s00340-012-5080-z.

[142] H. Schneider, C. Schönbein, M. Walther, K. Schwarz, J. Fleissner, and P. Koidl. "Photovoltaic quantum well infrared photodetectors: The four-zone scheme". *Applied Physics Letters* **71** (1997) p. 246. doi: 10.1063/1.119510.

[143] C. Gmachl, F. Capasso, D. L. Sivco, and A. Y. Cho. "Recent progress in quantum cascade lasers and applications". *Reports on Progress in Physics* **64** (2001) pp. 1533–1601. doi: 10.1088/0034-4885/64/11/204.

[144] C. Schwarzer. "Advanced Quantum Cascade Ring Lasers". PhD thesis. Institut of Solid State Electronics, TU Wien, Vienna, Austria, 2014.

[145] H. Krömer. *Quantum Mechanics For Engineering, Material Science and Applied Science*. Prentice hall, 1994.

[146] S. S. Howard, Z. Liu, D. Wasserman, A. J. Hoffman, T. S. Ko, and C. F. Gmachl. "High-Performance Quantum Cascade Lasers: Optimized Design Through Waveguide and Thermal Modeling". *IEEE Journal of Selected Topics Quantum Electronics* **13** (2007) pp. 1054–1064. doi: 10.1109/jstqe.2007.906121.

[147] A. Wittmann, T. Gresch, E. Gini, L. Hvozdara, N. Hoyler, M. Giovannini, and J. Faist. "High-Performance Bound-to-Continuum Quantum-Cascade Lasers for Broad-Gain Applications". *IEEE Journal of Quantum Electronics* **44** (2008) pp. 36–40. doi: 10.1109/jqe.2007.909516.

[148] J. Faist, F. Capasso, C. Sirtori, D. L. Sivco, J. N. Baillargeon, A. L. Hutchinson, S.-N. G. Chu, and A. Y. Cho. "High power mid-infrared ($\lambda \sim 5\,\mu m$) quantum cascade lasers operating above room temperature". *Applied Physics Letters* **68** (1996) p. 3680. doi: 10.1063/1.115741.

[149] J. Faist, M. Beck, T. Aellen, and E. Gini. "Quantum-cascade lasers based on a bound-to-continuum transition". *Applied Physics Letters* **78** (2001) p. 147. doi: 10.1063/1.1339843.

[150] G. Scamarcio. "High-Power Infrared (8-Micrometer Wavelength) Superlattice Lasers". *Science* **276** (1997) pp. 773–776. doi: 10.1126/science.276.5313.773.

[151] F. Capasso, A. Tredicucci, C. Gmachl, D. Sivco, A. Hutchinson, A. Cho, and G. Scamarcio. "High-performance superlattice quantum cascade lasers". *IEEE Journal of Selected Topics Quantum Electronics* **5** (1999) pp. 792–807. doi: 10.1109/2944.788453.

[152] Y. Yao, X. Wang, J.-Y. Fan, and C. F. Gmachl. "High performance "continuum-to-continuum" quantum cascade lasers with a broad gain bandwidth of over 400 cm[sup -1]". *Applied Physics Letters* **97** (2010) p. 081115. doi: 10.1063/1.3484279.

[153] M. Graf, G. Scalari, D. Hofstetter, J. Faist, H. Beere, E. Linfield, D. Ritchie, and G. Davies. "Terahertz range quantum well infrared photodetector". *Applied Physics Letters* **84** (2004) p. 475. doi: 10.1063/1.1641165.

[154] L. Gendron, C. Koeniguer, V. Berger, and X. Marcadet. "High resistance narrow band quantum cascade photodetectors". *Applied Physics Letters* **86** (2005) p. 121116. doi: 10.1063/1.1884257.

[155] F. R. Giorgetta, E. Baumann, M. Graf, Q. Yang, C. Manz, K. Kohler, H. E. Beere, D. A. Ritchie, E. Linfield, A. G. Davies, Y. Fedoryshyn, H. Jackel, M. Fischer, J. Faist, and D. Hofstetter. "Quantum Cascade Detectors". *IEEE Journal of Quantum Electronics* **45** (2009) pp. 1039–1052. doi: 10.1109/jqe.2009.2017929.

[156] F. R. Giorgetta, E. Baumann, D. Hofstetter, C. Manz, Q. Yang, K. Köhler, and M. Graf. "InGaAs/AlAsSb quantum cascade detectors operating in the near infrared". *Applied Physics Letters* **91** (2007) p. 111115. doi: 10.1063/1.2784289.

[157] S. Sakr, E. Giraud, A. Dussaigne, M. Tchernycheva, N. Grandjean, and F. H. Julien. "Two-color GaN/AlGaN quantum cascade detector at short infrared wavelengths of 1 and 1.7 µm". *Applied Physics Letters* **100** (2012) p. 181103. doi: 10.1063/1.4707904.

[158] P. Reininger, T. Zederbauer, B. Schwarz, H. Detz, D. MacFarland, A. M. Andrews, W. Schrenk, and G. Strasser. "InAs/AlAsSb based quantum cascade detector". *Applied Physics Letters* **107** (2015) p. 081107. doi: 10.1063/1.4929501.

[159] A. Gomez, N. Péré-Laperne, L.-A. de Vaulchier, C. Koeniguer, A. Vasanelli, A. Nedelcu, X. Marcadet, Y. Guldner, and V. Berger. "Dark current analysis of quantum cascade detectors by magnetoresistance measurements". *Physical Review B* **77**, 8 (2008). doi: 10.1103/physrevb.77.085307.

[160] A. Harrer. "Resonance Tuning of Photonic Crystal Intersubband Detectors". Diploma thesis. Institut of Solid State Electronics, TU Wien, Vienna, Austria, 2013.

[161] F. Giorgetta. "Design, fabrication, and testing of intersubband infrared photodetectors operating at wavelengths between 2 µm and 17 µm". PhD thesis. Faculté des Sciences de l'Université de Neuchâtel, Neuchâtel, Switzerland, 2007.

[162] P. Reininger, B. Schwarz, R. Gansch, H. Detz, D. MacFarland, T. Zederbauer, A. M. Andrews, W. Schrenk, and G. Strasser. "Quantum cascade detector utilizing the diagonal-transition scheme for high quality cavities". *Optics Express* **23** (2015) p. 6283. doi: 10.1364/oe.23.006283.

[163] P. Reininger. "Quantum Cascade Photodetectors: Combining Optical and Electronic Engineering". PhD thesis. Institut of Solid State Electronics, TU Wien, Vienna, Austria, 2015.

[164] J. B. Johnson. "Thermal Agitation of Electricity in Conductors". *Physical Review* **32** (1928) pp. 97–109. doi: 10.1103/physrev.32.97.

[165] H. Nyquist. "Thermal Agitation of Electric Charge in Conductors". *Physical Review* **32** (1928) pp. 110–113. doi: 10.1103/physrev.32.110.

[166] C. Koeniguer, G. Dubois, A. Gomez, and V. Berger. "Electronic transport in quantum cascade structures at equilibrium". *Physical Review B* **74**, 23 (2006). doi: 10.1103/physrevb.74.235325.

[167] A. Delga, L. Doyennette, M. Carras, V. Trinité, and P. Bois. "Johnson and shot noises in intersubband detectors". *Applied Physics Letters* **102** (2013) p. 163507. doi: 10.1063/1.4803447.

[168] D. Hofstetter, F. R. Giorgetta, E. Baumann, Q. Yang, C. Manz, and K. Köhler. "Midinfrared quantum cascade detector with a spectrally broad response". *Applied Physics Letters* **93** (2008) p. 221106. doi: 10.1063/1.3036897.

[169] A. Harrer, B. Schwarz, R. Gansch, P. Reininger, H. Detz, T. Zederbauer, A. M. Andrews, W. Schrenk, and G. Strasser. "Plasmonic lens enhanced mid-infrared quantum cascade detector". *Applied Physics Letters* **105** (2014) p. 171112. doi: 10.1063/1.4901043.

[170] M. Beck, J. Faist, U. Oesterle, M. Ilegems, E. Gini, and H. Melchior. "Buried heterostructure quantum cascade lasers with a large optical cavity waveguide". *IEEE Photonics Technology Letters* **12** (2000) pp. 1450–1452. doi: 10.1109/68.887653.

[171] C. Sirtori, J. Faist, F. Capasso, D. L. Sivco, A. L. Hutchinson, and A. Y. Cho. "Quantum cascade laser with plasmon-enhanced waveguide operating at 8.4 μm wavelength". *Applied Physics Letters* **66** (1995) p. 3242. doi: 10.1063/1.113391.

[172] Comsol Inc. *COMSOL Multiphysics®*. web link.

[173] S. Ahn, C. Schwarzer, T. Zederbauer, H. Detz, A. M. Andrews, W. Schrenk, and G. Strasser. "Enhanced light output power of quantum cascade lasers from a tilted front facet". *Optics Express* **21** (2013) p. 15869. doi: 10.1364/oe.21.015869.

[174] I. Tsukerman. *Plasmonics and plasmonic metamaterials analysis and applications*. Hackensack, N.J: World Scientific, 2012. ISBN: 9789814355285.

[175] K. A. Willets and R. P. V. Duyne. "Localized Surface Plasmon Resonance Spectroscopy and Sensing". *Annual Review of Physical Chemistry* **58** (2007) pp. 267–297. doi: 10.1146/annurev.physchem.58.032806.104607.

[176] A. G. Brolo. "Plasmonics for future biosensors". *Nature Photonics* **6** (2012) pp. 709–713. doi: 10.1038/nphoton.2012.266.

[177] S. Kawata, Y. Inouye, and P. Verma. "Plasmonics for near-field nano-imaging and superlensing". *Nature Photonics* **3** (2009) pp. 388–394. doi: 10.1038/nphoton.2009.111.

[178] E. Ozbay. "Plasmonics: Merging Photonics and Electronics at Nanoscale Dimensions". *Science* **311** (2006) pp. 189–193. doi: 10.1126/science.1114849.

[179] R. Stanley. "Plasmonics in the mid-infrared". *Nature Photonics* **6** (2012) pp. 409–411. doi: 10.1038/nphoton.2012.161.

[180] *FP7 project PLASmonic Innovative Sensing in the IR*. 2015. web link.

[181] S. A. Maier. *Plasmonics: fundamentals and applications*. Springer US, 2007. ISBN: 9780387331508. doi: 10.1007/0-387-37825-1.

[182] J. C. M. Garnett. "Colours in Metal Glasses and in Metallic Films". *Philosophical Transactions of the Royal Society of London A: Mathematical, Physical and Engineering Sciences* **203** (1904) pp. 385–420. doi: 10.1098/rsta.1904.0024.

[183] G. Mie. "Beiträge zur Optik trüber Medien, speziell kolloidaler Metallösungen". *Annalen der Physik* **330** (1908) pp. 377–445. doi: 10.1002/andp.19083300302.

[184] S. Hayashi and T. Okamoto. "Plasmonics: visit the past to know the future". *Journal of Physics D: Applied Physics* **45** (2012) p. 433001. doi: 10.1088/0022-3727/45/43/433001.

[185] C. F. Bohren and D. R. Huffman. *Absorption and Scattering of Light by Small Particles*. Wiley-VCH Verlag GmbH, 2007. ISBN: 9783527618156. doi: 10.1002/9783527618156.fmatter.

[186] S Pillai, K. Catchpole, T Trupke, and M. Green. "Surface plasmon enhanced silicon solar cells". *Journal of Applied Physics* **101** (2007) p. 093105. doi: 10.1063/1.2734885.

[187] K. M. Mayer and J. H. Hafner. "Localized surface plasmon resonance sensors". *Chemical reviews* **111** (2011) pp. 3828–3857. doi: 10.1021/cr100313v.

[188] T. W. Ebbesen, H. J. Lezec, H. F. Ghaemi, T. Thio, and P. A. Wolff. "Extraordinary optical transmission through sub-wavelength hole arrays". *Nature* **391** (1998) pp. 667–669. doi: 10.1038/35570.

[189] D. Fleisch. *A Student's Guide to Maxwell's Equations*. Cambridge University Press (CUP), 2008. doi: 10.1017/cbo9780511984624.

[190] M. A. Ordal, R. J. Bell, J. Ralph W. Alexander, L. L. Long, and M. R. Querry. "Optical properties of Au, Ni, and Pb at submillimeter wavelengths". *Applied Optics* **26** (1987) p. 744. doi: 10.1364/ao.26.000744.

[191] R. L. Olmon, B. Slovick, T. W. Johnson, D. Shelton, S.-H. Oh, G. D. Boreman, and M. B. Raschke. "Optical dielectric function of gold". *Physical Review B* **86**, 23 (2012). doi: 10.1103/physrevb.86.235147.

[192] S. Babar and J. H. Weaver. "Optical constants of Cu, Ag, and Au revisited". *Applied Optics* **54** (2015) p. 477. doi: 10.1364/ao.54.000477.

[193] G. A. Reider. *Photonik*. Springer Science + Business Media, 2005. doi: 10.1007/b138741.

[194] S. Law, V. Podolskiy, and D. Wasserman. "Towards nano-scale photonics with micro-scale photons: the opportunities and challenges of mid-infrared plasmonics". *Nanophotonics* **2**, 2 (2013). doi: 10.1515/nanoph-2012-0027.

[195] N. Yu, J. Fan, Q. J. Wang, C. Pflügl, L. Diehl, T. Edamura, M. Yamanishi, H. Kan, and F. Capasso. "Small-divergence semiconductor lasers by plasmonic collimation". *Nature Photonics* **2** (2008) pp. 564–570. doi: 10.1038/nphoton.2008.152.

[196] Z. Yu, G. Veronis, S. Fan, and M. L. Brongersma. "Design of midinfrared photodetectors enhanced by surface plasmons on grating structures". *Applied Physics Letters* **89** (2006) p. 151116. doi: 10.1063/1.2360896.

[197] J. Homola, S. S. Yee, and G. Gauglitz. "Surface plasmon resonance sensors: review". *Sensors and Actuators B: Chemical* **54** (1999) pp. 3–15. doi: 10.1016/s0925-4005(98)00321-9.

[198] M. Schnell, P. Alonso-González, L. Arzubiaga, F. Casanova, L. E. Hueso, A. Chuvilin, and R. Hillenbrand. "Nanofocusing of mid-infrared energy with tapered transmission lines". *Nature Photonics* **5** (2011) pp. 283–287. doi: 10.1038/nphoton.2011.33.

[199] J. B. Pendry. "Mimicking Surface Plasmons with Structured Surfaces". *Science* **305** (2004) pp. 847–848. doi: 10.1126/science.1098999.

[200] N. Yu, Q. J. Wang, M. A. Kats, J. A. Fan, S. P. Khanna, L. Li, A. G. Davies, E. H. Linfield, and F. Capasso. "Designer spoof surface plasmon structures collimate terahertz laser beams". *Nature Materials* **9** (2010) pp. 730–735. doi: 10.1038/nmat2822.

[201] A. Rusina, M. Durach, and M. I. Stockman. "Theory of spoof plasmons in real metals". *Applied Physics A* **100** (2010) pp. 375–378. doi: 10.1007/s00339-010-5866-y.

[202] B. N. III, D. Korobkin, C. Fietz, D. Carole, G. Ferro, and G. Shvets. "Critically coupled surface phonon-polariton excitation in silicon carbide". *Optics Letters* **34** (2009) p. 2667. doi: 10.1364/ol.34.002667.

[203] R. Hillenbrand, T. Taubner, and F. Keilmann. "Phonon-enhanced light–matter interaction at the nanometre scale". *Nature* **418** (2002) pp. 159–162. doi: 10.1038/nature00899.

[204] K. S. Novoselov, A. K. Geim, S. V. Morozov, D. Jiang, M. I. Katsnelson, I. V. Grigorieva, S. V. Dubonos, and A. A. Firsov. "Two-dimensional gas of massless Dirac fermions in graphene". *Nature* **438** (2005) pp. 197–200. doi: 10.1038/nature04233.

[205] M. Jablan, H. Buljan, and M. Soljačić. "Plasmonics in graphene at infrared frequencies". *Physical Review B* **80**, 24 (2009). doi: 10.1103/physrevb.80.245435.

[206] F. H. L. Koppens, D. E. Chang, and F. J. G. de Abajo. "Graphene Plasmonics: A Platform for Strong Light–Matter Interactions". *Nano Letters* **11** (2011) pp. 3370–3377. doi: 10.1021/nl201771h.

[207] A. N. Grigorenko, M. Polini, and K. S. Novoselov. "Graphene plasmonics". *Nature Photonics* **6** (2012) pp. 749–758. doi: 10.1038/nphoton.2012.262.

[208] F Marquier, K Joulain, J. Mulet, R Carminati, and J. Greffet. "Engineering infrared emission properties of silicon in the near field and the far field". *Optics Communications* **237** (2004) pp. 379–388. doi: 10.1016/j.optcom.2004.04.024.

[209] J. C. Ginn, R. L. Jarecki, E. A. Shaner, and P. S. Davids. "Infrared plasmons on heavily-doped silicon". *Journal of Applied Physics* **110** (2011) p. 043110. doi: 10.1063/1.3626050.

[210] D. Li and C. Z. Ning. "All-semiconductor active plasmonic system in mid-infrared wavelengths". *Optics Express* **19** (2011) p. 14594. doi: 10.1364/oe.19.014594.

[211] S. Law, D. C. Adams, A. M. Taylor, and D. Wasserman. "Mid-infrared designer metals". *Optics Express* **20** (2012) p. 12155. doi: 10.1364/oe.20.012155.

[212] B. Steinberger, A. Hohenau, H. Ditlbacher, A. L. Stepanov, A. Drezet, F. R. Aussenegg, A. Leitner, and J. R. Krenn. "Dielectric stripes on gold as surface plasmon waveguides". *Applied Physics Letters* **88** (2006) p. 094104. doi: 10.1063/1.2180448.

[213] T. Holmgaard and S. Bozhevolnyi. "Theoretical analysis of dielectric-loaded surface plasmon-polariton waveguides". *Physical Review B* **75**, 24 (2007). doi: 10.1103/physrevb.75.245405.

[214] M. A. Ordal, L. L. Long, R. J. Bell, S. E. Bell, R. R. Bell, J. R. W. Alexander, and C. A. Ward. "Optical properties of the metals Al, Co, Cu, Au, Fe, Pb, Ni, Pd, Pt, Ag, Ti, and W in the infrared and far infrared". *Applied Optics* **22** (1983) p. 1099. doi: 10.1364/ao.22.001099.

[215] E. Kretschmann and H. Raether. "Notizen: Radiative Decay of Non Radiative Surface Plasmons Excited by Light". *Zeitschrift für Naturforschung A* **23**, 12 (1968). doi: 10.1515/zna-1968-1247.

[216] A. Otto. "Excitation of nonradiative surface plasma waves in silver by the method of frustrated total reflection". *Zeitschrift für Physik* **216** (1968) pp. 398–410. doi: 10.1007/bf01391532.

[217] B. Hecht, H. Bielefeldt, L. Novotny, Y. Inouye, and D. W. Pohl. "Local Excitation, Scattering, and Interference of Surface Plasmons". *Physical Review Letters* **77** (1996) pp. 1889–1892. doi: 10.1103/physrevLetters77.1889.

[218] J.-P. Tetienne, A. Bousseksou, D. Costantini, R. Colombelli, A. Babuty, I. Moldovan-Doyen, Y. D. Wilde, C. Sirtori, G. Beaudoin, L. Largeau, O. Mauguin, and I. Sagnes. "Injection of midinfrared surface plasmon polaritons with an integrated device". *Applied Physics Letters* **97** (2010) p. 211110. doi: 10.1063/1.3519985.

[219] E. A. Ash and G. Nicholls. "Super-resolution Aperture Scanning Microscope". *Nature* **237** (1972) pp. 510–512. doi: 10.1038/237510a0.

[220] F. Keilmann and R. Hillenbrand. "Near-field microscopy by elastic light scattering from a tip". *Philosophical Transactions of the Royal Society A: Mathematical, Physical and Engineering Sciences* **362** (2004) pp. 787–805. doi: 10.1098/rsta.2003.1347.

[221] E. Betzig, J. K. Trautman, T. D. Harris, J. S. Weiner, and R. L. Kostelak. "Breaking the Diffraction Barrier: Optical Microscopy on a Nanometric Scale". *Science* **251** (1991) pp. 1468–1470. doi: 10.1126/science.251.5000.1468.

[222] B. Knoll and F. Keilmann. "Near-field probing of vibrational absorption for chemical microscopy". *Nature* **399** (1999) pp. 134–137. doi: 10.1038/20154.

[223] N. M. Jokerst, L. Luan, S. Palit, M. Royal, S. Dhar, M. A. Brooke, and T. Tyler. "Progress in chip-scale photonic sensing". *IEEE Transactions on Biomedical Circuits and Systems* **3** (2009) pp. 202–211. doi: 10.1109/TBCAS.2009.2020693.

[224] J. E. Bertie and Z. Lan. "Infrared Intensities of Liquids XX: The Intensity of the OH Stretching Band of Liquid Water Revisited, and the Best Current Values of the Optical Constants of H_2O(l) at 25°C between 15,000 and 1 cm^{-1}". *Applied Spectroscopy* **50** (1996) pp. 1047–1057. doi: 10.1366/0003702963905385.

[225] J. Kischkat, S. Peters, B. Gruska, M. Semtsiv, M. Chashnikova, M. Klinkmüller, O. Fedosenko, S. Machulik, A. Aleksandrova, G. Monastyrskyi, Y. Flores, and W. T. Masselink. "Mid-infrared optical properties of thin films of aluminum oxide, titanium dioxide, silicon dioxide, aluminum nitride, and silicon nitride". *Applied Optics* **51** (2012) p. 6789. doi: 10.1364/ao.51.006789.

[226] A. A. Kosterev, F. K. Tittel, R. Köhler, C. Gmachl, F. Capasso, D. L. Sivco, A. Y. Cho, S. Wehe, and M. G. Allen. "Thermoelectrically Cooled Quantum-Cascade-Laser-Based Sensor for the Continuous Monitoring of Ambient Atmospheric Carbon Monoxide". *Applied Optics* **41** (2002) p. 1169. doi: 10.1364/ao.41.001169.

[227] D. Ristanic, B. Schwarz, P. Reininger, H. Detz, T. Zederbauer, A. M. Andrews, W. Schrenk, and G. Strasser. "Monolithically integrated mid-infrared sensor using narrow mode operation and temperature feedback". *Applied Physics Letters* **106** (2015) p. 041101. doi: 10.1063/1.4906802.

[228] *QuantaRed Technologies*. web link (visited on 11/06/2015).

[229] S. Kalchmair. "Photonic Crystal Intersubband Photodetectors". PhD thesis. Institut of Solid State Electronics, TU Wien, Vienna, Austria, 2012.

Abbreviations

Symbol	Meaning
AFM	Atomic force microscope
AR	Active region
CPU	Central processing unit
DC	Direct current
DFB	Distributed feedback
DL-SPP	Dielectric loaded surface plasmon polariton
DOS	Density of states
DTGS	Deuterated triglycine sulfate
DWELL	Dots in a well
FP	Fabry Perót
FTIR	Fourier transform infrared
ICL	Interband cascade laser
ICP	Inductively coupled plasma
ISB	Intersubband
LIV	Light current voltage
LO	Longitudinal optical
LSP	Localized surface plasmon
MBE	Molecular beam epitaxy
MCT	Mercury cadmium telluride (HgCdTe)
MIR	Mid-infrared
NEGF	Non equilibrium Green's functions
NEP	Noise equivalent power
NETD	Noise equivalent temperature difference
PECVD	Plasma enhanced chemical vapor deposition
QCD	Quantum cascade detector
QCL	Quantum cascade laser
QCLD	Quantum cascade laser and detector
QWIP	Quantum well infrared photodetector
RF	Radio frequency
RIE	Reactive ion etching

SEM	Scanning electron microscope
SNOM	Scanning near-field optical microscope
SPP	Surface plasmon polariton
TE	Transverse electric
TEM	Transverse electromagnetic or tunneling electron microscope
TM	Transverse magnetic
VSP	Vienna Schrödinger Poisson

Notation

Symbol	Meaning
∂_t, $\frac{d}{dt}$	time derivative
$\vec{\nabla}$	Nabla operator
$\vec{\nabla}\cdot$	divergence
$\vec{\nabla}\times$	rotation
h, $\hbar$	Planck constant ($h = 6.62607004 \times 10^{-34}$ J/s, $\hbar = \frac{h}{2\pi}$))
c	speed of light in vacuum (2.99792458×10^{8} m/s)
$\mathrm{k_B}$	Boltzmann constant ($1.3806503 \times 10^{-23}$ J/K)
e	elementary charge ($1.602176487 \cdot 10^{-19}$C)
m_0	Electron mass ($9.10938356 \times 10^{-31}$ kg)
ε_0	dielectric permittivity of vacuum ($8.854187817 \times 10^{-12}$ F/m)
μ_0	magnetic permeability of vacuum ($4\pi \times 10^{-7}$ H/m)
T	temperature
f	frequency
$\tilde{\nu}$	wavenumber
$\hat{H}$	Hamiltonian
$\hat{H}_0$	Unperturbed Hamiltonian
$\hat{W}$, $\hat{H}_{\mathrm{int}}$	Perturbation Hamiltonian
$m*$	Effective electron mass
m_c^*	Effective electron mass at conduction band edge
$m_c^*(E)$	Effective electron mass of conduction band
p_{cm}	Interband matrix element between bands c and m
V	Background potential
$\vec{r}$	Spacial vector
$\vec{k}$ $\psi(\vec{k}, \vec{r})$	Wavefunction
$u(\vec{k}, \vec{r})$	Bloch function
$f(\vec{r})$	Envelope wave function
E_{c}, E_{v}	conductance/valence band-edge energy at k=0
$E_{\mathrm{c}}(\vec{k})$, $E_{\mathrm{v}}(\vec{k})$	k-dependent conductance/valence band-edge energy

Δ_{so}	spin-orbit splitting energy
E_{g}	band gap energy
E_{p}	Kane energy
F	Kane parameter
γ	non-parabolicity coefficient
W_{if}	Scattering rate from initial to final state
E_{i}, E_{f}	Energy of initial and final state
k_{i}, k_{f}	In-plane momentum of initial and final state
δE	Energy of scattering mechanism
$E_{\mathrm{LO}} = \hbar\omega_{\mathrm{LO}}$	Longitudinal optical phonon energy
e_x, e_y, e_z	polarization vectrors
t_{if}	optical dipole matrix element between state i and f
δ	Dirac function
Γ	Line shape or mode confinement factor
α	optical absorption coefficient
σ	electric conductivity or standard deviation
σ_{g}	optical gain cross section
N_{D}	donor impurity concentration
n	electron concentration or electron sheet concentration
n, n_{r}	optical refractive index
a_{w}, a_{b}	lattice constants of the well and barrier materials
$a_{\|\|}$, $a_{\perp}$	in-plane and perpendicular lattice constants
G_{w}, G_{b}	shear modulus of the well and barrier materials
$\epsilon_{\|\|}$, $\epsilon_{\perp}$	in-plane and perpendicular strain
c_{11}, c_{12}	elastic constants
δE_{c}, δE_{v}	effect of strain onto the conduction and valence band-edge energy
τ_i	lifetime of state i
τ_{if}	scattering time from state i to f
τ_{eff}	effective scattering time of a 3-level system
η_{inj}	injection efficiency
I_z	light intensity with polarization in growth direction
L_{p}	length of one active region period
N_{p}	number of active region periods
g	optical gain coefficient
g_0	unsaturated optical gain coefficient
I_{sat}	gain saturation intensity
J	electric current density
J_{tran}, J_{th}, J_{rad}	transparency, threshold and radiative current density
α_{tot}, α_{w}, α_{m}	total, waveguide and mirror loss of the laser cavity

η_{slope}, η_{wp}	slope and wallplug efficiency of a laser
η_{int}, η_{ext}	internal and external quantum efficiency of a detector
η_{abs}, p_{e}	absorption and extraction efficiency of a detector
α_{isb}	absorption due to intersubband transitions
$\mathcal{R}$	responsivity
T_{facet}	facet transmittivity
R_{AR}, R_{cont}	resistance of the active region and the contact
i_{n}	root mean square of current noise
NEP	noise equivalent power
D^*_{J}	Johnson/thermal noise limited specific detectivity
Δf	bandwidth
D^*_{BL}	background limited specific detectivity
P_{B}	optical power of background radiation
$NETD$	noise equivalent temperature difference
$\vec{E}$	electric field intensity
$\vec{D}$	electric flux density
ϱ	electric charge density
$\vec{H}$	magnetic field intensity
$\vec{B}$	magnetic flux density
$\vec{A}$	electric vector potential
ε	dielectric permittivity (isotropic)
ε_∞	high frequency dielectric permittivity
ε_r	relative dielectric permittivity (isotropic)
μ	magnetic permeability (isotropic) or mobility
ω_{p}	plasma frequency
β	propagation constant
Δc	limit of detection for chemical sensors
L_{eff}	effective absorption length

List of publications

Peer-reviewed publications

[1] P. Reininger, T. Zederbauer, B. Schwarz, H. Detz, D. MacFarland, A. M. Andrews, W. Schrenk, and G. Strasser. "InAs/AlAsSb based quantum cascade detector". *Applied Physics Letters* **107** (2015) p. 081107. doi: 10.1063/1.4929501.

[2] B. Schwarz, D. Ristanic, P. Reininger, T. Zederbauer, D. MacFarland, H. Detz, A. M. Andrews, W. Schrenk, and G. Strasser. "High performance bi-functional quantum cascade laser and detector". *Applied Physics Letters* **107** (2015) p. 071104. doi: 10.1063/1.4927851.

[3] **(invited)** P. Reininger, B. Schwarz, R. Gansch, H. Detz, D. MacFarland, T. Zederbauer, A. M. Andrews, W. Schrenk, and G. Strasser. "Quantum cascade detector utilizing the diagonal-transition scheme for high quality cavities". *Optics Express* **23** (2015) p. 6283. doi: 10.1364/oe.23.006283.

[4] D. Ristanic, B. Schwarz, P. Reininger, H. Detz, T. Zederbauer, A. M. Andrews, W. Schrenk, and G. Strasser. "Monolithically integrated mid-infrared sensor using narrow mode operation and temperature feedback". *Applied Physics Letters* **106** (2015) p. 041101. doi: 10.1063/1.4906802.

[5] A. Harrer, B. Schwarz, R. Gansch, P. Reininger, H. Detz, T. Zederbauer, A. M. Andrews, W. Schrenk, and G. Strasser. "Plasmonic lens enhanced mid-infrared quantum cascade detector". *Applied Physics Letters* **105** (2014) p. 171112. doi: 10.1063/1.4901043.

[6] P. Reininger, B. Schwarz, H. Detz, D. MacFarland, T. Zederbauer, A. M. Andrews, W. Schrenk, O. Baumgartner, H. Kosina, and G. Strasser. "Diagonal-transition quantum cascade detector". *Applied Physics Letters* **105** (2014) p. 091108. doi: 10.1063/1.4894767.

[7] B. Schwarz, P. Reininger, D. Ristanić, H. Detz, A. M. Andrews, W. Schrenk, and G. Strasser. "Monolithically integrated mid-infrared lab-on-a-chip using plasmonics and quantum cascade structures". *Nature Communications* **5**, 4085 (2014). doi: 10.1038/ncomms5085.

[8] P. Reininger, B. Schwarz, A. Harrer, T. Zederbauer, H. Detz, A. M. Andrews, R. Gansch, W. Schrenk, and G. Strasser. "Photonic crystal slab quantum cascade detector". *Applied Physics Letters* **103** (2013) p. 241103. doi: 10.1063/1.4846035.

[9] B. Schwarz, P. Reininger, H. Detz, T. Zederbauer, A. Andrews, W. Schrenk, and G. Strasser. "Monolithically Integrated Mid-Infrared Quantum Cascade Laser and Detector". *Sensors* **13** (2013) pp. 2196–2205. doi: 10.3390/s130202196.

[10] B. Schwarz, P. Reininger, H. Detz, T. Zederbauer, A. M. Andrews, S. Kalchmair, W. Schrenk, O. Baumgartner, H. Kosina, and G. Strasser. "A bi-functional quantum cascade device for same-frequency lasing and detection". *Applied Physics Letters* **101** (2012) p. 191109. doi: 10.1063/1.4767128.

[11] J. Franco, B. Kaczer, M. Toledano-Luque, P. Roussel, G. Groeseneken, B. Schwarz, M. Bina, M. Waltl, P.-J. Wagner, and T. Grasser. "Reduction of the BTI Time-Dependent Variability in Nanoscaled MOSFETs by Body Bias". *Proceedings of International Reliability Physics Symposium (IRPS 2013)*. IEEE. 2013 p. 2D.3. doi: 10.1109/IRPS.2013.6531958.

[12] M. Bina, O. Triebl, B. Schwarz, M. Karner, B. Kaczer, and T. Grasser. "Simulation of Reliability on Nanoscale Devices". *Proceedings of the 17th International Conference on Simulation of Semiconductor Processes and Devices (SISPAD 2012)*. IEEE. 2012 pp. 109–112. web link.

[13] B. Kaczer, J. Franco, M. Toledano-Luque, P. Roussel, M. F. Bukhori, A. Asenov, B. Schwarz, M. Bina, T. Grasser, and G. Groeseneken. "The relevance of deeply-scaled FET threshold voltage shifts for operation lifetimes". *Proceedings of International Reliability Physics Symposium (IRPS 2012)*. IEEE. 2012 5A–2. doi: 10.1109/IRPS.2012.6241839.

Other publications

[1] B. Schwarz, P. Reininger, H. Detz, and G. Strasser. "Integrierte Flüssigkeitssensoren für Vor-Ort-Analysen". *Labor Praxis, reprint Special Issue: Mikro Fluidik*, (August 2014 and Mai 2015). web link.

Seminar presentation

[1] **(invited)** Benedikt Schwarz. "Monolithic integration of mid-infrared photonics". Massachusetts Institute of Technology, Lincoln Laboratory, USA; 2015-04-29. Massachusetts, USA. 2015.

Oral conference presentation

[1] **(accepted, invited)** P. Reininger, T. Zederbauer, B. Schwarz, H. Detz, D. MacFarland, A. M. Andrews, W. Schrenk, and G. Strasser. "A low effective mass material system for quantum cascade detectors". SPIE Photonics West, San Francisco; 2013-02-13 – 2013-02-18. 2016.

[2] **(accepted)** T. S. Mansuripur, C. Vernet, G. Aoust, B. Schwarz, Y. Wang, A. A. Belyanin, and F. Capasso. "Single-mode to multimode transition in quantum cascade lasers caused by the dynamic Stark effect". SPIE Photonics West, San Francisco; 2013-02-13 – 2013-02-18. 2016.

[3] **(accepted)** A. Harrer, B. Schwarz, P. Reininger, R. Szedlak, T. Zederbauer, H. Detz, D. MacFarland, A. M. Andrews, W. Schrenk, and G. Strasser. "An optimized bi-functional material for integrated mid-infrared quantum cascade based sensors". SPIE Photonics West, San Francisco; 2013-02-13 – 2013-02-18. 2016.

[4] B. Schwarz, A. Harrer, D. Ristanic, P. Reininger, H. Detz, T. Zederbauer, A. M. Andrews, W. Schrenk, and G. Strasser. "Bi-functional quantum cascade laser/detectors: From design to applications". International Conference on Intersubband Transitions in Quantum Wells (ITQW), Vienna, Austria; 2015-09-06 – 2015-09-11. 2015.

[5] P. Reininger, T. Zederbauer, B. Schwarz, H. Detz, D. MacFarland, A. M. Andrews, W. Schrenk, and G. Strasser. "InAs/AlAsSb for quantum cascade detectors". International Conference on Intersubband Transitions in Quantum Wells (ITQW), Vienna, Austria; 2015-09-06 – 2015-09-11. 2015.

[6] A. Harrer, B. Schwarz, R. Szedlak, J. P. Waclawek, H. Moser, D. MacFarland, T. Zederbauer, H. Detz, A. M. Andrews, W. Schrenk, B. Lendl, and G. Strasser. "A bi-functional surface emitting and detecting mid-infrared device for sensing applications". ÖPG-Jahrestagung, Wien; 2015-09-01 – 2015-09-04. 2015.

[7] **(invited)** G. Strasser, D. Ristanic, B. Schwarz, P. Reininger, H. Detz, A. M. Andrews, T. Zederbauer, D. MacFarland, and W. Schrenk. "A Mid-Infrared On-Chip Sensor Array Based on Bi-functional Quantum Cascade Structures and Plasmonics". ICAVS8, Wien; 2015-07-12 – 2015-07-17. 2015.

[8] A. Harrer, P. Reininger, R. Gansch, B. Schwarz, D. MacFarland, T. Zederbauer, H. Detz, A. M. Andrews, W. Schrenk, O. Baumgartner, H. Kosina, and G. Strasser. "Quantum Cascade Detectors for Sensing Applications". ICAVS8, Wien; 2015-07-12 – 2015-07-17. 2015.

[9] A. Harrer, R. Szedlak, M. Holzbauer, B. Schwarz, H. Moser, E. Mujagic, D. MacFarland, T. Zederbauer, H. Detz, A. M. Andrews, W. Schrenk, B. Lendl, and G. Strasser. "Monolithic integrated on-chip sensing utilizing plasmonics". 1st NextLite Workshop, Hirschwang an der Rax; 2015-06-18 – 2015-06-19. 2015.

[10] R. Szedlak, A. Harrer, M. Holzbauer, B. Schwarz, H. Moser, E. Mujagic, C. Deutsch, D. MacFarland, T. Zederbauer, H. Detz, A. M. Andrews, W. Schrenk, K. Unterrainer, B. Lendl, and G. Strasser. "Infrared and terahertz spectroscopy with ring quantum cascade lasers". German THz Conference 2015, Dresden; 2015-06-08 – 2015-06-10. 2015.

[11] D. Ristanic, B. Schwarz, P. Reininger, H. Detz, A. M. Andrews, W. Schrenk, and G. Strasser. "Monolithical Absorption Sensor Array Based on Bi-functional Quantum Cascade Structures". CLEO 2015, San Jose; 2014-05-10 – 2014-05-15. 2015.

[12] B. Schwarz, D. Ristanic, P. Reininger, H. Detz, A. M. Andrews, W. Schrenk, and G. Strasser. "A mid-infrared on-chip sensor based on bi-functional quantum cascade structures and plasmonics". SPIE Photonics West 2015, San Francisco; 2015-02-07 – 2015-02-12. 2015.

[13] P. Reininger, B. S. H. Detz, A. M. Andrews, W. Schrenk, and G. Strasser. "High-responsivity photovoltaic intersubband detectors". SPIE Photonics West 2015, San Francisco; 2015-02-07 – 2015-02-12. 2015.

[14] B. Schwarz, D. Ristanic, P. Reininger, A. Harrer, H. Detz, A. M. Andrews, W. Schrenk, and G. Strasser. "Monolithically integrated chemical sensor based on intersubband transitions and plasmonics". International Quantum Cascade Lasers School & Workshop (IQCLSW 2014), Bari; 2014-09-07 – 2014-09-14. 2014.

[15] P. Reininger, B. Schwarz, A. Harrer, T. Zederbauer, H. Detz, A. M. Andrews, R. Gansch, W. Schrenk, and G. Strasser. "Room temperature quantum cascade detector". International Quantum Cascade Lasers School & Workshop (IQCLSW 2014), Bari; 2014-09-07 – 2014-09-14. 2014.

[16] B. Schwarz, P. Reininger, D. Ristanic, A. M. Andrews, W. Schrenk, and G. Strasser. "Plasmonics and quantum cascade structures for on-chip-sensing". Nanoforum 2014, Linz; 2014-06-01 – 2014-06-24. 2014.

[17] B. Schwarz, D. Ristanic, P. Reininger, H. Detz, A. M. Andrews, W. Schrenk, and G. Strasser. "A mid-infrared Lab-on-a-Chip: Generating, Guiding and Detecting Light in a Monolithic Device". *Laser Science to Photonic Applications*. CLEO 2014, San Jose; 2014-06-08 – 2014-06-13. 2014. ISBN: 978-1-55752-999-2. web link.

[18] **(invited)** B. Schwarz, P. Reininger, D. Ristanic, O. Baumgartner, H. Detz, T. Zederbauer, D. MacFarland, A. M. Andrews, W. Schrenk, H. Kosina, and G. Strasser. "On-Chip mid-infrared light generation and detection". ITQW, New York, USA; 2013-09-15 – 2013-09-20. 2013.

[19] P. Reininger, B. Schwarz, A Wirthmüller, A. Harrer, O. Baumgartner, H. Detz, T. Zederbauer, D. MacFarland, A. M. Andrews, W. Schrenk, L. Hvozdara, H. Kosina, and G. Strasser. "Towards higher temperature operation of quantum cascade detectors". ITQW, New York, USA; 2013-09-15 – 2013-09-20. 2013.

[20] **(invited)** G. Strasser, B. Schwarz, P. Reininger, O. Baumgartner, W. Schrenk, T. Zederbauer, H. Detz, A. M. Andrews, and H. Kosina. "Bi-functional Quantum Cascade Laser/Detectors for Integrated Photonics". ÖPG-Jahrestagung, Linz; 2013-09-02 – 2013-09-06. 2013.

[21] B. Schwarz, P. Reininger, O. Baumgartner, T. Zederbauer, H. Detz, A. M. Andrews, W. Schrenk, H. Kosina, and G. Strasser. "Towards Mid-Infrared On-Chip Sensing utilizing a bi-functional Quantum Cascade Laser/Detector". Conference on Electronic Properties of Two-Dimensional Systems / Modulated Semiconductor Structures (EP2Ds-MSS), Wroclaw, Polen; 2013-07-01 – 2013-07-05. 2013.

[22] B. Schwarz, P. Reininger, W. Schrenk, H. Detz, O. Baumgartner, T. Zederbauer, A. M. Andrews, H. Kosina, and G. Strasser. "Monolithically integrated quantum cascade laser and detector". CLEO Europe 2013, München, Deutschland; 2013-05-12 – 2013-05-16. 2013.

[23] B. Schwarz, P. Reininger, H. Detz, T. Zederbauer, A. M. Andrews, W. Schrenk, O. Baumgartner, H. Kosina, and G. Strasser. "Same-frequency detector and laser utilizing bi-functional quantum cascade active regions". SPIE Photonics West 2013, San Francisco; 2013-02-02 – 2013-02-07. 2013.

[24] B. Schwarz, P. Reininger, O. Baumgartner, Z. Stanojevic, H. Kosina, and G. Strasser. "Optimization of intersubband devices for dual-color emission, absorption and detection". ÖPG-Jahrestagung, Graz; 2012-09-18 – 2012-09-21. 2012.

[25] B. Schwarz, P. Reininger, O. Baumgartner, Z. Stanojevic, H. Kosina, and G. Strasser. "Dual wavelength quantum cascade structure that can act both as laser and detector". MIRTHE-IROn-SensorCAT virtual conference 2012, Princeton; 2012-06-26 – 2012-06-27. 2012.

Poster conference presentation

[1] A. Harrer, R. Szedlak, B. Schwarz, H. Moser, T. Zederbauer, H. Detz, A. M. Andrews, W. Schrenk, B. Lendl, and G. Strasser. "Towards a monolithic integrated surface emitting and detecting mid-infrared gas sensor". ITQW, Wien; 2015-09-06 – 2015-09-11. 2015.

[2] A. Harrer, B. Schwarz, R. Gansch, P. Reininger, H. Detz, T. Zederbauer, A. M. Andrews, W. Schrenk, and G. Strasser. "Mid-infrared detectors with on-chip light collection". International Quantum Cascade Lasers School & Workshop (IQCLSW 2014), Bari; 2014-09-07 – 2014-09-14. 2014.

[3] P. Reininger, B. Schwarz, A. Harrer, T. Zederbauer, H. Detz, A. M. Andrews, R. Gansch, W. Schrenk, and G. Strasser. "2.5 D photonic crystal quantum cascade detector". *Laser Science to Photonic Applications*. CLEO 2014, San Jose; 2014-06-08 – 2014-06-13. 2014. ISBN: 978-1-55752-999-2. web link.

[4] B. Schwarz, P. Reininger, D. Ristanic, H. Detz, T. Zederbauer, D. MacFarland, A. M. Andrews, W. Schrenk, and G. Strasser. "Towards mid-infrared on-chip sensing". *New Developments in Solid State Physics - Mauterndorf 2014*. 18th International Winterschool on New Developments in Solid State Physics, Mauterndorf; 2014-02-23 – 2014-02-28. 2014 pp. 106–107.

[5] A. Harrer, B. Schwarz, R. Gansch, P. Reininger, H. Detz, T. Zederbauer, A. M. Andrews, W. Schrenk, and G. Strasser. "Mid-infrared Plasmonic Lens Intersubband Photodetector". *New Developments in Solid State Physics - Mauterndorf 2014*. 18th International Winterschool on New Developments in Solid State Physics, Mauterndorf; 2014-02-23 – 2014-02-28. 2014 pp. 108–109.

[6] P. Reininger, B. Schwarz, A. Harrer, T. Zederbauer, H. Detz, A. M. Andrews, R. Gansch, W. Schrenk, and G. Strasser. "Photonic crystal quantum cascade detector". *New Developments in Solid State Physics*. 18th International Winterschool on New Developments in Solid State Physics, Mauterndorf; 2014-02-23 – 2014-02-28. 2014 pp. 92–93. web link.

[7] A Wirthmüller, B. Schwarz, P. Reininger, M. Rothermund, H. Oppermann, L. Hvozdara, G. Strasser, and D. Hofstetter. "The ICARUS sensing instrument for QCD-assisted human survivor detection in post-disaster areas". ITQW, New York, USA; 2013-09-15 – 2013-09-20. 2013.

[8] A. Harrer, R. Gansch, P. Reininger, B. Schwarz, H. Detz, A. M. Andrews, T. Zederbauer, D. MacFarland, W. Schrenk, and G. Strasser. "Tuning of resonances in photonic crystal photodetectors". Joint Annual Meeting of ÖPG, SPG, ÖGAA und SGAA 2013, Linz; 2013-09-02 – 2013-09-06. 2013.

[9] B. Schwarz, P. Reininger, O. Baumgartner, Z. Stanojevic, H. Kosina, and G. Strasser. "Dual-color quantum cascade structure for coherent emission and detection". International Quantum Cascade Lasers School & Workshop 2012 (IQCLSW 2012), Baden; 2012-09-02 – 2012-09-06. 2012.

[10] P. Reininger, B. Schwarz, S. Kalchmair, R. Gansch, O. Baumgartner, Z. Stanojevic, H. Kosina, W. Schrenk, and G. Strasser. "Simulation of a dual wavelength quantum cascade laser in a photonic crystal cavity". International Quantum Cascade Lasers School & Workshop 2012 (IQCLSW 2012), Baden; 2012-09-02 – 2012-09-06. 2012.

[11] B. Schwarz, P. Reininger, O. Baumgartner, Z. Stanojevic, H. Kosina, and G. Strasser. "A mid-infrared dual wavelenght quantum cascade structure designed for both emission and detection". International Conference on Physics of Semiconductor (ICPS), Zürich, Schweiz; 2012-07-29 – 2012-08-03. 2012.

[12] P. Reininger, B. Schwarz, O. Baumgartner, Z. Stanojevic, H. Kosina, and G. Strasser. "Simulation of Dual Wavelength Photonic Crystal Quantum Cascade Laser". International Conference on Physics of Semiconductor (ICPS), Zürich, Schweiz; 2012-07-29 – 2012-08-03. 2012.

Curriculum vitae

Personal information

Address	Kölblgasse 22/29, 1030 Wien, Austria
Telephone	+43 (650) 2360802
E-mail	benedikt.schwarz@tuwien.ac.at
Web-page	http://www.qcllab.at
Nationality	Austria, European Union
Birth	14.12.1986 in Ehenbichl, Austria

Academic career

2011–Present **PhD in technical Sciences**, *TU Wien*, Vienna, Austria.
Institute of Solid State Electronics, Vienna, Austria

thesis: Monolithic integration of mid-infrared photonics

supervisor: Prof. Gottfried Strasser

teaching: exercises in solid state physics

3–6/2015 **Visiting Researcher**, *Harvard University*, Cambridge, Massachusetts, United States of America.
Fellow of School of Engineering and Applied Sciences

topics: Nonlinearities, multi-mode operation and saturation effects in quantum cascade lasers

supervisor: Prof. Federico Capasso

7–11/2011 **Research Assistant**, *TU Wien*, Vienna, Austria.
Institute of Microelectronics

topic: Electrostatic modeling of single and multiple charged oxide traps in modern CMOS devices in the presence of random discrete dopants.

supervisor: Prof. Tibor Grasser

2010–6/2011	**Dipl.Ing./Master of Science** (with honors), *TU Wien*, Austria. MSc in Microelectronics
thesis	Simulation of random dopant fluctuations with a quantum corrected drift diffusion model
supervisor	Prof. Tibor Grasser
description	The general purpose semiconductor device simulator Minimos-NT was extended to a high efficient "atomistic" quantum-corrected drift-diffusion simulator to study parameter fluctuations of modern CMOS devices due to random discrete dopants.
teaching	exercises in programming, analog chip design
2007–2010	**Bachelor of Science** (with honors), *TU Wien*, Vienna, Austria. BSc in Electrical Engineering and Information Technology

Awards and scholarships

2013	**Best Paper Award IRPS 2012**, B. Kaczer et al. "The Relevance of Deeply-Scaled FET Threshold Voltage Shifts for Operation Lifetimes".
2012	**Förderungsstipendium**, Scholarship of the Faculty of Electrical Engineering and Information Technology, TU Wien.
2011	**Würdigungspreis des BMWF**, High honors from the Austrian Federal Ministry of Science and Research for an outstanding graduation.
2008, 2009, 2010, 2011	**Leistungsstipendium**, Scholarships for Excellence of the Faculty of Electrical Engineering and Information Technology, TU Wien.

Research interest and activity

Optoelectonics, mid-infrared photonics, intersubband laser and detectors, plasmonics, integrated photonics, microelectronics, numerical simulation and modeling

13 peer-reviewed publications, h-index of 7 (Google Scholar, November 2015)
1 invited seminar
25 oral presentations (4 invited) at conferences
12 poster presentations at conferences
Reviewer for Superlattices and Microstructures